Head Office: Università degli Studi di Padova

Centro di Ateneo di Studi e Attività Spaziali "Giuseppe Colombo" - CISAS

Ph.D. COURSE IN: Scienze, Tecnologie e Misure Spaziali (STMS)

CURRICULUM: Scienze e Tecnologie per Applicazioni Satellitari e Aeronautiche (STASA)

SERIES XXXIV

Simulation of damage propagation in materials and structures by using peridynamics

Coordinator: *Ch.mo Prof. Francesco Picano*

Supervisor: *Ch.mo Prof. Ugo Galvanetto*

Co-Supervisor: *Ch.mo Prof. Mirco Zaccariotto*

Ph.D. student: *Greta Ongaro*

To *Loreta, Piero, Teresa*
and all my family

Summary

In the last century, the application of innovative high specific stiffness materials like composites and nanocomposites has rapidly increased due to the need of the aerospace industry to employ lighter and more efficient components for aircraft structures. The reduction of aircraft mass has consequently contributed in decreasing fuel consumption and, therefore, in cutting costs and carbon emissions. The main problems, which have however come to light, derive from the difficulty in predicting events that are described by complex laws, and concern the understanding of damage initiation and evolution mechanisms. In order to achieve an accurate description of these complex materials, several approaches based on the classical theory have been employed during the past years. However, their application for damage propagation introduces some difficulties related to the presence of spatial derivatives of displacements in the governing equations, which are undefined wherever continuity of displacement fields is not verified. Many scientists have therefore tried to equip these methods with the capability to simulate crack formation and propagation, but all the proposed strategies present some drawbacks.

Innovative methods based on the peridynamic theory, which is a nonlocal reformulation of classical continuum mechanics, have recently been proposed to overcome these limitations. Considering that the theory deals with integral equations rather than spatial differentiation, peridynamics-based approaches can handle material discontinuities, thus allowing for the modelling of the interfaces between different phases and for the treatment of fracture as a natural material response. Moreover, the introduction of a length parameter enables the analysis of material response at different length scales, from macroscale to nanoscale, thus making the theory suited also to the study of nanocomposite materials. However, peridynamic models are

computationally more expensive than classical continuum ones due to their nonlocal nature, which hinders their application in large-scale simulations. Moreover, since the application of boundary conditions in peridynamics is nonlocal, it is more challenging than that in the classical theory framework. Hence, it is convenient to couple computational methods based on classical continuum mechanics with those based on peridynamics.

In this context, the main purposes of the thesis are the study of local-to-nonlocal coupling, with a focus on the analysis of overall equilibrium issues, and the application of peridynamics for modelling nanocomposite mechanical properties.

The first part of the thesis, i.e., Chapter 2, addresses, for the first time, the problem of the overall equilibrium in the coupling of classical continuum mechanics and peridynamics. The main original contributions of this work are the analytical and numerical evidences that the main reason for the existence of out-of-balance forces is a lack of balance between the local and nonlocal tractions at the coupling interface. Other important contributions are represented by the study of the impact of the shape of the coupling interface on the overall equilibrium, and by the analysis of the effect of the location of the coupling interface in the context of damage propagation problems.

In the second part of the thesis, i.e., in Chapter 3, peridynamics is exploited to model the tensile modulus of polymer-based nanocomposites. The main original contribution of this work is the development of a new approach capable of simulating randomly distributed nanofillers with different sizes and orientations, and of modelling different interphase properties, nanofiller agglomeration phenomena, and nanofiller curvature. The work provides the fundamental bases for a future study of crack formation and propagation in nanocomposite materials.

Sommario

Nel corso dell'ultimo secolo, l'applicazione di materiali innovati ad elevata rigidezza specifica, come compositi e nanocompositi, è aumentata rapidamente a causa della necessità da parte dell'industria aerospaziale di utilizzare componenti sempre più leggeri e performanti. La riduzione della massa degli aeromobili ha contribuito alla diminuzione del consumo di carburante e, quindi, al taglio di costi ed emissioni di anidride carbonica. I maggiori problemi che sono tuttavia emersi derivano dalla difficoltà nel predire eventi che sono descritti da leggi complesse, e riguardano la comprensione dei meccanismi di innesco ed evoluzione delle cricche. Per ottenere una descrizione accurata di questi materiali sono stati impiegati diversi approcci basati sulla teoria classica del continuo. Tuttavia, la loro applicazione allo studio della propagazione di cricche introduce alcune difficoltà legate alla presenza di derivate spaziali degli spostamenti nelle equazioni del moto, le quali non sono definite laddove la continuità dei campi di spostamento non sia verificata. Molti ricercatori hanno perciò dotato questi metodi della capacità di simulare la formazione e propagazione delle cricche, ma tutte le strategie proposte presentano delle criticità.

Per superare questi limiti, sono stati proposti dei metodi basati sulla teoria della peridinamica, una riformulazione non-locale della teoria classica del continuo. Considerando che questa teoria prevede l'utilizzo di equazioni integrali anziché di derivate spaziali, essa è efficace anche in corrispondenza di discontinuità del materiale, e permette quindi la modellazione delle interfacce tra diverse fasi e della frattura come risposta naturale del materiale. L'introduzione di un parametro di lunghezza interno consente inoltre l'analisi della risposta del materiale a diverse scale di grandezza, dalla macroscala alla nanoscala, rendendo la teoria adatta anche allo studio di nanocompositi. Tuttavia, a causa della loro natura non-locale, i

modelli peridinamici hanno un costo computazionale superiore a quello dei modelli basati sulla teoria classica del continuo, e sono quindi difficilmente applicabili allo studio di strutture di grandi dimensioni. La natura non-locale della teoria causa complicazioni anche nell'applicazione delle condizioni al contorno. Di conseguenza, è conveniente accoppiare metodi basati sulla teoria classica del continuo con quelli basati sulla peridinamica.

In questo contesto, gli obiettivi principali della tesi sono lo studio dell'accoppiamento tra meccanica classica del continuo e peridinamica, con particolare attenzione all'analisi dell'equilibrio globale, e l'applicazione della peridinamica allo studio delle proprietà meccaniche dei nanocompositi.

La prima parte della tesi, cioè il Capitolo 2, tratta per la prima volta la questione dell'equilibrio globale in sistemi accoppiati. La maggiore innovazione è rappresentata dai risultati analitici e numerici ottenuti, che provano che la mancanza di equilibrio tra trazioni locali e non-locali nella zona di interfaccia tra i due metodi è la causa del disequilibrio statico strutturale. Altri importanti contributi derivano dallo studio dell'impatto della forma e della posizione della zona di interfaccia sull'entità delle forze di disequilibrio e in problemi che coinvolgono la propagazione di cricche.

Nella seconda parte della tesi, ossia nel Capitolo 3, la peridinamica è utilizzata per studiare le proprietà a trazione di nanocompositi. La maggiore innovazione è costituita dallo sviluppo di un approccio in grado di simulare la distribuzione randomica di nanocariche di diverse dimensioni e orientazioni, e di modellare diverse proprietà di interfaccia, l'agglomerazione e la curvatura delle nanocariche. Questo studio fornisce le basi fondamentali per una futura analisi della formazione e propagazione delle cricche in materiali nanocompositi.

Acknowledgements

First of all, I would like to express my deep gratitude to my Supervisor, Professor Ugo Galvanetto, and my Co-Supervisor, Professor Mirco Zaccariotto, for their continuous support, for inspiring me to do even better, especially in the most stressful periods of this journey, and for being present and ready to help me every time I needed, always with big smiles on their faces.

I am deeply grateful to Doctor Pablo Seleson, for giving me the opportunity to work with him during my Ph.D. study. His immense experience in the fields of peridynamics and computational mechanics has allowed me to significantly increase my knowledge in those areas, while his passion and his deep dedication to the pursuit of perfection have greatly inspired me during my research activity.

I must express my gratitude to Professor Roberta Bertani, for giving me the opportunity to collaborate with her in the preparation, characterization and testing of nanocomposite materials. The possibility to support her in the preparation and analysis of these materials has allowed me to acquire practical skills to work effectively in a laboratory environment.

I'd also like to thank Professor Flora Faleschini and Doctor Sabrina Pastore for their support in the performance of the tensile testing campaign carried out at the Construction materials testing laboratory of the ICEA Department of the University of Padova.

A special thanks to Professor Michele Zappalorto, Professor Marino Quaresimin, Doctor Alessandro Pontefisso and Doctor Mirko Simonetto for supporting me in the performance of the fracture testing campaign carried out at the Multiaxial fatigue and Experimental mechanics laboratories of the DTG Department of the University of Padova.

I'm deeply grateful to my family, especially to my mother and my father, for always believing in me and supporting me during all the phases of this incredible journey. I'd like to thank them for all the sacrifices they made for me and for encouraging me to always give my best and focus on my goals, especially in the most complex and stressful moments.

I would also like to thank all my friends and colleagues for their support and encouragement during these last three years, and especially for the moments of leisure and fun spent together. First of all, Arman, who has always supported me and encouraged me to believe in myself and to be proud of myself, and who has taught me lots of things, especially during my first year of research.
I'd then like to thank Lucia, Giulia, Veronica, Soheil, Francesco, Tao, Alex, Erica and Gloria for their psychological support during this challenging period, for all the funny moments spent together in the office and especially outside the University. A very special thanks to Lucia, Giulia and Veronica, who helped me to spend these three years in a more carefree way.

A special thanks goes to Anna, my best friend, who is like a sister for me and has always been present during all the stages of my life.

Publications

Articles

G. Ongaro, P. Seleson, U. Galvanetto, T. Ni, M. Zaccariotto. Overall equilibrium in the coupling of peridynamics and classical continuum mechanics. *Computer Methods in Applied Mechanics and Engineering*, 381:113515, 2021.

Proceedings

G. Ongaro, R. Bertani, U. Galvanetto, M. Zaccariotto. Peridynamic modelling and experimental verification of nanocomposite properties. In: *Proceedings of the XXVI AIDAA International Congress of Aeronautics and Astronautics*, *In Press*, Persiani Editore, 2021.

M. Zaccariotto, G. Ongaro, T. Ni, P. Seleson, U. Galvanetto. Computational methods coupling peridynamics with classical mechanics: out-of-balance forces in overall structural equilibrium. In: *Proceedings of the XXV AIDAA International Congress of Aeronautics and Astronautics*, Persiani Editore, 2021.

Abstracts

G. Ongaro, P. Seleson, U. Galvanetto, T. Ni, M. Zaccariotto. Overall Equilibrium in the Coupling of Peridynamics and Classical Continuum Mechanics. International Mechanical Engineering Congress & Exposition (IMECE 2021), Virtual Conference, November $1 - 5$, 2021.

G. Ongaro, R. Bertani, U. Galvanetto, M. Zaccariotto. Peridynamic modelling and experimental characterization of polymer/clay nanocomposites. XVI International Conference on Computational Plasticity. Fundamentals and Applications (COMPLAS 2021), Barcelona, Spain, September 7 – 10, 2021.

G. Ongaro, R. Bertani, U. Galvanetto, M. Zaccariotto. Peridynamic modelling and experimental verification of nanocomposites properties. Italian Association of Aeronautics and Astronautics (AIDAA) XXVI International Congress, On-line event hosted by the Tuscany AIDAA Section in Pisa, August 31 – September 3, 2021.

G. Ongaro, P. Seleson, U. Galvanetto, T. Ni, M. Zaccariotto. Overall Equilibrium in the Coupling of Peridynamics and Classical Continuum Mechanics. 16^{th} U.S. National Congress on Computational Mechanics (USNCCM16), Chicago, Illinois, USA, July 25 – 29, 2021.

M. Zaccariotto, G. Ongaro, T. Ni, P. Seleson, U. Galvanetto. Out-of-balance forces in computational methods coupling peridynamics with classical mechanics. 14^{th} World Congress on Computational Mechanics (WCCM XIV and ECCOMAS 2020), Virtual Congress, January 11 – 15, 2021.

P. Seleson, G. Ongaro, U. Galvanetto, T. Ni, M. Zaccariotto. Overall Equilibrium in the Coupling of Peridynamics and Classical Continuum Mechanics. International Mechanical Engineering Congress & Exposition (IMECE 2020), Virtual Conference, November 16 – 19, 2020.

G. Ongaro, U. Galvanetto, T. Ni, P. Seleson, M. Zaccariotto. Overall Equilibrium in Coupled FEM-PD Models. International Mechanical Engineering Congress & Exposition (IMECE 2019), Salt Lake City, Utah, USA, November 10 – 14, 2019.

T. Ni, G. Ongaro, P. Seleson, M. Zaccariotto, U. Galvanetto. Is coupling PD with FEM the way forward to solve in an efficient way crack propagation problems?. In: *2019−Sustainable Industrial Processing Summit*, Vol. 7, pp. 83 – 84, Flogen Star Outreach, Sustainable Industrial Processing Summit & Exhibition

(SIPS2019), Paphos, Cyprus, October 23 – 27, 2019.

U. Galvanetto, T. Ni, G. Ongaro, P. Seleson, M. Zaccariotto. Global Equilibrium in Computational Methods Coupling Peridynamics with Classical Mechanics. 15^{th} U.S. National Congress on Computational Mechanics (USNCCM15), Austin, Texas, USA, July 28 – August 1, 2019.

U. Galvanetto, T. Ni, G. Ongaro, P. Seleson, M. Zaccariotto. The Problem of Static Equilibrium in Computational Methods Coupling Classical Mechanics and Peridynamics. The 10^{th} International Conference on Computational Methods (ICCM2019), Singapore, July 9 – 13, 2019.

M. Zaccariotto, T. Ni, G. Ongaro, P. Seleson, U. Galvanetto. Overall structural equilibrium in Computational Methods Coupling Peridynamics with Classical Mechanics. VI International Conference on Computational Modeling of Fracture and Failure of Materials and Structures (CFRAC 2019), Braunschweig, Germany, June 12 – 14, 2019.

Contents

List of Tables

List of Figures

Abbreviations

ASTM	American Society for Testing and Materials
CCM	Classical continuum mechanics
CCM-PD	Classical continuum mechanics-Peridynamics
CEC	Cation exchange capacity
CT	Compact tension
DB	Dog-bone
D.E.R.^{TM}	Dow Epoxy Resin
DGEBA	Diglycidyl ether of bisphenol A epoxide
ESEM	Environmental Scanning Electron Microscopy
FE	Finite Element
FEM	Finite Element Method
ISO	International Organization for Standardization
MMT	Montmorillonite
$Na^{+}Mt$	Sodium montmorillonite
PD	Peridynamics
PGW	Polymer grade Wyoming
PMB	Prototype microelastic brittle
RVE	Representative volume element
SEM	Scanning Electron Microscopy
TEM	Transmission Electron Microscopy
UC	Unit cell
vdW	van der Waals
XRF	X-ray fluorescence

Nomenclature

A	Bar cross-sectional area
AR	Nanofiller aspect ratio
a	Coefficient
a	Crack length in a compact tension specimen
a_{11}, a_{21}, a_{12}, a_{22}, a_{33}	Material elastic constants
B	Compact tension specimen thickness
B_1, B_2	Subdomains
$\mathcal{B}$	Domain
$\mathcal{B}^+$, $\mathcal{B}^-$	Subregions of the domain $\mathcal{B}$
$\mathcal{B}_{\text{PD}}$	PD subdomain
$\mathcal{B}_{\text{CCM}}$	CCM subdomain
$\overline{\overline{\mathcal{B}}}$	Union of the domain $\mathcal{B}$ and its nonlocal boundary
$\mathbf{b}$	Prescribed body force density field
$\mathbf{C}(\boldsymbol{\xi})$	Material's micromodulus function
C_{ij}	Micromodulus function of the bond connecting nodes i and j
c	Bond stiffness
c_w	Speed of sound in the material
$D^2(\mathbf{u})$	Indicator for the distribution of overall second-order derivatives
d	Coefficient
$d\boldsymbol{\eta}$	Differential vector path length along the closed curve Γ'
$d\hat{l}$	Differential path length over $\mathcal{L}$
$dV_{\mathbf{x}}$	Infinitesimal volume associated to the material point $\mathbf{x}$

$\frac{dV}{V}$	Volume dilatation in the CCM framework
$\partial\mathcal{B}$	Boundary of the domain $\mathcal{B}$
E	Young's modulus
E_{agglm}	Agglomeration Young's modulus
E_{intph}	Interphase Young's modulus
E_m	Matrix Young's modulus
E_{nf}	Nanofiller Young's modulus
E_{11}, E_{22}	Effective tensile moduli obtained by imposing uniaxial tensile strain along x- and y-directions, respectively
$\underline{e}$	Extension scalar state
$\underline{e}^d$	Deviatoric extension state
e_r	Relative out-of-balance error
e_{r_x}, e_{r_y}	Relative out-of-balance errors evaluated in the x- and y-directions
e_{rel}	Relative error
$\{\mathbf{e}_1, \mathbf{e}_2\}$	Normals corresponding to the standard Cartesian orthonormal basis
$F(\boldsymbol{\eta}, \boldsymbol{\xi})$	Scalar-valued even function
F_{ext}	External force
F_{y_A}, F_{y_B}, F_{y_C}	Vertical reaction forces (two-dimensional case)
F_{z_A}, F_{z_B}, F_{z_C}, F_{z_D}	Vertical reaction forces (three-dimensional case)
$\{F_i\}_{i=1,\ldots,N}$	External nodal forces ('reactions' when displacements are imposed)
$F_{1\,i}$, $F_{2\,i}$	x- and y-components of the reaction force
$\boldsymbol{\mathcal{F}}$	Net out-of-balance force
$\mathcal{F}_1$, $\mathcal{F}_2$	x- and y-components of the net out-of-balance force
$\mathbf{f}$	Pairwise force function
$\boldsymbol{f}$	Function equal to the difference between the force vector states at the bond ends
f	Scalar-valued peridynamic force function
f(x)	Function of the ratio x

G_0	Critical energy release rate
g	Coefficient
$\mathcal{H}$	Bond domain
$\mathcal{H}_{\mathbf{x}}$	Finite neighbourhood of the material point $\mathbf{x}$
h	Plate thickness
$\mathbf{I}$	Identity matrix
K	Bulk modulus
K_{Ic}	Mode I fracture toughness
$\underline{\underline{\mathbb{K}}}$	Double state
k	Coefficient
k'	Positive constant
L	Bar length
L_x, L_y	Plate dimensions and RVE side lengths along x- and y-directions
L_{PDx}, L_{PDy}	PD portion side lengths along x- and y-directions
$\mathcal{L}$	Set of collinear material points
$\mathcal{L}_m$	Set of all tensors of order m
$\mathcal{L}_1$	Set of all vector states
$\underline{\mathbf{M}}\,(\underline{\mathbf{Y}})$	Deformed direction vector state
m	Weighted volume
m	Ratio between δ and Δx, usually referred to as m-ratio
N	Total number of nodes
N_{PD}	Total number of PD nodes
N_{FEM}	Total number of FEM nodes
$\mathbf{n}$	Unit vector
$\mathbf{n}(\mathbf{x})$	Outward unit normal to the boundary $\partial\mathcal{B}$ at $\mathbf{x}$
n	Time step number
$\mathrm{P_{cr}}$	Peak or fracture load
$\mathcal{P}$	Plane
Q	Circular subdomain
q	Weighted volume in two dimensions

q	Coefficient
R	Radius of the subdomain Q
$\mathbb{R}$	Set of real numbers
r	Spatial dimension
$\mathcal{S}_{\mathrm{PD}}$	Set of PD nodes x_i^{PD}
$\mathcal{S}_{\mathrm{FEM}}$	Set of FEM nodes x_j^{FEM}
s	Scalar bond stretch
s_0	Critical bond stretch
$\underline{\mathbf{T}}$	Force vector state
$\underline{t}$	Scalar force state
$\mathbf{t}(\mathbf{x}, \mathbf{n})$	Local traction at $\mathbf{x}$ with normal $\mathbf{n}(\mathbf{x})$
t_1, t_2	x- and y-components of the local traction
$\mathrm{t}^{\mathrm{num}}$	Numerically computed local traction
t	Time
$\mathrm{tot}_{\mathrm{nodes}}$	Total number of nodes
$\underline{\mathbf{U}}$	Displacement state
$\mathbf{u}$	Displacement field
$\ddot{\mathbf{u}}$	Second derivative in time of the displacement field $\mathbf{u}$
u_1, u_2	x- and y-components of the displacement field $\mathbf{u}$
$\{u_i\}_{i=1,\dots,N}$	Nodal displacements
u_i^{PD}	Displacements of the PD nodes
u_j^{FEM}	Displacements of the FEM nodes
$u_{x_{IR}}^{\mathrm{FEM}}$, $u_{x_{IR}}^{\mathrm{PD}}$	Displacements of FEM and PD nodes closest to the interface x_{IR}
u_y	Downward vertical displacement (two-dimensional case)
u_z	Downward vertical displacement (three-dimensional case)
V_i	Discretized volume associated to node i
vol	Filler volume fraction
W	Compact tension specimen ligament
W	Total elastic potential energy per unit volume
w	Micropotential

$w_0(\boldsymbol{\xi})$	Work required to break a single bond
wt	Filler weight fraction
$\underline{\mathbf{X}}\langle\boldsymbol{\xi}\rangle$	Reference position vector state
$\underline{x}$	Reference position scalar state
$\mathbf{x}$	Material point
x	Ratio between the crack length a and the ligament W
x_{IL}, x_{IR}	Left and right coupling interfaces
X_Q, Y_Q	x- and y-coordinates of the centre of the subdomain Q
X_1, X_2, Y_1, Y_2, Y_B	Parameters used to define curves and bounds of subdomains
$\underline{\mathbf{Y}}\langle\boldsymbol{\xi}\rangle$	Deformation vector state
$\underline{y}$	Deformation scalar state
α	Positive constant
α'	Positive constant proportional to the shear modulus
$\beta(\boldsymbol{\xi})$	Partial-volume correction factor
Γ	Interface between the PD and CCM subdomains
Γ'	Closed curve
γ	Correction factor
Δx	Grid spacing in the x-direction
Δy	Grid spacing in the y-direction
Δz	Grid spacing in the z-direction
Δt	Time step
Δt_{crit}	Critical time step
δ	PD horizon radius
ε_{ij}	ij component of the infinitesimal strain tensor
ε^d_{ij}	ij component of the deviatoric strain tensor
$\overline{\varepsilon}_{ij}$	ij component of the average strain tensor
$\boldsymbol{\eta}$	Relative displacement vector
θ	Volume dilatation
κ_{intph}	Interphase factor
$\lambda(\|\boldsymbol{\xi}\|)$	Micromodulus function
μ	Shear modulus

$\mu(\boldsymbol{\xi}, t)$	History-dependent scalar-valued function in bond-based PD
ν	Poisson's ratio
ν_m	Matrix Poisson's ratio
ν_{nf}	Nanofiller Poisson's ratio
ν_{21}, ν_{12}	Effective Poisson's ratios obtained by imposing uniaxial tensile strain along x- and y-directions, respectively
$\boldsymbol{\xi}$	Initial relative position vector
$(\boldsymbol{\xi}, \boldsymbol{\zeta})$	Pairs of bonds
ρ	Volumetric mass density
ρ_m	Matrix volumetric mass density
ρ_{nf}	Nanofiller volumetric mass density
$\underline{\varrho}$	History-dependent scalar-valued function in state-based PD
$\boldsymbol{\sigma}$	Piola-Kirchhoff stress tensor
σ_{ij}	ij component of the stress tensor
$\overline{\sigma}_{ij}$	ij component of the average stress tensor
$\boldsymbol{\tau}(\mathbf{x}, \mathbf{n})$	Areal force density at a point $\mathbf{x}$ in $\mathcal{B}$ in the direction of $\mathbf{n}$, and nonlocal traction at $\mathbf{x}$ with normal $\mathbf{n}(\mathbf{x})$
τ_1, τ_2	x- and y-components of the nonlocal traction
τ^{num}	Numerically computed nonlocal traction
$\varphi(\mathbf{x}, t)$	Local damage index in bond-based PD
$\varphi_{\mathbf{x}}$	Local damage index in state-based PD
$\chi_\delta(\|\boldsymbol{\xi}\|)$	Characteristic function
Ω_A, Ω_B	Non-overlapping subdomains
$\underline{\omega}$	Influence function

Introduction

Material properties modelling and failure analysis in the framework of classical continuum mechanics

Accurate material properties modelling is a major issue for many practical applications. Considering that experimental testing is very expensive and time-consuming, numerical analysis is an essential tool for characterising the properties of various materials and modelling their performance, thus enabling the increase of their reliability and the expansion of their application fields. During the past years, several analytical and numerical approaches based on classical continuum mechanics (CCM) have been employed to these ends. Despite the effectiveness of CCM-based methods in dealing with the modelling of the macroscopically relevant properties of various materials, CCM approaches lack an internal length parameter which could enable the modelling of materials and structures at different scales [1]. Furthermore, the unavoidable presence of small or large cracks in many engineering structures still represents a major challenge for the simulation of a full structural life cycle [2, Chapter 16], [3–6]. Even though classical continuum mechanics-based numerical methods are extensively used for the simulation of different structural problems, their application for damage prediction introduces some challenges arising from the presence of spatial derivatives of displacements in the governing equations, which are undefined when the displacement fields are discontinuous [7], [8, Chapter 1]. Since cracks are, in fact, discontinuities in the domain where the problem is defined, they do not satisfy the basic underlying continuum hypothesis of classical continuum mechanics. In order to achieve an accurate description of large and complex structures, which can be affected by different levels of damage in their various parts or components, many scientists have tried to equip CCM-based numerical methods, in particular

the finite element method (FEM), with the capability to simulate crack formation and propagation [9]. The most popular approaches that have been developed in the last years are: partition of unity finite element method [10, 11], extended finite element method [12, 13], element erosion [14, 15], phase field model [16–19], and interface elements with a cohesive zone model [20–22]. Even if these different strategies have all been used so far, they all present some drawbacks [8, Chapter 10], [9]. The computational burdens and complexity of the partition of unity finite element method prevent its implementation in three-dimensional problems as well as its application for the solution of problems involving dynamic crack branching and multiple crack growth and interaction in complex patterns. Moreover, another inherent drawback of this method is the unavoidable presence of a blending region in correspondence with the neighbouring elements of the tip element in which the crack tip is positioned. Since the partition of unity does not hold for those elements, the blending region is characterized by a lower solution accuracy [23]. The issues related to the use of the extended finite element method to model propagating cracks are manifold. First, in dynamic brittle fracture problems, one may need to significantly modify the input fracture energy in the numerical method in order to match the values of the crack propagation speeds obtained from experimental investigations [24, 25]. Second, this method requires crack path tracking, phenomenological damage models, extra damage criteria regarding the angle of propagation and the stress state around the crack tip, and branching criteria, which are not reliable in practice [25, 26]. Third, the implementation of this method may introduce some computational burdens related to the need to subdivide the cut elements to perform the numerical integration process [8, Chapter 10], [25]. Although element erosion has been extensively used to simulate fracture in a number of application areas, this approach suffers from the problem of nonconvergence of the numerical solution under mesh refinement [8, Chapter 10]. The phase field model presents instead issues concerning spurious branching formation and inconsistency of branching patterns and angles with respect to the ones observed in experiments [27–29]. In addition, the relationship between quantitative phase field model predictions of dynamical branching instabilities and experimental observations is not yet clear and well un-

derstood [30]. Even though interface elements coupled with cohesive zone models have been successfully implemented, their application is limited due to the need of an a priori knowledge of the crack path, since cracks can only propagate along the element boundaries [22, 31, 32]. Furthermore, as in the case of the extended finite element method, cohesive zone models require extra damage criteria [26].

Alternative approaches: from classical continuum mechanics to peridynamics

In recent years, innovative computational methods based on peridynamics have been proposed and implemented in order to solve complex problems involving discontinuities, such as damage initiation, crack propagation and material interfaces. The peridynamic (PD) theory is a nonlocal reformulation of classical continuum mechanics based on integro-differential equations, since it defines the equation of motion by substituting the divergence of the stress tensor, involved in the classical theory formulation, with an integral operator. Considering that the theory deals with integral equations rather than spatial differentiation, the peridynamic governing equations are valid even in presence of discontinuous displacement fields, and are therefore defined even at crack surfaces, allowing fracture and failure to be treated as a natural material response. Peridynamics introduces a concept of damage for a material point, allowing to predict the evolution of cracks, including their nucleation, their propagation direction, and the points where they start and stop, without having to define any criteria for triggering, bifurcation, and deviation phenomena [9]. The PD theory was proposed in the year 2000. The original bond-based version of the theory was presented in [7], and then extended in the year 2007 to its final form, called state-based PD theory, in [33]. Other nonlocal models were previously proposed in [34–37].

The name of the theory derives from the Greek roots for near ("*peri*") and force ("*dyna*"), and reflects its main assumption, which is that the body is composed of material points which can interact with each other provided that they are located within a finite distance called PD horizon. The concept of horizon is introduced in the PD formulation to indicate the size of the region where nonlocal interactions of a

material point with other points take place. The introduction of this length parameter is another important feature of peridynamics, since the horizon size assumes the role of characteristic length scale of the materials and the phenomena under investigation [38]. As a consequence, PD enables the modelling of material properties and the analysis of material response at different length scales, from macroscale to nanoscale [39].

In recent years, peridynamics has been exploited to model several material systems, including ductile metals [40], ceramics [41, 42], polycrystalline materials [43], concrete [44] and composite materials [45–50]. PD theory has also been employed for the analysis of impact [51,52], fatigue [53], and dynamic fracture [54–57], and for the modelling of other physical fields, including thermal [58,59] and diffusion [60–62] fields, and of corrosion damage mechanics [63, 64].
Several PD models have also been developed to study multiphysics problems including thermo-mechanical [41,42,65], chemo-mechanical [65,66], hydro-mechanical [67], and electro-mechanical [68] phenomena. Moreover, as already stated, peridynamics is not limited to macroscale analysis, but can also be applied to model microscale and nanoscale systems and to implement homogenization and multiscale schemes.

Despite the effectiveness of PD models in solving problems concerning crack propagation [46, 51, 55, 56, 69–78], PD models are computationally more expensive than CCM models due to their nonlocal nature. The computational expense issue is even more evident when implicit time integration is considered, since the number of nonzero elements in the PD tangent stiffness matrix is typically much bigger than that in the corresponding CCM model solved with the FEM [8, Chapter 14]. Therefore, the considerable computational cost of PD models hinders their application in large-scale, geometrically complex simulations [61]. Furthermore, PD numerical implementations may be affected by some additional difficulties related to the definition of nonlocal boundary conditions [7]. In nonlocal theories the boundaries are fuzzy, so that prescribed displacement or load conditions have to be imposed in finite volumetric regions rather than on boundary surfaces [79–82]. Most of the time, such extension of classical boundary conditions is not clearly defined [8, Chapter 14]. Another weak point of PD models is the so called surface effect, which consists in

the presence of some spurious effects affecting the numerical solution in the region close to the boundary of a finite domain [55, 83]. The occurrence of these effects is related to the fact that the peridynamic material parameters are derived under the assumptions of a infinite domain and of a fully embedded neighbourhood for each material point in the solution domain, which are not valid for material points close to the boundary. In a PD model, the mechanical properties of the portion of the domain close to the boundary result to be artificially different from those of the bulk region. Hence, it would be convenient to couple PD and CCM models in order to take advantage of the benefits of both models while avoiding their drawbacks [9, 84, 85].

Following the analysis of the various features, benefits, drawbacks, and application fields of the peridynamic theory, we decided to concentrate our attention on two particularly interesting and topical aspects, that is the study of local-to-nonlocal coupling, with a focus on the analysis of the overall static equilibrium issues affecting CCM-PD coupled systems, and the application of PD for modelling the mechanical properties of polymer-based nanocomposites.

Local-to-nonlocal coupling

In CCM-PD coupling, usually small areas of a domain, which might be affected by the presence of discontinuities, are described with a PD model, whereas the remaining parts of the domain are represented through a more efficient CCM model [9, 86, 87]. In particular, it is common practice to couple PD models based on the meshfree discretization of [51] with CCM models discretized using the FEM. Even though PD models can be also discretized with the FEM [88], in the work presented in this thesis FEM is used only to denote discretization of CCM models. Coupling FEM meshes with PD grids (or, more generally, coupling local and nonlocal models) is not as simple as sharing nodes between meshes, as it is frequently done in FEM codes when different types of elements are connected to each other [9, 89].

As summarized in [9], local-to-nonlocal coupling has led to a great research effort (much of it concerning the coupling of CCM and PD models) resulting in the development of a variety of techniques, including the optimization-based [90–92],

partitioned [93,94], Arlequin [95], morphing [96–99], quasi-nonlocal [100,101], blending [102, 103], splice [104], variable horizon [104], and partial stress [104] methods, among others; a recent comprehensive review of these methods can be found in [105]. In the context of the PD theory, the first paper to deal with this type of coupling was [106], in which bond-based PD grids and FEM meshes were coupled by embedding PD nodes within FEM elements. Other early works on the coupling of FEM meshes and PD grids can be found in [107–110]. CCM-PD coupling is still an area in which active research is carried out, because most of the coupling methods proposed in the above listed papers are affected by some kind of arbitrariness or spurious effects that need to be overcome [9]. In the first part of this thesis, i.e., in Chapter 2, we are interested in the coupling technique proposed in a series of papers [57, 84, 111–113], which can be seen as an application of the splice method. For the first time, we address the problem of the overall equilibrium in CCM-PD coupled models by studying the origin of out-of-balance forces and discussing possible ways to reduce them [9].

The analysis presented in Chapter 2 shows that the absence of overall equilibrium in a CCM-PD coupled system results from the lack of balance between the local and nonlocal tractions at the coupling interface [9]. The concept of lack of force reciprocity in CCM-PD coupled models and how it leads to failure of Newton's third law between two given objects was discussed in [102]. However, a thorough investigation of this effect and its manifestation in global structural equilibrium in CCM-PD coupled systems has not been presented. The closest studies in this regard from the literature concern patch-test consistency and the so-called "ghost" forces; these are non-physical forces that arise in the transition between local and nonlocal regions whenever a coupling method does not pass a patch test [105]. Unfortunately, such studies generally provide only a qualitative assessment of whether a CCM-PD coupled model passes or not a patch test and often limit the analysis to a simple constant strain solution (i.e., a linear patch test) [9]. In Chapter 2, in contrast, we present a detailed analysis of the balance between local and nonlocal tractions at coupling interfaces along with a practical quantitative way to assess the resulting out-of-balance error through computation of the reaction forces. Part of the work

presented in Chapter 2 has been published in [9].

Peridynamics as a tool for modelling nanocomposite properties

In the second part of this thesis, i.e., in Chapter 3, we are interested in the study of nanocomposite mechanical properties. Following the ever-increasing interest shown by the scientific community for polymer-based materials reinforced with nanoclay platelets, we decided to focus our investigation on this specific class of materials, although the PD-based approach presented in Chapter 3 can be easily exploited for the analysis of different types of nanocomposites.

The enhancement of the performance of polymer-based nanocomposites and the increase of their reliability require a proper understanding of their properties. Several investigations focused on the experimental characterization of polymer-based nanocomposites are reported in literature [114–117]. The analytical and numerical approaches that have been developed and employed for the modelling of nanocomposite properties can be in principle divided into three categories, i.e., atomistic, continuum, and multiscale modelling techniques. As concerns atomistic modelling approaches, their capability is limited to the performance of simulations at very short time and small length scales [118,119]. The results obtained through these molecular-scale analyses cannot be easily scaled up, since the selected model domains (i.e., unit cells) are not statistically representative of the whole material. Moreover, atomistic modelling techniques neglect the interaction between different particles and cannot capture nanofillers orientation and agglomeration phenomena [120]. In continuum mechanics, the phenomena taking place at nanoscale are not directly modeled, since the starting point of continuum simulations is moved to the microscale and the reinforcing filler is treated as a continuum medium. From analytical point of view, both micromechanics rules and homogenization techniques were and still are employed to model the mechanical behaviour of polymer-based nanocomposites. Some of the most widely used models are the dilute concentration approximation [121], the Mori-Tanaka approach [122–125], the double inclusion model [126] and the self-consistent techniques [127, 128], which are all developed based on Eshelby equivalent inclusion approach [129,130]. Apart from these Eshelby-type micromechanical models, various

micromechanics rules have also been employed to study nanocomposite properties. Among them, the most commonly used are the rule of mixture [131–133], Halpin-Tsai [134–137] and Tsai-Hahn [138] models. However, an important limitation which affects conventional micromechanics rules is the incapability to model the interactions between different particles. From numerical point of view, the modelling of polymer-based nanocomposites was and still is most of the time accomplished using finite element-based techniques [139–143]. Even though FE-based approaches are widely employed both in academia and industry, they present some limitations. For instance, some meshing problems could arise when modelling regions containing particles characterized by an high aspect ratio (i.e., the ratio between nanofillers characteristic length and thickness) due to elements distortion issues, which cause a huge decrease of the precision of the computations [143]. Another complexity lies in the modelling of the interphase region, since it is the portion of the domain where the stress transfer mechanism takes place, thus requiring a proper selection of element types, geometrical and mechanical properties. Moreover, in some FEM-based analyses reported in literature, the interphase between nanofillers and polymer matrix was neglected and a perfect bonding condition was assumed [140,144,145]. The accurate modelling of this peculiar region cannot be overlooked, due to its strong influence on the overall properties of the nanocomposite material [127,146–150]. In multiscale analyses, atomistic and continuum mechanics-based approaches are merged together in the same computational framework [127,151–156]. The need to develop bridging methods to transfer structure-property relations between different length and time scales over several orders of magnitude introduces, however, some complexities and is considered the main challenge of these modelling techniques.

In the work presented in Chapter 3, peridynamics is exploited for modelling the tensile modulus of polymer/clay nanocomposites. As already stated, peridynamics is not limited to macroscale analyses, but can instead be applied to model microscale and nanoscale systems and to implement homogenization and multiscale schemes. The growing interest in composite and nanocomposite technologies has in fact given a boost to the development of computational homogenization schemes based on the representative volume element (RVE) or unit cell (UC) con-

cepts [157–159]. In [160], a PD-based unit cell model was developed to compute the effective properties of composites trough a microstructure informed homogenization scheme, whereas, in [161], the authors presented a new PD-based homogenization approach to model microstructures with orthotropic constituents in a finite element framework. In [162], bond-based PD was employed to develop an RVE-based model to study fibre reinforced composites, whereas, in [163] and [164], the RVE concept was exploited to model polymer-based nanocomposite properties.

In Chapter 3, a mesoscale representative volume element homogenization is implemented in a bond-based PD framework to model the effective tensile modulus of polymer/clay nanocomposites. The inherently stochastic nature of nanocomposites, originating from the stochastic properties of the nanofillers and the randomness involved with the manufacturing processes, is taken into account by selecting the most suitable probability distribution function for each random geometrical or mechanical property in the model. The proposed method has the capability to model randomly distributed nanofillers with different sizes and orientations, and to easily simulate interphase regions characterized by different properties, including both strong and weak interfacial adhesion and compatibility, and nanofiller agglomeration phenomena without the need to implement multistep homogenization procedures or to define equivalent homogenized particles or effective particles [139, 165–167]. Thanks to these features, the tensile modulus of nanocomposites with different nanoclay contents and various interfacial, dispersion and distribution characteristics, resulting from the employment of different processing techniques, can be accurately reproduced. In addition to the possibility to simulate the effect of nanoclay agglomerations, which is an aspect which is often overlooked in the literature, a further innovative feature of the newly developed algorithm is the capability to model nanofillers curvature. Even if the non-straight shape assumed by clay platelets when dispersed within a host matrix (as a result of their inherently high aspect ratio) is clearly visible from electron microscopy images [168–172], the modelling of nanoclays curvature is almost absent in literature. Almost all studies conducted so far have in fact assumed and simulated straight nanoplatelets, except from [145], where the authors simulated the clays curvature using FEM, and [164], where bond-based PD

was instead exploited to model a polymer matrix nanomodified through a different kind of filler, i.e., carbon nanotubes.
Moreover, the meshless nature of the proposed method avoids elements distortion issues affecting FEM-based models dealing with high aspect ratio of nanofillers, and makes it possible to easily simulate common high aspect ratio values without experiencing any reduction in the accuracy of calculations [143]. In order to validate the capabilities of the newly developed approach, we compare the numerical results with experimental data reported in literature. In addition, the effectiveness and versatility of the proposed PD-based technique are further demonstrated by performing an experimental characterization of clay-loaded epoxy resins, whose results are reported in Chapter 3 together with a comparison with the numerically computed data.

The effective tensile moduli obtained through the mesoscale RVE analysis presented in Chapter 3 represent the fundamental bases for a future study focused on the modelling of crack nucleation and propagation in polymer-based nanocomposites and on the investigation of the dependence of the material fracture toughness on the nanofiller weight content. Appendix B reports some preliminary experimental results obtained by performing fracture tests on clay-loaded epoxy resins, which can be exploited in future for model validation purposes.

Chapter 1

Overview of the peridynamic theory

1.1 Mathematical formulation of the bond-based version of PD theory

In a domain $\mathcal{B} \subset \mathbb{R}^r$ with r the spatial dimension, described with a PD model, each material point $\mathbf{x} \in \mathcal{B}$ interacts with all the other material points located within a finite neighbourhood, $\mathcal{H}_{\mathbf{x}}$, of that material point. The bond-based peridynamic equation of motion for any material point $\mathbf{x} \in \mathcal{B}$ at time $t \geqslant 0$ is given by [7]:

$$\rho(\mathbf{x})\ddot{\mathbf{u}}(\mathbf{x},t) = \int_{\mathcal{H}_{\mathbf{x}}} \mathbf{f}\left(\mathbf{u}\left(\mathbf{x}',t\right) - \mathbf{u}\left(\mathbf{x},t\right), \mathbf{x}' - \mathbf{x}\right) dV_{\mathbf{x}'} + \mathbf{b}(\mathbf{x},t), \tag{1.1}$$

where ρ is the mass density, $\ddot{\mathbf{u}}$ is the second derivative in time of the displacement field $\mathbf{u}$, $\mathbf{f}$ denotes the pairwise force function, with units of force per unit volume squared, that the material point $\mathbf{x}'$ exerts on the material point $\mathbf{x}$, and $\mathbf{b}$ is a prescribed body force density field. The neighbourhood $\mathcal{H}_{\mathbf{x}}$ is defined by:

$$\mathcal{H}_{\mathbf{x}} := \{\mathbf{x}' \in \mathcal{B} : \|\mathbf{x}' - \mathbf{x}\| \leqslant \delta\}, \tag{1.2}$$

where $\delta > 0$ is the PD horizon radius (see Figure 1.1). For material points in the bulk of the body, i.e., material points $\mathbf{x} \in \mathcal{B}$ further than δ from the boundary of the body, $\partial\mathcal{B}$, the neighbourhood $\mathcal{H}_{\mathbf{x}}$ represents a line segment in one dimension, a disk in two dimensions, and a ball in three dimensions centered at $\mathbf{x}$. As shown in Figures 1.1 and 1.2, the relative position vector of the two material points $\mathbf{x}$ and $\mathbf{x}'$

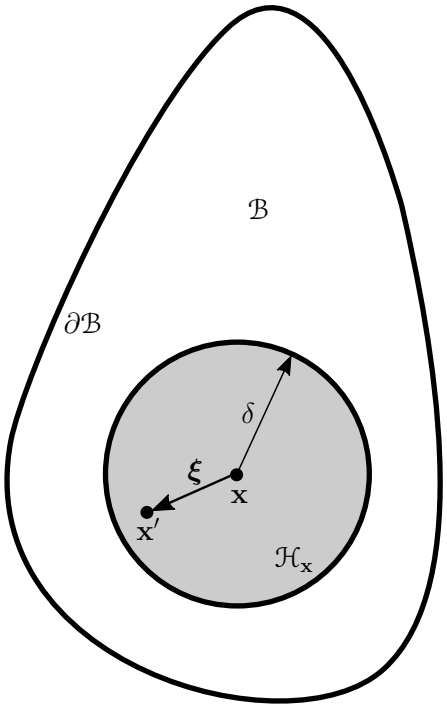

Figure 1.1: Representation of a generic PD domain $\mathcal{B}$; each material point $\mathbf{x}$ interacts directly with the material points in its neighbourhood $\mathcal{H}_{\mathbf{x}}$ through bonds.

in the reference configuration (or initial relative position vector) is denoted by:

$$\boldsymbol{\xi} := \mathbf{x}' - \mathbf{x}, \tag{1.3}$$

which represents the standard peridynamic notation for a bond. In the deformed configuration at time $t > 0$, the two material points $\mathbf{x}$ and $\mathbf{x}'$ would be displaced, respectively, by $\mathbf{u}(\mathbf{x}, t)$ and $\mathbf{u}(\mathbf{x}', t)$. As represented in Figure 1.2, the corresponding relative displacement vector is denoted by:

$$\boldsymbol{\eta} := \mathbf{u}(\mathbf{x}', t) - \mathbf{u}(\mathbf{x}, t) = \mathbf{u}'(t) - \mathbf{u}(t). \tag{1.4}$$

The force vector $\mathbf{f}$, also called bond force, is required to satisfy the following condition [51]:

$$\mathbf{f}(-\boldsymbol{\eta}, -\boldsymbol{\xi}) = -\mathbf{f}(\boldsymbol{\eta}, \boldsymbol{\xi}) \quad \forall \boldsymbol{\eta}, \boldsymbol{\xi}, \tag{1.5}$$

in order to assure the conservation of the linear momentum, and it is also required to assure the conservation of the angular momentum, which is expressed by the following relation [51]:

$$(\boldsymbol{\eta} + \boldsymbol{\xi}) \times \mathbf{f}(\boldsymbol{\eta}, \boldsymbol{\xi}) = \mathbf{0} \quad \forall \boldsymbol{\eta}, \boldsymbol{\xi}. \tag{1.6}$$

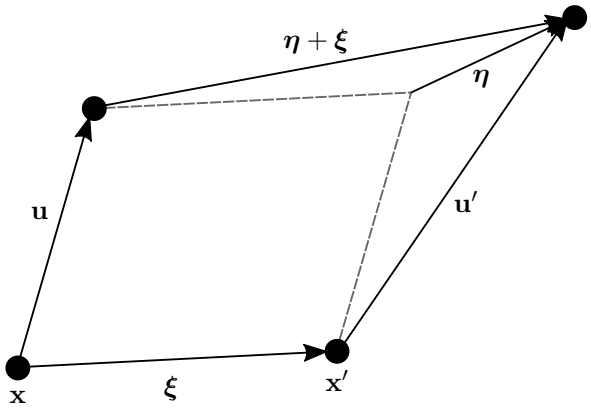

Figure 1.2: Representation of the relative position vectors (initial and current) and the relative displacement vector between the two material points $\mathbf{x}$ and $\mathbf{x}'$.

As a direct consequence of (1.6), the force vector must act in the direction of the line connecting the two material points $\mathbf{x}$ and $\mathbf{x}'$, i.e., in the direction of their relative position vector in the deformed configuration ($\boldsymbol{\eta}+\boldsymbol{\xi}$), usually referred to as current relative position vector (see Figure 1.2), so as not to produce any moment on them. In light of (1.5) and (1.6), $\mathbf{f}(\boldsymbol{\eta},\boldsymbol{\xi})$ can be also expressed as [7]

$$\mathbf{f}(\boldsymbol{\eta},\boldsymbol{\xi}) = F(\boldsymbol{\eta},\boldsymbol{\xi})(\boldsymbol{\eta}+\boldsymbol{\xi}) \quad \forall \boldsymbol{\eta},\boldsymbol{\xi}, \tag{1.7}$$

where $F(\boldsymbol{\eta},\boldsymbol{\xi})$ is an appropriate scalar-valued even function.

1.1.1 Elasticity in bond-based PD

In bond-based peridynamics, the elastic behaviour of a material is defined by introducing the concept of microelasticity. A material is described as microelastic if it complies with the following condition [7]:

$$\oint_{\Gamma'} \mathbf{f}(\boldsymbol{\eta},\boldsymbol{\xi}) \cdot d\boldsymbol{\eta} = 0 \quad \forall \textit{closed curve } \Gamma',\ \forall \boldsymbol{\xi} \neq 0, \tag{1.8}$$

where $d\boldsymbol{\eta}$ is the differential vector path length along the closed curve Γ'. Such condition states that, when dealing with a microelastic material, the line integral is path independent, thus the net work done by the response force along any closed curve is zero, as in classical elasticity. Furthermore, recalling Stoke's Theorem, if the force vector $\mathbf{f} = (f_1, f_2, f_3)$ is continuously differentiable with respect to $\boldsymbol{\eta} = (\eta_1, \eta_2, \eta_3)$, then (1.8) is fulfilled when the following necessary and sufficient condition holds:

$$\nabla_{\boldsymbol{\eta}} \times \mathbf{f} = \left(\frac{\partial f_3}{\partial \eta_2} - \frac{\partial f_2}{\partial \eta_3}\right)\mathbf{i} + \left(\frac{\partial f_1}{\partial \eta_3} - \frac{\partial f_3}{\partial \eta_1}\right)\mathbf{j} + \left(\frac{\partial f_2}{\partial \eta_1} - \frac{\partial f_1}{\partial \eta_2}\right)\mathbf{k} = \mathbf{0} \quad \forall \boldsymbol{\xi} \neq \mathbf{0}, \tag{1.9}$$

where $(\mathbf{i}, \mathbf{j}, \mathbf{k})$ represents the orthonormal base of the reference system $Oxyz$. Moreover, on the basis of Stoke's Theorem, given that the peridynamic force field is conservative and irrotational, the force vector $\mathbf{f}$ can be derived from a scalar-valued and differentiable function w, called micropotential, as follows [7]:

$$\mathbf{f}(\boldsymbol{\eta}, \boldsymbol{\xi}) = \frac{\partial w}{\partial \boldsymbol{\eta}}(\boldsymbol{\eta}, \boldsymbol{\xi}) \quad \forall \boldsymbol{\eta}, \boldsymbol{\xi}. \tag{1.10}$$

The micropotential, which is defined as the energy in a single bond, has dimensions of energy per unit volume squared, and depends only on the relative displacement vector $\boldsymbol{\eta}$ through the scalar distance between the deformed points [51]. Consequently, a scalar-valued function $\hat{w}$ can be defined for an isotropic microelastic material as [7]:

$$w(\boldsymbol{\eta}, \boldsymbol{\xi}) := \hat{w}(\|\boldsymbol{\eta} + \boldsymbol{\xi}\|, \boldsymbol{\xi}) \quad \forall \boldsymbol{\eta}, \boldsymbol{\xi}, \tag{1.11}$$

which, substituted in (1.10), allows to define a general peridynamic force function aligned with the relative position vector [7]:

$$\mathbf{f}(\boldsymbol{\eta}, \boldsymbol{\xi}) = f(\|\boldsymbol{\eta} + \boldsymbol{\xi}\|, \boldsymbol{\xi})(\boldsymbol{\eta}, \boldsymbol{\xi}) \quad \forall \boldsymbol{\eta}, \boldsymbol{\xi}, \tag{1.12}$$

where $f(\|\boldsymbol{\eta} + \boldsymbol{\xi}\|, \boldsymbol{\xi})$ is a scalar-valued even function which is obtained by deriving the micropotential such that [7]

$$f(p, \boldsymbol{\xi}) = \frac{\partial \hat{w}}{\partial p}(p, \boldsymbol{\xi}), \quad p = \|\boldsymbol{\eta} + \boldsymbol{\xi}\|, \quad \forall \boldsymbol{\eta}, \boldsymbol{\xi}, \tag{1.13}$$

and that actually corresponds to $F(\boldsymbol{\eta}, \boldsymbol{\xi})$ in (1.7), but with an highlight on the dependence of the scalar part on the relative distance.

To conclude, the total elastic potential energy per unit volume at a given material point $\mathbf{x}$ (i.e., the local strain energy density), W, can be computed by integrating the micropotential in (1.10) over all the bonds connected to the material point $\mathbf{x}$, such that [51]

$$W = \frac{1}{2} \int_{\mathcal{H}_{\mathbf{x}}} w(\boldsymbol{\eta}, \boldsymbol{\xi}) dV_{\mathbf{x}'}, \tag{1.14}$$

where the factor $\frac{1}{2}$ is introduced because each of the two interacting material points at the end of a bond possesses half the potential energy in the bond.

1.1.2 Linearized version of the theory

The PD theory can be applied to study a wide range of problems without any restriction on the magnitude of the deformation to which a system is subjected. However, since the case studies addressed in this thesis are focused on the elastic behaviour of materials, the assumption of small deformations and displacements is made herein. In this sense, the linearized version of the force vector $\mathbf{f}$ can be derived by assuming that $(\|\boldsymbol{\eta}+\boldsymbol{\xi}\|-\|\boldsymbol{\xi}\|)/\|\boldsymbol{\xi}\| \ll 1$ for all $\boldsymbol{\xi}$, and by performing a first-order Taylor expansion of $\mathbf{f}(\boldsymbol{\eta},\boldsymbol{\xi})$ in (1.7) about $\boldsymbol{\eta}$ such that

$$\mathbf{f}(\boldsymbol{\eta},\boldsymbol{\xi}) = \mathbf{C}(\boldsymbol{\xi})\boldsymbol{\eta} + \mathbf{f}(\mathbf{0},\boldsymbol{\xi}) \quad \forall \boldsymbol{\eta},\boldsymbol{\xi}, \tag{1.15}$$

where $\mathbf{C}(\boldsymbol{\xi})$ is defined as the material's micromodulus function, whose value is a second-order tensor of the force vector $\mathbf{f}$ given by [51]:

$$\mathbf{C}(\boldsymbol{\xi}) := \frac{\partial \mathbf{f}}{\partial \boldsymbol{\eta}}(\mathbf{0},\boldsymbol{\xi}) = \begin{bmatrix} \frac{\partial f_1}{\partial \eta_1}(\mathbf{0},\boldsymbol{\xi}) & \frac{\partial f_1}{\partial \eta_2}(\mathbf{0},\boldsymbol{\xi}) & \frac{\partial f_1}{\partial \eta_3}(\mathbf{0},\boldsymbol{\xi}) \\ \frac{\partial f_2}{\partial \eta_1}(\mathbf{0},\boldsymbol{\xi}) & \frac{\partial f_2}{\partial \eta_2}(\mathbf{0},\boldsymbol{\xi}) & \frac{\partial f_2}{\partial \eta_3}(\mathbf{0},\boldsymbol{\xi}) \\ \frac{\partial f_3}{\partial \eta_1}(\mathbf{0},\boldsymbol{\xi}) & \frac{\partial f_3}{\partial \eta_2}(\mathbf{0},\boldsymbol{\xi}) & \frac{\partial f_3}{\partial \eta_3}(\mathbf{0},\boldsymbol{\xi}) \end{bmatrix}. \tag{1.16}$$

The second-order tensor from (1.16) can be expressed as (*cf.* (1.7)):

$$\mathbf{C}(\boldsymbol{\xi}) = \boldsymbol{\xi} \otimes \frac{\partial F}{\partial \boldsymbol{\eta}}(\mathbf{0},\boldsymbol{\xi}) + F(\mathbf{0},\boldsymbol{\xi})\mathbf{I} \quad \forall \boldsymbol{\xi}, \tag{1.17}$$

where $\otimes$ is the dyadic or tensor product between two vectors which results in a tensor of the second-order, and $\mathbf{I}$ is the identity matrix. On the basis of Stoke's Theorem (*cf.* (1.9)), for a linear microelastic material, the micromodulus $\mathbf{C}(\boldsymbol{\xi})$ results to be symmetric, such that

$$\mathbf{C}(\boldsymbol{\xi}) = \mathbf{C}^T(\boldsymbol{\xi}) \quad \forall \boldsymbol{\xi}, \tag{1.18}$$

which implies the existence of a scalar-valued even function $\lambda(\boldsymbol{\xi})$ that satisfies the following relation [7]:

$$\boldsymbol{\xi} \otimes \frac{\partial F}{\partial \boldsymbol{\eta}}(\mathbf{0},\boldsymbol{\xi}) = \lambda(\boldsymbol{\xi})\boldsymbol{\xi} \otimes \boldsymbol{\xi} \quad \forall \boldsymbol{\xi}, \tag{1.19}$$

where $\lambda(\boldsymbol{\xi})$ is defined by:

$$\lambda(\boldsymbol{\xi}) := \frac{\boldsymbol{\xi}}{\|\boldsymbol{\xi}^2\|} \frac{\partial F}{\partial \boldsymbol{\eta}}(\mathbf{0},\boldsymbol{\xi}) \quad \forall \boldsymbol{\xi}. \tag{1.20}$$

Substituting (1.19) in (1.17), the micromodulus function of a microelastic material can be expressed as:

$$\mathbf{C}(\boldsymbol{\xi}) = \lambda(\boldsymbol{\xi})\boldsymbol{\xi} \otimes \boldsymbol{\xi} + F(\mathbf{0}, \boldsymbol{\xi})\mathbf{I} \quad \forall \boldsymbol{\xi}, \tag{1.21}$$

and, consequently, the linearized version of the peridynamic force function vector $\mathbf{f}$ can be written as:

$$\mathbf{f}(\boldsymbol{\eta}, \boldsymbol{\xi}) = \left[\lambda(\boldsymbol{\xi})\boldsymbol{\xi} \otimes \boldsymbol{\xi} + F(\mathbf{0}, \boldsymbol{\xi})\mathbf{I}\right] \boldsymbol{\eta} + \mathbf{f}(\mathbf{0}, \boldsymbol{\xi}) \quad \forall \boldsymbol{\eta}, \boldsymbol{\xi}. \tag{1.22}$$

Recalling (1.7) and (1.13), $\lambda(\boldsymbol{\xi})$ can be reformulated as follows:

$$\lambda(\boldsymbol{\xi}) = \frac{1}{\|\boldsymbol{\xi}\|} \frac{\partial f}{\partial p}(\|\boldsymbol{\xi}\|, \boldsymbol{\xi}) \quad \forall \boldsymbol{\xi}, \tag{1.23}$$

and, therefore, the linearized force vector $\mathbf{f}$ for a microelastic material is ultimately expressed as:

$$\mathbf{f}(\boldsymbol{\eta}, \boldsymbol{\xi}) = \left[\frac{1}{\|\boldsymbol{\xi}\|} \frac{\partial f}{\partial p}(\|\boldsymbol{\xi}\|, \boldsymbol{\xi}) + f(\mathbf{0}, \boldsymbol{\xi})\mathbf{I}\right] (\boldsymbol{\xi} \otimes \boldsymbol{\xi})\boldsymbol{\eta} + \mathbf{f}(\mathbf{0}, \boldsymbol{\xi}) \quad \forall \boldsymbol{\eta}, \boldsymbol{\xi}. \tag{1.24}$$

1.1.3 The concept of areal force density

This section briefly introduces the notion of areal force density, which is exploited in the theoretical analysis presented in Section 2.5. The concept of force per unit area in the framework of the peridynamic theory was first introduced in [7] to establish a connection between the bond-based PD and the classical linear elasticity.

Consider an infinite, homogeneous, microelastic body $\mathcal{B}$ undergoing a homogeneous deformation and assume that a plane $\mathcal{P}$, normal to the unit vector $\mathbf{n}$ passing through a material point $\mathbf{x}$ of the body $\mathcal{B}$, divides the body into two subregions, namely $\mathcal{B}^+$ and $\mathcal{B}^-$ (see Figure 1.3). Considering that material points belonging to $\mathcal{B}^+$ exert some force not only on material points laying on the surface of $\mathcal{B}^-$, but also on some material points located below the surface (depending on their relative position $\|\boldsymbol{\xi}\|$), and dividing this force by the area of $\mathcal{P} \cap \mathcal{B}$, the notion of force per unit area can be introduced. To be more precise, the two subregions $\mathcal{B}^+$ and $\mathcal{B}^-$ are defined as follows [7]:

$$\mathcal{B}^+ := \left\{\mathbf{x}' \in \mathcal{B} : (\mathbf{x}' - \mathbf{x}) \cdot \mathbf{n} \geq 0\right\}, \quad \mathcal{B}^- := \left\{\mathbf{x}' \in \mathcal{B} : (\mathbf{x}' - \mathbf{x}) \cdot \mathbf{n} \leq 0\right\}. \tag{1.25}$$

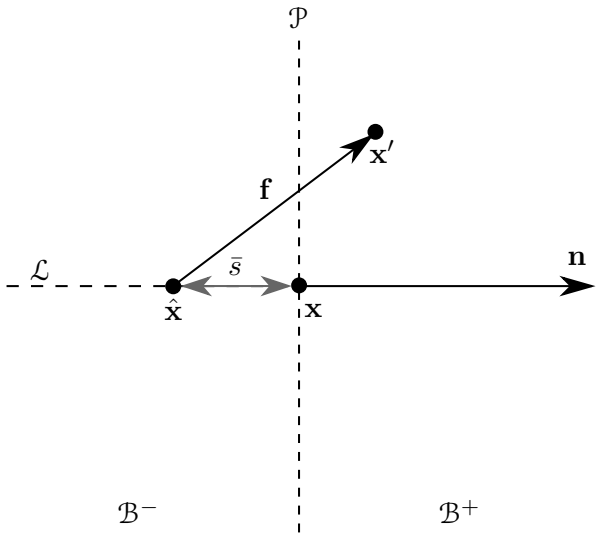

Figure 1.3: Schematic representation of the concept of areal force density.

Introducing $\mathcal{L}$ as a set of collinear material points belonging to the subregion $\mathcal{B}^-$ (see Figure 1.3), such that [7]

$$\mathcal{L} := \left\{ \hat{\mathbf{x}} \in \mathcal{B}^- : \hat{\mathbf{x}} = \mathbf{x} - \bar{s}\mathbf{n}, 0 \leq \bar{s} < \infty \right\}, \tag{1.26}$$

it is possible to define the areal force density $\boldsymbol{\tau}(\mathbf{x}, \mathbf{n})$ at a point $\mathbf{x}$ in $\mathcal{B}$ in the direction of the aforementioned unit vector $\mathbf{n}$ as [7]:

$$\boldsymbol{\tau}(\mathbf{x}, \mathbf{n}) := \int_{\mathcal{L}} \int_{\mathcal{B}^+} \mathbf{f}(\mathbf{u}' - \hat{\mathbf{u}}, \mathbf{x}' - \hat{\mathbf{x}}) dV_{\mathbf{x}'} d\hat{l}, \tag{1.27}$$

where $d\hat{l}$ represents the differential path length over $\mathcal{L}$.

In light of the hypothesis of homogeneous deformation, it is possible to introduce a stress tensor $\boldsymbol{\sigma}$, independent of $\mathbf{x}$, such that [7]

$$\boldsymbol{\tau}(\mathbf{x}, \mathbf{n}) = \boldsymbol{\sigma}\mathbf{n} \quad \forall \mathbf{n}, \tag{1.28}$$

where $\boldsymbol{\sigma}$ can be referred to as a Piola-Kirchhoff stress tensor, since $\boldsymbol{\tau}$ is evaluated as force per unit area in the reference configuration.

1.1.4 Prototype microelastic brittle material model

In the peridynamic theory, the simplest constitutive model that has been developed is the prototype microelastic brittle (PMB) material model, which was first presented in [51]. In this material model, the interaction (i.e., the bond) between

two material points can be thought of as a spring in classical theory of solid mechanics, where the peridynamic force acting in the direction of the line connecting these two material points is a linear function of the spring stiffness c, usually referred to as bond stiffness. The relationship between the force vector $\mathbf{f}$ and this stiffness coefficient is established through the scalar bond stretch s, which is defined by the following relation:

$$s := \frac{\|\boldsymbol{\eta} + \boldsymbol{\xi}\| - \|\boldsymbol{\xi}\|}{\|\boldsymbol{\xi}\|}. \tag{1.29}$$

In the PMB model, failure can be introduced by establishing a predefined limit value for the bond stretch s_0, usually referred to as critical stretch, and considering a bond to be broken when its current stretch exceeds this limit value [51]. A detailed description on how this limit value is computed is presented in Section 1.1.5. The rupture of a bond is an irreversible process, i.e., once the bond fails, the interaction between the two material points at its ends cannot be recovered, and the contribution of this bond is no longer taken into account in the computation.

For this material model, the previously defined function f is a linear function of the bond stiffness c and the bond stretch s such that

$$f(\|\boldsymbol{\eta} + \boldsymbol{\xi}\|, \boldsymbol{\xi}, t) = \frac{c(\boldsymbol{\xi})\mu(\boldsymbol{\xi}, t)s}{\|\boldsymbol{\eta} + \boldsymbol{\xi}\|}, \tag{1.30}$$

where $\mu(\boldsymbol{\xi}, t)$ is a history-dependent scalar-valued function which is introduced as a bond-breaking parameter, and can therefore assume either of the following two values:

$$\mu(\boldsymbol{\xi}, t) := \begin{cases} 1 & \text{if } \; s < s_0 \quad \forall\, 0 < t^{'} < t, \\ 0 & \text{otherwise.} \end{cases} \tag{1.31}$$

For a PMB material, the force vector $\mathbf{f}$ can be expressed as follows:

$$\mathbf{f}(\boldsymbol{\eta}, \boldsymbol{\xi}, t) = c(\boldsymbol{\xi})s\mu(\boldsymbol{\xi}, t)\frac{\boldsymbol{\eta} + \boldsymbol{\xi}}{\|\boldsymbol{\eta} + \boldsymbol{\xi}\|}. \tag{1.32}$$

Furthermore, under the assumptions of linearity in terms of material response and of small strains and displacements, and considering $c(\boldsymbol{\xi})$ to be a constant function with respect to $\boldsymbol{\xi}$, the previous equation can be reformulated as follows:

$$\mathbf{f}(\boldsymbol{\eta}, \boldsymbol{\xi}, t) = cs\mu(\boldsymbol{\xi}, t)\frac{\boldsymbol{\xi}}{\|\boldsymbol{\xi}\|}, \quad \|\boldsymbol{\eta}\| \ll \|\boldsymbol{\xi}\|. \tag{1.33}$$

The bond stiffness c can therefore be defined through the following strategy, which considers the linearized form of the stretch s, i.e., $s = \|\boldsymbol{\eta}\|/\|\boldsymbol{\xi}\|$. Assuming an infinite, homogeneous, microelastic body undergoing an isotropic deformation such that s is constant for all $\boldsymbol{\xi}$, and defining, for simplicity, $\xi = \|\boldsymbol{\xi}\|$ and $\eta = \|\boldsymbol{\eta}\|$, it is possible to observe that $\eta = s\xi$ and to express the scalar-valued function f in (1.30) as [51]:

$$f = cs = c\frac{\eta}{\xi}. \tag{1.34}$$

Recalling (1.10), the micropotential can then be rewritten as follows [51]:

$$w = \int f d\eta = c\frac{\eta}{\xi}d\eta = \frac{c\eta^2}{2\xi} = \frac{cs^2\xi}{2}. \tag{1.35}$$

Substituting (1.35) in (1.14) and using spherical coordinates (three-dimensional case), the strain energy density is reformulated as [51]:

$$W = \frac{1}{2}\int_0^\delta \left(\frac{cs^2\xi}{2}\right) 4\pi\xi^2 d\xi = \frac{\pi c s^2 \delta^4}{4}. \tag{1.36}$$

The bond stiffness c can be obtained by equating the strain energy density in (1.36) to the strain energy density in the classical theory of elasticity for the same material and deformation field, which is computed through the following relation:

$$W = \frac{9Ks^2}{2}, \tag{1.37}$$

where K represents the bulk modulus of the material. Setting the energy in (1.36) equal to the energy in (1.37) and solving for c leads to the bond stiffness for a three-dimensional PMB material model [51]

$$c = \frac{18K}{\pi\delta^4} = \frac{6E}{\pi\delta^4(1-2\nu)}, \tag{1.38}$$

where E is the Young's modulus, while ν indicates the Poisson's ratio of the material. It is important to highlight that, as a consequence of the bond-based PD formulation, in which the bonds are characterized based only on pairwise interactions, the Poisson's ratio is restricted to a fixed value that depends on the case under study, i.e., two-dimensional (plane stress or plane strain condition) or three-dimensional case. For three-dimensional and two-dimensional plane strain cases, the Poisson's ratio is fixed to $\nu = 1/4$, whereas for the two-dimensional plane stress case it is constrained

to $\nu = 1/3$ [7, 173]. This limitation has been removed in the state-based version of the theory presented in [33] and briefly introduced in Section 1.2. Considering the Poisson's ratio restrictions, (1.38) can be reformulated as:

$$c = \frac{12E}{\pi\delta^4}. \tag{1.39}$$

Following the same procedure adopted for the three-dimensional case, it is possible to derive the bond stiffness for two-dimensional (both for plane stress and plane strain conditions) and one-dimensional models, as presented in [173] and [174], respectively. As regards the two-dimensional case, the spring constant is computed by performing a surface-integration of a infinite plate subjected to a uniform expansion loading and a pure shear loading, which are applied separately. The strain energy density due to the uniform expansion loading derived from the conventional theory of linear elasticity is required to be equal to the strain energy density derived from the peridynamic theory for the same loading case. The same applies for the strain energy densities corresponding to the pure shear loading case. By simultaneously satisfying the previous two equalities (both for plane stress and plane strain conditions), and considering that the bond stiffness value is required to be the same for the two loading cases, the fixed value of the Poisson's ratio can be obtained both for plane stress and plane strain conditions [173], and the values of the bond stiffness can be therefore computed as:

$$c = \frac{9E}{\pi h\delta^3}, \quad \textit{plane stress condition}, \tag{1.40}$$

$$c = \frac{48E}{5\pi h\delta^3}, \quad \textit{plane strain condition}, \tag{1.41}$$

where h indicates the plate thickness. As for the one-dimensional case, the spring constant can be evaluated through the following relation [174]:

$$c = \frac{2E}{A\delta^2}, \tag{1.42}$$

where A is the cross-sectional area of the bar.

1.1.5 Failure criterion

The PD theory introduces a concept of damage for a material point, allowing to predict the evolution of cracks, including their nucleation, their propagation direction, and their interaction, and allowing to manage material discontinuities without

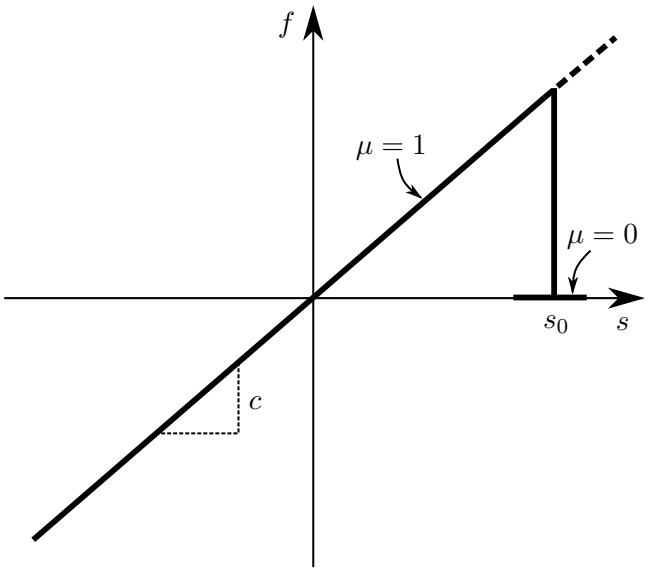

Figure 1.4: Peridynamic force versus bond stretch for the PMB material model. Redrawn, with modifications, from [51].

having to define any ad hoc criteria [9]. As previously mentioned in Section 1.1.4, in bond-based PD, the concept of material failure is introduced by defining a critical value for the bond stretch, s_0, after which a bond is considered to be broken and, consequently, no tensile force can be sustained by the bond (see Figure 1.4). The adopted failure criterion is therefore referred to as a maximum stretch criterion. The critical stretch s_0 can be related to measurable macroscopic quantities such as the critical energy release rate of the material G_0, which is defined as the dissipated energy per unit area of fracture surface during the growing of a crack or as the value assumed at fracture initiation by the energy release rate of a body undergoing an isotropic extension. The relationship between s_0 and G_0 can then be derived by assuming the complete separation of a planar fracture surface in the internal region of a infinite homogeneous body and the absence of any other dissipative phenomena near the crack tip [51]. In the framework of the PD theory, this translates into the requirement of breaking all the bonds crossing the aforementioned fracture surface, i.e., all the bonds connecting material points on the opposite sides of the fracture surface. In the PMB material model, the work which is required to break a single

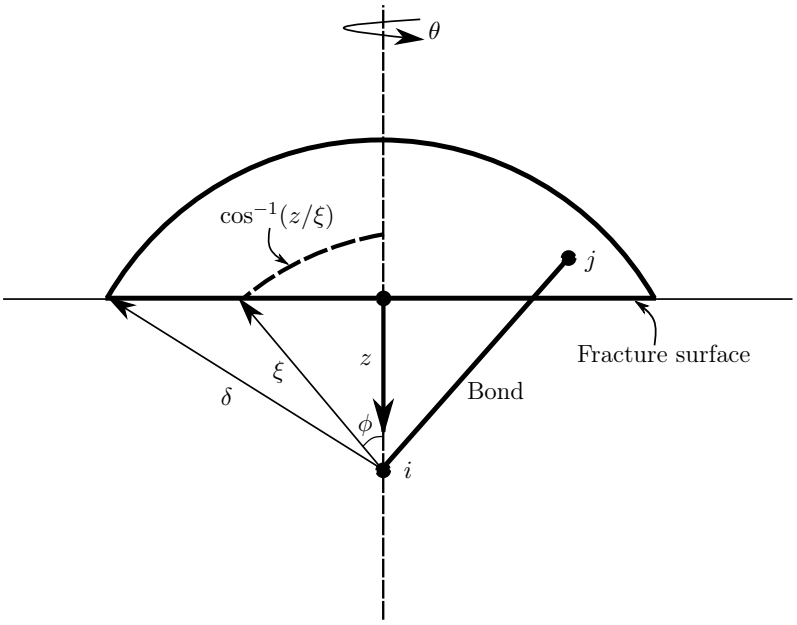

Figure 1.5: Schematic representation of the variables involved in the computation of the critical stretch s_0 (see (1.44)). Redrawn, with modifications, from [51].

bond can be computed by the following relation (recall (1.34) and (1.35)):

$$w_0(\boldsymbol{\xi}) = \int_0^{s_0} f(s)d\eta = \int_0^{s_0} f(s)\xi ds = \frac{cs_0^2\xi}{2}. \tag{1.43}$$

Moreover, the total work per unit surface area required to break all the bonds crossing the fracture surface is assumed to be equal to the critical energy release rate G_0 of classical continuum mechanics, as stated in Griffith's theory [175]. The criterion proposed in Griffith's theory can be considered nonlocal, since it derives from the computation of the energy balance of the whole material surrounding the crack [175]. The relationship between the aforementioned energies is expressed as follows [51]:

$$G_0 = \int_0^{\delta}\int_0^{2\pi}\int_z^{\delta}\int_0^{\cos^{-1}(z/\xi)} \left(\frac{cs_0^2\xi}{2}\right)\xi^2 \sin\phi d\phi d\xi dz d\theta = \frac{\pi cs_0^2\delta^5}{10}, \tag{1.44}$$

where the variables involved in the computation are represented in Figure 1.5. The critical stretch for a three-dimensional PMB material model can then be obtained by solving (1.44) for s_0 and by recalling (1.38) such that

$$s_0 = \sqrt{\frac{10G_0}{\pi c\delta^5}} = \sqrt{\frac{5G_0}{9K\delta}}, \tag{1.45}$$

which in turn, considering the Poisson's ratio restriction introduced in Section 1.1.4, can be expressed as:

$$s_0 = \sqrt{\frac{5G_0}{6E\delta}}. \tag{1.46}$$

For two-dimensional PMB material models, s_0 can instead be computed through the following relations:

$$s_0 = \sqrt{\frac{4\pi G_0}{9E\delta}}, \quad \textit{plane stress condition}, \tag{1.47}$$

$$s_0 = \sqrt{\frac{5\pi G_0}{12E\delta}}, \quad \textit{plane strain condition}. \tag{1.48}$$

In the case of mode I crack opening displacement, the critical energy release rate can be expressed as a function of the fracture toughness K_{Ic}, which is also a material property, by [175, 176]:

$$G_0 = \frac{K_{Ic}^2}{E'}, \tag{1.49}$$

where E' assumes either of the following two values:

$$E' = \begin{cases} E, & \text{plane stress condition}, \\ \dfrac{E}{1-\nu^2}, & \text{plane strain condition}. \end{cases} \tag{1.50}$$

To conclude, the concept of damage at a material point $\mathbf{x}$ is expressed by introducing a local damage index, $\varphi(\mathbf{x}, t)$, which is defined as follows [51]:

$$\varphi(\mathbf{x}, t) := 1 - \frac{\int_{\mathcal{H}_\mathbf{x}} \mu(\mathbf{x}, \boldsymbol{\xi}, t) dV_{\mathbf{x}'}}{\int_{\mathcal{H}_\mathbf{x}} dV_{\mathbf{x}'}}, \tag{1.51}$$

where $\mu(\mathbf{x}, \boldsymbol{\xi}, t)$ includes $\mathbf{x}$ as one of its arguments, in order to remind that it is a function of the location of the material point in the body. The damage index is therefore defined as the ratio of the number of broken bonds to the total number of bonds initially connected with the material point $\mathbf{x}$. This index takes a value between 0 and 1, where $\varphi(\mathbf{x}, t) = 0$ represents the undamaged state of the material, while $\varphi(\mathbf{x}, t) = 1$ indicates the complete disconnection of the material point $\mathbf{x}$ from all the material points located within its neighbourhood [51].

1.2 Mathematical formulation of the state-based version of PD theory

The state-based version of PD theory is a generalization of the bond-based formulation introduced in [7] and briefly presented in the previous section (see Section 1.1). This extended version, which was first proposed in [33], was developed in order to overcome the intrinsic limitations of the original version of the theory, which can be summarized in the following points [33, 51]:

- The assumption that any pair of material points interacts only through a central potential which is independent of the other local conditions is, in many cases, an oversimplification. This assumption is the cause of the Poisson's ratio restrictions (see Section 1.1.4), since an isotropic, linear, microelastic solid which involves only two-particle interactions is always characterized by $\nu = 1/4$. It is therefore necessary to improve the theory, to allow the strain energy density to be dependent on local volume change in addition to pairwise interactions.

- The theory needs to be modified to enable the modelling of plastic response. In fact, even if it would be possible to model plasticity by allowing the bonds to permanently deform, this would result in the permanent deformation of materials subjected to a volumetric strain (no shear deformation). This approach could be suitable for modelling porous materials, whereas it would be unsuitable for modelling metals, since it has been experimentally demonstrated that only shear deformations can induce a plastic response in these materials.

- The reformulation of material models in terms of the pairwise force function makes it difficult to describe the constitutive behaviour of materials in terms of a stress tensor, as it is usually done in classical continuum mechanics.

To overcome these limitations, it is necessary to rewrite the material-dependent part of the original formulation, i.e., the part containing all the constitutive information, which is represented by the pairwise force function $\mathbf{f}$. The approach proposed in [33] requires the introduction of the concept of force state, which is a mathematical

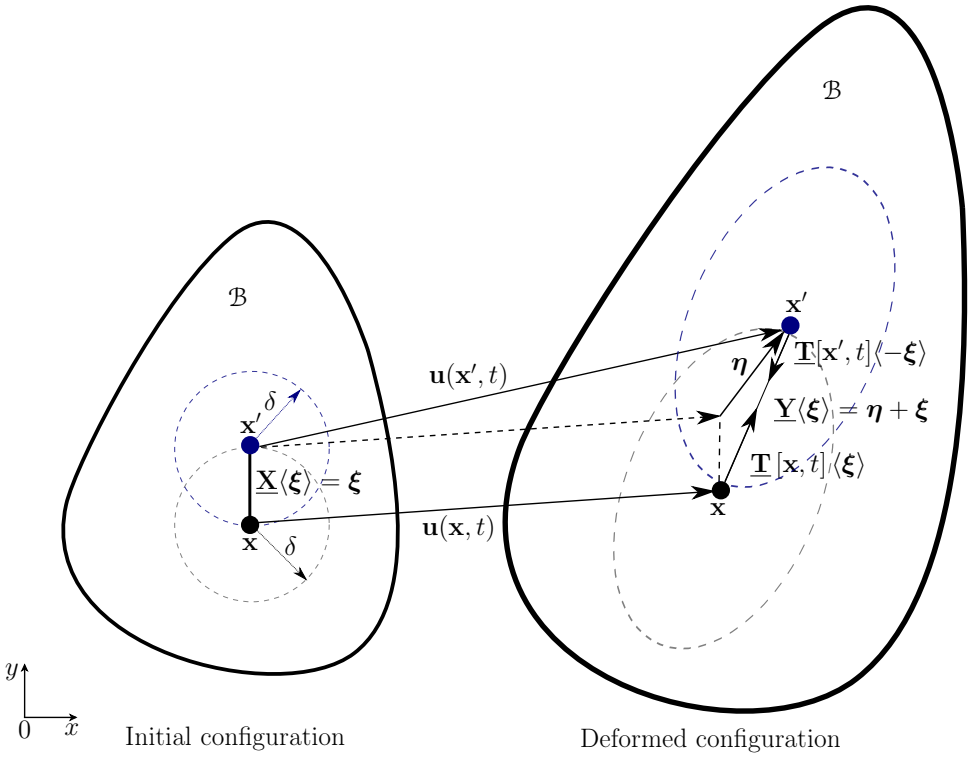

Figure 1.6: Representation of the positions of two material points $\mathbf{x}$ and $\mathbf{x}'$ in the initial and deformed configurations and of the main states involved in the state-based PD formulation.

object that shares some similarities with the stress tensor of CCM. Thanks to the introduction of this notion, it is possible to equip the theory with the capability to model materials with any Poisson's ratio, and to incorporate constitutive models from CCM directly in the PD framework [33]. In the following part, a brief outline of the concept of peridynamic state and of the main features of the state-based formulation is provided. More details can be found in [33], where the theory was first presented, and in [177], where it was investigated more comprehensively.

In a domain $\mathcal{B} \subset \mathbb{R}^r$ with r the spatial dimension, described with a PD model, each material point $\mathbf{x} \in \mathcal{B}$ interacts with all the other material points located within a finite neighbourhood, $\mathcal{H}_\mathbf{x}$, of that material point. The state-based PD equation of motion for any material point $\mathbf{x} \in \mathcal{B}$ at time $t \geqslant 0$ is given by [33]:

$$\rho(\mathbf{x})\ddot{\mathbf{u}}(\mathbf{x},t) = \int_{\mathcal{H}_\mathbf{x}} \left\{ \underline{\mathbf{T}}\left[\mathbf{x},t\right]\langle \mathbf{x}'-\mathbf{x}\rangle - \underline{\mathbf{T}}[\mathbf{x}',t]\langle \mathbf{x}-\mathbf{x}'\rangle \right\} dV_{\mathbf{x}'} + \mathbf{b}(\mathbf{x},t), \tag{1.52}$$

where ρ is the mass density, $\ddot{\mathbf{u}}$ is the second derivative in time of the displacement

field $\mathbf{u}$, $\underline{\mathbf{T}}[\mathbf{x},t]\langle\mathbf{x}'-\mathbf{x}\rangle$ is the force vector state defined at the material point $\mathbf{x}$ at time t mapping the bond $\mathbf{x}'-\mathbf{x}$ to force per unit volume squared, $\underline{\mathbf{T}}[\mathbf{x}',t]\langle\mathbf{x}-\mathbf{x}'\rangle$ is the force vector state defined at the material point $\mathbf{x}'$ at time t mapping the bond $\mathbf{x}-\mathbf{x}'$ to force per unit volume squared (the values of the two force vector states can be different), $\mathbf{b}$ is a prescribed body force density field, and $\mathcal{H}_{\mathbf{x}}$ is a spherical neighbourhood of radius δ, where $\delta>0$ is referred to as the horizon radius and indicates the maximum interaction length for each material point $\mathbf{x}\in\mathcal{B}$ (see Figure 1.6). As for bond-based PD, the relative position vector of the two material points $\mathbf{x}$ and $\mathbf{x}'$ in the reference (or initial) configuration is defined as follows:

$$\boldsymbol{\xi}:=\mathbf{x}'-\mathbf{x}, \tag{1.53}$$

which represents the standard PD notation for a bond. As shown in Figure 1.6, in the deformed configuration at time $t>0$, the two material points $\mathbf{x}$ and $\mathbf{x}'$ would be displaced, respectively, by $\mathbf{u}(\mathbf{x},t)$ and $\mathbf{u}(\mathbf{x}',t)$. The corresponding relative displacement vector is therefore denoted by:

$$\boldsymbol{\eta}:=\mathbf{u}(\mathbf{x}',t)-\mathbf{u}(\mathbf{x},t)=\mathbf{u}'(t)-\mathbf{u}(t). \tag{1.54}$$

Differently from the bond-based theory, in the state-based formulation the concept of bond domain is introduced to define the peridynamic states, such that

$$\mathcal{H}:=\left\{\boldsymbol{\xi}\in\left(\mathbb{R}^3\setminus\mathbf{0}\right)\,|\,(\boldsymbol{\xi}+\mathbf{x})\in\mathcal{H}_{\mathbf{x}}\cap\mathcal{B}\right\}, \tag{1.55}$$

which contains vectors, i.e., bonds, and is centred at $\mathbf{0}$ [33]. In general, a peridynamic state can be described as a function, defined in the bond domain $\mathcal{H}$, which can be applied to one or more bonds in order to map them into a quantity. It is possible to identify different types of states, depending on the nature of the output quantity. Among them, there are three types of states which are involved in the state-based PD formulation, i.e., the scalar state, characterized by a scalar output quantity, the vector state, in which the output quantity is a vector, and the double state, which maps pairs of bonds $(\boldsymbol{\xi},\boldsymbol{\zeta})\in\mathcal{H}$ into second-order tensors [33]. It is important to notice that, even if a vector state is the equivalent of a second-order tensor in CCM, unlike the latter, it is not in general a linear and continuous function of $\boldsymbol{\xi}$, but it can instead be a nonlinear and noncontinuous function of the PD bond.

Before proceeding with the derivation of the state-based formulation, it is necessary to introduce some notations and mathematical definitions useful in the context of peridynamic states [33, 177, 178]. As for the notations, the uppercase, bold font with an underscore is usually employed to indicate a state, the bond on which the function is applied is identified by angle brackets $\langle\cdot\rangle$, the state on which the function depends (if present) is shown in parentheses $(\cdot)$, while square brackets $[\cdot]$ are used to indicate other quantities on which the state might depend, such as the time step t and the material point $\mathbf{x}$ (*cf.* (1.52)). The main mathematical definitions which are exploited in the state-based formulation are the sum and the difference of two states, the composition of states, the point product, the dot product, the magnitude state, the norm of a state and the Fréchet derivative [33, 177, 178]. As for the sum and the difference of two states of the same order m, they are defined, respectively, as follows:

$$(\underline{\mathbf{A}} + \underline{\mathbf{B}})\langle\boldsymbol{\xi}\rangle := \underline{\mathbf{A}}\langle\boldsymbol{\xi}\rangle + \underline{\mathbf{B}}\langle\boldsymbol{\xi}\rangle \quad \forall\boldsymbol{\xi} \in \mathcal{H}, \tag{1.56}$$

$$(\underline{\mathbf{A}} - \underline{\mathbf{B}})\langle\boldsymbol{\xi}\rangle := \underline{\mathbf{A}}\langle\boldsymbol{\xi}\rangle - \underline{\mathbf{B}}\langle\boldsymbol{\xi}\rangle \quad \forall\boldsymbol{\xi} \in \mathcal{H}, \tag{1.57}$$

where $\underline{\mathbf{A}}\langle\cdot\rangle : \mathcal{H} \mapsto \mathcal{L}_m$, $\underline{\mathbf{B}}\langle\cdot\rangle : \mathcal{H} \mapsto \mathcal{L}_m$, and $\mathcal{L}_m$ is the set of all tensors of order m. Concerning the composition of states, it is expressed as:

$$(\underline{\mathbf{A}} \circ \underline{\mathbf{V}})\langle\boldsymbol{\xi}\rangle := \underline{\mathbf{A}}\langle\underline{\mathbf{V}}\langle\boldsymbol{\xi}\rangle\rangle \quad \forall\boldsymbol{\xi} \in \mathcal{H}, \tag{1.58}$$

where $\underline{\mathbf{V}}\langle\cdot\rangle : \mathcal{H} \mapsto \mathcal{L}_1$, and $\mathcal{L}_1$ represents the set of all vector states. Moreover, the point product of two states can be defined through the following expression:

$$(\underline{\mathbf{AB}})_{i_1,i_2,\cdots,i_m}\langle\boldsymbol{\xi}\rangle := \underline{A}_{i_1,i_2,\cdots,i_m,j_1,j_2,\cdots,j_p}\langle\boldsymbol{\xi}\rangle\underline{B}_{j_1,j_2,\cdots,j_p}\langle\boldsymbol{\xi}\rangle \quad \forall\boldsymbol{\xi} \in \mathcal{H}, \tag{1.59}$$

where $\underline{\mathbf{A}} : \mathcal{H} \mapsto \mathcal{L}_{m+p}$, $\underline{\mathbf{B}} : \mathcal{H} \mapsto \mathcal{L}_p$, and $\underline{A}_{i_1,i_2,\cdots,i_m}$ represent the m components of an m-order state in a Cartesian coordinate system. As regards the dot product of two states, it is defined through the following relation:

$$\underline{\mathbf{A}} \bullet \underline{\mathbf{B}} := \int_{\mathcal{H}} (\underline{\mathbf{AB}})\langle\boldsymbol{\xi}\rangle dV_{\boldsymbol{\xi}}, \tag{1.60}$$

where the previous notation for the differential volume, $dV_{\mathbf{x}'}$, has been changed to $dV_{\boldsymbol{\xi}}$ to highlight the fact that the domain of states is composed of bonds, even

though the two differential volumes are actually equivalent. The magnitude state, also referred to as scalar state, is defined as:

$$|\underline{\mathbf{A}}|\langle\boldsymbol{\xi}\rangle := \sqrt{(\underline{\mathbf{A}}\underline{\mathbf{A}})\langle\boldsymbol{\xi}\rangle} \quad \forall\boldsymbol{\xi} \in \mathcal{H}. \tag{1.61}$$

Differently from the states of order $m \geq 1$, the scalar state is indicated by using a lower case, non-bold font with an underscore, such as:

$$\underline{a} := |\underline{\mathbf{A}}|\langle\boldsymbol{\xi}\rangle \quad \forall\boldsymbol{\xi} \in \mathcal{H}. \tag{1.62}$$

The norm of a state is instead expressed as follows:

$$\|\underline{\mathbf{A}}\| := \sqrt{\underline{\mathbf{A}} \bullet \underline{\mathbf{A}}}. \tag{1.63}$$

In order to introduce the Fréchet derivative, it is first necessary to define the notion of function of a state. The function of a state may be scalar-valued or tensor-valued, and the quantity on which this function depends is enclosed in parentheses, such as, for example, $\Psi(\underline{\mathbf{B}})$. Consider Ψ to be a function of a state, such as $\Psi(\cdot) : \mathcal{L}_m \mapsto \mathcal{L}_n$, and suppose the existence of a state-valued function $\nabla\Psi \in \mathcal{L}_{m+n}$ such that, for any state $\underline{\mathbf{A}} \in \mathcal{L}_m$ and any $\Delta\underline{\mathbf{A}} \in \mathcal{L}_m$,

$$\Psi(\underline{\mathbf{A}} + \Delta\underline{\mathbf{A}}) := \Psi(\underline{\mathbf{A}}) + \nabla\Psi(\underline{\mathbf{A}}) \bullet \Delta\underline{\mathbf{A}} + o(\|\Delta\underline{\mathbf{A}}\|). \tag{1.64}$$

Then Ψ is differentiable and $\nabla\Psi$ is referred to as the Fréchet derivative of Ψ. Further details concerning the peridynamic states and their mathematical framework can be found in [33, 177, 178].

Going back to the state-based formulation, it is now possible to introduce two important states, i.e., the reference position vector state $\underline{\mathbf{X}}\langle\boldsymbol{\xi}\rangle$, which associates each pair of material points to their initial relative position vector, and the deformation vector state $\underline{\mathbf{Y}}\langle\boldsymbol{\xi}\rangle$, which associates each pair of material points to their current relative position vector (see Figure 1.6). These two vector states are defined through the following expressions:

$$\underline{\mathbf{X}}\langle\boldsymbol{\xi}\rangle := \boldsymbol{\xi} \quad \forall\boldsymbol{\xi} \in \mathcal{H}, \tag{1.65}$$

$$\underline{\mathbf{Y}}\langle\boldsymbol{\xi}\rangle := \boldsymbol{\eta} + \boldsymbol{\xi} \quad \forall\boldsymbol{\xi} \in \mathcal{H}, \tag{1.66}$$

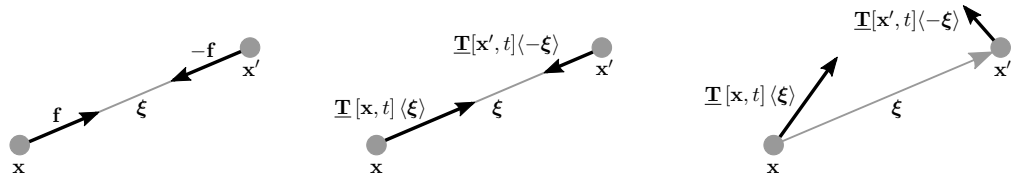

Bond-based PD model | Ordinary state-based PD model | Non-ordinary state-based PD model

Figure 1.7: Representation of bond-based, ordinary and non-ordinary state-based material response. Redrawn, with modifications, from [33].

while their scalar counterparts, i.e., the reference position scalar state $\underline{x}$ and the deformation scalar state $\underline{y}$, are expressed, respectively, as follows:

$$\underline{x} := |\underline{\mathbf{X}}|\langle\boldsymbol{\xi}\rangle = |\boldsymbol{\xi}|, \tag{1.67}$$

$$\underline{y} := |\underline{\mathbf{Y}}|\langle\boldsymbol{\xi}\rangle = |\boldsymbol{\eta} + \boldsymbol{\xi}|, \tag{1.68}$$

where $\underline{x}$ and $\underline{y}$ associate each pair of material points to their bond length in the initial and current configuration, respectively. Recalling 1.66 and 1.68, it is possible to define another important peridynamic state, i.e., the deformed direction vector state $\underline{\mathbf{M}}\,(\underline{\mathbf{Y}})$, which is a function that associates each pair of material points to their relative position unit vector, such as:

$$\underline{\mathbf{M}}\,(\underline{\mathbf{Y}}) := \frac{\underline{\mathbf{Y}}\langle\boldsymbol{\xi}\rangle}{|\underline{\mathbf{Y}}|\langle\boldsymbol{\xi}\rangle} = \frac{\boldsymbol{\eta} + \boldsymbol{\xi}}{|\boldsymbol{\eta} + \boldsymbol{\xi}|}. \tag{1.69}$$

Moreover, recalling the force vector state $\underline{\mathbf{T}}$ introduced in (1.52), if for any deformation of a material there exist a scalar state $\underline{t}$ such that

$$\underline{\mathbf{T}} = \underline{t}\underline{\mathbf{M}}, \tag{1.70}$$

then the material is referred to as ordinary, and $\underline{t}$ is named the scalar force state, otherwise the material is called non-ordinary (see Figure 1.7). A state-based PD model which is developed only for ordinary materials takes the name of ordinary state-based PD model. Since the modelling of non-ordinary materials is not addressed in this thesis, when referring to state-based PD, only the ordinary version of the theory is considered. When dealing with ordinary materials, the following relation applies:

$$\frac{\underline{\mathbf{T}}\langle\boldsymbol{\xi}\rangle}{|\underline{\mathbf{T}}|\langle\boldsymbol{\xi}\rangle} = \frac{\underline{\mathbf{Y}}\langle\boldsymbol{\xi}\rangle}{|\underline{\mathbf{Y}}|\langle\boldsymbol{\xi}\rangle}, \quad \underline{t}\langle\boldsymbol{\xi}\rangle \neq 0, \tag{1.71}$$

which implies that, in ordinary materials, pairs of material points apply to each other force vectors which have the same magnitude, are opposite in direction, and are parallel to their relative deformed position [33] (see Figure 1.6). Furthermore, it is required that $\underline{\mathbf{T}}$ satisfies the balance of linear and angular momenta for any bounded domain $\mathcal{B}$, such that

$$\int_{\mathcal{B}} \rho(\mathbf{x})\ddot{\mathbf{u}}(\mathbf{x},t)dV_{\mathbf{x}} = \int_{\mathcal{B}} \mathbf{b}(\mathbf{x},t)dV_{\mathbf{x}} \quad \forall t \geq 0, \tag{1.72}$$

$$\int_{\mathcal{B}} \mathbf{y}\left(\mathbf{x},t\right) \times \left(\rho(\mathbf{x})\ddot{\mathbf{u}}(\mathbf{x},t) - \mathbf{b}(\mathbf{x},t)\right) dV_{\mathbf{x}} = 0 \quad \forall t \geq 0, \tag{1.73}$$

where (1.72) and (1.73) express the balance of the linear and angular momentum, respectively, and $\mathbf{y}\left(\mathbf{x},t\right)$ is defined as:

$$\mathbf{y}\left(\mathbf{x},t\right) := \mathbf{x} + \mathbf{u}(\mathbf{x},t) \quad \forall t \geq 0, \quad \mathbf{x} \in \mathcal{B}. \tag{1.74}$$

In ordinary materials, both (1.72) and (1.73) are automatically satisfied (see Figure 1.7). Moreover, consider a material characterized by a scalar-valued function $f\left(\cdot,\cdot\right) : \mathbb{R}^3 \times \mathbb{R}^3 \mapsto \mathbb{R}$ such that $f\left(-\boldsymbol{\eta},-\boldsymbol{\xi}\right) = f\left(\boldsymbol{\eta},\boldsymbol{\xi}\right)$ for all $\boldsymbol{\eta},\boldsymbol{\xi}$, and define an ordinary material through

$$\underline{t}\left[\mathbf{x},t\right]\left\langle \mathbf{x}' - \mathbf{x}\right\rangle = \frac{1}{2} f\left(\mathbf{u}' - \mathbf{u}, \mathbf{x}' - \mathbf{x}\right) \quad \forall \mathbf{x} \in \mathcal{B}, \mathbf{x}' \in \mathcal{H}_{\mathbf{x}}, t \geq 0. \tag{1.75}$$

Recalling (1.70) and substituting (1.75) in (1.52), (1.52) becomes equal to (1.1), which then proves that the bond-based version of PD can be considered as a special case of the state-based formulation (see Figure 1.7). The relation between the force vector state $\underline{\mathbf{T}}$ in state-based PD and the pairwise force function $\mathbf{f}$ in bond-based PD can then be expressed as follows [33]:

$$\underline{\mathbf{T}}\left[\mathbf{x},t\right]\left\langle \boldsymbol{\xi}\right\rangle = \frac{1}{2}\mathbf{f}\left(\boldsymbol{\eta},\boldsymbol{\xi}\right). \tag{1.76}$$

1.2.1 Ordinary linear isotropic elastic models

In [33], the scalar force state $\underline{t}$ for a three-dimensional linear, isotropic, elastic model is expressed as follows:

$$\underline{t} = \frac{3K\theta}{\mathrm{m}}\underline{\omega x} + \alpha'\underline{\omega e}^{d}, \tag{1.77}$$

where K is the bulk modulus of the material, and α' indicates a positive constant which is proportional to the shear modulus. Before defining the other quantities introduced in (1.77), it is necessary to identify the two parts by which $\underline{t}$ is composed, i.e., the co-isotropic and the co-deviatoric parts. The co-isotropic part, which corresponds to the first term on the right-hand side of (1.77), is related to the part of the force which determines a pure change of volume of the horizon sphere of a material point, whereas the co-deviatoric part, which corresponds to the second term on the right-hand side of (1.77), is related to the force which induces a pure change of shape of the horizon sphere. The co-isotropic part of the scalar force state $\underline{t}$ is therefore identified as follows:

$$\underline{t}_{iso} = \frac{3K\theta}{\mathrm{m}}\underline{\omega x}, \tag{1.78}$$

where $\underline{\omega}$ is a nonnegative scalar state, called influence function, which has been introduced in [33] as a mean to select which bonds, for a certain deformation state, participate in the determination of the force state, and to assess the weight of each bond contribution to the global behaviour of the material. $\underline{\omega}$ can be defined as $\underline{\omega} := 1$ [179], $\underline{\omega} := exp\left(-\frac{\|\boldsymbol{\xi}\|^2}{\delta^2}\right)$ [180], $\underline{\omega} := \frac{\delta^3}{\|\boldsymbol{\xi}\|^3}$ [179], and by other formulae reported in [99, 181, 182]. m is a weighted volume which, taking into account the number of bonds within the horizon sphere of a material point, indicates whether the selected point is located near a free surface or in the bulk of the body, such that

$$\mathrm{m} := (\underline{\omega x}) \bullet \underline{x} = \int_{\mathcal{H}_{\mathbf{x}}} \underline{\omega}\|\boldsymbol{\xi}\|^2 dV_{\mathbf{x}'}. \tag{1.79}$$

The scalar-valued function θ, referred to as the volume dilatation, expresses the deformation of the horizon neighbourhood of a material point by taking into account how the horizon radius changes throughout the deformation, and is defined through the following relation:

$$\theta := \frac{3}{\mathrm{m}} (\underline{\omega x}) \bullet \underline{e} = \frac{3}{\mathrm{m}} \int_{\mathcal{H}_{\mathbf{x}}} (\underline{\omega x e})\, dV_{\mathbf{x}'}, \tag{1.80}$$

where $\underline{e}$ represents the extension scalar state, which, in turn, is defined as:

$$\underline{e} := \underline{y} - \underline{x} = |\boldsymbol{\eta} + \boldsymbol{\xi}| - |\boldsymbol{\xi}|, \tag{1.81}$$

and associates each pair of material points to their bond elongation. The co-deviatoric part of the scalar force state $\underline{t}$ is instead expressed as follows:

$$\underline{t}_{dev} = \alpha' \underline{\omega e}^d, \tag{1.82}$$

where $\underline{e}^d$ is the deviatoric extension state, which associates each pair of material points to the portion of their bond elongation which is linked to the change of shape of the horizon sphere, and is identified by the following relation:

$$\underline{e}^d := \underline{e} - \frac{\theta \underline{x}}{3} = |\boldsymbol{\eta} + \boldsymbol{\xi}| - \frac{(\theta + 3)\,|\boldsymbol{\xi}|}{3}. \tag{1.83}$$

The previous formulation was derived for three-dimensional isotropic linear elastic models. As for two-dimensional isotropic linear elastic models, they were first developed and presented in [183], where the authors derived the strain energy in the peridynamic framework starting from the strain and stress tensors of CCM. For the plane stress case, the volume dilation θ can be obtained by rearranging the expression for the strain energy density in CCM in terms of volume dilatation, such that [183]

$$W = \left[\frac{K}{2} + \mu\left(\frac{\nu + 1}{3\,(2\nu - 1)}\right)^2\right]\left(\frac{dV}{V}\right)^2 + \mu \sum_{i,j=x,y} \varepsilon_{ij}^d \varepsilon_{ij}^d \tag{1.84}$$

where μ represents the shear modulus, ν is the Poisson's ratio, ε_{ij}^d is the ij component of the deviatoric strain tensor, and $\left(\frac{dV}{V}\right)$ represents the volume dilatation in the CCM framework, which, assuming small homogeneous deformations, is equivalent to the previously introduced PD scalar-valued function θ. For the two-dimensional plane stress case, the volume dilatation θ is therefore computed as follows:

$$\theta = \frac{2\,(2\nu - 1)}{\nu - 1} \frac{\underline{\omega x} \bullet \underline{e}}{\mathrm{q}}, \tag{1.85}$$

where $\mathrm{q} = \underline{\omega x} \bullet \underline{x}$ is the equivalent of the three-dimensional weighted volume m in (1.79), but in two dimensions. After some calculations which are comprehensively outlined in [183], it is possible to define the scalar force state $\underline{t}$ for two-dimensional plane stress models such that

$$\underline{t} = \frac{2\,(2\nu - 1)}{\nu - 1}\left(k'\theta - \frac{\alpha'}{3}\left(\underline{\omega e}^d\right) \bullet \underline{x}\right)\frac{\underline{\omega x}}{\mathrm{q}} + \alpha' \underline{\omega e}^d, \tag{1.86}$$

where k' and α' are positive constants obtained by equating the classical and peridynamic strain energy densities, which, for plane stress conditions, are expressed as follows:

$$k' = K + \frac{\mu}{9}\frac{(\nu+1)^2}{(2\nu-1)^2}, \tag{1.87}$$

$$\alpha' = \frac{8\mu}{\mathrm{q}}. \tag{1.88}$$

The classical strain energy density under plane strain conditions is instead expressed by the following relation:

$$W = \left[\frac{K}{2} + \frac{\mu}{9}\right]\left(\frac{dV}{V}\right)^2 + \mu \sum_{i,j=x,y} \varepsilon_{ij}^d \varepsilon_{ij}^d, \tag{1.89}$$

where the classical volume dilatation $\left(\frac{dV}{V}\right)$ is equivalent to the PD scalar-valued function θ, which, in this case, is computed through the following expression:

$$\theta = 2\frac{\underline{\omega x} \bullet \underline{e}}{\mathrm{q}}. \tag{1.90}$$

After some mathematical manipulations which are, also in this case, thoroughly discussed in [183], it is possible to derive the scalar force state $\underline{t}$ for two-dimensional models under plane strain conditions such that

$$\underline{t} = 2\left(k'\theta - \frac{\alpha'}{3}\left(\underline{\omega e}^d\right) \bullet \underline{x}\right)\frac{\underline{\omega x}}{\mathrm{q}} + \alpha' \underline{\omega e}^d, \tag{1.91}$$

where k' and α' are positive constants obtained by equating the classical and peridynamic strain energy densities, which, for plane strain conditions, are expressed as follows:

$$k' = K + \frac{\mu}{9}, \tag{1.92}$$

$$\alpha' = \frac{8\mu}{\mathrm{q}}. \tag{1.93}$$

1.2.2 Failure criteria

Material failure and crack propagation can be modelled by defining a suitable failure criterion. Considering that, in the state-based theory, both the isotropic and deviatoric parts of the deformation participate in the determination of the force state, various failure criteria have been developed and exploited to describe the discontinuities in the material domain [51, 184–187]. The three types of failure criteria

which are commonly used are the critical bond stretch criterion [51], the bond-level energy based failure criterion [184], and an alternative bond failure criterion based on strain invariants [185]. It has been demonstrated that all three criteria are suitable for studying mode I fracture problems and can accurately reproduce available experimental results [186]. Considering that, following the recommendations reported in [180], the failure criterion adopted in this thesis is the critical bond stretch one (see Section 2.7), only this criterion is discussed in detail in the following part of this section. For a comprehensive derivation of the other criteria, please refer to the aforementioned dedicated literature. As reported in [113], the stretch of a bond is expressed as:

$$s\langle\boldsymbol{\xi}\rangle := \frac{\underline{e}\langle\boldsymbol{\xi}\rangle}{\underline{x}\langle\boldsymbol{\xi}\rangle}, \tag{1.94}$$

while the critical stretch value is computed as follows [84, 188]:

$$s_0 = \sqrt{\frac{5G_0}{6E\delta}}, \quad three-dimensional\ case, \tag{1.95}$$

$$s_0 = \sqrt{\frac{4\pi G_0}{9E\delta}}, \quad two-dimensional\ plane\ stress\ case, \tag{1.96}$$

$$s_0 = \sqrt{\frac{5\pi G_0}{12E\delta}}, \quad two-dimensional\ plane\ strain\ case, \tag{1.97}$$

where E is the Young's modulus of the material, and G_0 represents the critical energy release rate for mode I fracture. Even if (1.95), (1.96) and (1.97) have been derived for bond-based PD models and their adoption in the state-based PD framework is not fully justifiable, their use is usually accepted [180, 186]. Moreover, a history-dependent scalar-valued function, $\underline{\varrho}$, is introduced in the state-based model as a bond-breaking parameter, i.e., with the function to indicate the status of the bonds (*cf.* (1.31)). This scalar state can therefore assume either of the following two values [84, 188]:

$$\underline{\varrho}\langle\boldsymbol{\xi}\rangle := \begin{cases} 1 & \text{if } \ s\langle\boldsymbol{\xi}\rangle < s_0 \quad \forall\ 0 < \bar{t} < t, \\ 0 & \text{otherwise.} \end{cases} \tag{1.98}$$

To conclude, the concept of damage at a material point $\mathbf{x}$ is introduced by defining a local damage index, $\varphi_{\mathbf{x}}$, such that

$$\varphi_{\mathbf{x}} := 1 - \frac{\int_{\mathcal{H}_{\mathbf{x}}} \underline{\omega}\langle\boldsymbol{\xi}\rangle \underline{\varrho}\langle\boldsymbol{\xi}\rangle dV_{\mathbf{x}'}}{\int_{\mathcal{H}_{\mathbf{x}}} \underline{\omega}\langle\boldsymbol{\xi}\rangle dV_{\mathbf{x}'}}, \tag{1.99}$$

where $\varphi_{\mathbf{x}}$ takes a value between 0 and 1, where $\varphi_{\mathbf{x}} = 0$ represents the undamaged state of the material, while $\varphi_{\mathbf{x}} = 1$ indicates the complete disconnection of the material point $\mathbf{x}$ from all the material points located within its neighbourhood. A crack can then be identified wherever $\varphi_{\mathbf{x}} \geq 0.5$.

1.3 Numerical discretization

The numerical discretization of peridynamic models can be pursued by employing different numerical methods [189]. In all the examples presented in this thesis, the meshfree approach introduced in [51] is adopted.

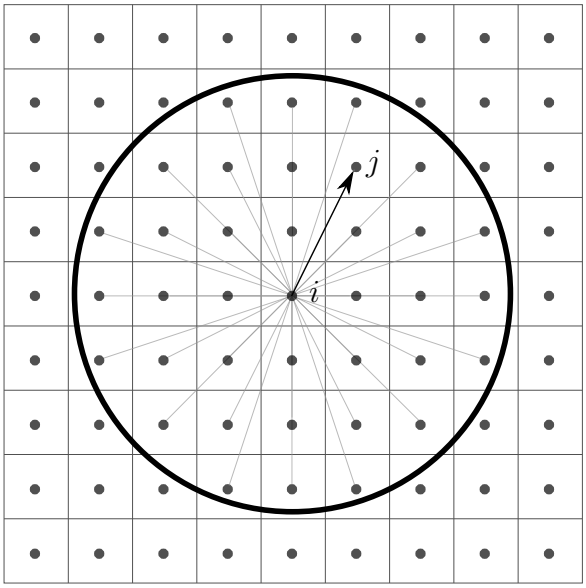

Figure 1.8: Example of a uniform spatial discretization of a peridynamic domain. The neighbourhood of the source node i is set out as suggested in [190].

1.3.1 Spatial integration

The numerical approximation of the peridynamic equation requires the subdivision of the domain into a grid of points called nodes: in a domain $\mathcal{B}$, described with a PD model, each node $i \in \mathcal{B}$ is associated to a certain finite volume in the reference configuration, such that the union of all volumes appropriately covers the volume of the entire domain (see Figure 1.8). No elements or other geometrical connections between nodes are foreseen [51]. The meshfree discretization implemented in this

thesis considers a uniform distribution of nodes (see Figure 1.8), where the distance between two nearest neighbouring nodes is referred to as grid spacing. A uniform grid with $\Delta x = \Delta y = \Delta z = \Delta$ is therefore employed, where Δx, Δy and Δz are the grid spacings in the x-, y- and z-directions, respectively. The volume associated to each node, referred to as node volume, is then computed as a cube of volume $V = \Delta x \cdot \Delta y \cdot \Delta z = \Delta x^3$ for three-dimensional models, or as a square cell of volume $V = \Delta x \cdot \Delta y \cdot h = \Delta x^2 \cdot h$ for the planar cases, where h represents the plate thickness. For one-dimensional systems, the node volume is instead computed as $V = A \cdot \Delta x$, where A is the constant cross-sectional area of the bar. The node of interest i at which the volume is centred is termed source node.

The discretized form of the bond-based PD equation of motion (*cf.* (1.1)) for any source node $i \in \mathcal{B}$ can be written as:

$$\rho_i \ddot{\mathbf{u}}_i^n = \sum_j \mathbf{f}(\mathbf{u}_j^n - \mathbf{u}_i^n, \mathbf{x}_j - \mathbf{x}_i)\beta(\boldsymbol{\xi})V_j + \mathbf{b}_i^n \quad \forall j \in \mathcal{H}_i, \tag{1.100}$$

where the integral in (1.1) is replaced by a finite sum taken over all nodes j, referred to as family nodes, such that $\|\mathbf{x}_j - \mathbf{x}_i\| \leqslant \delta$, $\mathbf{f}$ is the pairwise force function that the family node j exerts on the source node i (*cf.* (1.12)), n represents the time step number, subscripts refer to the node number, e.g., $\mathbf{u}_i^n = \mathbf{u}(\mathbf{x}_i, t^n)$, V_j is the discretized volume associated to the family node j, and $\beta(\boldsymbol{\xi})$ is a partial-volume correction factor used to evaluate the portion of V_j that falls within the neighbourhood of the source node i, $\mathcal{H}_i$, as recommended in [190, 191]. The use of this correction factor is a consequence of the fact that the volumes associated to family nodes located close to the boundary of the neighbourhood of i have only a partial overlapping with $\mathcal{H}_i$. The introduction of this factor helps to improve the accuracy of the spatial integration, which is performed by adopting the one-point Gauss quadrature rule. In this thesis, the assumption of small strains and displacements is made, so that, according to [51], the linearized version of (1.100) can be expressed as:

$$\rho_i \ddot{\mathbf{u}}_i^n = \sum_j \mathbf{C}(\mathbf{x}_j - \mathbf{x}_i)(\mathbf{u}_j^n - \mathbf{u}_i^n)\beta(\boldsymbol{\xi})V_j + \mathbf{b}_i^n \quad \forall j \in \mathcal{H}_i, \tag{1.101}$$

where $\mathbf{C}$ is the material's micromodulus function defined in (1.16).

Concerning the state-based formulation, the discretized form of the equation of

motion (*cf.* (1.52)) for any source node $i \in \mathcal{B}$ can be written as:

$$\rho_i \ddot{\mathbf{u}}_i^n = \sum_j \left\{ \underline{\mathbf{T}}\left[\mathbf{x}_i^n\right] \langle \mathbf{x}_j^n - \mathbf{x}_i^n \rangle - \underline{\mathbf{T}}\left[\mathbf{x}_j^n\right] \langle \mathbf{x}_i^n - \mathbf{x}_j^n \rangle \right\} \beta(\boldsymbol{\xi}) V_j + \mathbf{b}_i^n \quad \forall j \in \mathcal{H}_i, \tag{1.102}$$

where the integral in (1.52) is replaced by Riemann sums taken over all nodes j, referred to as family nodes, such that $\|\mathbf{x}_j^n - \mathbf{x}_i^n\| \leqslant \delta$, n is the time step number, $\underline{\mathbf{T}}\left[\mathbf{x}_i^n\right] \langle \mathbf{x}_j^n - \mathbf{x}_i^n \rangle$ is the force vector state defined at the source node i at time t^n mapping the bond $\mathbf{x}_j^n - \mathbf{x}_i^n$ to force per unit volume squared (*cf.* (1.70)), and $\beta(\boldsymbol{\xi})$ is the partial-volume correction factor previously introduced in (1.100) [190,191]. The linearized version of (1.102) can then be expressed as:

$$\begin{aligned} \rho_i \ddot{\mathbf{u}}_i^n = \sum_j \Big\{ & \left(\underline{\mathbf{T}}\left[\mathbf{x}_i^{n-1}\right] + \underline{\underline{\mathbb{K}}}\left[\mathbf{x}_i^{n-1}\right] \bullet \underline{\mathbf{U}}\left[\mathbf{x}_i^n\right] \right) \langle \mathbf{x}_j^n - \mathbf{x}_i^n \rangle \\ & - \left(\underline{\mathbf{T}}\left[\mathbf{x}_j^{n-1}\right] + \underline{\underline{\mathbb{K}}}\left[\mathbf{x}_j^{n-1}\right] \bullet \underline{\mathbf{U}}\left[\mathbf{x}_j^n\right] \right) \langle \mathbf{x}_i^n - \mathbf{x}_j^n \rangle \Big\} \beta(\boldsymbol{\xi}) V_j + \mathbf{b}_i^n \quad \forall j \in \mathcal{H}_i, \end{aligned} \tag{1.103}$$

where $\underline{\mathbf{U}}\left[\mathbf{x}_i^n\right]$ is the displacement state evaluated at the source node i at time t^n, which associates to the pair of nodes i and j their relative displacement vector and is defined as $\underline{\mathbf{U}}\left[\mathbf{x}_i, t^n\right] \langle \boldsymbol{\xi} \rangle := \mathbf{u}\left(\mathbf{x}_j, t^n\right) - \mathbf{u}\left(\mathbf{x}_i, t^n\right) = \boldsymbol{\eta}$, and $\underline{\underline{\mathbb{K}}}\left[\mathbf{x}_i^{n-1}\right]$ is a double state evaluated at the source node i at time t^{n-1} which is computed as the first Fréchet derivative of the force state, such that $\underline{\underline{\mathbb{K}}} = \nabla \underline{\mathbf{T}}$.

1.3.2 Time integration

The time integration of peridynamic models can be performed by adopting different schemes, such as the explicit central time difference method and the velocity-Verlet time integration algorithm. In [51], the authors adopted the following explicit central difference formula for the acceleration:

$$\ddot{\mathbf{u}}_i^n = \frac{\mathbf{u}_i^{n+1} - 2\mathbf{u}_i^n + \mathbf{u}_i^{n-1}}{\Delta t^2}, \tag{1.104}$$

where Δt represents the constant time step size. The velocity-Verlet scheme is instead commonly used in molecular dynamics and has been also extensively adopted in the peridynamic framework thanks to its good numerical stability. Knowing the initial conditions for each node $i \in \mathcal{B}$, i.e., $\mathbf{u}_i^0, \dot{\mathbf{u}}_i^0, \ddot{\mathbf{u}}_i^0$, the time step Δt and the time increment law $t^{n+1} = t^n + \Delta t$, the time integration can be performed as follows:

1. Computation of the velocity at time $t^{n+\frac{1}{2}}$: $\dot{\mathbf{u}}_i^{n+\frac{1}{2}} = \dot{\mathbf{u}}_i^n + \frac{1}{2}\ddot{\mathbf{u}}_i^n \Delta t$
2. Computation of the displacement at time t^{n+1}: $\mathbf{u}_i^{n+1} = \mathbf{u}_i^n + \dot{\mathbf{u}}_i^{n+\frac{1}{2}} \Delta t$
3. Computation of the acceleration at time t^{n+1}, $\ddot{\mathbf{u}}_i^{n+1}$, from (1.100) or (1.102) employing the updated configuration $\mathbf{u}_i^{n+1}$
4. Computation of the velocity at time t^{n+1}: $\dot{\mathbf{u}}_i^{n+1} = \dot{\mathbf{u}}_i^{n+\frac{1}{2}} + \frac{1}{2}\ddot{\mathbf{u}}_i^{n+1} \Delta t$

For numerical stability reasons, the time step Δt adopted during the simulations must be smaller than a predefined critical time step Δt_{crit}. The computation of this critical step size has been the subject of many studies reported in literature, such as [51, 180]. In [51], the authors evaluated the critical time step for the PMB material model as follows:

$$\Delta t_{crit} = \sqrt{\frac{2\rho}{\sum_j V_j C_{ij}}}, \tag{1.105}$$

where j iterates over all the family nodes of the source node i, and C_{ij} represents the micromodulus function of the bond connecting nodes i and j and is defined as $C_{ij} = |\mathbf{C}(\mathbf{x}_j - \mathbf{x}_i)|$. An alternative solution is represented by the so called maximum critical time step, which is evaluated through the Courant-Friedrichs-Lewy (CFL) approach such that [180]

$$\Delta t_{crit} = \frac{\Delta x}{c_w}, \tag{1.106}$$

where c_w represents the speed of sound in the material and is defined by the following relation:

$$c_w = \sqrt{\frac{K}{\rho}}, \tag{1.107}$$

where K is the bulk modulus of the material. Substituting (1.107) in (1.106), it is then possible to express the critical time step as:

$$\Delta t_{crit} = \Delta x \sqrt{\frac{\rho}{K}}. \tag{1.108}$$

1.3.3 Numerical convergence studies

The PD horizon, in its discretized form, is expressed by the following relation:

$$\delta = m \cdot \Delta x, \tag{1.109}$$

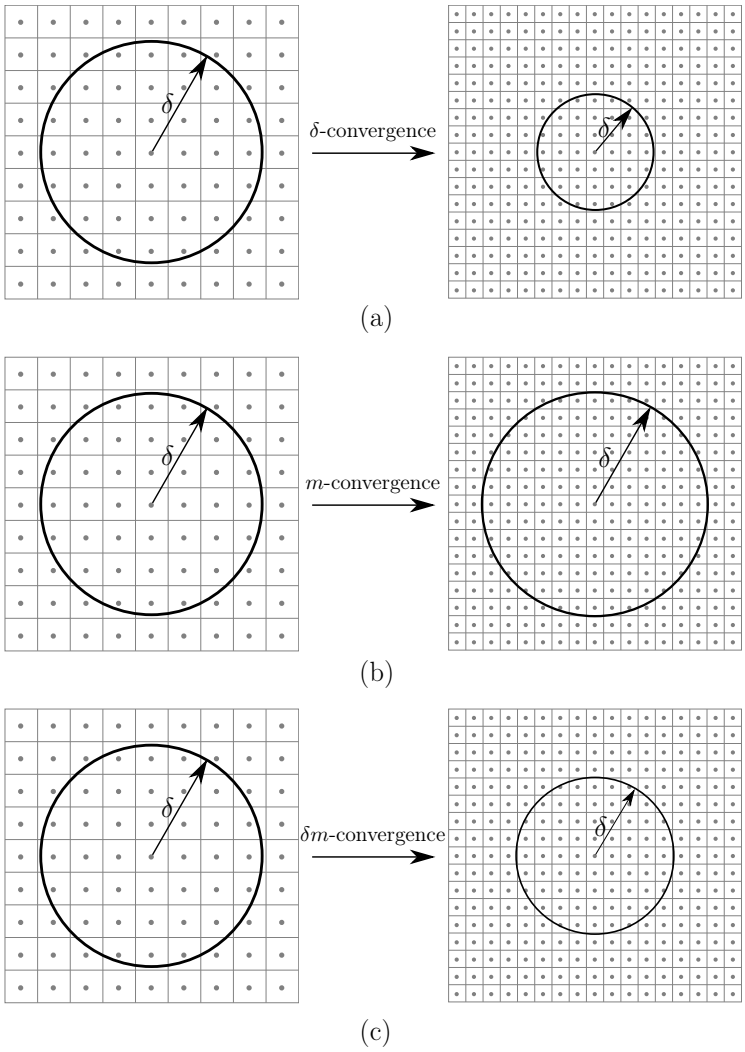

Figure 1.9: Schematic representation of (a) δ-convergence, (b) m-convergence, and (c) δm-convergence in PD.

where m is the ratio between the horizon δ and the grid spacing Δx and is usually referred to as m-ratio. The value assumed by the m-ratio is related to the number of family nodes which are located within the neighbourhood $\mathcal{H}_i$ of a source node i. The horizon radius δ and the m-ratio are, therefore, the two parameters which determine the number of interactions which have to be considered for each node in a discretized PD model. Bearing this in mind, in order to compare the solutions of PD and CCM models, it is necessary to perform some convergence studies. In [58] and [174], the authors introduced three types of convergence, namely δ-convergence, m-convergence, and δm-convergence (see Figure 1.9).

The δ-convergence is performed by keeping fixed the value of m while decreasing δ; in this way, the value of Δx decreases, resulting in an increase in the total number of nodes (see Figure 1.9a). Carrying out this kind of study, the numerical solution converges to an approximated local classical solution.

Regarding the m-convergence, this study is performed by keeping δ fixed while increasing the value of m, which again results in the decrease of the value of Δx and, consequently, in an increase in the total number of nodes (see Figure 1.9b). In this case, the numerical solution converges to the exact nonlocal PD solution for the given horizon radius.

The third type of convergence is the δm-convergence, in which the value of δ is decreased while m is increased but with a higher rate of change than that of δ (see Figure 1.9c). In this case, the numerical solution converges to both the exact nonlocal peridynamic solution and the local classical solution.

1.4 Loading and boundary conditions in peridynamics

The nonlocal nature of peridynamics introduces an important issue regarding the application of boundary conditions. Considering that the PD equilibrium equations are based on integral operators instead of partial differential operators, their variational nature does not result in natural boundary conditions, as is the case of CCM models [106]. As a consequence, in a domain described with a PD model, the prescribed displacements or loads need to be applied through a finite volume of boundary layers, rather than on a surface. The depth of the boundary layer along the material boundary is usually set to be equal to δ, since this value enables an accurate reflection of the imposed constraints in the model domain, as suggested by the numerical investigations carried out in [106].

1.5 The peridynamic surface effect

Another issue which is encountered when considering a finite domain described with a PD model is the so called surface effect, which consists in the presence of some spurious effects affecting the numerical solution in the region close to the boundary of the domain [55, 83]. The occurrence of these effects is related to the

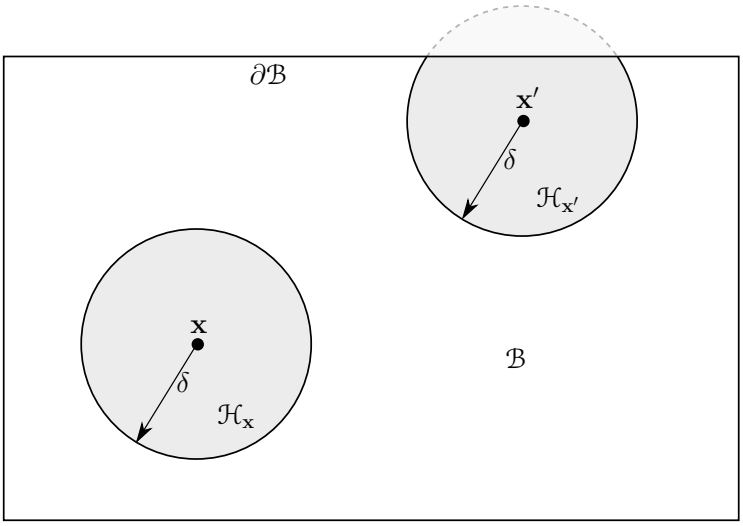

Figure 1.10: Representation of the surface effect in a finite domain $\mathcal{B}$ described with a PD model.

fact that the peridynamic material parameters are derived under the assumptions of a infinite domain and, therefore, of a fully embedded neighbourhood $\mathcal{H}_{\mathbf{x}}$ for each material point $\mathbf{x}$ in the solution domain $\mathcal{B}$, which are actually not valid for material points close to the boundary. As shown in Figure 1.10, the neighbourhood $\mathcal{H}_{\mathbf{x}'}$ of a material point $\mathbf{x}'$ located near the boundary $\partial\mathcal{B}$ is only partially contained within the model domain $\mathcal{B}$, and thus assumes a truncated shape. As a direct consequence, the portion of the neighbourhood which falls outside the domain does not contribute to the deformation energy of that material point, therefore resulting in a potential energy density which is lower than that of a material point located in the bulk of the domain (*cf.* (1.36)). As a global effect, the mechanical properties of the portion of the domain close to the boundary result to be artificially different from those of the bulk region.

Various studies reported in literature proposed some solutions to address this issue, such as [82–84, 106, 192]. In this thesis, the surface effect is eliminated either by exploiting the coupling approach outlined in Section 2.1 or by using a layer of fictitious nodes surrounding the model domain with a depth equalling the horizon, which can be also employed to impose the boundary conditions.

Chapter 2

Overall equilibrium in the coupling of peridynamics and classical continuum mechanics

Part of the work presented in this chapter has been published in [9].

2.1 Overview of the CCM-PD coupling method developed by the research group

The proposed coupling approach is based on the idea presented in [112], where the coupled stiffness matrix is defined and used to solve linear static bond-based PD problems, and then extended to dynamic problems in [84] and to models discretized using a non-uniform grid size in [193]. A further extension of this coupling approach to state-based PD models is presented in [113].

In the proposed CCM-PD coupling technique, the domain $\mathcal{B}$ is partially described with a CCM model discretized using the FEM. The remaining part of the domain is described with a PD model discretized with a meshfree method based on [51]. The two parts of the domain have to be coupled in a way that ensures an adequate transfer of force between the two regions. Figure 2.1 illustrates the CCM-PD coupled model in a one-dimensional system, where diamonds represent FEM nodes and circles represent PD nodes. Thick straight lines are FEM elements and curved thin lines are PD bonds. Nodes are either of FEM type or of PD type, and no overlapping region exists in the proposed approach in terms of the nature

of the nodes. In this example, the horizon δ is taken as twice the grid spacing, i.e., $\delta = 2\Delta x$. In this case, each PD node is connected by PD bonds to four other nodes. For instance, nodes 5, 6, 8, and 9 interact with node 7 and are called its family nodes. FEM nodes are connected by FEM elements, whereas PD nodes are connected by PD bonds. At the transition between the CCM and PD regions, it is assumed that the last FEM node (i.e., node 4 in Figure 2.1) is connected to the PD region by a single FEM element (i.e., element d in Figure 2.1), whereas the first PD node (i.e., node 5 in Figure 2.1) is nonlocally connected by PD bonds to all nodes, FEM or PD nodes, within its neighbourhood. In a similar way, all PD nodes, the neighbourhood of which contains FEM nodes, are nonlocally interacting through PD bonds with those FEM nodes.

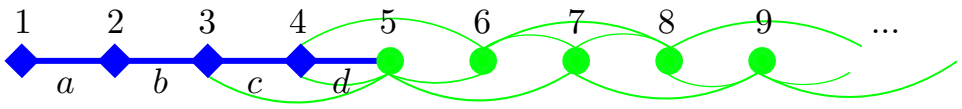

Figure 2.1: Illustration of the CCM-PD coupled model in a one-dimensional system. Blue diamonds are FEM nodes and green circles are PD nodes. Blue thick straight lines represent FEM elements and green thin curved lines represent PD bonds. Adapted from [112].

2.1.1 Assembly of the global stiffness matrix

The proposed CCM-PD coupling technique assumes that internal forces acting on a node are of the same nature as the node itself: only internal forces evaluated using the FEM approach act on FEM nodes, whereas only internal forces computed through the PD formulation are applied on PD nodes. A coupling zone can be defined where forces are exchanged between the CCM and PD parts of the domain. In the example presented in Figure 2.1, the coupling zone is composed of the FEM nodes 3 and 4; the PD nodes 5 and 6; the PD bonds $3-5$, $4-5$, and $4-6$; and the FEM element d. The coupling method assumes that the internal force exerted by the FEM element d acts only on the FEM node 4, whereas the internal forces exerted by the PD bonds $3-5$ and $4-5$ as well as $4-6$ act only on the PD nodes 5 and 6, respectively. Consequently, the assembly of the global stiffness matrix is

performed by making sure that equilibrium equations of FEM nodes contain only terms coming from the FEM approach while equilibrium equations of PD nodes include only terms derived from the PD formulation.

The case of Figure 2.1 produces the following system of equations:

$$\begin{bmatrix} l & -l & 0 & 0 & 0 & 0 & 0 & 0 & 0 & \vdots \\ -l & 2l & -l & 0 & 0 & 0 & 0 & 0 & 0 & \vdots \\ 0 & -l & 2l & -l & 0 & 0 & 0 & 0 & 0 & \vdots \\ 0 & 0 & -l & 2l & -l & 0 & 0 & 0 & 0 & \vdots \\ 0 & 0 & -\frac{1}{4}p & -p & \frac{5}{2}p & -p & -\frac{1}{4}p & 0 & 0 & \vdots \\ 0 & 0 & 0 & -\frac{1}{4}p & -p & \frac{5}{2}p & -p & -\frac{1}{4}p & 0 & \vdots \\ 0 & 0 & 0 & 0 & -\frac{1}{4}p & -p & \frac{5}{2}p & -p & -\frac{1}{4}p & \vdots \\ 0 & 0 & 0 & 0 & \cdots & \cdots & \cdots & \ddots & \vdots & \vdots \\ \cdots & \cdots & \cdots & \cdots & \cdots & \cdots & \cdots & \cdots & \ddots & \vdots \end{bmatrix} \begin{bmatrix} u_1 \\ u_2 \\ u_3 \\ u_4 \\ u_5 \\ \vdots \\ \vdots \\ \vdots \\ u_N \end{bmatrix} = \begin{bmatrix} F_1 \\ F_2 \\ F_3 \\ F_4 \\ F_5 \\ \vdots \\ \vdots \\ \vdots \\ F_N \end{bmatrix}, \quad (2.1)$$

where $l := EA/\Delta x$ [89], $p := cA^2\Delta x$ [174], N is the total number of nodes (including FEM and PD nodes), $\{u_i\}_{i=1,\dots,N}$ are the nodal displacements, $\{F_i\}_{i=1,\dots,N}$ are the external nodal forces, E is Young's modulus, c is the micromodulus constant, and the cross-sectional area A is assumed to be $A = 1$; the same assumption applies hereafter. To obtain (2.1), we assumed a CCM model given by (2.41) and a PD model given by (2.48) with a micromodulus function $c(|\xi|) = c/|\xi|$. The meshfree PD discretization employed in (2.1) uses a partial-volume correction [191], which applies a factor of $\frac{1}{2}$ to the contribution of second-nearest neighbours. The solution of a single equation satisfies node equilibrium. The overall equilibrium of the whole structure, however, requires the sum of the external nodal forces to be equal to zero.

In the numerical examples of Sections 2.4 and 2.6, a nodal displacement vector will be input into the system and the relevant external nodal forces (i.e., 'reactions', since the displacements are imposed) will be computed according to a system of the type of (2.1) in the one-dimensional case and a corresponding system in the two-dimensional case. In some cases of CCM-PD coupled systems, the force vector will have a non-zero resultant, i.e., $\sum_{i=1}^{N} F_i \neq 0$, and therefore overall equilibrium will not be satisfied, even if this type of CCM-PD coupling exactly satisfies all standard

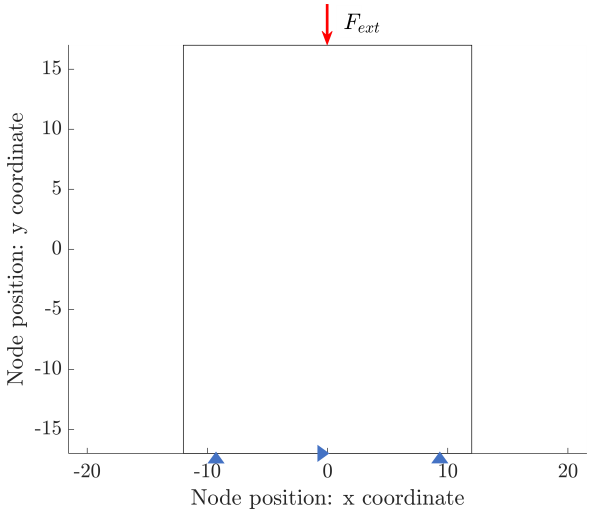

Figure 2.2: Two-dimensional rectangular plate used to study the static equilibrium issue. The arrow identifies the applied vertical force and the triangles indicate the constrained points of the structure.

numerical tests for static coupling problems carried out by imposing rigid body motions as well as uniform and linear strain distributions [84, 112, 113].

2.2 Statement of the problem: lack of overall equilibrium in CCM-PD coupled models

In Figure 2.2, a two-dimensional homogeneous, isotropic linear elastic rectangular plate is shown. This structure with dimensions 24×34 (L_x and L_y, respectively) is studied imposing as a load condition a vertical force ($F_{ext} = 10$) acting at the centre of the top edge. The plate is constrained so that the points of the bottom edge with coordinates $(-9, -17)$ and $(+9, -17)$ cannot move in the vertical direction, i.e., $u_2 = 0$, whereas the central point of the bottom edge cannot move in the horizontal direction, i.e., $u_1 = 0$, where u_1 and u_2 are the horizontal and vertical components, respectively, of the two-dimensional displacement field $\mathbf{u} = (u_1, u_2)$. The values of the main problem parameters are $E = 1$ (Young's modulus), $\nu = 1/3$ (Poisson's ratio), and $h = 1$ (plate thickness). Problem parameters such as L_x, L_y, E, and h are in consistent units. This study considers a plane stress condition. In order to numerically investigate the static equilibrium of this structure, three models have been implemented: a fully CCM model, a fully PD model, and the CCM-PD

coupled model described in Section 2.1. Since the problem is linear in terms of material response and deformation, the CCM model used is based on classical linear elasticity, whereas the employed PD model is given by a two-dimensional linear bond-based model [7, 178].

The discretization of the domain employs a uniform grid with $\Delta x = \Delta y = 1$. All three two-dimensional simulations are composed of 875 nodes as shown in Figure 2.3. The region corresponding to the PD portion of the coupled model has a size of $L_{PDx} = L_{PDy} = 10$, and its centre has coordinates $(0, 0)$. The fully CCM model and the CCM part of the CCM-PD coupled model are both discretized using four-node square plane stress FEM elements for which the element stiffness matrix has been evaluated with exact integration [194]. For the fully PD model and the PD portion of the CCM-PD coupled model, we employ a meshfree discretization with a partial-volume correction [190]. The PD horizon is taken as $\delta = 3$ (i.e., $m = \delta/\Delta x = 3$) and the micromodulus constant c has been evaluated through (1.40), assuming a plate thickness of $h = 1$. Table 2.1 reports the values of the reaction forces for the three models and the resulting relative errors, defined by the following relation:

$$e_{rel} := \frac{F_{ext} + \sum Reactions}{|F_{ext}|}, \tag{2.2}$$

where $\sum Reactions$ is the sum of the reaction forces generated on the vertically constrained nodes, which is evaluated using the following equation:

$$\sum Reactions = R_{y_L} + R_{y_R}, \tag{2.3}$$

where R_{y_L} is the resulting vertical reaction force at the bottom-left constrained node and R_{y_R} is the resulting vertical reaction force at the bottom-right constrained node. Table 2.1 clearly shows that the static equilibrium equations are not exactly fulfilled by the CCM-PD coupled model.

The following sections of this chapter study the origin of out-of-balance forces and discuss possible ways to reduce them. In the first part of the chapter, an extensive analysis of the consistency between linear bond-based PD and CCM models is presented, discussing its theoretical background in Section 2.3 and related numerical examples in Section 2.4. The second part of the chapter focuses more thoroughly on the overall static equilibrium issue, presenting a comprehensive analysis of the

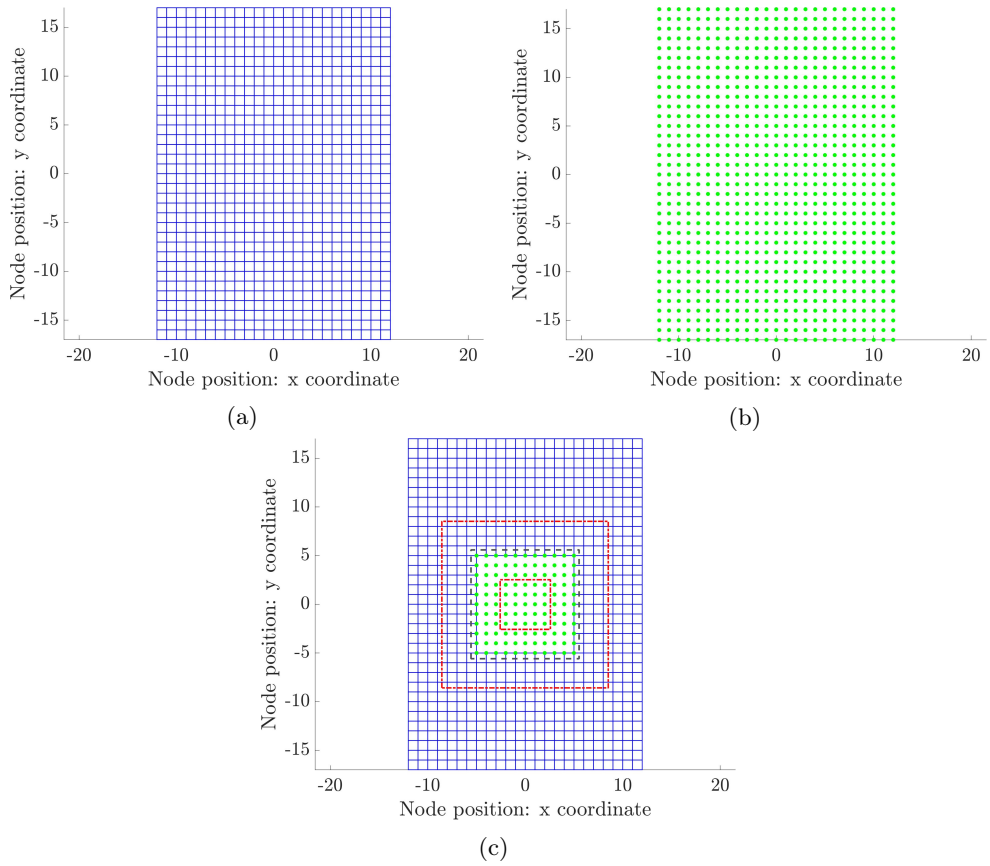

Figure 2.3: Discretization of the two-dimensional example under investigation: (a) fully CCM model, (b) fully PD model, and (c) CCM-PD coupled model. The blue mesh is composed of conventional four-node plane stress FEM elements, while green circles represent PD nodes. In (c), the dashed grey lines represent the interface between the PD and CCM regions, while the portion of the domain bounded by the dashed–dotted red lines is the coupling zone. In the figure, $\Delta x = \Delta y = 1$ and $m = \delta/\Delta x = 3$.

force balance in one-dimensional and two-dimensional CCM–PD coupled models in Section 2.5. Some numerical examples to assess the out-of-balance in CCM-PD coupled models and confirm the analytical results, involving one-dimensional and two-dimensional cases, are provided in Section 2.6. In the last part of the chapter, i.e., in Section 2.7, the numerical study of the out-of-balance issue is extended to a two-dimensional and a fully three-dimensional crack propagation problem. In all the cases considered in this chapter, the out-of-balance forces are 'small' compared to the applied forces, but they are not as small as round-off errors.

Computational technique	F_{ext}	$\sum Reactions$	e_{rel}
Fully CCM model	-10	9.9999	-2.51×10^{-13}
Fully PD model	-10	10.0000	5.55×10^{-13}
CCM-PD coupled model	-10	10.1425	1.42×10^{-02}

Table 2.1: Reaction forces and relative errors resulting from each numerical simulation.

2.3 Theoretical background: consistency between linear bond-based PD and CCM models

In Sections 2.3.1 and 2.3.2, the consistency between CCM and PD models is studied through the analysis of the corresponding governing equations.

The theoretical analysis presented in the following sections has been mainly derived by Doctor Pablo Seleson, Research Scientist at the Oak Ridge National Laboratory (ORNL), Oak Ridge, United States [9].

2.3.1 One-dimensional case

Assume a domain $\mathcal{B} \subset \mathbb{R}$ and let a one-dimensional linear bond-based PD model be given by (*cf.* (1.22)):

$$\rho(x)\ddot{u}(x,t) = \int_{\mathcal{H}_x} c(|x'-x|)(u(x',t)-u(x,t))dx' + b(x,t), \tag{2.4}$$

where ρ is the mass density, $\ddot{u}$ is the second derivative in time of the displacement field u, $c(|\xi|)$ is a micromodulus function with $\xi = x' - x$ a PD bond, $\mathcal{H}_x$ is the neighbourhood of the material point x, and b is a prescribed body force density field. The relation $c(|\xi|) = \lambda(|\xi|)|\xi|^2$ (*cf.* (1.20)) holds in one dimension. For points in the bulk of the body, the neighbourhood is $\mathcal{H}_x = [x-\delta, x+\delta]$ and we can use the change of variable $\xi = x' - x$ to express (2.4) as

$$\rho(x)\ddot{u}(x,t) = \int_{-\delta}^{\delta} c(|\xi|)(u(x+\xi,t)-u(x,t))d\xi + b(x,t). \tag{2.5}$$

To establish a connection between (2.5) and the corresponding CCM model, given by the classical wave equation

$$\rho(x)\ddot{u}(x,t) = E\frac{\partial^2 u}{\partial x^2}(x,t) + b(x,t) \tag{2.6}$$

with E Young's modulus, we assume the displacement field is smooth and perform a Taylor expansion of $u(x+\xi,t)$ about x:

$$u(x+\xi,t) = u(x,t) + \frac{\partial u}{\partial x}(x,t)\xi + \frac{1}{2}\frac{\partial^2 u}{\partial x^2}(x,t)\xi^2 + \frac{1}{3!}\frac{\partial^3 u}{\partial x^3}(x,t)\xi^3 + \frac{1}{4!}\frac{\partial^4 u}{\partial x^4}(x,t)\xi^4 + \dots. \tag{2.7}$$

Substituting (2.7) in (2.5), we obtain

$$\rho(x)\ddot{u}(x,t) = \int_{-\delta}^{\delta} c(|\xi|)\bigg(\frac{\partial u}{\partial x}(x,t)\xi + \frac{1}{2}\frac{\partial^2 u}{\partial x^2}(x,t)\xi^2 + \frac{1}{3!}\frac{\partial^3 u}{\partial x^3}(x,t)\xi^3 + \frac{1}{4!}\frac{\partial^4 u}{\partial x^4}(x,t)\xi^4 + \dots\bigg)d\xi + b(x,t). \tag{2.8}$$

We observe that terms with an odd power of ξ vanish due to their antisymmetry and the symmetry of the integration domain. Then, we have

$$\rho(x)\ddot{u}(x,t) = \left[\frac{1}{2}\int_{-\delta}^{\delta} c(|\xi|)\xi^2 d\xi\right]\frac{\partial^2 u}{\partial x^2}(x,t) + \left[\frac{1}{4!}\int_{-\delta}^{\delta} c(|\xi|)\xi^4 d\xi\right]\frac{\partial^4 u}{\partial x^4}(x,t) + \dots + b(x,t). \tag{2.9}$$

Assuming fourth-order and higher derivatives of displacements are negligible, we obtain

$$\rho(x)\ddot{u}(x,t) = \left[\frac{1}{2}\int_{-\delta}^{\delta} c(|\xi|)\xi^2 d\xi\right]\frac{\partial^2 u}{\partial x^2}(x,t) + b(x,t). \tag{2.10}$$

This allows us to relate the micromodulus function $c(|\xi|)$ in (2.5) to Young's modulus E in (2.6):

$$\frac{1}{2}\int_{-\delta}^{\delta} c(|\xi|)\xi^2 d\xi = E, \tag{2.11}$$

so that the PD model (2.5) reduces to the CCM model (2.6).

We conclude that for a smooth displacement field, if fourth-order and higher derivatives of displacements can be neglected, the one-dimensional linear bond-based PD equation (2.5) reduces to the CCM equation (2.6), assuming relation (2.11) holds. In particular, this implies that, given the same body force density field and consistent boundary conditions, the PD and CCM models possess the same static solution for problems with constant, linear, quadratic, or cubic solutions. To characterize the model discrepancy between the PD and CCM models, we now assume a particular form for the micromodulus function.

Model discrepancy between PD and CCM models in one dimension

Assume a micromodulus function of the following form:

$$c(|\xi|) = \frac{c}{|\xi|^\alpha} \tag{2.12}$$

with c a constant and $\alpha < 3$ (see below). Then, we can compute the following integrals appearing in (2.9):

$$\frac{1}{2}\int_{-\delta}^{\delta} c(|\xi|)\xi^2 d\xi = \int_0^{\delta} c\,\xi^{2-\alpha} d\xi = \frac{\delta^{3-\alpha}}{3-\alpha}c, \tag{2.13}$$

$$\frac{1}{4!}\int_{-\delta}^{\delta} c(|\xi|)\xi^4 d\xi = \frac{2}{4!}\int_0^{\delta} c\,\xi^{4-\alpha} d\xi = \frac{2}{4!}\frac{\delta^{5-\alpha}}{5-\alpha}c. \tag{2.14}$$

Equating (2.11) and (2.13), we obtain

$$c = \frac{(3-\alpha)E}{\delta^{3-\alpha}}. \tag{2.15}$$

Note that the case $\alpha = 1$ recovers the micromodulus definition reported in [174] for a one-dimensional bar with unit cross-sectional area (*cf.* (1.42)). Using (2.13)–(2.15) in (2.9), we get

$$\rho(x)\ddot{u}(x,t) = E\left[\frac{\partial^2 u}{\partial x^2}(x,t) + \frac{1}{12}\left(\frac{3-\alpha}{5-\alpha}\right)\delta^2\frac{\partial^4 u}{\partial x^4}(x,t) + \ldots\right] + b(x,t). \tag{2.16}$$

In the limit as $\delta \to 0$, we have

$$\rho(x)\ddot{u}(x,t) = E\frac{\partial^2 u}{\partial x^2}(x,t) + O(\delta^2) + b(x,t), \tag{2.17}$$

so that the PD model (2.5) converges to the CCM model (2.6) at a rate of $\mathcal{O}(\delta^2)$. The leading term in the model discrepancy is of order $\mathcal{O}(\delta^2)$.

2.3.2 Two-dimensional case

Assume a domain $\mathcal{B} \subset \mathbb{R}^2$ and let a two-dimensional linear bond-based PD model be given by (*cf.* (1.22)):

$$\rho(\mathbf{x})\ddot{\mathbf{u}}(\mathbf{x},t) = \int_{\mathcal{H}_\mathbf{x}} \lambda(\|\mathbf{x}'-\mathbf{x}\|)(\mathbf{x}'-\mathbf{x})\otimes(\mathbf{x}'-\mathbf{x})(\mathbf{u}(\mathbf{x}',t)-\mathbf{u}(\mathbf{x},t))d\mathbf{x}'+\mathbf{b}(\mathbf{x},t), \tag{2.18}$$

where ρ is the mass density, $\ddot{\mathbf{u}}$ is the second derivative in time of the displacement field $\mathbf{u}$, $\lambda(\|\boldsymbol{\xi}\|)$ is a micromodulus function with $\boldsymbol{\xi} = \mathbf{x}' - \mathbf{x}$ a PD bond, $\mathcal{H}_\mathbf{x}$ is the neighbourhood of the material point $\mathbf{x}$, and $\mathbf{b}$ is a prescribed body force density field.

For points in the bulk of the body, we can use the change of variable $\boldsymbol{\xi} = \mathbf{x}' - \mathbf{x}$ to express (2.18) as

$$\rho(\mathbf{x})\ddot{\mathbf{u}}(\mathbf{x},t) = \int_{\mathcal{H}} \lambda(\|\boldsymbol{\xi}\|)\boldsymbol{\xi}\otimes\boldsymbol{\xi}(\mathbf{u}(\mathbf{x}+\boldsymbol{\xi},t)-\mathbf{u}(\mathbf{x},t))d\boldsymbol{\xi} + \mathbf{b}(\mathbf{x},t), \tag{2.19}$$

where

$$\mathcal{H} := \left\{\boldsymbol{\xi}\in\mathbb{R}^2 : \|\boldsymbol{\xi}\| \leqslant \delta\right\}. \tag{2.20}$$

We would like to establish a connection between the PD model (2.19) and the two-dimensional classical linear elasticity plane stress model given by:[1]

$$\rho(\mathbf{x})\ddot{u}_1(\mathbf{x},t) = \frac{9E}{8}\left[\frac{\partial^2 u_1}{\partial x^2}(\mathbf{x},t) + \frac{2}{3}\frac{\partial^2 u_2}{\partial x\partial y}(\mathbf{x},t) + \frac{1}{3}\frac{\partial^2 u_1}{\partial y^2}(\mathbf{x},t)\right] + b_1(\mathbf{x},t), \tag{2.23a}$$

$$\rho(\mathbf{x})\ddot{u}_2(\mathbf{x},t) = \frac{9E}{8}\left[\frac{\partial^2 u_2}{\partial y^2}(\mathbf{x},t) + \frac{2}{3}\frac{\partial^2 u_1}{\partial x\partial y}(\mathbf{x},t) + \frac{1}{3}\frac{\partial^2 u_2}{\partial x^2}(\mathbf{x},t)\right] + b_2(\mathbf{x},t), \tag{2.23b}$$

where E is Young's modulus and we assumed a Poisson's ratio of $\nu = 1/3$ [173,195]. For this purpose, we assume the displacement field is smooth and perform a Taylor expansion of $\mathbf{u}(\mathbf{x}+\boldsymbol{\xi},t)$ about $\mathbf{x}$:

$$\begin{aligned} u_j(\mathbf{x}+\boldsymbol{\xi},t) = u_j(\mathbf{x},t) &+ \frac{\partial u_j}{\partial x_k}(\mathbf{x},t)\xi_k + \frac{1}{2}\frac{\partial^2 u_j}{\partial x_k\partial x_l}(\mathbf{x},t)\xi_k\xi_l + \frac{1}{3!}\frac{\partial^3 u_j}{\partial x_k\partial x_l\partial x_m}(\mathbf{x},t)\xi_k\xi_l\xi_m \\ &+ \frac{1}{4!}\frac{\partial^4 u_j}{\partial x_k\partial x_l\partial x_m\partial x_n}(\mathbf{x},t)\xi_k\xi_l\xi_m\xi_n + \ldots, \quad j = 1,2, \end{aligned} \tag{2.24}$$

where repeated indices imply a summation by 1 and 2. Employing (2.24) for the ith

[1] In classical linear elasticity, the stress-strain relation for isotropic materials under plane stress is given by:

$$\begin{bmatrix} \sigma_{11} \\ \sigma_{22} \\ \sigma_{12} \end{bmatrix} = \frac{E}{1-\nu^2}\begin{bmatrix} 1 & \nu & 0 \\ \nu & 1 & 0 \\ 0 & 0 & 1-\nu \end{bmatrix}\begin{bmatrix} \varepsilon_{11} \\ \varepsilon_{22} \\ \varepsilon_{12} \end{bmatrix}, \tag{2.21}$$

where E is Young's modulus, ν is Poisson's ratio, σ_{ij} are the components of the stress tensor, and ε_{ij} are the components of the infinitesimal strain tensor, $\varepsilon_{ij} = \frac{1}{2}\left(\frac{\partial u_i}{\partial x_j} + \frac{\partial u_j}{\partial x_i}\right)$; both $\boldsymbol{\sigma}$ and $\boldsymbol{\varepsilon}$ are symmetric tensors. The equation of motion is given, in component form, by

$$\rho(\mathbf{x})\ddot{u}_i(\mathbf{x},t) = \frac{\partial\sigma_{ij}}{\partial x_j}(\mathbf{x},t) + b_i(\mathbf{x},t), \quad i = 1,2, \tag{2.22}$$

where repeated indices imply summation by 1 and 2.

component of (2.19), we obtain

$$\begin{aligned}\rho(\mathbf{x})\ddot{u}_i(\mathbf{x},t) &= \int_{\mathcal{H}} \lambda(\|\boldsymbol{\xi}\|)\xi_i\xi_j(u_j(\mathbf{x}+\boldsymbol{\xi},t)-u_j(\mathbf{x},t))d\boldsymbol{\xi} + b_i(\mathbf{x},t)\\ &= \int_{\mathcal{H}} \lambda(\|\boldsymbol{\xi}\|)\xi_i\xi_j\left(\frac{\partial u_j}{\partial x_k}(\mathbf{x},t)\xi_k + \frac{1}{2}\frac{\partial^2 u_j}{\partial x_k\partial x_l}(\mathbf{x},t)\xi_k\xi_l\right.\\ &\quad + \frac{1}{3!}\frac{\partial^3 u_j}{\partial x_k\partial x_l\partial x_m}(\mathbf{x},t)\xi_k\xi_l\xi_m + \frac{1}{4!}\frac{\partial^4 u_j}{\partial x_k\partial x_l\partial x_m\partial x_n}(\mathbf{x},t)\xi_k\xi_l\xi_m\xi_n + \ldots\Big)d\boldsymbol{\xi}\\ &\quad + b_i(\mathbf{x},t). \end{aligned} \tag{2.25}$$

We observe that terms with an odd number of components of $\boldsymbol{\xi}$ vanish due to their antisymmetry and the symmetry of the integration domain. Then, we have

$$\begin{aligned}\rho(\mathbf{x})\ddot{u}_i(\mathbf{x},t) &= \left[\frac{1}{2}\int_{\mathcal{H}} \lambda(\|\boldsymbol{\xi}\|)\xi_i\xi_j\xi_k\xi_l d\boldsymbol{\xi}\right]\frac{\partial^2 u_j}{\partial x_k\partial x_l}(\mathbf{x},t)\\ &\quad + \left[\frac{1}{4!}\int_{\mathcal{H}} \lambda(\|\boldsymbol{\xi}\|)\xi_i\xi_j\xi_k\xi_l\xi_m\xi_n d\boldsymbol{\xi}\right]\frac{\partial^4 u_j}{\partial x_k\partial x_l\partial x_m\partial x_n}(\mathbf{x},t)\\ &\quad + \ldots + b_i(\mathbf{x},t). \end{aligned} \tag{2.26}$$

Assuming fourth-order and higher derivatives of displacements are negligible, we obtain

$$\rho(\mathbf{x})\ddot{u}_i(\mathbf{x},t) = \left[\frac{1}{2}\int_{\mathcal{H}} \lambda(\|\boldsymbol{\xi}\|)\xi_i\xi_j\xi_k\xi_l d\boldsymbol{\xi}\right]\frac{\partial^2 u_j}{\partial x_k\partial x_l}(\mathbf{x},t) + b_i(\mathbf{x},t). \tag{2.27}$$

Employing polar coordinates, $\xi_1 = r\cos(\theta)$ and $\xi_2 = r\sin(\theta)$, we can compute the following integrals (see [9]):

$$\frac{1}{2}\int_{\mathcal{H}} \lambda(\|\boldsymbol{\xi}\|)\xi_1^4 d\boldsymbol{\xi} = \left(\frac{1}{2}\int_0^\delta \lambda(r)r^5 dr\right)\int_0^{2\pi}\cos^4(\theta)d\theta = \Lambda, \tag{2.28a}$$

$$\frac{1}{2}\int_{\mathcal{H}} \lambda(\|\boldsymbol{\xi}\|)\xi_1^2\xi_2^2 d\boldsymbol{\xi} = \left(\frac{1}{2}\int_0^\delta \lambda(r)r^5 dr\right)\int_0^{2\pi}\cos^2(\theta)\sin^2(\theta)d\theta = \frac{\Lambda}{3}, \tag{2.28b}$$

$$\frac{1}{2}\int_{\mathcal{H}} \lambda(\|\boldsymbol{\xi}\|)\xi_2^4 d\boldsymbol{\xi} = \left(\frac{1}{2}\int_0^\delta \lambda(r)r^5 dr\right)\int_0^{2\pi}\sin^4(\theta)d\theta = \Lambda, \tag{2.28c}$$

$$\frac{1}{2}\int_{\mathcal{H}} \lambda(\|\boldsymbol{\xi}\|)\xi_1^3\xi_2 d\boldsymbol{\xi} = \frac{1}{2}\int_{\mathcal{H}} \lambda(\|\boldsymbol{\xi}\|)\xi_1\xi_2^3 d\boldsymbol{\xi} = 0, \tag{2.28d}$$

where

$$\Lambda := \frac{3\pi}{4}\left(\frac{1}{2}\int_0^\delta \lambda(r)r^5 dr\right). \tag{2.29}$$

Substituting (2.28) in (2.27), we get (see [9])

$$\rho(\mathbf{x})\ddot{u}_1(\mathbf{x},t) = \Lambda\left[\frac{\partial^2 u_1}{\partial x^2}(\mathbf{x},t) + \frac{2}{3}\frac{\partial^2 u_2}{\partial x\partial y}(\mathbf{x},t) + \frac{1}{3}\frac{\partial^2 u_1}{\partial y^2}(\mathbf{x},t)\right] + b_1(\mathbf{x},t), \tag{2.30a}$$

$$\rho(\mathbf{x})\ddot{u}_2(\mathbf{x},t) = \Lambda\left[\frac{\partial^2 u_2}{\partial y^2}(\mathbf{x},t) + \frac{2}{3}\frac{\partial^2 u_1}{\partial x\partial y}(\mathbf{x},t) + \frac{1}{3}\frac{\partial^2 u_2}{\partial x^2}(\mathbf{x},t)\right] + b_2(\mathbf{x},t). \tag{2.30b}$$

Equating (2.30a) and (2.23a) or (2.30b) and (2.23b), we obtain

$$\Lambda = \frac{9E}{8}. \tag{2.31}$$

As in the one-dimensional case in Section 2.3.1, we conclude that for a smooth displacement field, if fourth-order and higher derivatives of displacements can be neglected, the two-dimensional linear bond-based PD equation (2.19) reduces to the CCM equation (2.23), assuming relation (2.31) holds (*cf.* (2.29)). In particular, this implies that given the same body force density field and consistent boundary conditions, the PD and CCM models possess the same static solution for problems with constant, linear, quadratic, or cubic solutions. To characterize the model discrepancy between the PD and CCM models, we now assume a particular form for the micromodulus function.

Model discrepancy between PD and CCM models in two dimensions

Assume a micromodulus function of the following form:

$$\lambda(\|\boldsymbol{\xi}\|) = \frac{c}{\|\boldsymbol{\xi}\|^{\alpha}} \tag{2.32}$$

with c a constant and $\alpha < 6$ (see below). Then, we can compute Λ in (2.29):

$$\Lambda = \frac{3\pi}{4}\left(\frac{1}{2}\int_0^{\delta} cr^{5-\alpha}dr\right) = c\frac{3\pi}{8}\frac{\delta^{6-\alpha}}{6-\alpha}. \tag{2.33}$$

By equating (2.33) and (2.31), we get

$$c = \frac{3(6-\alpha)E}{\pi\delta^{6-\alpha}}. \tag{2.34}$$

Note that the case $\alpha = 3$ recovers the micromodulus definition reported in [173] for a plane stress structure with unit thickness (*cf.* (1.40)). Employing polar coordinates as in (2.28), we can express the coefficients of the fourth-order derivatives in (2.26) as (see [9])

$$\frac{1}{4!}\int_{\mathcal{H}} \lambda(\|\boldsymbol{\xi}\|)\xi_i\xi_j\xi_k\xi_l\xi_m\xi_n d\boldsymbol{\xi} = \frac{1}{4!}\left(\int_0^{\delta}\lambda(r)r^7dr\right)\int_0^{2\pi}(\cos(\theta))^a(\sin(\theta))^{6-a}d\theta, \tag{2.35}$$

where a is the number of 1s in $\{i, j, k, l, m, n\}$. We now have (*cf.* (2.32) and (2.34)),

$$\int_0^{\delta}\lambda(r)r^7dr = \int_0^{\delta} cr^{7-\alpha}dr = c\frac{\delta^{8-\alpha}}{8-\alpha} = \frac{3}{\pi}\frac{6-\alpha}{8-\alpha}E\delta^2. \tag{2.36}$$

In the limit as $\delta \to 0$, (2.26) gives (*cf.* (2.30) and (2.31))

$$\rho(\mathbf{x})\ddot{u}_1(\mathbf{x},t) = \frac{9E}{8}\left[\frac{\partial^2 u_1}{\partial x^2}(\mathbf{x},t) + \frac{2}{3}\frac{\partial^2 u_2}{\partial x \partial y}(\mathbf{x},t) + \frac{1}{3}\frac{\partial^2 u_1}{\partial y^2}(\mathbf{x},t)\right] + O(\delta^2) + b_1(\mathbf{x},t), \tag{2.37a}$$

$$\rho(\mathbf{x})\ddot{u}_2(\mathbf{x},t) = \frac{9E}{8}\left[\frac{\partial^2 u_2}{\partial y^2}(\mathbf{x},t) + \frac{2}{3}\frac{\partial^2 u_1}{\partial x \partial y}(\mathbf{x},t) + \frac{1}{3}\frac{\partial^2 u_2}{\partial x^2}(\mathbf{x},t)\right] + O(\delta^2) + b_2(\mathbf{x},t), \tag{2.37b}$$

so that the PD model (2.19) converges to the CCM model (2.23) at a rate of $\mathcal{O}(\delta^2)$. The leading term in the model discrepancy is of order $\mathcal{O}(\delta^2)$, similar to the result obtained in Section 2.3.1.

2.4 Numerical assessment of the consistency between linear bond-based PD and CCM models

The present section aims at numerically confirming the theoretical analysis of the consistency between CCM and PD models discussed in Section 2.3 with examples involving one-dimensional models in Section 2.4.1 and two-dimensional models in Section 2.4.2. All numerical examples are linear in terms of material response and deformation [7].

2.4.1 One-dimensional case

In this section, an equilibrium check is carried out on one-dimensional cases adopting the CCM-PD coupling strategy described in Section 2.1. We consider a bar discretized with $N = 31$ nodes uniformly distributed with $\Delta x = 1$ as shown in Figure 2.4. The PD portion of the domain is composed of nodes with coordinates in the interval $[10 \,..\, 20]$, while the remaining part of the domain is modelled with a CCM model discretized using two-node bar FEM elements with linear shape functions. The values of the main problem parameters are $L = 30$ (bar length), $E = 1$ (Young's modulus), and $A = 1$ (bar cross-sectional area) in consistent units. We assume a CCM model given by (2.6) and a PD model given by (2.5) with a micromodulus function $c(|\xi|) = c/|\xi|$. The PD horizon is taken as $\delta = 3$ (i.e., $m = \delta/\Delta x = 3$) and the micromodulus constant c has been evaluated through (1.42). The PD portion of the domain employs a meshfree discretization with a partial-volume correction [191].

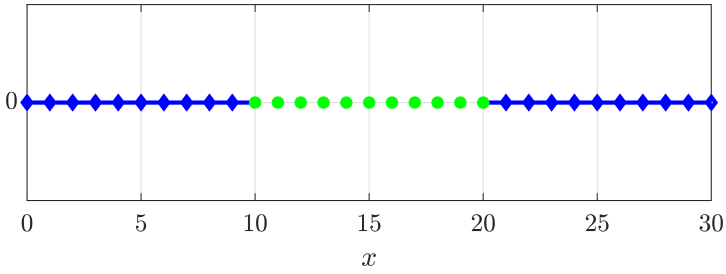

Figure 2.4: CCM-PD coupled model for the one-dimensional case. Blue diamonds are FEM nodes, green circles are PD nodes, and blue solid lines represent FEM elements.

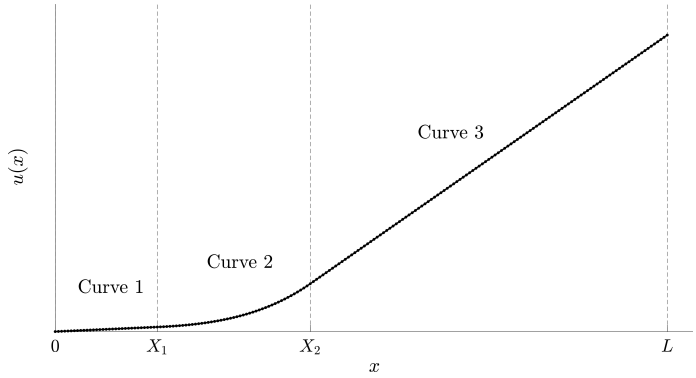

Figure 2.5: Imposed displacement field along the bar length.

In the CCM-PD coupled model, a displacement is imposed on all the nodes and the reaction forces are computed using a system of the type of (2.1). The imposed displacement field is a piecewise polynomial function composed of three curves: two linear functions connected by a quartic function as shown in Figure 2.5. The quartic function has been selected to ensure C^1 continuity of the displacement field (i.e., continuity of the displacement field and its first derivative) along the bar length. The three curves used for the imposed displacement field are described in Table 2.2; the value of the coefficient a is set to $a = 0.0001$.

The following part of this section presents five different cases of displacement distributions imposed on the bar. For all the cases, we keep fixed the location of the PD portion of the domain and all the problem parameters, while only changing the position of the quartic displacement curve along the bar length. The resulting relative

Displacement type	Displacement field equation	Domain
Curve 1: linear	$u(x) = ax$	$x \in (0, X_1)$
Curve 2: quartic	$u(x) = \frac{a}{4X_1^3}x^4 + \frac{3a}{4}X_1$	$x \in (X_1, X_2)$
Curve 3: linear	$u(x) = a\left(\frac{X_2}{X_1}\right)^3 (x - X_2) + \frac{a}{4X_1^3}\left(X_2^4 + 3X_1^4\right)$	$x \in (X_2, L)$

Table 2.2: Piecewise displacement field for the one-dimensional case.

out-of-balance error is evaluated through the following quantity:

$$e_r := \frac{\left|\sum_{i=1}^{N} F_i\right|}{\sum_{i=1}^{N} |F_i|}, \tag{2.38}$$

where F_i is the reaction force generated at node i after the imposition of the displacement field. In the case of overall equilibrium of the whole structure, the sum of the reaction forces is equal to zero (see Section 2.1.1).

Table 2.3 lists the results in terms of relative out-of-balance error for the five different cases investigated (see Figure 2.6). In the first three cases, i.e., configurations (a), (b), and (c) in Figure 2.6, the quartic displacement curve is located away from the two coupling zones. In the configurations (a) and (c) the quartic displacement curve is placed within the CCM portion of the domain, whereas in the configuration (b) the quartic displacement curve is located in the PD region. As shown in Table 2.3, none of these cases exhibit out-of-balance, since the magnitude of the resulting relative out-of-balance errors is on the order of machine precision. In the last two cases, i.e., configurations (d) and (e) in Figure 2.6, the quartic displacement curve is located over the left and right coupling zones, respectively. As it is clearly reported in Table 2.3, in these cases the resulting relative out-of-balance errors are about twelve orders of magnitude larger than the ones computed for the first three cases. These results demonstrate that the resulting relative out-of-balance error changes significantly when varying the position of the quartic displacement curve with respect to the location of the coupling zone in the CCM-PD coupled model. This is consistent with the theoretical background presented in Section 2.3.1.

In the last part of this section, the outputs obtained by performing both an m- and a δ-convergence study (see Section 1.3.3) are presented in order to examine

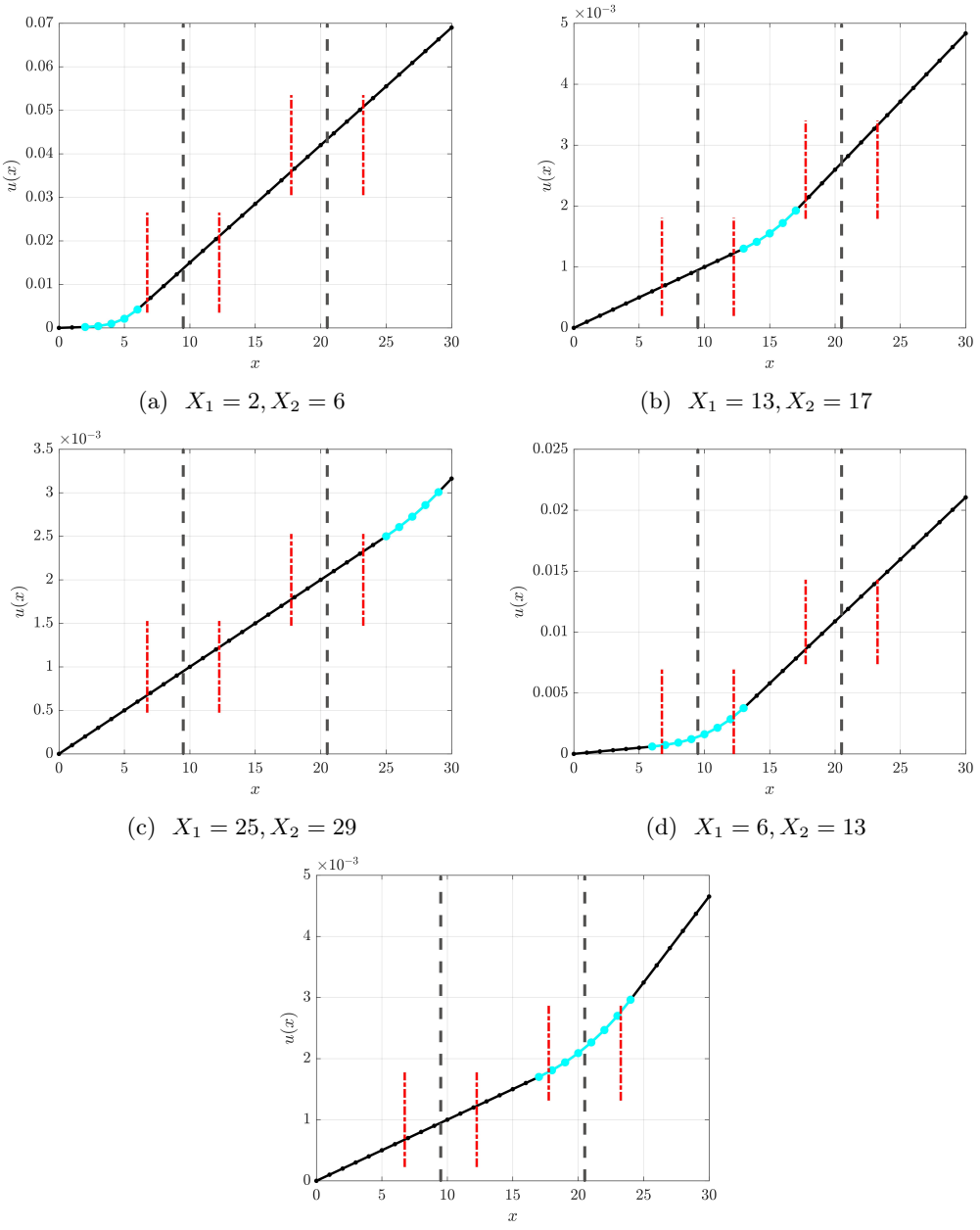

(a) $X_1 = 2, X_2 = 6$

(b) $X_1 = 13, X_2 = 17$

(c) $X_1 = 25, X_2 = 29$

(d) $X_1 = 6, X_2 = 13$

(e) $X_1 = 17, X_2 = 24$

Figure 2.6: Imposed displacement fields on the CCM-PD coupled model with a quartic displacement curve placed in different locations along the bar. The quartic displacement curve, represented by cyan lines, is located in (a) the left CCM region, (b) the central PD part, (c) the right CCM region, (d) the left coupling zone, and (e) the right coupling zone. Long dashed gray vertical lines indicate the interfaces between the PD and CCM portions of the domain, while short dashed-dotted red vertical lines define the coupling zones of the model. The values of the parameters X_1 and X_2 defining the curves in Table 2.2 are indicated for each case. For clarity reasons, the vertical axis scale changes from plot to plot.

Coupled model	e_r
Case (a)	1.93×10^{-15}
Case (b)	4.24×10^{-16}
Case (c)	2.60×10^{-16}
Case (d)	4.34×10^{-03}
Case (e)	1.48×10^{-03}

Table 2.3: Relative out-of-balance errors for the configurations described in Figure 2.6.

the effects of these two parameters on the magnitude of the relative out-of-balance error. Both studies considered the configuration (e) in Figure 2.6, where the quartic displacement curve is located over the right coupling zone. The resulting relative out-of-balance errors are listed in Table 2.4, where it is evident that the increase in m has no clear effect on the out-of-balance level of the CCM-PD coupled model (see cases (f) and (g)). On the contrary, when a δ-convergence study is performed, the out-of-balance level decreases with the horizon value (see cases (h) and (i)). To verify the δ-dependence of the model discrepancy between PD and CCM models, Table 2.4 also lists the sum of the reaction forces, $\sum_{i=1}^{N} F_i$, scaled by δ^2. The results confirm the analysis presented in Section 2.3.1, where the leading term in the model discrepancy depends on δ^2 (see (2.17)). The reason why the results in Table 2.4 give only an approximated quadratic dependence of the model discrepancy on δ, i.e., the values of the scaled sum of the reaction forces in cases (h) and (i) are not exactly the same as the one in case (e), might be that the value of m is not large enough to provide the required numerical accuracy. For this reason, Table 2.5 reports the results obtained by performing a δ-convergence study using a larger value of m, chosen as m= 8, and keeping it fixed during the analysis. As in the previous cases reported in Table 2.4, this study considered the configuration (e) in Figure 2.6, where the quartic displacement curve is located over the right coupling zone. Using a larger value of m, the results give an exact quadratic dependence of the model discrepancy on δ.

Coupled model	e_r	$\left(\sum_{i=1}^{N} F_i\right)/\delta^2$
Case (e), $\delta = 3$, $m = 3$	1.48×10^{-03}	-9.27×10^{-08}
Case (f), $\delta = 3$, $m = 6$	1.60×10^{-03}	-1.00×10^{-07}
Case (g), $\delta = 3$, $m = 12$	1.62×10^{-03}	-1.02×10^{-07}
Case (h), $\delta = 1.5$, $m = 3$	3.66×10^{-04}	-9.16×10^{-08}
Case (i), $\delta = 0.5$, $m = 3$	4.04×10^{-05}	-9.08×10^{-08}

Table 2.4: Relative out-of-balance errors and scaled sums of reaction forces for the m- and δ-convergence studies.

Coupled model	e_r	$\left(\sum_{i=1}^{N} F_i\right)/\delta^2$
Case (l), $\delta = 3$, $m = 8$	1.60×10^{-03}	-1.00×10^{-07}
Case (m), $\delta = 1.5$, $m = 8$	4.00×10^{-04}	-1.00×10^{-07}
Case (n), $\delta = 0.5$, $m = 8$	4.46×10^{-05}	-1.00×10^{-07}

Table 2.5: Relative out-of-balance errors and scaled sums of reaction forces for the δ-convergence study.

2.4.2 Two-dimensional case

In this section, equilibrium checks are carried out on two-dimensional plane stress cases adopting the CCM-PD coupling strategy described in Section 2.1. We consider a two-dimensional rectangular plate with an internal PD region as shown in Figure 2.7. The PD portion of the domain is a square of edge length $L_{PDx} = L_{PDy} = 10$, and the remaining part of the domain, the CCM region, is discretized using four-node square plane stress FEM elements for which the element stiffness matrix has been evaluated with exact integration [194]. The discretization of the domain employs a uniform grid with $\Delta x = \Delta y = 0.125$. The values of the main problem parameters are $L_x = 24$ and $L_y = 34$ (plate dimensions), $E = 1$ (Young's modulus), $\nu = \frac{1}{3}$ (Poisson's ratio), and $h = 1$ (plate thickness) in consistent units. We assume a CCM model given by the classical linear elasticity plane stress isotropic model (*cf.* (2.23)) and a PD model given by a linear bond-based isotropic model (*cf.* (2.19)) with a micromodulus function $\lambda(\|\boldsymbol{\xi}\|) = \frac{c}{\|\boldsymbol{\xi}\|^3}$. The PD horizon is taken as $\delta = 0.375$ (i.e., $m = \delta/\Delta x = 3$) and the micromodulus constant c has been evaluated through the following relation (*cf.* (1.40)):

$$c = \frac{9E}{\pi\delta^3}\gamma, \tag{2.39}$$

which corresponds to a plane stress condition, where γ is a correction factor (see Remark A.2 in Appendix A.2). The PD portion of the domain employs a meshfree discretization with a partial-volume correction [190].

In this CCM-PD coupled problem a displacement is imposed on all nodes. Similarly to the one-dimensional numerical examples in Section 2.4.1, a piecewise polynomial displacement field is imposed. However, since in this case the problem is two-dimensional, the imposed displacement field is composed of six curves, three along the x-direction and three along the y-direction. A displacement field given by two linear functions connected by a quartic function is imposed on both directions as shown in Figure 2.8, where u_1 and u_2 are the x- and y-components, respectively, of the displacement field $\mathbf{u} = (u_1, u_2)$. The quartic function has been selected to ensure C^1 continuity of the displacement field along both the x- and y-directions. The imposed displacement field is described by the set of equations defined in Table 2.6, where the value of the coefficient k is set to $k = 0.1$. The portion of the

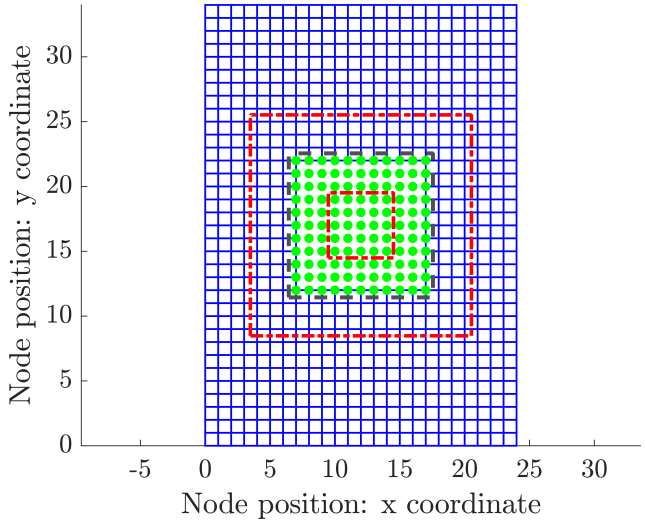

Figure 2.7: CCM-PD coupled model for the two-dimensional case. Green circles are PD nodes and blue (empty) squares are FEM elements. The dashed gray lines represent the interface between the PD and CCM regions, while the portion of the domain bounded by the dashed-dotted red lines is the coupling zone. For clarity reasons, in the figure, $\Delta x = \Delta y = 1$ and $m = \delta/\Delta x = 3$.

domain $x \in (X_1, X_2) \wedge y \in (0, L_y)$ represents the quartic displacement region of the u_1 component of the displacement field and is referred to as the quartic vertical band, whereas the portion of the domain $x \in (0, L_x) \wedge y \in (Y_1, Y_2)$ represents the quartic displacement region of the u_2 component of the displacement field and is referred to as the quartic horizontal band.

Four different cases are considered. For all the cases, we impose the same displacement field (i.e., we keep fixed the values assigned to the parameters X_1, X_2, Y_1, and Y_2) while changing the position of the PD region within the plate. Figure 2.9 shows the four cases and Table 2.7 provides the information about the location of the PD region and the position of the quartic horizontal and vertical bands for each of the four cases.

The resulting relative out-of-balance error is evaluated in the x- and y-directions

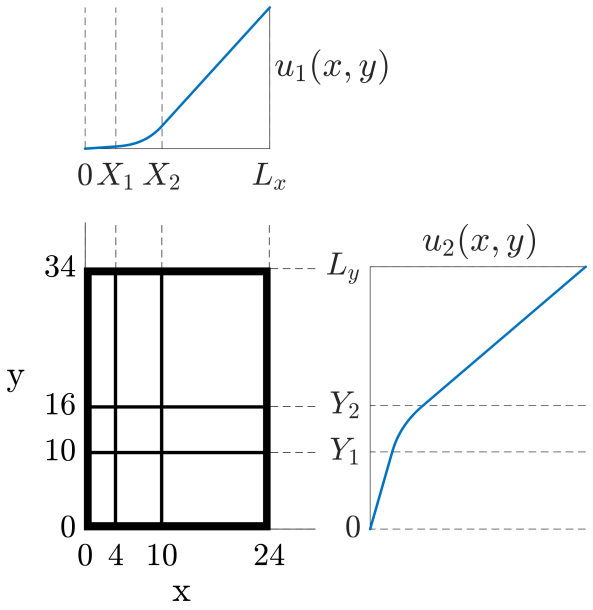

Figure 2.8: Imposed displacement field on the plate showing the quartic horizontal and vertical bands.

Displacement type	Displacement field equation	Domain
Linear	$u_1(x,y) = kx$	$x \in (0, X_1)$
Quartic	$u_1(x,y) = \frac{k}{4X_1^3}x^4 + \frac{3k}{4}X_1$	$x \in (X_1, X_2)$
Linear	$u_1(x,y) = k\left(\frac{X_2}{X_1}\right)^3 (x - X_2) + \frac{k}{4X_1^3}\left(X_2^4 + 3X_1^4\right)$	$x \in (X_2, L_x)$

(a)

Displacement type	Displacement field equation	Domain
Linear	$u_2(x,y) = ky$	$y \in (0, Y_1)$
Quartic	$u_2(x,y) = \frac{k}{4Y_1^3}y^4 + \frac{3k}{4}Y_1$	$y \in (Y_1, Y_2)$
Linear	$u_2(x,y) = k\left(\frac{Y_2}{Y_1}\right)^3 (y - Y_2) + \frac{k}{4Y_1^3}\left(Y_2^4 + 3Y_1^4\right)$	$y \in (Y_2, L_y)$

(b)

Table 2.6: Equations representing the displacement field imposed on the plate: (a) u_1 component of the displacement, (b) u_2 component of the displacement.

CCM-PD coupled model ($\delta = 0.375$, $m = 3$)	PD_{Centre}	X_1	X_2	Y_1	Y_2
Case I	$(16, 24)$	4	10	10	16
Case II	$(11.875, 18.875)$	4	10	10	16
Case III	$(16, 18.875)$	4	10	10	16
Case IV	$(11.875, 24)$	4	10	10	16

Table 2.7: Location of the centre of the PD region and position of the quartic horizontal and vertical bands for each of the four cases presented in Figure 2.9.

through the following quantities:

$$e_{r_x} := \frac{\left|\sum_{i=1}^{N} F_{1\,i}\right|}{\sum_{i=1}^{N} |F_{1\,i}|}, \tag{2.40a}$$

$$e_{r_y} := \frac{\left|\sum_{i=1}^{N} F_{2\,i}\right|}{\sum_{i=1}^{N} |F_{2\,i}|}, \tag{2.40b}$$

where N is the total number of nodes and $F_{1\,i}$ and $F_{2\,i}$ are the x- and y-components, respectively, of the reaction force generated at node i after the imposition of the displacement field. In the case of overall equilibrium of the whole structure, the sum of the reaction forces for each component is equal to zero (see Section 2.1.1). Table 2.8 lists the results obtained in terms of relative out-of-balance error along the x- and y-directions for the four cases presented in Figure 2.9.

In Case I in Figure 2.9, the coupling zone is located outside both the quartic horizontal and vertical bands. As it is clearly shown in Table 2.8, in this case the force equilibrium is verified along both the x- and y-directions. In contrast, in Case II shown in Figure 2.9, both e_{r_x} and e_{r_y} are not negligible, as reported in Table 2.8. In this case, the coupling zone is partially located inside both the quartic horizontal and vertical bands, and a 'small' portion of it is placed in the overlapping area of the two bands. In Case III shown in Figure 2.9, the force equilibrium turns out to be verified only along the x-direction, since the coupling zone is partially located inside the quartic horizontal band. Similarly, in Case IV shown in Figure 2.9, the force equilibrium turns out to be verified only along the y-direction, since the coupling

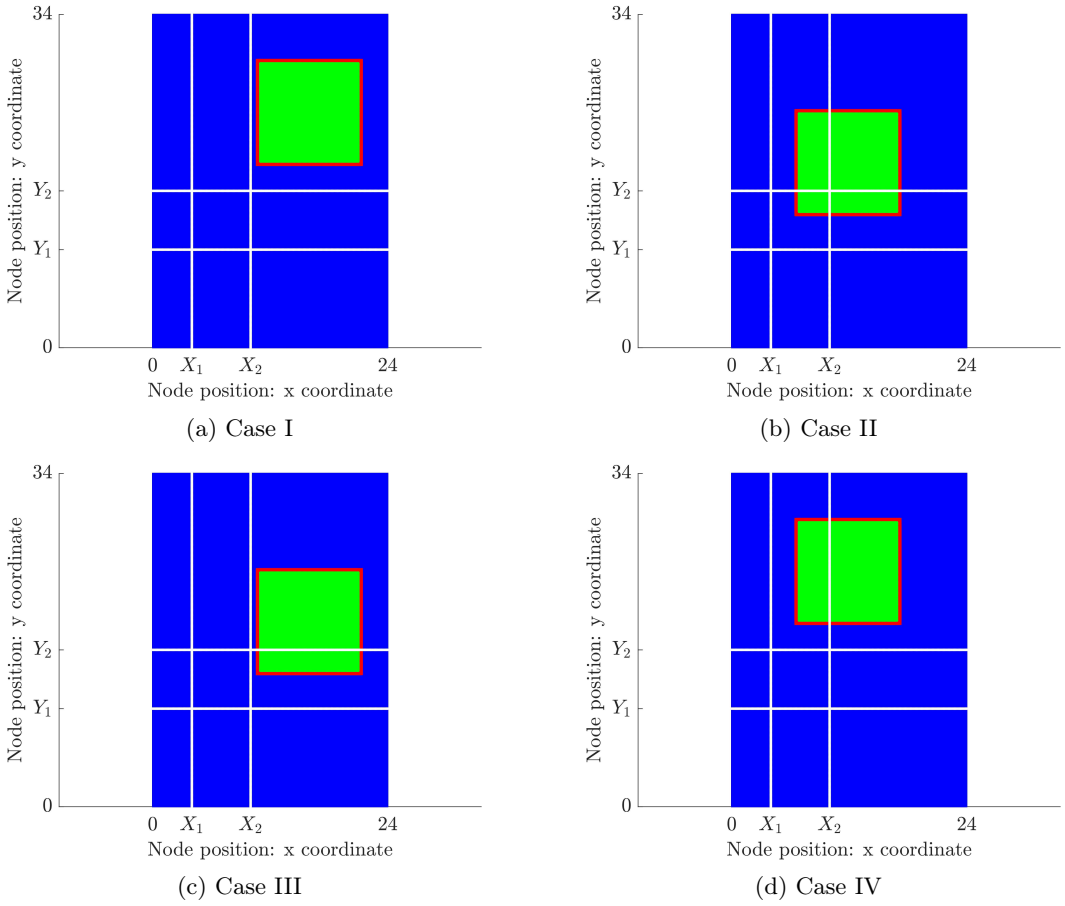

(a) Case I (b) Case II

(c) Case III (d) Case IV

Figure 2.9: CCM-PD coupled model configurations on a two-dimensional plate. The green area represents the PD region, whereas the blue area is the CCM region. The portion of the domain bounded by red lines is the coupling zone, while the thick straight white lines represent the bounds of the quartic horizontal and vertical bands. The only difference between the four cases is the position of the PD region within the plate, which leads to a variation in the location of the coupling zone with respect to the quartic horizontal and vertical bands. (a) the coupling zone is outside the two bands; (b) a portion of the coupling zone is inside both the horizontal and vertical bands; (c) a portion of the coupling zone is inside the horizontal band; and (d) a portion of the coupling zone is inside the vertical band.

CCM-PD coupled model ($\delta = 0.375$, $m = 3$)	e_{r_x}	e_{r_y}
Case I	3.20×10^{-14}	1.26×10^{-14}
Case II	2.96×10^{-05}	9.61×10^{-06}
Case III	4.19×10^{-14}	9.61×10^{-06}
Case IV	2.96×10^{-05}	1.93×10^{-14}

Table 2.8: Resulting relative out-of-balance errors along the x- and y-directions for the four cases presented in Figure 2.9.

zone is partially located inside the quartic vertical band. These results demonstrate that the resulting relative out-of-balance error changes significantly when varying the position of the coupling zone in the CCM-PD coupled model with respect to the locations of the quartic horizontal and vertical bands. This is consistent with the theoretical background presented in Section 2.3.2.

The theoretical analysis presented in Section 2.3 and the supporting numerical simulations reported in Section 2.4 demonstrate that high gradients of displacements are responsible for the discrepancy between the PD and CCM models. In the following section, the overall static equilibrium issue is investigated more deeply by performing a comprehensive analysis directly of the force balance in one-dimensional and two-dimensional CCM-PD coupled systems.

2.5 Theoretical background: out-of-balance analysis in CCM-PD coupled models

Traditionally, the consistency between CCM and PD models is studied through the analysis of the corresponding governing equations, as reported in Section 2.3. However, this analysis does not reveal the culprit responsible for the existence of out-of-balance forces in CCM–PD coupled systems. For this reason, a detailed analysis of the balance between local and nonlocal tractions at coupling interfaces in one-dimensional and two-dimensional CCM–PD coupled models is presented in

Sections 2.5.1 and 2.5.2, respectively.

The theoretical analysis presented in the following sections has been mainly derived by Doctor Pablo Seleson, Research Scientist at the Oak Ridge National Laboratory (ORNL), Oak Ridge, United States [9].

2.5.1 One-dimensional case

CCM model

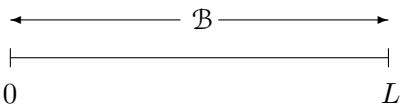

Figure 2.10: One-dimensional domain $\mathcal{B} = (0, L)$.

Assume a one-dimensional domain $\mathcal{B} = (0, L)$ as in Figure 2.10 and consider the CCM static equation

$$-E\frac{d^2u}{dx^2}(x) = b(x) \qquad x \in (0, L), \tag{2.41}$$

where E is Young's modulus. Integrating the equation over the domain $\mathcal{B}$, we obtain

$$-\int_0^L E\frac{d^2u}{dx^2}(x)dx = \int_0^L b(x)dx. \tag{2.42}$$

Performing the integration on the left-hand side, we have

$$-E\frac{du}{dx}(L) + E\frac{du}{dx}(0) = \int_0^L b(x)dx. \tag{2.43}$$

In this case, the stress at x_0 is given by:

$$\sigma(x_0) = E\frac{du}{dx}(x_0) \tag{2.44}$$

and the corresponding local traction is defined by:

$$\mathrm{t}(x_0, n) := \sigma(x_0)n, \tag{2.45}$$

where $n = \pm 1$ represents a normal in one dimension. Note that

$$\mathrm{t}(x_0, -n) = -\mathrm{t}(x_0, n). \tag{2.46}$$

We then obtain from (2.43) the force balance equation

$$\mathrm{t}(L, +1) + \mathrm{t}(0, -1) + \int_0^L b(x)dx = 0, \tag{2.47}$$

where $\mathrm{t}(L, +1)$ and $\mathrm{t}(0, -1)$ are boundary local tractions. The boundary local tractions balance the external forces.

PD model

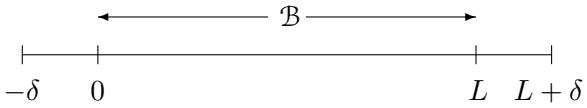

Figure 2.11: One-dimensional domain $\mathcal{B} = (0, L)$ with nonlocal boundary $[-\delta, 0] \cup [L, L + \delta]$.

Assume a one-dimensional domain $\mathcal{B} = (0, L)$ as in Figure 2.11, where $L \geqslant \delta > 0$, with nonlocal boundary $[-\delta, 0] \cup [L, L + \delta]$ and consider the bond-based PD static equation

$$-\int_{\mathcal{H}_x} c(|x' - x|)(u(x') - u(x))dx' = b(x) \qquad x \in (0, L), \tag{2.48}$$

where $c(|\xi|)$ is a micromodulus function and $\mathcal{H}_x = [x - \delta, x + \delta]$. Note the relation $c(|\xi|) = \lambda(|\xi|)|\xi|^2$ in one dimension with $\lambda(|\xi|)$ from (1.20). Introducing the characteristic function

$$\chi_\delta(|\xi|) := \begin{cases} 1 & |\xi| \leqslant \delta, \\ 0 & \text{else}, \end{cases} \tag{2.49}$$

we can extend the domain of integration in (2.48) to the union of the domain $\mathcal{B}$ and its nonlocal boundary (see Figure 2.11):

$$-\int_{-\delta}^{L+\delta} \chi_\delta(|x' - x|)c(|x' - x|)(u(x') - u(x))dx' = b(x) \qquad x \in (0, L). \tag{2.50}$$

We now integrate the equation over the domain $\mathcal{B}$:

$$-\int_0^L \int_{-\delta}^{L+\delta} \chi_\delta(|x' - x|)c(|x' - x|)(u(x') - u(x))dx'dx = \int_0^L b(x)dx. \tag{2.51}$$

Due to the antisymmetry of the integrand on the left-hand side of (2.51),

$$-\int_0^L \int_0^L \chi_\delta(|x' - x|)c(|x' - x|)(u(x') - u(x))dx'dx = 0, \tag{2.52}$$

meaning that internal forces are balanced in a bounded PD body. Consequently, we obtain

$$\begin{aligned} &-\int_0^L \int_{-\delta}^0 \chi_\delta(|x' - x|)c(|x' - x|)(u(x') - u(x))dx'dx \\ &-\int_0^L \int_L^{L+\delta} \chi_\delta(|x' - x|)c(|x' - x|)(u(x') - u(x))dx'dx = \int_0^L b(x)dx, \end{aligned} \tag{2.53}$$

which can now be written without the characteristic function (recall $L \geqslant \delta$) as

$$-\int_0^{\delta}\int_{x-\delta}^{0} c(|x'-x|)(u(x')-u(x))dx'dx \\ -\int_{L-\delta}^{L}\int_{L}^{x+\delta} c(|x'-x|)(u(x')-u(x))dx'dx = \int_0^L b(x)dx. \tag{2.54}$$

Following the concept of areal force density presented in [7] and briefly introduced in Section 1.1.3, we define the nonlocal traction at x_0 with normal $n = \pm 1$ in one dimension by:

$$\tau(x_0,n) := \begin{cases} \displaystyle\int_{x_0-\delta}^{x_0}\int_{x_0}^{x+\delta} c(|x'-x|)(u(x')-u(x))dx'dx & n=+1, \\ \displaystyle\int_{x_0}^{x_0+\delta}\int_{x-\delta}^{x_0} c(|x'-x|)(u(x')-u(x))dx'dx & n=-1. \end{cases} \tag{2.55}$$

Note that (see Remark A.1 in Appendix A.1)

$$\tau(x_0,-n) = -\tau(x_0,n). \tag{2.56}$$

We then obtain from (2.54) the force balance equation

$$\tau(L,+1) + \tau(0,-1) + \int_0^L b(x)dx = 0, \tag{2.57}$$

where $\tau(L,+1)$ and $\tau(0,-1)$ are boundary nonlocal tractions. The boundary nonlocal tractions balance the external forces.

CCM-PD coupled model

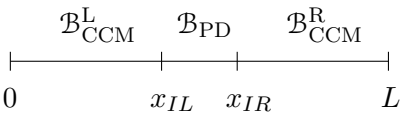

Figure 2.12: Decomposition of a one-dimensional domain $\mathcal{B} = (0, L)$ into a PD subdomain $\mathcal{B}_{\mathrm{PD}} = (x_{IL}, x_{IR})$ embedded into a CCM subdomain $\mathcal{B}_{\mathrm{CCM}} = \mathcal{B}^{\mathrm{L}}_{\mathrm{CCM}} \cup \mathcal{B}^{\mathrm{R}}_{\mathrm{CCM}} = (0, x_{IL}) \cup (x_{IR}, L)$. The transition between the PD and CCM subdomains occurs at the interfaces x_{IL} and x_{IR}.

Assume a one-dimensional domain $\mathcal{B} = (0, L)$ and consider a CCM-PD coupled configuration where a PD subdomain is embedded into a CCM subdomain, as illustrated in Figure 2.12. This configuration enables the use of classical local boundary conditions. Consider two interfaces, x_{IL} and x_{IR}, such that $0 < x_{IL} < x_{IR} < L$.

Assume points $x \in (x_{IL}, x_{IR})$ are described by the PD model (2.48), whereas points $x \in (0, x_{IL}) \cup (x_{IR}, L)$ are described by the CCM model (2.41). We assume the length of the PD subdomain is at least δ, so that $x_{IR} - x_{IL} \geqslant \delta$. We further assume the CCM subdomain is large enough, so that $x_{IL} - \delta \geqslant 0$ and $x_{IR} + \delta \leqslant L$. The corresponding coupled system of equations can be written as:

$$-E\frac{d^2u}{dx^2}(x) = b(x) \qquad x \in (0, x_{IL}), \tag{2.58a}$$

$$-\int_{\mathcal{H}_x} c(|x'-x|)(u(x')-u(x))dx' = b(x) \qquad x \in (x_{IL}, x_{IR}), \tag{2.58b}$$

$$-E\frac{d^2u}{dx^2}(x) = b(x) \qquad x \in (x_{IR}, L). \tag{2.58c}$$

Integrating the equations over their respective subdomains, we obtain

$$-\int_0^{x_{IL}} E\frac{d^2u}{dx^2}(x)dx = \int_0^{x_{IL}} b(x)dx, \tag{2.59a}$$

$$-\int_{x_{IL}}^{x_{IR}} \int_{\mathcal{H}_x} c(|x'-x|)(u(x')-u(x))dx'dx = \int_{x_{IL}}^{x_{IR}} b(x)dx, \tag{2.59b}$$

$$-\int_{x_{IR}}^{L} E\frac{d^2u}{dx^2}(x)dx = \int_{x_{IR}}^{L} b(x)dx. \tag{2.59c}$$

Adding the equations in (2.59), we get

$$-\int_0^{x_{IL}} E\frac{d^2u}{dx^2}(x)dx - \int_{x_{IL}}^{x_{IR}} \int_{\mathcal{H}_x} c(|x'-x|)(u(x')-u(x))dx'dx - \int_{x_{IR}}^{L} E\frac{d^2u}{dx^2}(x)dx = \int_0^{L} b(x)dx. \tag{2.60}$$

Performing the integration in the first and third terms on the left-hand side and using the characteristic function (2.49) for the second term on the left-hand side, we have

$$-E\frac{du}{dx}(x_{IL}) + E\frac{du}{dx}(0) - \int_{x_{IL}}^{x_{IR}} \int_{x_{IL}-\delta}^{x_{IR}+\delta} \chi_\delta(|x'-x|)c(|x'-x|)(u(x')-u(x))dx'dx - E\frac{du}{dx}(L) + E\frac{du}{dx}(x_{IR}) = \int_0^{L} b(x)dx. \tag{2.61}$$

Similar to (2.52),

$$-\int_{x_{IL}}^{x_{IR}} \int_{x_{IL}}^{x_{IR}} \chi_\delta(|x'-x|)c(|x'-x|)(u(x')-u(x))dx'dx = 0. \tag{2.62}$$

Therefore, we obtain

$$-E\frac{du}{dx}(x_{IL}) + E\frac{du}{dx}(0) - \int_{x_{IL}}^{x_{IR}} \int_{x_{IL}-\delta}^{x_{IL}} \chi_\delta(|x'-x|)c(|x'-x|)(u(x')-u(x))dx'dx \\ - \int_{x_{IL}}^{x_{IR}} \int_{x_{IR}}^{x_{IR}+\delta} \chi_\delta(|x'-x|)c(|x'-x|)(u(x')-u(x))dx'dx \\ - E\frac{du}{dx}(L) + E\frac{du}{dx}(x_{IR}) = \int_0^L b(x)dx. \tag{2.63}$$

Removing the characteristic function (recall $x_{IR}-x_{IL} \geqslant \delta$) and using the definitions for the local and nonlocal tractions in (2.45) and (2.55), respectively, we can express this equation as follows (see [9]):

$$\mathrm{t}(L,+1) + \mathrm{t}(0,-1) + \int_0^L b(x)dx = -\big\{\big[\mathrm{t}(x_{IL},+1) + \tau(x_{IL},-1)\big] \\ + \big[\tau(x_{IR},+1) + \mathrm{t}(x_{IR},-1)\big]\big\}. \tag{2.64}$$

The net force, $\mathcal{F}$, applied on the domain $\mathcal{B}$ is given by (*cf.* (2.47)):

$$\mathcal{F} = \mathrm{t}(L,+1) + \mathrm{t}(0,-1) + \int_0^L b(x)dx. \tag{2.65}$$

We then conclude that overall equilibrium, i.e., $\mathcal{F} = 0$, requires the balance between the local and nonlocal tractions at the interfaces (see (2.64)):

$$\tau(x_{IL},-1) = -\mathrm{t}(x_{IL},+1), \tag{2.66a}$$

$$\tau(x_{IR},+1) = -\mathrm{t}(x_{IR},-1). \tag{2.66b}$$

In the following section, the convergence of the nonlocal traction to the local traction is discussed, providing conditions under which (2.66) is satisfied.

Convergence of the nonlocal traction to the local traction in one dimension

This section presents for brevity only the main results derived from the analysis of the convergence of the nonlocal traction to the local traction in one-dimensional CCM-PD coupled models. For a comprehensive derivation, please refer to Appendix A.1.

Consider the nonlocal traction at $x_0 \in \mathcal{B}$ in the bulk of the body with normal $n = +1$, i.e., $\tau(x_0,+1)$ in (2.55) and assume a micromodulus function of the form

$c(|\xi|) = c/|\xi|^\alpha$ with c a constant and $\alpha < 2$. Assuming a smooth deformation and performing some Taylor expansions, we obtain

$$\tau(x_0, +1) = \mathrm{t}(x_0, +1) + \frac{1}{12}\frac{3-\alpha}{5-\alpha} E\delta^2 \frac{d^3u}{dx^3}(x_0) + \ldots, \tag{2.67}$$

where the relation $c = \frac{3-\alpha}{\delta^{3-\alpha}} E$ has been employed (*cf.* (2.15)), $\mathrm{t}(x_0, +1)$ is the local traction at x_0 with normal $n = +1$ (*cf.* (2.45)), and the dots indicate higher-order derivative terms. In the limit as $\delta \to 0$, we get

$$\tau(x_0, +1) = \mathrm{t}(x_0, +1) + \mathcal{O}(\delta^2), \tag{2.68}$$

i.e., the nonlocal traction converges to the local traction at a rate of $\mathcal{O}(\delta^2)$. Furthermore, this result reveals that, even though the discrepancy between the PD and CCM models depends upon fourth-order and higher derivatives of displacements (see Section 2.3.1), the discrepancy between the nonlocal and local tractions depends upon third-order and higher derivatives of displacements. Nevertheless, the leading terms in both the model and traction discrepancies are both of order $\mathcal{O}(\delta^2)$ (see Section 2.3.1).

The result in (2.67) implies that, if the deformation around the interfaces x_{IL} and x_{IR} in Figure 2.12 is smooth and third-order and higher derivatives of displacements are negligible, we have (recall (2.46) and (2.56))

$$\tau(x_{IL}, -1) = -\tau(x_{IL}, +1) = -\mathrm{t}(x_{IL}, +1), \tag{2.69a}$$

$$\tau(x_{IR}, +1) = \mathrm{t}(x_{IR}, +1) = -\mathrm{t}(x_{IR}, -1), \tag{2.69b}$$

so that (2.66) is satisfied and overall equilibrium is attained. However, whenever third-order or higher derivatives of displacements are not negligible around either of the interfaces, lack of overall equilibrium is in general expected. In this case, the net out-of-balance force is given by (*cf.* (2.65) and (2.64)):

$$\begin{aligned}\mathcal{F} &= -\left\{[\mathrm{t}(x_{IL}, +1) + \tau(x_{IL}, -1)] + [\tau(x_{IR}, +1) + \mathrm{t}(x_{IR}, -1)]\right\} \\ &= \frac{1}{12}\frac{3-\alpha}{5-\alpha} E\delta^2 \left(\frac{d^3u}{dx^3}(x_{IL}) - \frac{d^3u}{dx^3}(x_{IR})\right) + \ldots,\end{aligned} \tag{2.70}$$

where we employed (2.67) in combination with (2.46) and (2.56) in the last equality. In the limit as $\delta \to 0$, the net out-of-balance force vanishes at a rate of $\mathcal{O}(\delta^2)$.

2.5.2 Two-dimensional case

CCM model

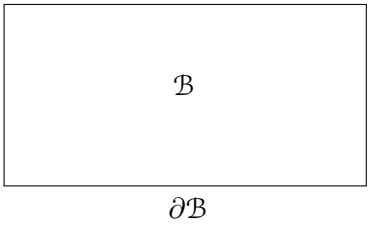

Figure 2.13: Two-dimensional domain $\mathcal{B}$ with boundary $\partial\mathcal{B}$.

Assume a two-dimensional domain $\mathcal{B}$ with boundary $\partial\mathcal{B}$ as in Figure 2.13 and consider the CCM static equation

$$-\nabla\cdot\boldsymbol{\sigma}(\mathbf{x})=\mathbf{b}(\mathbf{x})\qquad \mathbf{x}\in\mathcal{B}, \tag{2.71}$$

where $\boldsymbol{\sigma}$ is a Piola-Kirchhoff stress tensor field. Integrating the equation over the domain $\mathcal{B}$ and using Gauss's theorem for the left-hand side, we have (see [9])

$$-\int_{\partial\mathcal{B}}\boldsymbol{\sigma}(\mathbf{x})\cdot\mathbf{n}(\mathbf{x})dl=\int_{\mathcal{B}}\mathbf{b}(\mathbf{x})d\mathbf{x}, \tag{2.72}$$

where $\mathbf{n}(\mathbf{x})$ is the outward unit normal to the boundary $\partial\mathcal{B}$ at $\mathbf{x}\in\partial\mathcal{B}$ and the integral over $\partial\mathcal{B}$ is a line integral. The local traction is defined by:

$$\mathbf{t}(\mathbf{x},\mathbf{n}):=\boldsymbol{\sigma}(\mathbf{x})\cdot\mathbf{n}(\mathbf{x}). \tag{2.73}$$

Note that

$$\mathbf{t}(\mathbf{x},-\mathbf{n})=-\mathbf{t}(\mathbf{x},\mathbf{n}). \tag{2.74}$$

We then obtain from (2.72) the force balance equation

$$\int_{\partial\mathcal{B}}\mathbf{t}(\mathbf{x},\mathbf{n})dl+\int_{\mathcal{B}}\mathbf{b}(\mathbf{x})d\mathbf{x}=\mathbf{0}, \tag{2.75}$$

where the boundary local tractions balance the external forces.

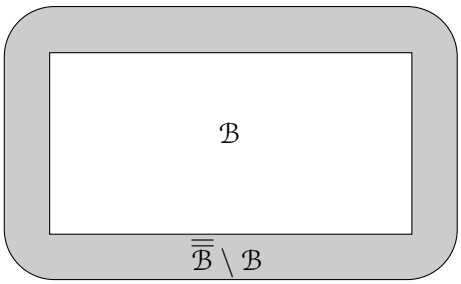

Figure 2.14: Two-dimensional domain $\mathcal{B}$ with nonlocal boundary layer (in gray).

PD model

Assume a two-dimensional domain $\mathcal{B}$ with a nonlocal boundary layer as in Figure 2.14 and consider the PD static equation

$$-\int_{\mathcal{H}_{\mathbf{x}}} \boldsymbol{f}(\mathbf{x}', \mathbf{x}) d\mathbf{x}' = \mathbf{b}(\mathbf{x}) \qquad \mathbf{x} \in \mathcal{B}, \tag{2.76}$$

where (*cf.* (1.52))

$$\boldsymbol{f}(\mathbf{x}', \mathbf{x}) := \underline{\mathbf{T}}\,[\mathbf{x}, t]\,\langle \mathbf{x}' - \mathbf{x} \rangle - \underline{\mathbf{T}}[\mathbf{x}', t]\langle \mathbf{x} - \mathbf{x}' \rangle \tag{2.77}$$

and $\mathcal{H}_{\mathbf{x}}$ is the neighbourhood of $\mathbf{x}$. Note that the following antisymmetric property holds:

$$\boldsymbol{f}(\mathbf{x}, \mathbf{x}') = -\boldsymbol{f}(\mathbf{x}', \mathbf{x}). \tag{2.78}$$

Introducing the characteristic function

$$\chi_\delta(\|\boldsymbol{\xi}\|) := \begin{cases} 1 & \|\boldsymbol{\xi}\| \leqslant \delta, \\ 0 & \text{else}, \end{cases} \tag{2.79}$$

we can extend the domain of integration in (2.76) to the union of the domain $\mathcal{B}$ and its nonlocal boundary, which we denote together by $\overline{\overline{\mathcal{B}}}$:

$$-\int_{\overline{\overline{\mathcal{B}}}} \chi_\delta(\|\mathbf{x}' - \mathbf{x}\|) \boldsymbol{f}(\mathbf{x}', \mathbf{x}) d\mathbf{x}' = \mathbf{b}(\mathbf{x}) \qquad \mathbf{x} \in \mathcal{B}. \tag{2.80}$$

We now integrate the equation over the domain $\mathcal{B}$:

$$-\int_{\mathcal{B}} \int_{\overline{\overline{\mathcal{B}}}} \chi_\delta(\|\mathbf{x}' - \mathbf{x}\|) \boldsymbol{f}(\mathbf{x}', \mathbf{x}) d\mathbf{x}' d\mathbf{x} = \int_{\mathcal{B}} \mathbf{b}(\mathbf{x}) d\mathbf{x}. \tag{2.81}$$

Due to the antisymmetric property (2.78), we have

$$-\int_{\mathcal{B}}\int_{\mathcal{B}}\chi_\delta(\|\mathbf{x}'-\mathbf{x}\|)\boldsymbol{f}(\mathbf{x}',\mathbf{x})d\mathbf{x}'d\mathbf{x}=\mathbf{0}, \tag{2.82}$$

meaning that internal forces are balanced in a bounded PD body. Consequently, we obtain

$$-\int_{\mathcal{B}}\int_{\overline{\overline{\mathcal{B}}\setminus\mathcal{B}}}\chi_\delta(\|\mathbf{x}'-\mathbf{x}\|)\boldsymbol{f}(\mathbf{x}',\mathbf{x})d\mathbf{x}'d\mathbf{x}=\int_{\mathcal{B}}\mathbf{b}(\mathbf{x})d\mathbf{x}. \tag{2.83}$$

We now have the force balance equation

$$\int_{\mathcal{B}}\int_{\overline{\overline{\mathcal{B}}\setminus\mathcal{B}}}\chi_\delta(\|\mathbf{x}'-\mathbf{x}\|)\boldsymbol{f}(\mathbf{x}',\mathbf{x})d\mathbf{x}'d\mathbf{x}+\int_{\mathcal{B}}\mathbf{b}(\mathbf{x})d\mathbf{x}=\mathbf{0}. \tag{2.84}$$

Assume there exists a function $\boldsymbol{\tau}(\mathbf{x},\mathbf{n})$ satisfying

$$\int_{\partial\mathcal{B}}\boldsymbol{\tau}(\mathbf{x},\mathbf{n})dl=\int_{\mathcal{B}}\int_{\overline{\overline{\mathcal{B}}\setminus\mathcal{B}}}\chi_\delta(\|\mathbf{x}'-\mathbf{x}\|)\boldsymbol{f}(\mathbf{x}',\mathbf{x})d\mathbf{x}'d\mathbf{x}, \tag{2.85}$$

where $\mathbf{n}=\mathbf{n}(\mathbf{x})$ is the outward unit normal to the boundary $\partial\mathcal{B}$ at $\mathbf{x}\in\partial\mathcal{B}$. In this case, we refer to $\boldsymbol{\tau}(\mathbf{x},\mathbf{n})$ as the nonlocal traction at $\mathbf{x}$ with normal $\mathbf{n}(\mathbf{x})$, and we can express (2.84) as

$$\int_{\partial\mathcal{B}}\boldsymbol{\tau}(\mathbf{x},\mathbf{n})dl+\int_{\mathcal{B}}\mathbf{b}(\mathbf{x})d\mathbf{x}=\mathbf{0}, \tag{2.86}$$

where the boundary nonlocal tractions balance the external forces.

CCM-PD coupled model

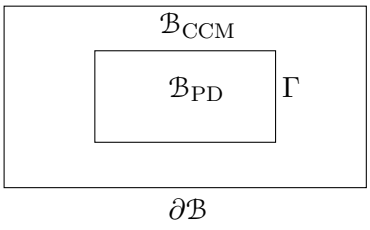

Figure 2.15: Decomposition of a two-dimensional domain $\mathcal{B}$ with boundary $\partial\mathcal{B}$ into a PD subdomain $\mathcal{B}_{\text{PD}}$ embedded into a CCM subdomain $\mathcal{B}_{\text{CCM}}$. The interface between the PD and CCM subdomains is denoted by Γ.

Assume a two-dimensional domain $\mathcal{B}$ with boundary $\partial\mathcal{B}$ and consider a CCM-PD coupled configuration where a PD subdomain, $\mathcal{B}_{\text{PD}}$, is embedded into a CCM

subdomain, $\mathcal{B}_{\text{CCM}}$, as illustrated in Figure 2.15, such that $\overline{\mathcal{B}} = \overline{\mathcal{B}_{\text{PD}}} \cup \overline{\mathcal{B}_{\text{CCM}}}$, $\mathcal{B}_{\text{PD}} \cap \mathcal{B}_{\text{CCM}} = \emptyset$, and $\overline{\mathcal{B}_{\text{PD}}} \cap \overline{\mathcal{B}_{\text{CCM}}} = \partial\mathcal{B}_{\text{PD}} =: \Gamma$. This configuration enables the use of classical local boundary conditions. We assume the CCM subdomain is large enough, so that $\overline{\overline{\mathcal{B}_{\text{PD}}} \setminus \mathcal{B}_{\text{PD}}} \subset \overline{\mathcal{B}_{\text{CCM}}}$. The corresponding coupled system of equations can be written as:

$$-\nabla \cdot \boldsymbol{\sigma}(\mathbf{x}) = \mathbf{b}(\mathbf{x}) \qquad \mathbf{x} \in \mathcal{B}_{\text{CCM}}, \tag{2.87a}$$

$$-\int_{\mathcal{H}_{\mathbf{x}}} \boldsymbol{f}(\mathbf{x}', \mathbf{x}) d\mathbf{x}' = \mathbf{b}(\mathbf{x}) \qquad \mathbf{x} \in \mathcal{B}_{\text{PD}}. \tag{2.87b}$$

Integrating the equations over their respective subdomains and adding them, we get (see [9])

$$-\int_{\mathcal{B}_{\text{CCM}}} \nabla \cdot \boldsymbol{\sigma}(\mathbf{x}) d\mathbf{x} - \int_{\mathcal{B}_{\text{PD}}} \int_{\mathcal{H}_{\mathbf{x}}} \boldsymbol{f}(\mathbf{x}', \mathbf{x}) d\mathbf{x}' d\mathbf{x} = \int_{\mathcal{B}} \mathbf{b}(\mathbf{x}) d\mathbf{x}. \tag{2.88}$$

Using Gauss's theorem for the first term on the left-hand side and the characteristic function (2.79) for the second term on the left-hand side, we have

$$-\int_{\partial\mathcal{B}_{\text{CCM}}} \boldsymbol{\sigma}(\mathbf{x}) \cdot \mathbf{n}(\mathbf{x}) dl - \int_{\mathcal{B}_{\text{PD}}} \int_{\overline{\overline{\mathcal{B}_{\text{PD}}}}} \chi_\delta(\|\mathbf{x}' - \mathbf{x}\|) \boldsymbol{f}(\mathbf{x}', \mathbf{x}) d\mathbf{x}' d\mathbf{x} = \int_{\mathcal{B}} \mathbf{b}(\mathbf{x}) d\mathbf{x}. \tag{2.89}$$

Note that $\partial\mathcal{B}_{\text{CCM}} = \partial\mathcal{B} \cup \Gamma$ (see Figure 2.15). In addition, similar to (2.82),

$$-\int_{\mathcal{B}_{\text{PD}}} \int_{\mathcal{B}_{\text{PD}}} \chi_\delta(\|\mathbf{x}' - \mathbf{x}\|) \boldsymbol{f}(\mathbf{x}', \mathbf{x}) d\mathbf{x}' d\mathbf{x} = \mathbf{0}. \tag{2.90}$$

Using the definition for the local traction in (2.73), we obtain (see [9])

$$\int_{\partial\mathcal{B}} \mathbf{t}(\mathbf{x}, \mathbf{n}) dl + \int_{\mathcal{B}} \mathbf{b}(\mathbf{x}) d\mathbf{x} = -\left[\int_{\Gamma} \mathbf{t}(\mathbf{x}, \mathbf{n}) dl + \int_{\mathcal{B}_{\text{PD}}} \int_{\mathcal{B}_{\text{CCM}}} \chi_\delta(\|\mathbf{x}' - \mathbf{x}\|) \boldsymbol{f}(\mathbf{x}', \mathbf{x}) d\mathbf{x}' d\mathbf{x} \right], \tag{2.91}$$

where we used the assumption $\overline{\overline{\mathcal{B}_{\text{PD}}} \setminus \mathcal{B}_{\text{PD}}} \subset \overline{\mathcal{B}_{\text{CCM}}}$ to rewrite the inner domain of integration of the second term inside the square brackets on the right-hand side (for further details please refer to [9]). We recall that the normal $\mathbf{n}$ on Γ in the first term inside the square brackets on the right-hand side points outwards relative to $\mathcal{B}_{\text{CCM}}$. The net force, $\boldsymbol{\mathcal{F}}$, applied on the domain $\mathcal{B}$ is given by (*cf.* (2.75)):

$$\boldsymbol{\mathcal{F}} = \int_{\partial\mathcal{B}} \mathbf{t}(\mathbf{x}, \mathbf{n}) dl + \int_{\mathcal{B}} \mathbf{b}(\mathbf{x}) d\mathbf{x}. \tag{2.92}$$

We then conclude that overall equilibrium, i.e., $\boldsymbol{\mathcal{F}} = \mathbf{0}$, requires (see (2.91))

$$\int_{\mathcal{B}_{\text{PD}}} \int_{\mathcal{B}_{\text{CCM}}} \chi_\delta(\|\mathbf{x}' - \mathbf{x}\|) \boldsymbol{f}(\mathbf{x}', \mathbf{x}) d\mathbf{x}' d\mathbf{x} = -\int_{\Gamma} \mathbf{t}(\mathbf{x}, \mathbf{n}) dl. \tag{2.93}$$

Similar to (2.85), assume there exists a nonlocal traction $\boldsymbol{\tau}(\mathbf{x}, -\mathbf{n})$ satisfying

$$\int_{\Gamma} \boldsymbol{\tau}(\mathbf{x}, -\mathbf{n}) dl = \int_{\mathcal{B}_{\mathrm{PD}}} \int_{\mathcal{B}_{\mathrm{CCM}}} \chi_{\delta}(\|\mathbf{x}' - \mathbf{x}\|) \boldsymbol{f}(\mathbf{x}', \mathbf{x}) d\mathbf{x}' d\mathbf{x}, \tag{2.94}$$

where, in this case, $-\mathbf{n}$ on Γ points outwards relative to $\mathcal{B}_{\mathrm{PD}}$. Then, we can express (2.93) as

$$\int_{\Gamma} \boldsymbol{\tau}(\mathbf{x}, -\mathbf{n}) dl = -\int_{\Gamma} \mathbf{t}(\mathbf{x}, \mathbf{n}) dl, \tag{2.95}$$

i.e., overall equilibrium requires the balance between the local and nonlocal tractions at the interface Γ. In particular, overall equilibrium is attained if the following (stronger) condition is satisfied:

$$\boldsymbol{\tau}(\mathbf{x}, -\mathbf{n}) = -\mathbf{t}(\mathbf{x}, \mathbf{n}) \qquad \mathbf{x} \in \Gamma. \tag{2.96}$$

In the following section, the convergence of the nonlocal traction to the local traction is discussed, providing conditions under which (2.96) is satisfied.

Convergence of the nonlocal traction to the local traction in two dimensions

This section presents for brevity only the main results derived from the analysis of the convergence of the nonlocal traction to the local traction in two-dimensional CCM-PD coupled models. For a comprehensive derivation, please refer to Appendix A.2.

We consider the simplified case of two non-overlapping subdomains Ω_A and Ω_B with a straight interface Γ connecting them, i.e., $\Omega_A \cap \Omega_B = \emptyset$ and $\overline{\Omega_A} \cap \overline{\Omega_B} = \Gamma$. We assume the normal $\mathbf{n}$ to the interface Γ points outwards relative to Ω_A. In this case, following the concept of areal force density presented in [7] and briefly introduced in Section 1.1.3, we define the nonlocal traction at $\mathbf{x}_0 \in \Gamma$ with normal $\mathbf{n}$ by:

$$\boldsymbol{\tau}(\mathbf{x}_0, \mathbf{n}) := \int_{\mathcal{L}} \int_{\Omega_B} \chi_{\delta}(\|\mathbf{x}' - \mathbf{x}\|) \boldsymbol{f}(\mathbf{x}', \mathbf{x}) d\mathbf{x}' d\ell, \tag{2.97}$$

where

$$\mathcal{L} := \{\mathbf{x} \in \Omega_A : \mathbf{x} = \mathbf{x}_0 - s\mathbf{n}, 0 \leqslant s \leqslant \delta\}. \tag{2.98}$$

Given the linear isotropic bond-based PD model (1.22), we can express (2.97) as (recall (2.77) and (1.76)):

$$\boldsymbol{\tau}(\mathbf{x}_0,\mathbf{n}) = \int_{\mathcal{L}}\int_{\Omega_B} \chi_\delta(\|\mathbf{x}'-\mathbf{x}\|)\lambda(\|\mathbf{x}'-\mathbf{x}\|)(\mathbf{x}'-\mathbf{x})\otimes(\mathbf{x}'-\mathbf{x})(\mathbf{u}(\mathbf{x}')-\mathbf{u}(\mathbf{x}))d\mathbf{x}'d\ell \tag{2.99}$$

or, in component form,

$$\tau_i(\mathbf{x}_0,\mathbf{n}) = \int_{\mathcal{L}}\int_{\Omega_B} \chi_\delta(\|\boldsymbol{\xi}\|)\lambda(\|\boldsymbol{\xi}\|)\xi_i\xi_j(u_j(\mathbf{x}+\boldsymbol{\xi})-u_j(\mathbf{x}))d\mathbf{x}'d\ell, \qquad i=1,2, \tag{2.100}$$

where we used the notation $\boldsymbol{\xi} = \mathbf{x}' - \mathbf{x}$ for brevity and repeated indices imply a summation by 1 and 2. We consider below two cases, the first one given by a horizontal interface Γ with normal $\mathbf{n} = \mathbf{e}_2$ (see Figure A.3a) and the second one given by a vertical interface Γ with normal $\mathbf{n} = \mathbf{e}_1$ (see Figure A.3b); the normals $\{\mathbf{e}_1, \mathbf{e}_2\}$ correspond to the standard Cartesian orthonormal basis. In both cases, the normal points outwards relative to Ω_A. We assume the point $\mathbf{x}_0$ is in the bulk of the body. We further assume a micromodulus function of the form $\lambda(\|\boldsymbol{\xi}\|) = c/\|\boldsymbol{\xi}\|^\alpha$ with c a constant and $\alpha < 6$.

Horizontal Interface. Assuming a smooth deformation and performing some Taylor expansions, we obtain (see (A.26))

$$\tau_1(\mathbf{x}_0,\mathbf{e}_2) = \mathrm{t}_1(\mathbf{x}_0,\mathbf{e}_2) + \frac{2E}{5\pi}\frac{6-\alpha}{7-\alpha}\delta\left(\frac{3}{2}\frac{\partial^2 u_1}{\partial x^2}(\mathbf{x}_0) + \frac{\partial^2 u_2}{\partial x\partial y}(\mathbf{x}_0)\right) + \ldots, \tag{2.101a}$$

$$\tau_2(\mathbf{x}_0,\mathbf{e}_2) = \mathrm{t}_2(\mathbf{x}_0,\mathbf{e}_2) + \frac{2E}{5\pi}\frac{6-\alpha}{7-\alpha}\delta\left(\frac{\partial^2 u_1}{\partial x\partial y}(\mathbf{x}_0) + \frac{\partial^2 u_2}{\partial x^2}(\mathbf{x}_0)\right) + \ldots, \tag{2.101b}$$

where the relation $c = \frac{3(6-\alpha)E}{\pi\delta^{6-\alpha}}$ has been employed (*cf.* (2.34)), $\mathrm{t}_1(\mathbf{x}_0,\mathbf{e}_2)$ and $\mathrm{t}_2(\mathbf{x}_0,\mathbf{e}_2)$ are the x- and y-components, respectively, of the local traction (*cf.* (2.73)) evaluated at $\mathbf{x}_0 \in \Gamma$ in classical plane stress (*cf.* (2.21)) for $\nu = 1/3$, and the dots indicate higher-order derivative terms. In the limit as $\delta \to 0$, we get

$$\boldsymbol{\tau}(\mathbf{x}_0,\mathbf{e}_2) = \mathbf{t}(\mathbf{x}_0,\mathbf{e}_2) + \mathcal{O}(\delta), \tag{2.102}$$

i.e., the nonlocal traction converges to the local traction at a rate of $\mathcal{O}(\delta)$. Equation (2.101) implies that, if the deformation around the interface Γ is smooth and second-order and higher derivatives of displacements are negligible, (2.96) is satisfied

(note $\mathbf{t}(\mathbf{x}_0, \mathbf{e}_2) = -\mathbf{t}(\mathbf{x}_0, -\mathbf{e}_2)$ by (2.74)) and overall equilibrium is attained. However, whenever second-order or higher derivatives of displacements are not negligible around the interface Γ, lack of overall equilibrium is in general expected. In this case, the components of the net out-of-balance force are given by (see (2.91), (2.92), and (2.94)):

$$\mathcal{F}_1 \approx -\int_\Gamma \frac{2E}{5\pi}\frac{6-\alpha}{7-\alpha}\delta\left(\frac{3}{2}\frac{\partial^2 u_1}{\partial x^2}(x, y_0) + \frac{\partial^2 u_2}{\partial x \partial y}(x, y_0)\right) dx + \ldots, \tag{2.103a}$$

$$\mathcal{F}_2 \approx -\int_\Gamma \frac{2E}{5\pi}\frac{6-\alpha}{7-\alpha}\delta\left(\frac{\partial^2 u_1}{\partial x \partial y}(x, y_0) + \frac{\partial^2 u_2}{\partial x^2}(x, y_0)\right) dx + \ldots, \tag{2.103b}$$

where all points along Γ have y-coordinate y_0. Note that approximations and not equalities appear in (2.103). The reason for that is the fact that (2.101) holds for a point $\mathbf{x}_0$ in the bulk of the body; this assumption may not hold for all the points in Γ, which may then introduce a surface effect [83]. Nevertheless, this effect, if present, would normally vanish in the limit as $\delta \to 0$; in this limit, the net out-of-balance force thus vanishes at a rate of $\mathcal{O}(\delta)$.

Vertical Interface. The treatment of the case with a vertical interface is identical to that of the horizontal interface, except that the limits of integration change. Assuming a smooth deformation and performing some Taylor expansions, we obtain (see (A.30))

$$\tau_1(\mathbf{x}_0, \mathbf{e}_1) = \mathrm{t}_1(\mathbf{x}_0, \mathbf{e}_1) + \frac{2E}{5\pi}\frac{6-\alpha}{7-\alpha}\delta\left(\frac{\partial^2 u_1}{\partial y^2}(\mathbf{x}_0) + \frac{\partial^2 u_2}{\partial x \partial y}(\mathbf{x}_0)\right) + \ldots, \tag{2.104a}$$

$$\tau_2(\mathbf{x}_0, \mathbf{e}_1) = \mathrm{t}_2(\mathbf{x}_0, \mathbf{e}_1) + \frac{2E}{5\pi}\frac{6-\alpha}{7-\alpha}\delta\left(\frac{\partial^2 u_1}{\partial x \partial y}(\mathbf{x}_0) + \frac{3}{2}\frac{\partial^2 u_2}{\partial y^2}(\mathbf{x}_0)\right) + \ldots, \tag{2.104b}$$

where the relation $c = \frac{3(6-\alpha)E}{\pi\delta^{6-\alpha}}$ has been employed (*cf.* (2.34)), $\mathrm{t}_1(\mathbf{x}_0, \mathbf{e}_1)$ and $\mathrm{t}_2(\mathbf{x}_0, \mathbf{e}_1)$ are the x- and y-components, respectively, of the local traction (*cf.* (2.73)) evaluated at $\mathbf{x}_0 \in \Gamma$ in classical plane stress (*cf.* (2.21)) for $\nu = 1/3$, and the dots indicate higher-order derivative terms. In the limit as $\delta \to 0$, we get

$$\boldsymbol{\tau}(\mathbf{x}_0, \mathbf{e}_1) = \mathbf{t}(\mathbf{x}_0, \mathbf{e}_1) + \mathcal{O}(\delta), \tag{2.105}$$

i.e., the nonlocal traction converges to the local traction at a rate of $\mathcal{O}(\delta)$. Equation (2.104) implies that, if the deformation around the interface Γ is smooth and second-order and higher derivatives of displacements are negligible, (2.96) is satisfied

(note $\mathbf{t}(\mathbf{x}_0, \mathbf{e}_1) = -\mathbf{t}(\mathbf{x}_0, -\mathbf{e}_1)$ by (2.74)) and overall equilibrium is attained. However, whenever second-order or higher derivatives of displacements are not negligible around the interface Γ, lack of overall equilibrium is in general expected. In this case, the components of the net out-of-balance force are given by (see (2.91), (2.92), and (2.94)):

$$\mathcal{F}_1 \approx -\int_\Gamma \frac{2E}{5\pi}\frac{6-\alpha}{7-\alpha}\delta\left(\frac{\partial^2 u_1}{\partial y^2}(x_0, y) + \frac{\partial^2 u_2}{\partial x \partial y}(x_0, y)\right) dy + \ldots, \tag{2.106a}$$

$$\mathcal{F}_2 \approx -\int_\Gamma \frac{2E}{5\pi}\frac{6-\alpha}{7-\alpha}\delta\left(\frac{\partial^2 u_1}{\partial x \partial y}(x_0, y) + \frac{3}{2}\frac{\partial^2 u_2}{\partial y^2}(x_0, y)\right) dy + \ldots, \tag{2.106b}$$

where all points along Γ have x-coordinate x_0. Note that, similar to (2.103), approximations and not equalities appear in (2.106). In the limit as $\delta \to 0$, the net out-of-balance force vanishes at a rate of $\mathcal{O}(\delta)$.

We showed that, for a straight (horizontal or vertical) interface and a smooth deformation, the nonlocal traction converges to the local traction in the limit as $\delta \to 0$ at a rate of $\mathcal{O}(\delta)$. The above derivations also reveal that, even though the discrepancy between the PD and CCM models depends upon fourth-order and higher derivatives of displacements (see Section 2.3.2), the discrepancy between the nonlocal and local tractions depends upon second-order and higher derivatives of displacements. Furthermore, the leading term in the traction discrepancy turns out to be of order $\mathcal{O}(\delta)$, while the one in the model discrepancy is of order $\mathcal{O}(\delta^2)$ (see Section 2.3.2).

2.6 Numerical assessment of the out-of-balance forces in CCM-PD coupled models

The present section aims at numerically confirming the theoretical analysis of the force balance in CCM-PD coupled systems outlined in Section 2.5 with examples involving one-dimensional models in Section 2.6.1 and two-dimensional models in Section 2.6.2. All numerical examples are linear in terms of material response and deformation [7].

2.6.1 One-dimensional case

In this section, an equilibrium check is carried out on one-dimensional cases adopting the CCM-PD coupling strategy described in Section 2.1. We consider the same one-dimensional system studied in Section 2.4.1 and showed in Figure 2.4. As in Section 2.4.1, the bar is discretized with $N = 31$ nodes uniformly distributed with $\Delta x = 1$. The PD portion of the domain is composed of nodes with coordinates in the interval $[10 \,..\, 20]$, while the remaining part of the domain is modelled with a CCM model discretized using two-node bar FEM elements with linear shape functions. The values of the main problem parameters are, here too, $L = 30$ (bar length), $E = 1$ (Young's modulus), and $A = 1$ (bar cross-sectional area) in consistent units. We assume a CCM model given by (2.6) and a PD model given by (2.5) with a micromodulus function $c(|\xi|) = c/|\xi|$. The PD horizon is taken as $\delta = 3$ (i.e., $m = \delta/\Delta x = 3$) and the micromodulus constant c has been evaluated through (1.42). The PD portion of the domain employs a meshfree discretization with a partial-volume correction [191].

As in Section 2.4.1, a displacement is imposed on all the nodes of the CCM-PD coupled model and the reaction forces are computed using a system of the type of (2.1). The imposed displacement field is a piecewise polynomial function composed of three curves: two linear functions connected by a cubic function, in contrast to the example in Section 2.4.1, where the two linear functions were connected by a quartic function. The cubic function has been selected to ensure C^1 continuity of the displacement field along the bar length. The three curves used for the imposed displacement field are described in Table 2.9; the value of the coefficient g is set to g = 0.0001.

This section presents five different cases of displacement distributions imposed on the one-dimensional system. As in Section 2.4.1, for all the cases, we keep fixed the location of the PD portion of the domain and all the problem parameters, while only changing the position of the cubic displacement curve along the bar length. The resulting relative out-of-balance error is evaluated through (2.38).

Table 2.10 lists the results in terms of relative out-of-balance error for the five different cases investigated (see Figure 2.16). In the first three cases, i.e., configurations

Displacement type	Displacement field equation	Domain
Curve 1: linear	$u(x) = \mathrm{g}x$	$x \in (0, X_1)$
Curve 2: cubic	$u(x) = \frac{\mathrm{g}}{3X_1^2}x^3 + \frac{2\mathrm{g}}{3}X_1$	$x \in (X_1, X_2)$
Curve 3: linear	$u(x) = \mathrm{g}\left(\frac{X_2}{X_1}\right)^2 (x - X_2) + \frac{\mathrm{g}}{3X_1^2}\left(X_2^3 + 2X_1^3\right)$	$x \in (X_2, L)$

Table 2.9: Piecewise displacement field for the one-dimensional case.

Coupled model	e_r
Case (a)	9.04×10^{-16}
Case (b)	1.59×10^{-16}
Case (c)	3.02×10^{-16}
Case (d)	1.98×10^{-03}
Case (e)	5.78×10^{-04}

Table 2.10: Relative out-of-balance errors for the configurations described in Figure 2.16.

(a), (b), and (c) in Figure 2.16, the cubic displacement curve is located away from the two coupling zones. In the configurations (a) and (c) the cubic displacement curve is placed within the CCM portion of the domain, whereas in the configuration (b) the cubic displacement curve is located in the PD region. As shown in Table 2.10, none of these cases exhibit out-of-balance, since the magnitude of the resulting relative out-of-balance errors is on the order of machine precision. In the last two cases, i.e., configurations (d) and (e) in Figure 2.16, the cubic displacement curve is located over the left and right coupling zones, respectively. In these cases, the resulting relative out-of-balance errors are about twelve orders of magnitude larger than the ones computed for the first three cases (see Table 2.10). These results confirm what was found in Section 2.5.1: if displacements across either of the interfaces between the PD and CCM portions of the domain are characterized by cubic or higher-order polynomial distributions, lack of overall equilibrium is experienced (*cf.* (2.70)).

We now present the outputs obtained by performing an m- and a δ-convergence

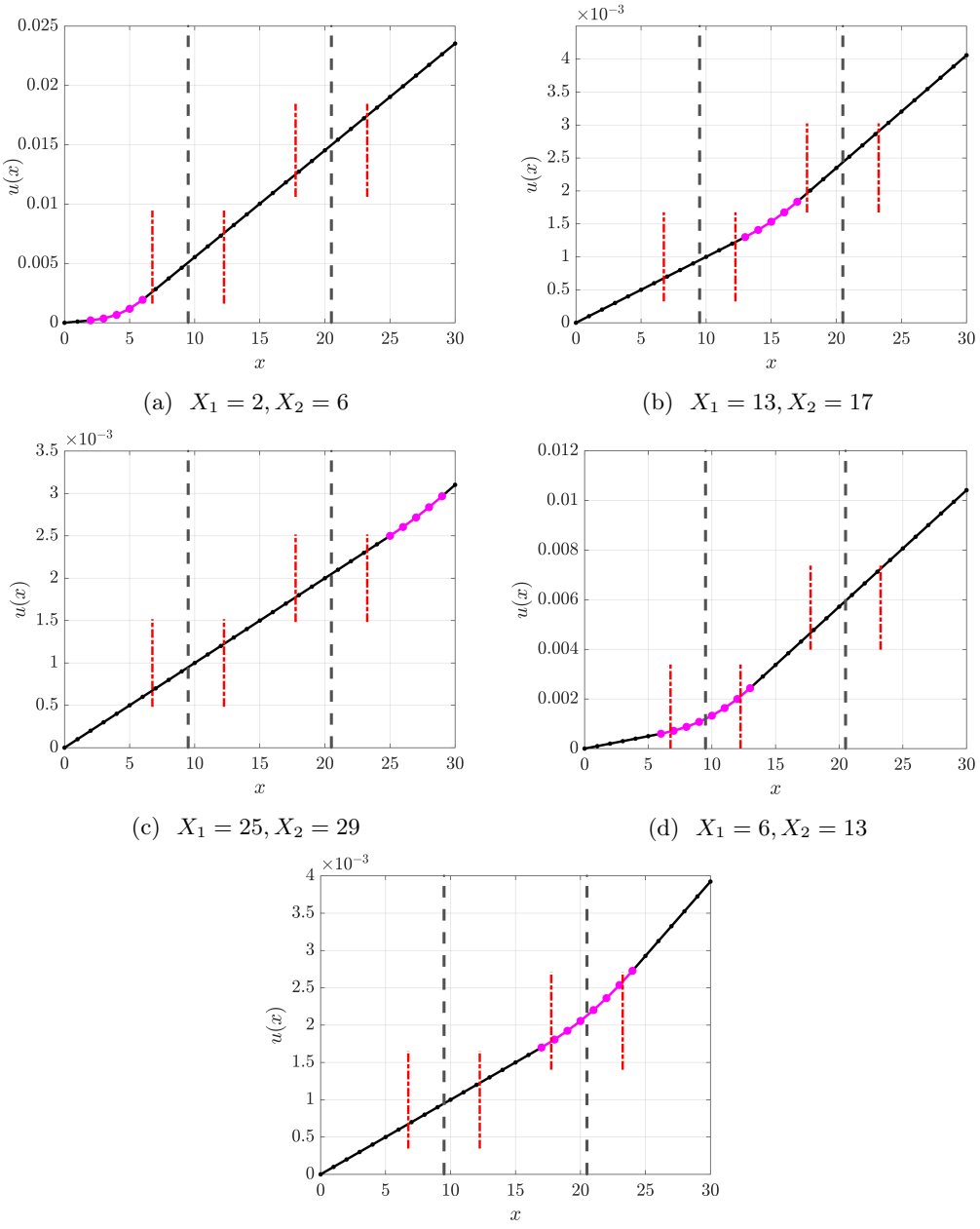

(a) $X_1 = 2, X_2 = 6$

(b) $X_1 = 13, X_2 = 17$

(c) $X_1 = 25, X_2 = 29$

(d) $X_1 = 6, X_2 = 13$

(e) $X_1 = 17, X_2 = 24$

Figure 2.16: Imposed displacement fields on the CCM-PD coupled model with a cubic displacement curve placed in different locations along the bar. The cubic displacement curve, represented by magenta lines, is located in (a) the left CCM region, (b) the central PD part, (c) the right CCM region, (d) the left coupling zone, and (e) the right coupling zone. Long dashed gray vertical lines indicate the interfaces between the PD and CCM portions of the domain, while short dashed-dotted red vertical lines define the coupling zones of the model. The values of the parameters X_1 and X_2 defining the curves in Table 2.9 are indicated for each case. For clarity reasons, the vertical axis scale changes from plot to plot.

Coupled model	e_r	$\left(\sum_{i=1}^{N} F_i\right)/\delta^2$
Case (e), $\delta = 3$, $m = 3$	5.78×10^{-04}	-2.56×10^{-08}
Case (f), $\delta = 3$, $m = 6$	6.33×10^{-04}	-2.80×10^{-08}
Case (g), $\delta = 3$, $m = 12$	6.46×10^{-04}	-2.86×10^{-08}
Case (h), $\delta = 1.5$, $m = 3$	1.45×10^{-04}	-2.56×10^{-08}
Case (i), $\delta = 0.5$, $m = 3$	1.61×10^{-05}	-2.56×10^{-08}

Table 2.11: Relative out-of-balance errors and scaled sums of reaction forces for the m- and δ-convergence studies.

study (see Section 1.3.3). Both studies consider the configuration (e) in Figure 2.16, where the cubic displacement curve is located over the right coupling zone. The resulting relative out-of-balance errors are listed in Table 2.11, where it is evident that the increase in m has no clear effect on the out-of-balance level of the CCM-PD coupled model (see cases (f) and (g)). On the contrary, when a δ-convergence study is performed, the out-of-balance level decreases with the horizon value (see cases (h) and (i)). To verify the δ-dependence of the out-of-balance, Table 2.11 also lists the sum of the reaction forces, $\sum_{i=1}^{N} F_i$, scaled by δ^2. The results confirm the analysis presented in Section 2.5.1, where the leading term of the net out-of-balance force, $\mathcal{F}$, depends on δ^2 (see (2.70)).

In the last part of this section, we present a quantitative comparison between the numerically computed sum of the reaction forces, $\sum_{i=1}^{N} F_i$, and the analytically calculated net out-of-balance force, $\mathcal{F}$, using (2.70). We consider the cases (e), (f), and (g) listed in Table 2.11. Additionally, we numerically compute the nonlocal and local tractions at the corresponding interface, $x_{IR} = 20 + \frac{\Delta x}{2}$, and report their sum. The nonlocal traction is computed by $\tau^{\text{num}}(x_{IR}, +1)$ in (A.15) and the local traction is computed by (*cf.* (2.1))

$$\mathrm{t}^{\text{num}}(x_{IR}, -1) := -\frac{E}{\Delta x}\left(u_{x_{IR}}^{\text{FEM}} - u_{x_{IR}}^{\text{PD}}\right), \tag{2.107}$$

where $u_{x_{IR}}^{\text{FEM}}$ and $u_{x_{IR}}^{\text{PD}}$ are the displacements of the FEM node and PD node, respectively, closest to the interface x_{IR}. The results are presented in Table 2.12. Various observations are drawn from these results. First, the sum of the reaction forces

has the same magnitude as, but opposite sign to the sum of the nonlocal and local tractions:

$$\sum_{i=1}^{N} F_i = -\left[\tau^{\text{num}}(x_{IR}, +1) + \mathrm{t}^{\text{num}}(x_{IR}, -1)\right], \tag{2.108}$$

which confirms the force balance equation (2.64); note that, in this case, the corresponding nonlocal and local tractions at x_{IL} are equal in magnitude because the displacement field around that interface is linear (*cf.* (2.67)). Second, the sum of the reaction forces provides a suitable approximation to the net out-of-balance force:

$$\mathcal{F} \approx \sum_{i=1}^{N} F_i, \tag{2.109}$$

and the numerical values approach the analytical ones as m increases. Third, as shown in Appendix A.1, the numerical nonlocal traction, $\tau^{\text{num}}(x_{IR}, +1)$, accurately reproduces the analytical nonlocal traction, $\tau(x_{IR}, +1)$, for linear, quadratic, and cubic displacement fields (see Table A.2). Consequently, the discrepancy between the sum of the reaction forces and the net out-of-balance force in Table 2.12 originates from a numerical error in the approximation of the local traction. To show this, consider the numerical local traction in (2.107), and note that $u^{\text{FEM}}_{x_{IR}} = u(x_{IR} + \frac{\Delta x}{2})$ and $u^{\text{PD}}_{x_{IR}} = u(x_{IR} - \frac{\Delta x}{2})$. Performing Taylor expansions (recall the displacement field is cubic around x_{IR}), we obtain

$$\begin{aligned}
\mathrm{t}^{\text{num}}(x_{IR}, -1) &= -\frac{E}{\Delta x}\left(u\left(x_{IR} + \tfrac{\Delta x}{2}\right) - u\left(x_{IR} - \tfrac{\Delta x}{2}\right)\right) \\
&= -E\left(\frac{du}{dx}(x_{IR}) + \frac{1}{4!}\frac{d^3u}{dx^3}(x_{IR})(\Delta x)^2\right) \\
&= -E\frac{du}{dx}(x_{IR}) + \mathcal{O}\left((\Delta x)^2\right) = \mathrm{t}(x_{IR}, -1) + \mathcal{O}\left((\Delta x)^2\right).
\end{aligned} \tag{2.110}$$

The numerical local traction, $\mathrm{t}^{\text{num}}(x_{IR}, -1)$, is thus an accurate estimator of the analytical local traction, $\mathrm{t}(x_{IR}, -1)$, for constant, linear, and quadratic displacement fields, while it is an order $\mathcal{O}((\Delta x)^2)$ approximation of the analytical local traction for cubic or higher-order polynomial displacement fields. The error in this approximation vanishes in the limit as $\Delta x \to 0$, which coincides with the limit of $m \to \infty$ in the m-convergence study, explaining why the sum of the reaction forces approaches the net out-of-balance force in this limit (see Table 2.12).

Remark 1 The observation concerning the numerical error in the approximation of the local traction provides an explanation of why the scaled sums of the reaction forces in Table 2.11 possess a fixed value for $m = 3$, regardless of the value of δ, while varying when changing m. To explain this, consider a scaled sum of the numerical nonlocal and local tractions. Using the fact that, for the cases considered in Table 2.11, the numerical nonlocal traction accurately estimates the analytical nonlocal traction, and employing (2.67), (2.110), and (2.46), we have (recall the displacement field is cubic around x_{IR}, $\alpha = 1$, and $\delta = m\Delta x$)

$$\begin{aligned}\frac{1}{\delta^2}\left(\tau^{\text{num}}(x_{IR},+1)+\text{t}^{\text{num}}(x_{IR},-1)\right) &= \frac{1}{\delta^2}\left(\tau(x_{IR},+1)+\text{t}^{\text{num}}(x_{IR},-1)\right)\\ &= \frac{1}{\delta^2}\left(\text{t}(x_{IR},+1)+\frac{1}{4!}E\delta^2\frac{d^3u}{dx^3}(x_{IR})\right.\\ &\qquad \left.+\text{t}(x_{IR},-1)-\frac{1}{4!}E(\Delta x)^2\frac{d^3u}{dx^3}(x_{IR})\right)\\ &= \frac{1}{4!}\left(1-\frac{1}{m^2}\right)E\frac{d^3u}{dx^3}(x_{IR}). \qquad (2.111)\end{aligned}$$

This expression is independent of δ for a fixed value of m, and it increases in magnitude with increasing m. Using (2.111) for the cases in Table 2.11 gives values with the same magnitude as, but opposite sign to the ones reported for the scaled sums of the reaction forces in that table.

Coupled model	$\sum_{i=1}^{N} F_i$	$\mathcal{F}$	$\tau^{\text{num}}(x_{IR},+1)+\text{t}^{\text{num}}(x_{IR},-1)$
Case (e), $\delta = 3$, $m = 3$	-2.31×10^{-07}	-2.60×10^{-07}	2.31×10^{-07}
Case (f), $\delta = 3$, $m = 6$	-2.52×10^{-07}	-2.60×10^{-07}	2.52×10^{-07}
Case (g), $\delta = 3$, $m = 12$	-2.58×10^{-07}	-2.60×10^{-07}	2.58×10^{-07}

Table 2.12: Comparison between sums of reaction forces, net out-of-balance forces, and sums of numerical nonlocal and local tractions.

Remark 2 The analytical expression for the net out-of-balance force in (2.70) implies that imposing a cubic displacement field along the whole bar results in $\mathcal{F} = 0$, because the contributions of the nonlocal tractions at the interfaces cancel each other (note that the third derivative of the displacement, in this case, is constant). For this reason, the numerical results in this section were based on cases where a cubic

displacement field occurs at most at one of the two interfaces. A similar reasoning is employed in Section 2.6.2 below in the choice of the imposed displacement fields for the two-dimensional case.

2.6.2 Two-dimensional case

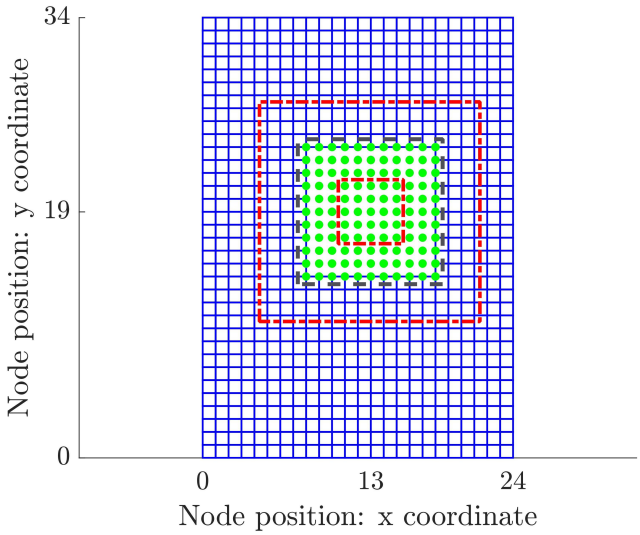

Figure 2.17: CCM-PD coupled model for the two-dimensional case. Green circles are PD nodes and blue (empty) squares are FEM elements. The dashed gray lines represent the interface between the PD and CCM regions, while the portion of the domain bounded by the dashed-dotted red lines is the coupling zone. For clarity reasons, in the figure, $\Delta x = \Delta y = 1$ and $m = \delta/\Delta x = 3$.

In this section, equilibrium checks are carried out on two-dimensional plane stress cases adopting the CCM-PD coupling strategy described in Section 2.1. We consider a two-dimensional rectangular plate with an internal PD region as shown in Figure 2.17. The PD portion of the domain is a square of edge length $L_{PDx} = L_{PDy} = 10$, and its centre has coordinates (13, 19). The remaining part of the domain, the CCM region, is discretized using four-node square plane stress FEM elements for which the element stiffness matrix has been evaluated with exact integration [194]. The discretization of the domain employs a uniform grid with $\Delta x = \Delta y = 0.25$. As in Section 2.4.2, the values of the main problem parameters are $L_x = 24$ and $L_y = 34$ (plate dimensions), $E = 1$ (Young's modulus), $\nu = \frac{1}{3}$ (Poisson's ratio), and $h = 1$ (plate thickness) in consistent units. We assume a CCM model given by the

Displacement type	Displacement field equation	Domain
Constant	$u_1(x,y) = 0$	$(x,y) \in \mathcal{B}$
Bilinear	$u_2(x,y) = d\dfrac{y - Y_1}{Y_B - Y_1}$	$(x,y) \in B_1$
	$u_2(x,y) = d\left(1 - \dfrac{y - Y_B}{Y_2 - Y_B}\right)$	$(x,y) \in B_2$
Constant	$u_2(x,y) = 0$	$(x,y) \in \mathcal{B} \setminus (B_1 \cup B_2)$

Table 2.13: Piecewise displacement field for the two-dimensional Case I.

classical linear elasticity plane stress isotropic model (*cf.* (2.23)) and a PD model given by a linear bond-based isotropic model (*cf.* (2.19)) with a micromodulus function $\lambda(\|\boldsymbol{\xi}\|) = \frac{c}{\|\boldsymbol{\xi}\|^3}$. The PD horizon is taken as $\delta = 0.75$ (i.e., $m = \delta/\Delta x = 3$) and the micromodulus constant c has been evaluated through (2.39). The PD portion of the domain employs a meshfree discretization with a partial-volume correction [190].

In all the cases considered in this section, a displacement is imposed on all the nodes of the plate in such a way as to examine either a single straight interface between the PD and CCM portions of the domain (Case I and Case II in the sections presented below) or a single interface corner (Case III in the section presented below). For all the cases, we keep fixed the location of the PD portion of the domain and all the problem parameters, while only changing the characteristics of the displacement distributions within the plate. The resulting relative out-of-balance error is evaluated both in the x- and y-directions through (2.40a) and (2.40b), respectively.

Case I: bilinear displacement over a straight interface

In this section, an equilibrium check is carried out by imposing a piecewise displacement field composed of a bilinear function connected to a constant function. The imposed displacement field is described by the set of equations in Table 2.13, where u_1 and u_2 are the x- and y-components, respectively, of the displacement field $\mathbf{u} = (u_1, u_2)$, and the value of the coefficient d is set to $d = 0.5$. The bilinear portion of the displacement component u_2 is shown in Figure 2.18, where the two

Coupled model	e_{r_x}	e_{r_y}
Case I	3.28×10^{-16}	5.64×10^{-17}

Table 2.14: Relative out-of-balance error along the x- and y-directions for Case I in Figure 2.18.

subdomains B_1 and B_2 are defined as follows:

$$B_1 := \{(x, y) \in \mathcal{B} : x \in (X_1, X_2) \wedge y \in (Y_1, Y_B)\}, \tag{2.112a}$$

$$B_2 := \{(x, y) \in \mathcal{B} : x \in (X_1, X_2) \wedge y \in (Y_B, Y_2)\}, \tag{2.112b}$$

where X_1, X_2, Y_1, Y_2, and Y_B are the bounds of the two subdomains, as shown in Figure 2.18c. The bilinear displacement portion is located over the lower horizontal interface (see Figure 2.18a and Figure 2.18b). The values of the bounds of the subdomains B_1 and B_2 are set to $X_1 = 9.25$, $X_2 = 13.75$, $Y_1 = 12.75$, $Y_2 = 17.25$, and $Y_B = (Y_1 + Y_2)/2 = 15$. Table 2.14 lists the results in terms of relative out-of-balance error along the x- and y-directions. In this case, the force equilibrium is verified along both the x- and y-directions. We performed a similar study by imposing instead the bilinear distribution described in Table 2.13 on the displacement component u_1 over a vertical interface. Also, in this case, no appreciable out-of-balance error was found. These results confirm what was found in Section 2.5.2: if displacements across a straight (horizontal or vertical) interface are characterized by linear or constant distributions, overall equilibrium is attained (*cf.* (2.103) and (2.106)).

Case II: quadratic displacement over a straight interface

In this section, an equilibrium check is carried out by imposing a piecewise displacement field composed of a quadratic function connected to a constant function. The imposed displacement field is described by the set of equations in Table 2.15, where the value of the coefficient q is set to $q = 15$. The quadratic portion of the displacement component u_2 is shown in Figure 2.19, and it is applied to a circular subdomain, Q, defined as follows:

$$Q := \left\{(x, y) \in \mathcal{B} : (x - X_Q)^2 + (y - Y_Q)^2 \leqslant R^2\right\}, \tag{2.113}$$

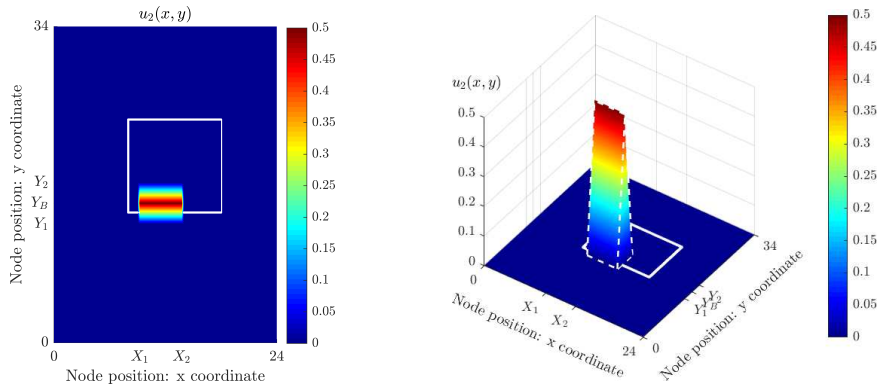

(a) Top view

(b) 3D view

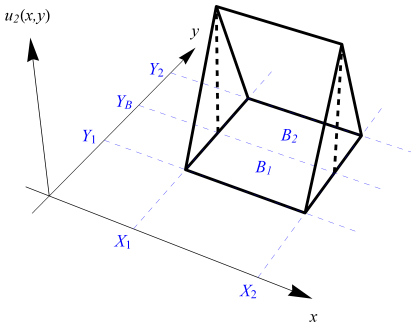

(c) Characteristic parameters

Figure 2.18: Imposed displacement field on the plate for Case I: (a) top view, (b) 3D view, and (c) characteristic parameters of the bilinear displacement portion. The square part of the domain bounded by thick straight white lines represents the PD region, while the remaining part of the domain is the CCM region.

Displacement type	Displacement field equation	Domain
Constant	$u_1(x,y) = 0$	$(x,y) \in \mathcal{B}$
Quadratic	$u_2(x,y) = \dfrac{-(x-X_Q)^2 - (y-Y_Q)^2 + R^2}{q^2}$	$(x,y) \in Q$
Constant	$u_2(x,y) = 0$	$(x,y) \in \mathcal{B} \setminus Q$

Table 2.15: Piecewise displacement field for the two-dimensional Case II.

Coupled model	e_{r_x}	e_{r_y}
Case II	1.40×10^{-16}	5.00×10^{-04}

Table 2.16: Relative out-of-balance error along the x- and y-directions for Case II in Figure 2.19.

where X_Q and Y_Q are the x- and y-coordinates, respectively, of the centre of the subdomain and R indicates its radius (see Figure 2.19c). The quadratic displacement portion is located over the lower horizontal interface (see Figure 2.19a and Figure 2.19b). The centre of Q has coordinates $X_Q = 11.5$ and $Y_Q = 15$, and its radius is set to $R = 2.25$. Table 2.16 lists the results obtained in terms of relative out-of-balance error along the x- and y-directions. In this case, the force equilibrium is verified only along the x-direction. This result is consistent with the net out-of-balance force in (2.103); specifically, in this case, $\mathcal{F}_1$ is expected to vanish, while $\mathcal{F}_2$ is expected to be non-zero due to the contribution of the second derivative of the displacement component u_2 with respect to x. We performed a similar study by imposing instead the quadratic distribution described in Table 2.15 on the displacement component u_1 over a vertical interface. In this case, the force equilibrium is verified only along the y-direction. This result is consistent with the net out-of-balance force in (2.106); specifically, in this case, $\mathcal{F}_2$ is expected to vanish, while $\mathcal{F}_1$ is expected to be non-zero due to the contribution of the second derivative of the displacement component u_1 with respect to y. These results confirm what was found in Section 2.5.2: if displacements across a straight (horizontal or vertical) interface are characterized by quadratic or higher-order polynomial distributions, lack of overall equilibrium is experienced (*cf.* (2.103) and (2.106)).

In the remaining part of this section, the outputs obtained by performing a δ-convergence study are presented. We consider the case where the quadratic displacement distribution described in Table 2.15, which is applied to the displacement component u_2, is located over the lower horizontal interface (see Figure 2.19). As demonstrated in Appendix A.2, large values of m are required to obtain accurate computations of nonlocal tractions (see Table A.4). For this reason, we perform the δ-convergence study using a larger value of m, chosen as $m = 8$; this value has been

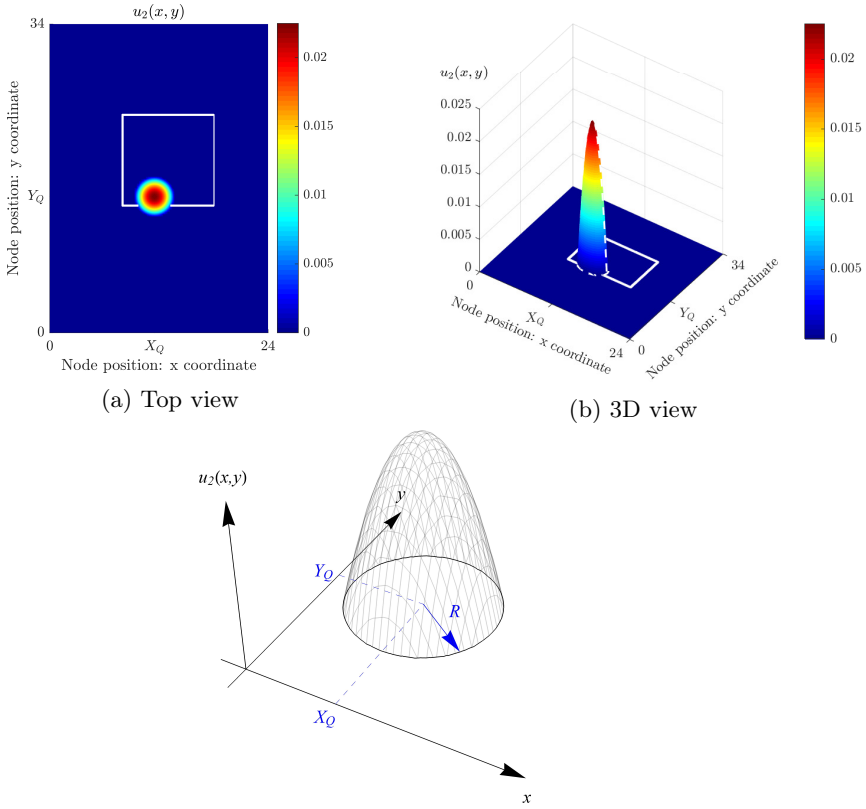

(a) Top view

(b) 3D view

(c) Characteristic parameters

Figure 2.19: Imposed displacement field on the plate for Case II: (a) top view, (b) 3D view, and (c) characteristic parameters of the quadratic displacement portion. The square part of the domain bounded by thick straight white lines represents the PD region, while the remaining part of the domain is the CCM region.

Coupled model	e_{r_x}	e_{r_y}	$\left(\sum_{i=1}^{N} F_{2\,i}\right)/\delta$
Case II, $\delta = 0.75$, $m = 8$	1.03×10^{-16}	1.86×10^{-03}	-8.08×10^{-04}
Case II, $\delta = 0.375$, $m = 8$	5.23×10^{-17}	7.23×10^{-04}	-7.05×10^{-04}
Case II, $\delta = 0.1875$, $m = 8$	1.05×10^{-15}	1.60×10^{-04}	-3.33×10^{-04}

Table 2.17: Relative out-of-balance errors and scaled sums of reaction forces for the δ-convergence study.

selected as a compromise between computational cost and numerical accuracy in two-dimensional simulations. The resulting relative out-of-balance errors are listed in Table 2.17, where, as expected, the force equilibrium is verified only along the x-direction. The results for e_{r_y} demonstrate that the out-of-balance level decreases with the horizon. To verify the δ-dependence of the out-of-balance, Table 2.17 also lists the sum of the y-component of the reaction forces, $\sum_{i=1}^{N} F_{2\,i}$, scaled by δ. The results do not exactly give a linear dependence on δ, which is the theoretically predicted behavior in (2.103). The potential reasons for this discrepancy are twofold. First, it is possible that the value of m is not large enough to provide the required numerical accuracy (*cf.* Table A.4). Second, the configuration presented in Figure 2.19 cannot satisfy one of the hypotheses on which the analytical derivations leading to (2.103) rely, i.e., the assumption that, for each PD node, the entire neighbourhood on the CCM side is subjected to a uniform, non-piecewise displacement field.

The reason for the choice of the piecewise displacement fields in Figure 2.18 and Figure 2.19 was to consider a displacement variation around a single straight (horizontal or vertical) interface, for consistency with the analysis presented in Section 2.6.1. In particular, that choice was aimed at isolating the effect of corners, i.e., non-straight interfaces; this effect is investigated in the following section.

Case III: bilinear displacement over an interface corner

The theoretical results for the net out-of-balance forces presented in Section 2.5.2 hold for a straight (horizontal or vertical) interface and may not hold for an interface of arbitrary shape (e.g., a corner). In this section, we consider a non-straight

Coupled model	e_{r_x}	e_{r_y}
Case III	4.31×10^{-03}	3.09×10^{-16}

Table 2.18: Relative out-of-balance error along the x- and y-directions for Case III in Figure 2.20.

interface. An equilibrium check is carried out by imposing the displacement field described in Table 2.13, with the bilinear displacement portion located over the lower right interface corner of the CCM-PD coupled model. In this case, the values of the bounds of the subdomains B_1 and B_2 are set to $X_1 = 14.75$, $X_2 = 19.25$, $Y_1 = 12.75$, $Y_2 = 17.25$, and $Y_B = 15$. Figure 2.20 shows the configuration under investigation. Table 2.18 lists the results obtained in terms of relative out-of-balance error along the x- and y-directions. In this case, the resulting relative out-of-balance error e_{r_x} is not negligible. This result demonstrates that, in contrast to the results reported in Table 2.14, if displacements across a non-straight interface are characterized by linear distributions, lack of overall equilibrium may be experienced.

For the sake of completeness, it is possible to observe that, unlike the results obtained in the current section, in Case I in Figure 2.9, the force equilibrium is verified along both the x- and y-directions, even if the coupling zone is entire located within the linear portion of the displacement field, i.e., even if the displacements across the interface corners are characterized by linear distributions. In this case, the absence of relative out-of-balance errors is a result of error compensation phenomena occurring in correspondence of the interface corners of the CCM-PD coupled model.

To conclude, the results of this section suggest that, for a two-dimensional CCM-PD coupled model, the overall static equilibrium is affected not only by the location of the coupling interface but also by its shape. Consequently, a future extension of the out-of-balance analysis in CCM-PD coupled models could be focused on controlling the relative out-of-balance error by optimizing the shape of the interface between the PD and CCM portions of the domain. In Section 2.7, we study the effect of the location of the coupling interface in the context of crack propagation problems.

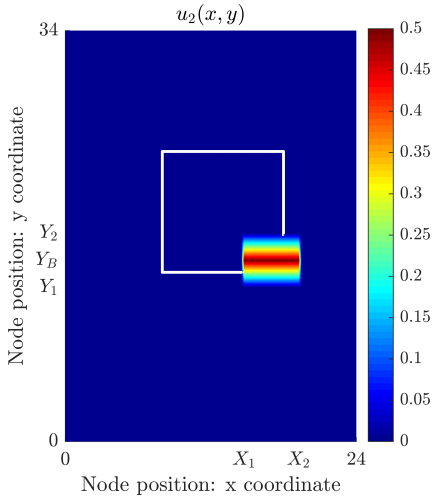

Figure 2.20: Imposed displacement field on the plate for Case III (top view). The square part of the domain bounded by thick straight white lines represents the PD region, while the remaining part of the domain is the CCM region.

2.7 Simulation of crack propagation using the CCM-PD coupled model

In this section, quasi-static crack propagation problems are presented. Initially, the entire domain with an initial crack is discretized with the FEM; then, a PD region is introduced, which adaptively follows an advancing crack [84, 113]. We show that the position of the coupling interface of the CCM-PD coupled model affects the values of the out-of-balance forces. The main idea is that, in crack propagation problems, high spatial strains normally appear in the region near the crack tip. Therefore, the coupling interface of the CCM-PD coupled model should not be too close to the crack tip. The CCM region is linear in terms of material response and deformation, and it is described by a classical linear elasticity model given by the plane stress isotropic model (*cf.* (2.23)) in two dimensions and the Navier equation in three dimensions. The PD region is described by the linearized state-based PD model from [178, 196]. The values given to the parameters of the problems are associated to the usual units.

2.7.1 Two-dimensional case: three-point bending test

In Figure 2.21, we present the geometric parameters and boundary conditions of a three-point bending test carried out in this section. The domain is discretized using a uniform grid with $\Delta x = \Delta y = 0.05$ [m], resulting in a total of 64,561 nodes. The material parameters are: $E = 2.4$ [GPa] (Young's modulus), $\nu = 0.25$ (Poisson's ratio), and $G_0 = 500$ [J/m^2] (fracture energy) [197]. The CCM region is discretized using four-node FEM elements with bilinear shape functions and four integration points. For the PD portion of the domain, we employ the same PD discretization used in Sections 2.2, 2.4.2 and 2.6.2. The horizon is taken as $\delta = 0.15$ [m] (i.e., $m = \delta/\Delta x = 3$), and the micromodulus function and influence function described in [113] are used. A downward vertical displacement of $u_y = 0.001$ [m] is imposed on the central point of the top edge of the plate. The imposed displacement is divided into 1000 steps. A crack at the bottom, the initial length of which is 1 [m], propagates in the vertical direction as the imposed vertical displacement increases. Using the algorithm in [197], we solve the structural problem and compute the three vertical reaction forces of the system: F_{y_A}, F_{y_B}, and F_{y_C}, the first two at the supports A and B, and the third one at C where the vertical displacement is imposed (see Figure 2.21). The relative out-of-balance error is given by:

$$e_r := \frac{|F_{y_A} + F_{y_B} + F_{y_C}|}{|F_{y_A}| + |F_{y_B}| + |F_{y_C}|}. \tag{2.114}$$

The second-order derivatives of the displacement field, $\frac{\partial^2 u_1}{\partial x^2}$, $\frac{\partial^2 u_1}{\partial y^2}$, $\frac{\partial^2 u_1}{\partial x \partial y}$, $\frac{\partial^2 u_2}{\partial x^2}$, $\frac{\partial^2 u_2}{\partial y^2}$, and $\frac{\partial^2 u_2}{\partial x \partial y}$, are calculated using the PD differential operators [198, 199]. An indicator for the distribution of the overall second-order derivatives is defined as:

$$D^2(\mathbf{u}) := \left|\frac{\partial^2 u_1}{\partial x^2}\right| + \left|\frac{\partial^2 u_1}{\partial y^2}\right| + \left|\frac{\partial^2 u_1}{\partial x \partial y}\right| + \left|\frac{\partial^2 u_2}{\partial x^2}\right| + \left|\frac{\partial^2 u_2}{\partial y^2}\right| + \left|\frac{\partial^2 u_2}{\partial x \partial y}\right|. \tag{2.115}$$

Given the configuration in Figure 2.21, the distribution of $D^2(\mathbf{u})$ for the CCM model with a displacement of $u_y = 1 \times 10^{-06}$ [m] is shown in Figure 2.22. It is obvious that the values of $D^2(\mathbf{u})$ around the crack tip as well as around the point C where the displacement is imposed and around the supports A and B are greater than in other zones, and this feature is preserved during the crack propagation. When the crack propagates, we adopt two switching schemes to convert FEM nodes to PD

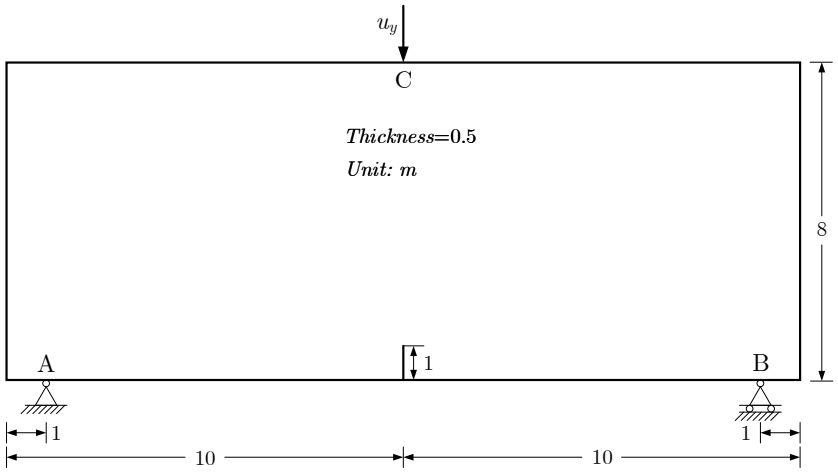

Figure 2.21: Geometric parameters and boundary conditions of the three-point bending test.

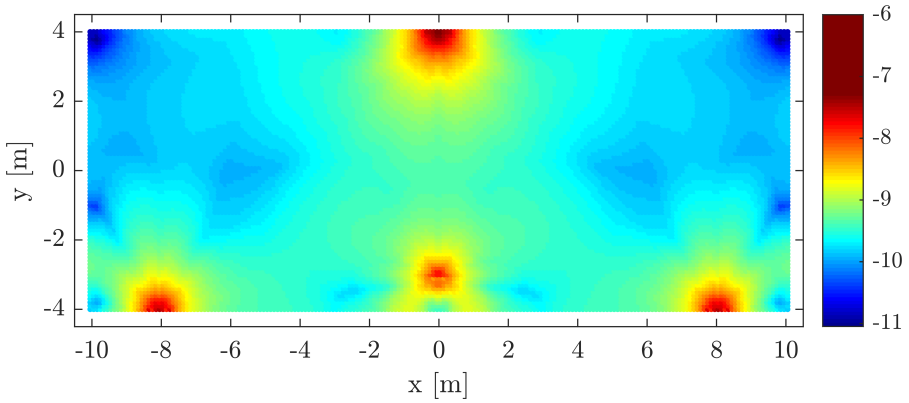

Figure 2.22: Distribution of $D^2(\mathbf{u})$ based on the CCM model for the three-point bending test in Figure 2.21 with an applied vertical displacement of $u_y = 1 \times 10^{-06}$ [m]. The colour plot is displayed in logarithmic scale.

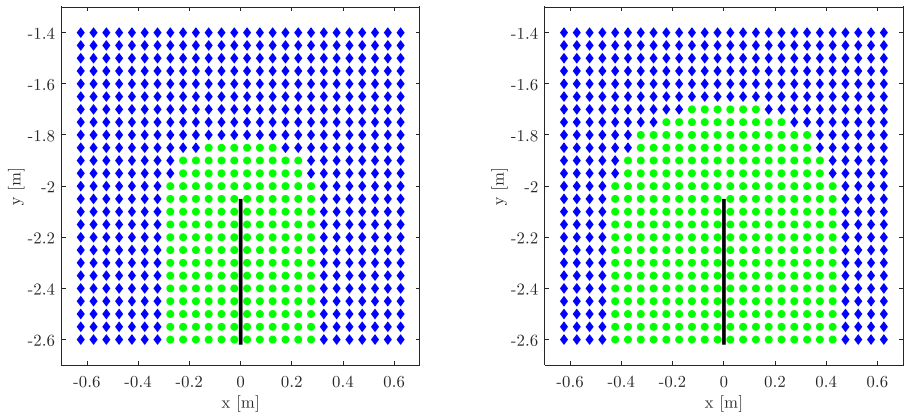

(a) Switching scheme 1

(b) Switching scheme 2

Figure 2.23: Schemes for switching nodes around the crack tip. Blue diamonds are FEM nodes and green circles are PD nodes. The black line represents the crack.

nodes $[84, 113]$:

Switching scheme 1: FEM nodes within one horizon radius from PD nodes with broken bonds are transformed into PD nodes, as shown in Figure 2.23a.

Switching scheme 2: FEM nodes within a distance of twice the horizon radius from PD nodes with broken bonds are transformed into PD nodes, as shown in Figure 2.23b.

In order to ensure that the solutions of the two switching schemes are comparable, we perform the simulation using the switching scheme 1, and then post-process the solution using both switching schemes to study the behaviour of the relative out-of-balance error.

Figure 2.24 shows the distribution of $D^2(\mathbf{u})$ around the crack tip for different load step numbers ($step = 200, 400, 600, 800, 1000$). The relative out-of-balance error computed with (2.114) is plotted in Figure 2.25. We observe that the relative out-of-balance error is larger when the interface between the CCM and PD regions falls into an area with larger values of $D^2(\mathbf{u})$ (switching scheme 1) compared to the case where that interface falls into an area with smaller values of $D^2(\mathbf{u})$ (switching scheme 2).

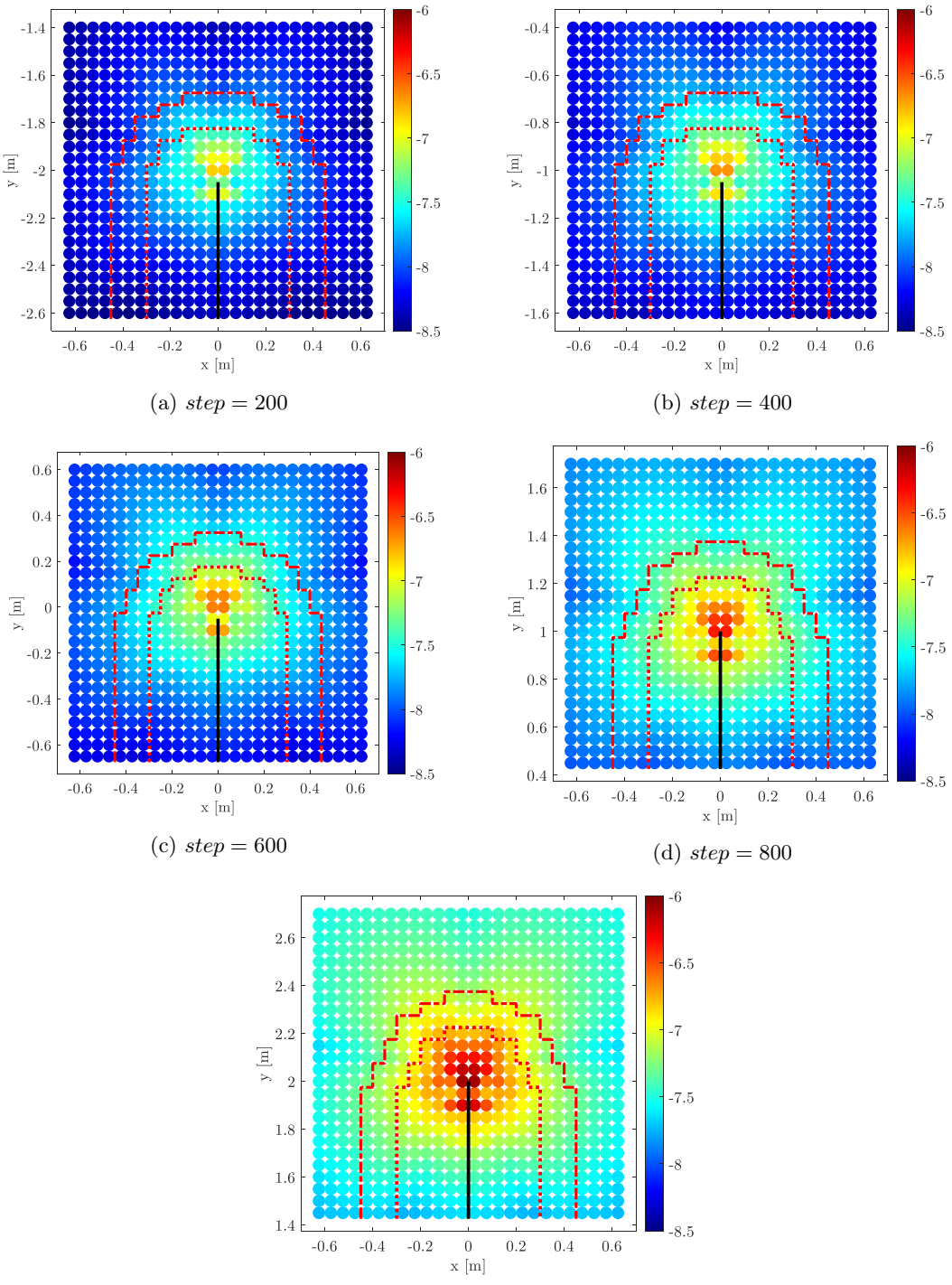

(a) $step = 200$

(b) $step = 400$

(c) $step = 600$

(d) $step = 800$

(e) $step = 1000$

Figure 2.24: Distribution of $D^2(\mathbf{u})$ around the crack tip for different load step numbers, based on the CCM-PD coupled model with the switching scheme 1, for the three-point bending test in Figure 2.21. The colour plot is displayed in logarithmic scale. The black solid line is the crack. The inner dotted piecewise linear red curve represents the interface between the CCM and PD regions generated by the switching scheme 1. The outer dashed-dotted piecewise linear red curve represents the corresponding interface generated by the switching scheme 2, which is used only for post-processing purposes.

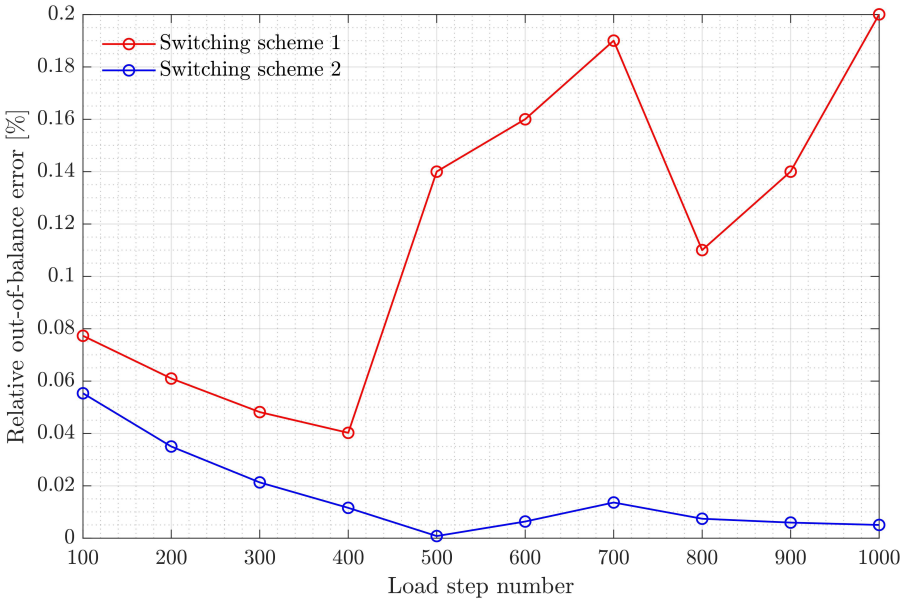

Figure 2.25: Relative out-of-balance error in the CCM-PD coupled model for different load step numbers for the three-point bending test in Figure 2.21 with the two switching schemes.

2.7.2 Three-dimensional case: Brokenshire torsion experiment

In this section, a crack propagation problem given by the Brokenshire torsion experiment, which is comprehensively described in [200], is considered. The geometric parameters of the prismatic specimen and the boundary conditions are presented in Figure 2.26. The CCM region is discretized using eight-node FEM elements with trilinear shape functions and eight integration points. The initial FEM mesh used in the simulation is shown in Figure 2.27. In the central part of the specimen a uniform hexahedral mesh with mesh size $\Delta x = \Delta y = \Delta z = 0.0025$ [m] is adopted, whereas the remaining parts of the domain are discretized using non-uniform hexahedral meshes to reduce the computational cost of the simulation. The FEM mesh has a total of 173,082 nodes and 161,824 elements. The material parameters are: $E = 35$ [GPa] (Young's modulus), $\nu = 0.2$ (Poisson's ratio), and $G_0 = 80$ [J/m^2] (fracture energy) [113]. For the PD portion of the domain, the standard meshfree PD discretization presented in [51] is employed. The horizon is taken as $\delta = 0.0075$ [m] (i.e., $m = \delta/\Delta x = 3$), and the micromodulus function and influence function described in [113] are used. A downward vertical displacement of $u_z = 0.001$ [m] is

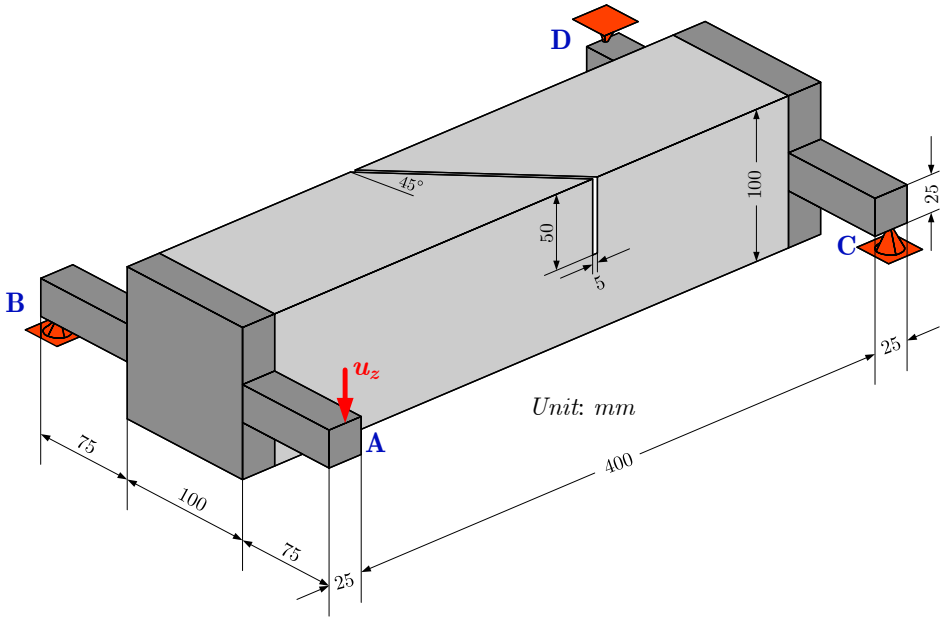

Figure 2.26: Geometric parameters and boundary conditions of the Brokenshire torsion experiment. Adapted from [113].

divided into 7000 steps and applied as shown in Figure 2.26. As the imposed vertical displacement increases, a non-planar crack propagates in the notched prismatic specimen. Using the algorithm in [197], we solve the fracture problem and compute the four vertical reaction forces of the system: F_{z_A}, F_{z_B}, F_{z_C}, and F_{z_D}, the first one at A where the vertical displacement u_z is imposed, and the other three at the supports B, C, and D (see Figure 2.26). The relative out-of-balance error is given by:

$$e_r := \frac{|F_{z_A} + F_{z_B} + F_{z_C} + F_{z_D}|}{|F_{z_A}| + |F_{z_B}| + |F_{z_C}| + |F_{z_D}|}. \tag{2.116}$$

Similar to Section 2.7.1, when the non-planar crack propagates, we employ a switching scheme to convert FEM nodes to PD nodes and adaptively follow the advancing crack [84, 113]. Following the same procedure adopted in Section 2.7.1, we perform the simulation using the switching scheme 1, and then post-process the solution using both switching schemes, i.e., the switching scheme 1 and the switching scheme 2, to study the behaviour of the relative out-of-balance error.

Figure 2.28 shows the shape of the propagating crack for different load step numbers ($step = 1000, 2000, 3000, 4000, 5000, 6000, 7000$). The corresponding relative out-of-balance error computed with (2.116) is plotted in Figure 2.29. This latter

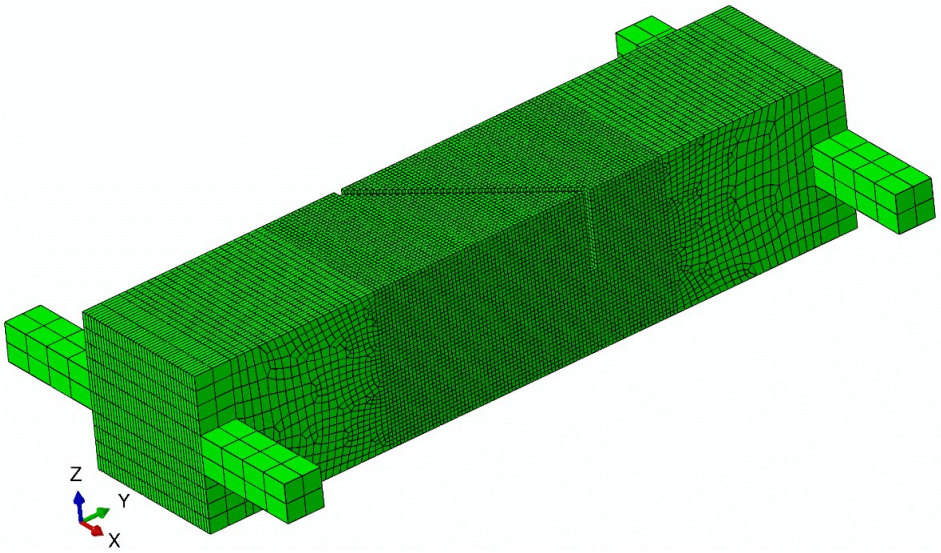

Figure 2.27: Initial FEM mesh used for the Brokenshire torsion experiment.

result is consistent with the output of the study carried out in Section 2.7.1 and plotted in Figure 2.25, since the switching scheme 2 again demonstrates to generally perform better than the switching scheme 1 in terms of relative out-of-balance error. As in the two-dimensional case in Section 2.7.1, we observe that the relative out-of-balance error is affected by the location of the coupling interface of the CCM-PD coupled model, since its magnitude is generally smaller when the interface between the CCM and PD regions is further from the crack tip (switching scheme 2), i.e., further from the area with larger values of high-order derivatives of displacements, compared to the case where the interface is closer to the crack tip (switching scheme 1).

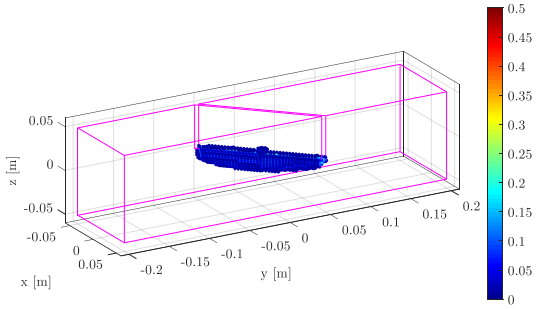

(a) *step* = 1000

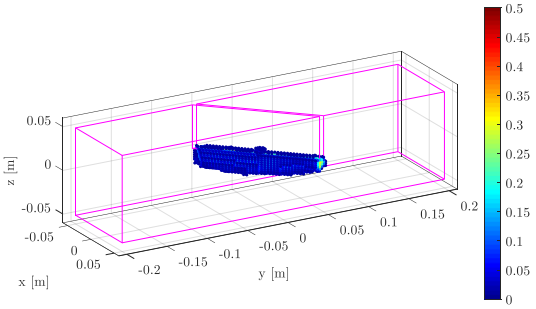

(b) *step* = 2000

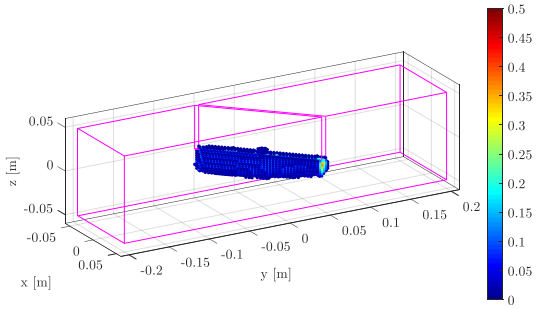

(c) *step* = 3000

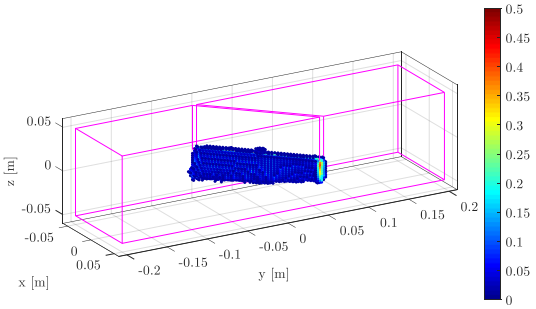

(d) *step* = 4000

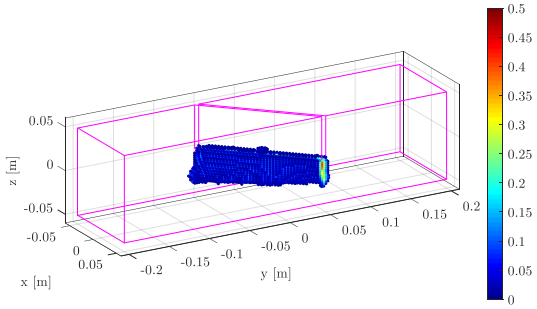

(e) *step* = 5000

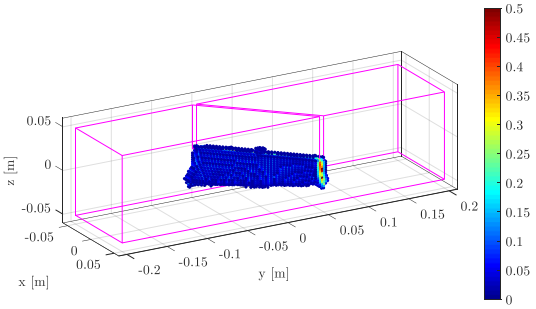

(f) *step* = 6000

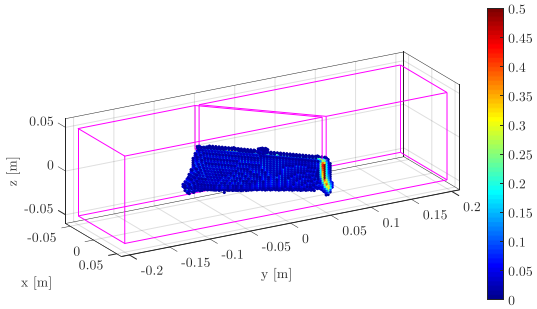

(g) *step* = 7000

Figure 2.28: Shapes of the non-planar crack for different load step numbers, based on the CCM-PD coupled model with the switching scheme 1, for the Brokenshire torsion experiment in Figure 2.26. The colours indicate damage [51].

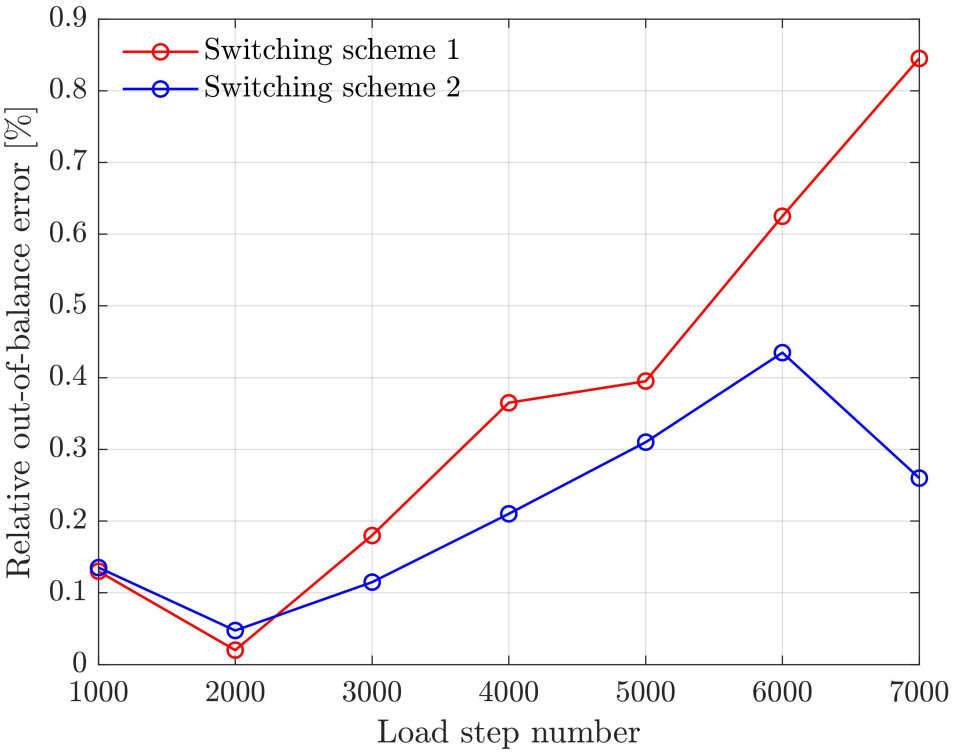

Figure 2.29: Relative out-of-balance error in the CCM-PD coupled model for the different load step numbers shown in Figure 2.28 for the Brokenshire torsion experiment in Figure 2.26 with the two switching schemes.

Chapter 3

Numerical modelling of the mechanical properties of heterogeneous materials

3.1 Polymer/clay nanocomposites

In the last years, the need of the aeronautical and aerospace industries to employ lighter and more efficient components for aircraft, satellite and launcher structures has led to an ever-increasing development of high specific stiffness materials like composites and nanocomposites. Among them, the interest of the academic and industrial communities has recently been attracted by polymer-based composites reinforced with nanoscale reinforcements, since they exhibit enhanced mechanical and barrier properties [144], superior performance in terms of thermal stability and flame retardancy [165], and excellent corrosion and fatigue resistances [201]. The application of these high performance materials is in fact expanding rapidly in a wide range of fields, such as aerospace, automotive, construction, transportation, packaging and waterlines [139, 202]. For example, as for the aerospace field, about 50% of the Boeing 787 aircraft structures are made of composite materials, whereas, in satellites, composites are employed for the construction of primary structures, payload supports and solar cells. The main advantages of such applications are the possibility to remarkably reduce the total mass of the structure and the consequent decrease in fuel consumption, carbon emissions and costs.

Nanocomposites are multicomponent materials comprising different phase do-

mains in which at least one of the phases has at least one characteristic dimension on the order of nanometers, typically ranging from 1 to 100 [nm] [203–205]. This new class of composite materials is in fact characterized by a matrix which is reinforced by organic or inorganic nanofillers [206]. The most commonly used matrix materials are polymers (e.g., epoxy, nylon, polyepoxide, polyetherimide), ceramics (e.g., alumina, glass, porcelain), and metals (e.g., iron, titanium, magnesium). The class of nanomaterials considered in this study is the polymer-based one, which has recently been the subject of extensive research due to its high commercial interest. The substantial difference between conventional composite materials and nano-reinforced composites lies in the much higher surface area per unit volume of nanofillers with respect to conventional microfillers or microfibres, and in the number of particles embedded in the matrix material for a given filler content. Different classifications of nanocomposite materials can be found in literature. The most common is the one based on the number of characteristic dimensions of the dispersed filler which are in the nanometer range [207, 208]. In this case, nanocomposite materials can be distinguished in three different classes: particulate materials, fibrous materials, and layered materials. The first type is characterized by nanofillers with three dimensions on the order of nanometers, which are referred to as isodimensional nanoparticles (e.g., spherical silica nanoparticles). The second type is characterized by the presence of nanofillers with two dimensions in the nanometer scale, which are commonly referred to as nanotubes or whiskers (e.g., carbon nanotubes or cellulose whiskers). The last class includes materials reinforced with nanofillers characterized by only one characteristic dimension in the nanometer range, which are referred to as platelets (e.g., clay nanoplatelets).

The nanocomposite materials considered in the present study are characterized by a polymer matrix reinforced with clay nanoplatelets. Nanoclays of layered mineral silicates are characterized by a very large surface area and are employed to modify polymer materials, due to their unusual mechanical, electrical, optical, and magnetic properties, their high aspect ratio and cation exchange capacity, their ease of modification and low-cost of production [144,202]. Nanoclays can be classified into several categories based on their chemical composition and morphology. The most

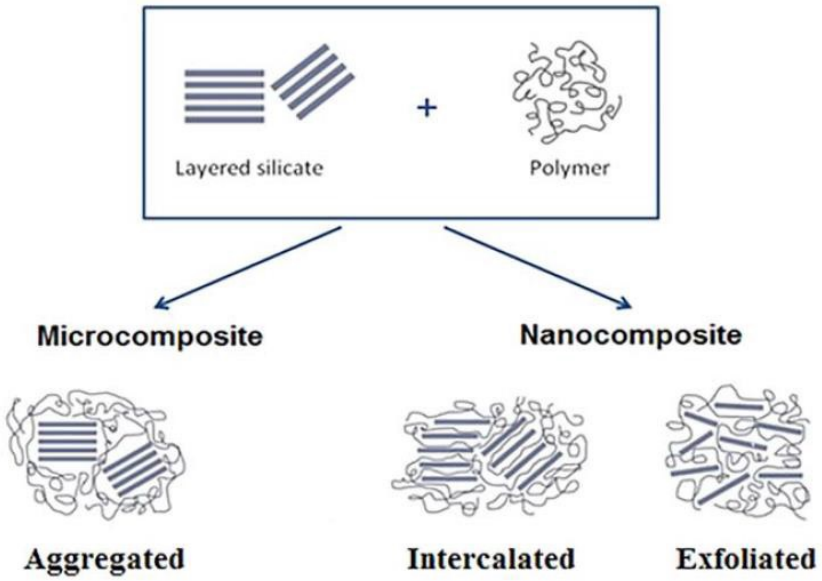

Figure 3.1: Classification of the different nanoclay morphologies in polymer-based nanocomposites. Source: [120].

common types are kaolinite, bentonite, halloysite, hectorite and montmorillonite, which is the one considered in the present study [209].

3.1.1 Structure and morphology of polymer/clay nanocomposites

Montmorillonite (MMT) is widely used in material applications because of its high aspect ratio and high swelling property in polar spaces. Montmorillonite layered crystals are characterized by aspect ratio values ranging from 100 to 1000 and by a thickness on the order of nanometers. The nanoplatelets are bonded parallel together by weak van der Waals (vdW) and electrostatic interactions, and the gaps between the different layers of mineral silicates are referred to as galleries [120]. The silicate layers tend in fact to organize themselves to form stacks characterized by regularly spaced galleries, whose dimension is a function of the crystal structure of the silicate [210]. In the case of dehydrated Na–Montmorillonite, this dimension is approximately 1 [nm] [211]. Analyses of layered silicates reported in literature show that clay minerals can organize themselves in several levels. The smallest particles have dimensions on the order of 10 [nm], and are composed of stacks of parallel lamellae. Microaggregates arise, instead, from the lateral joining of several small particles, whereas aggregates are composed of several small particles and microag-

gregates [210, 212]. Further analyses demonstrate that the large internal surface, typical of small reinforcing elements, induces the particles to agglomerate rather than to disperse homogeneously within the matrix material [213]. A way to improve the dispersion characteristics of reinforcing particles is to render the nanoclay organophilic through ion-exchange reactions induced by the application of cationic-organic surfactants. The surface modification of layered silicates is in fact effective in increasing the interlayer (or gallery) space between clay layers and, consequently, in facilitating the penetration and diffusion of organic species (i.e., polymers or pre-polymers) between them [214]. The capability to exchange ions acquired by layered silicates through surface modification can be quantified by a property referred to as cation exchange capacity (CEC), which is conventionally measured in [cmol_c/kg], or in the older, equivalent units [me/100g] and [meq/100g] [207, 215].

In general, it is possible to identify three types of nanoclay morphologies, depending on the dispersion state of silicate layers and on the extent of polymer penetration between the interlayer spaces. These three different morphologies are referred to as aggregated, intercalated and exfoliated (see Figure 3.1). The presence of one or more of these nanoclay structures within the matrix material is mainly related to the type of clay, the surface modification, the clay content, the type of polymer, the compatibility and degree of interaction between polymer and clay, and the processing technique and conditions [120]. The aggregated morphology is typical of immiscible systems, where the physical attraction and compatibility between the organic polymer and the inorganic silicate are so low that the two materials do not effectively mix and form a nanocomposite, but they separate into discrete phases. In this case, the nanoclay platelets incorporated into the polymer matrix are available in their original stacked status, since polymer chains are unable to penetrate between them. The resulting material is described as a phase-separated composite whose properties are in the same range as those of conventional microparticulate composites. The presence of particle agglomerations leads to severely limited improvements in the overall mechanical properties, inducing instead a reduction in strength and a weakening of the material. On the other hand, when at least a single extended polymer chain penetrates into the gallery space between parallel silicate layers, an interca-

lated morphology is obtained. In this case, the nanocomposite is characterized by a well ordered multilayer structure, where polymer chains alternate with silicate layers, keeping a regular repeat distance between them. The penetration and polymerization of monomers into the gallery space thus improve the dispersion of silicate layers into the polymer matrix [120,210]. The interactions between the two phases at molecular level lead to a modification of the portion of polymer matrix intercalated into the gallery space. Therefore, the properties of the polymer material located in this region are different from those of the bulk matrix, and the same applies to the portion of polymer matrix surrounding the nanoclay layers. In this latter case, the region where these molecular interactions take place is referred to as interphase, and is usually characterized by a thickness of few nanometers and by properties which are different from those of the bulk matrix. The nanoclay morphology which leads to the most significant improvements in terms of mechanical performance is the exfoliated or delaminated one. This particular configuration is found when a full separation of the clay nanoplatelets and their subsequent individual dispersion within the matrix material are obtained. This is the ideal morphology when the best improvements in mechanical properties are to be achieved, since the complete separation and homogeneous dispersion of the nanoplatelets allow the entire surface of the silicate layers to be exposed to the polymer. As a consequence, the interactions between the two constituents are maximized and the number of available reinforcing particles is increased, thus enabling a significant portion of the applied load to be carried by the fillers, thanks to the so called stress transfer mechanism, and facilitating the deflection of cracks [210,216]. Experimental studies reported in literature generally indicate that exfoliated structures mainly induce improvements in terms of tensile modulus (i.e., they act as material stiffeners), whereas intercalated structures are effective in improving the toughness of the material [217]. Due to the high anisotropy of nanoclays, which are characterized by lateral dimensions ranging from 100 to 1000 [nm], and to the consequent difficulty in randomly and homogeneously dispersing them within the polymer matrix, it is not easy to achieve a perfectly exfoliated configuration. Most of the time, in fact, polymer/clay nanocomposites are characterized by a coexistence between intercalated and exfoliated morphologies.

In summary, the description of the main characteristics of the different nanoclay morphologies suggests that the nanocomposite mechanical properties are strongly influenced by the structure of the reinforcing particles and by the quality of their dispersion and distribution within the matrix. In fact, the inhomogeneous dispersion of silicate layers leads to the formation of local aggregates, which negatively affect the mechanical performance of the composite [120]. A key role in the achievement of improved overall mechanical properties is played by the utilized processing technique and conditions. The choice of the method to be employed for nanocomposite production has a strong impact on the performance of the final material, since it influences the miscibility of the blend, the distribution and degree of exfoliation of clay nanoplatelets, and, consequently, the degree of interaction between polymer chains and clay reinforcements [207, 210, 218–220].

3.1.2 Overview of the mechanical properties of polymer/clay nanocomposites

The analysis of the relevant literature generally indicates that the addition of rigid nanoclay fillers, which are naturally resistant to straining due to their high moduli, induces the mechanical restraining of the softer polymer matrix. Moreover, thanks to the stress transfer mechanism, a significant portion of the applied load can be carried by the reinforcing elements, thus resulting in an improvement of the overall mechanical properties of the material. The experimental characterization of polymer/clay nanocomposites reveals that, due to the higher aspect ratio of nanoclay fillers compared to that of regular fillers (e.g., glass fibers), the addition of low concentrations of nanoclays in a polymer matrix results in significant enhancements of the tensile properties of the material in well dispersed conditions [114, 127, 151, 210, 216]. Although most experimental observations confirm the increase of the material stiffness with the incorporation of layered silicates [221–223], contradictory findings have been reported with regard to the overall tensile strength, since the property has proved to be either increased [122, 224] or decreased [122, 168, 225] by the nanomodification, depending on the employed processing method and on the material morphology. The stress and elongation at break depend, in fact, on various factors, such as the interfacial interactions between poly-

mer matrix and clay layers, and the dispersion and exfoliation degree of the reinforcing elements [216]. The experimental studies available in literature demonstrate that the understanding of the effects of the nanomodification on the fracture toughness, ductility and micro-deformation characteristics of polymer matrices is still quite vague, since test results are inconsistent and show different trends of these properties depending on the system under investigation. For example, in [217], it is shown that the intercalation of nanoclay platelets is the main responsible for the enhancement of the fracture toughness, whereas [214] indicates that the toughness is mainly improved by the formation of additional surface areas due to the propagation of cracks. In [226], it is instead demonstrated that the addition of nanoclays affects various fracture mechanisms like crack deflection, crack pinning and plastic deformation, whereas [227] shows that the nanomodification induces a strong enhancement of the fracture toughness of the material, while causing the reduction of its failure strength and strain.

An aspect which is highlighted by various studies is the weakening of the overall mechanical properties of polymer/clay nanocomposites that occurs when the optimum clay content, usually identified to be around 5% wt, where wt refers to the filler weight fraction, is exceeded, due to the formation of various localized agglomerations of nanoclay stacks. Once the saturation point of the nanofiller content is reached, the addition of higher amounts of reinforcing elements causes the deterioration of the overall mechanical properties of the material. The formation of nanoclay agglomerates at high clay contents induces, in fact, the reduction of the tensile modulus and tensile strength, a drop in the elongation at break and fracture toughness values, and the ineffectiveness of the stress transfer at the interface between clay platelets and polymer matrix [202, 225, 228–235]. The filler content value after which the overall mechanical properties of the nanocomposite suddenly drop is strongly related to the features of each individual system, and cannot be represented by a fixed value.

3.2 Experimental characterization of polymer/clay nanocomposites

The aim of this section is to describe the materials employed in the experimental activity, their preparation procedure, and the techniques used for the characterization of their morphological and mechanical properties.

3.2.1 Materials

In the present work, a diglycidyl ether of bisphenol A epoxide (DGEBA, Elan-Tech EC157) and the mixture of cycloapliphatic amines (Elan-Tech W152LR), both supplied by Elantas, were used as polymer matrix. Cloisite®15A, a natural montmorillonite modified with dimethyl dihydrogenated tallow quaternary ammonium salt having a cation exchange capacity (CEC) of 125 [meq/100 g], was purchased by Southern Clay Products and employed for nanomodification. Nanofiller weight fractions of 0%, 1%, 3%, and 5% wt were used to investigate the morphological and mechanical properties of the material as a function of the clay content.

3.2.2 Preparation of epoxy/clay nanocomposites

Dog-bone (DB) specimens were prepared through mechanical dispersion by mixing the epoxy resin with the organically-modified clays. The dispersion process was performed at room temperature under constant mechanical stirring for about 45 minutes. Then, the curing agent (the amine mixture) was added to the blend under mechanical stirring according to the stoichiometric ratio indicated on the supplier's datasheet (3 : 1 = epoxide/amine wt/wt). The mixing was performed for about 40 minutes under mechanical stirring and vacuum. The degassing process was performed by making use of a high vacuum pump in order to reduce the amount of trapped air and, consequently, to avoid the presence of voids in the resin. During the entire mixing process, the reacting blend was cooled to room temperature by an external bath suitable to avoid a possible resin overheating and an increase of blend viscosity (see Figure 3.2). A final degassing phase was carried out for about 10 minutes prior to pouring the blend inside open silicon moulds (see Figure 3.3). The demoulding of the specimens was performed after complete curing at room tem-

Figure 3.2: Mechanical stirring system used for the preparation of the epoxy/clay nanocomposites. The flask containing the reacting mixture was connected to a high vacuum pump system and was cooled by an external bath of cold water.

perature for about 48 hours, and was followed by a post-curing phase during which the specimens were placed in a oven at 60[°C] for 7 hours. Once completely cured, the specimens were polished up to the final thickness.

3.2.3 Characterization techniques

Hydrostatic Weighing

The volumetric mass densities of the different clay-loaded resins were measured by means of a hydrostatic balance. For each material configuration, at least three specimens were tested to obtain statistically representative results.

Figure 3.3: Dog-bone (DB) shaped silicon rubber moulds used for the production of the epoxy/clay nanocomposite samples.

Environmental Scanning Electron Microscopy

The microanalyses of the samples were performed by ESEM (Quanta 200 FEI-XRF embedded). The samples were observed directly on cross sections obtained by brittle fracture at the temperature of liquid nitrogen.

Transmission Electron Microscopy

To study the morphology of the nanomodified polymers, ultrathin sections ($90-100$ [nm]) were obtained by cutting the samples with a Leica Ultracut EM UC7 ultramicrotome, and viewed with a Tecnai G12 (FEI-Thermofisher) transmission electron microscope (TEM) operating at 100 [kV]. Images of the samples morphology were captured with a Veleta (Olympus Soft Imaging System) digital camera.

Tensile Testing

Tensile tests on dog-bone (DB) specimens were carried out taking advantage of a Galdabini SUN2500 universal mechanical testing machine equipped with a 25 [kN] load cell using a crosshead rate equal to 2 [mm/min] (see Figure 3.4). The specimen geometry was chosen according to ISO 527–2 (see Figure 3.5) [236]. For each clay content, at least seven specimens were tested to obtain statistically representative

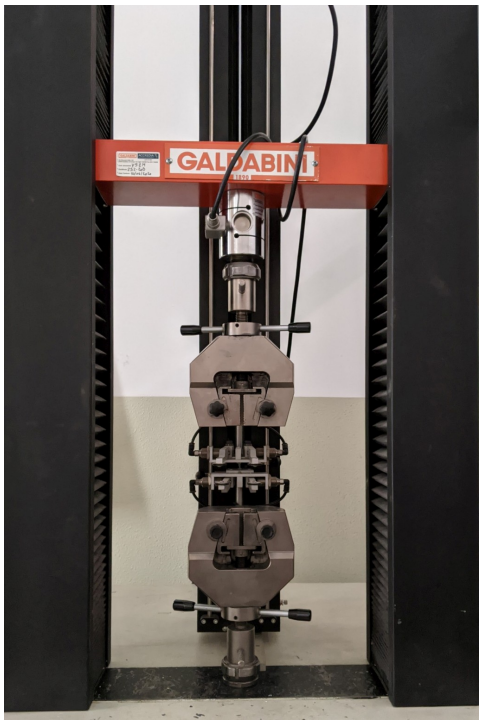

Figure 3.4: Galdabini SUN2500 universal mechanical testing machine employed in the present study to perform the tensile tests.

results. Figure 3.6 shows some of the dog-bone specimens produced in the present study. The different clay-loaded resins are clearly discernible from their characteristic color, since the polymer matrix took on a more and more brownish hue with increasing clay content. Figure 3.7 shows, instead, some of the 1% wt clay-loaded specimens after the performance of the tensile tests. As it is clearly visible from the figure, in almost all of the cases, failure took place in the gauge length of the specimens. The experimental results were rearranged according to ISO 527–2 [236].

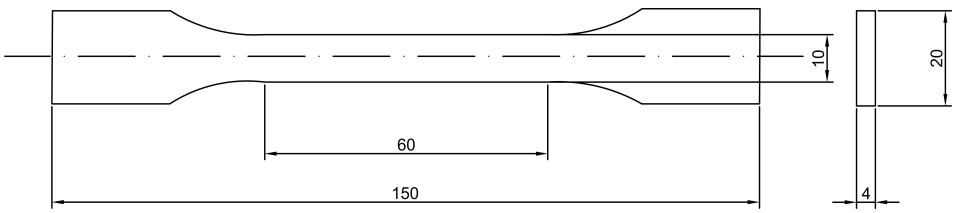

Figure 3.5: Geometry of the dog-bone specimens employed in the tensile tests [236]. All dimensions are expressed in [mm].

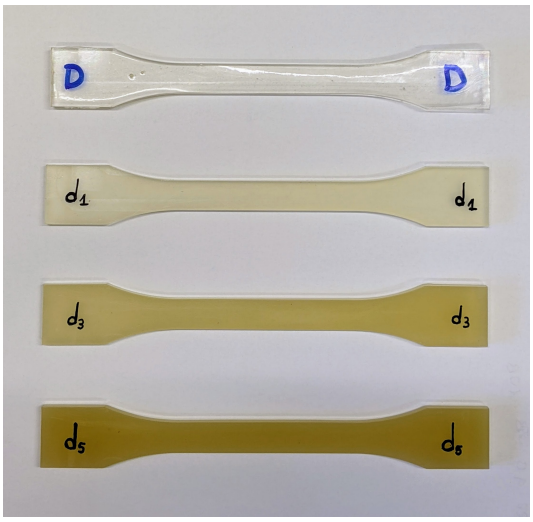

Figure 3.6: Examples of dog-bone specimens with different clay contents manufactured during the present study. From top to bottom: neat epoxy resin, 1%, 3%, and 5% wt clay-loaded resins.

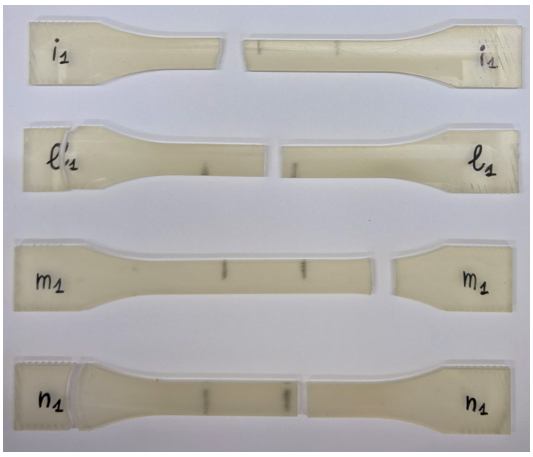

Figure 3.7: Examples of dog-bone specimens composed of 1% wt clay-loaded resin after tensile tests.

3.2.4 Results and discussion

Hydrostatic Weighing

The results of the hydrostatic balance measurements reported in Figure 3.8 clearly show that the addition of clay nanofillers did not remarkably affect the volumetric mass density of the epoxy resin.

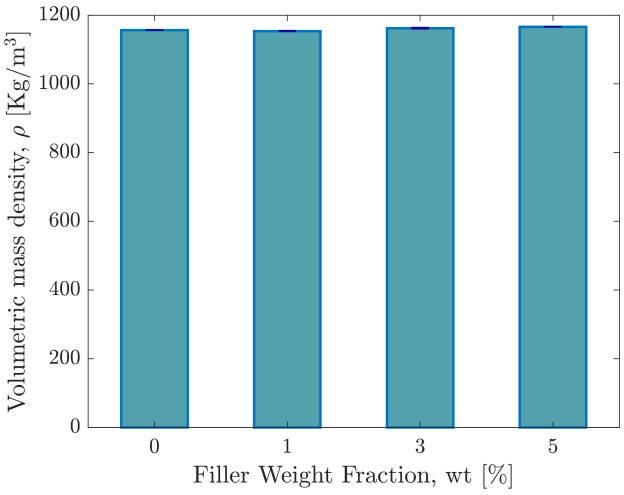

Figure 3.8: Volumetric mass density of the different material configurations tested.

Electron Microscopy

ESEM analyses along brittle fractures of neat epoxy and nanocomposite dog-bone samples containing 1%, 3%, and 5% wt of montmorillonite Cloisite®15A are reported in Figure 3.9. The neat epoxy resin presented a relatively smooth fracture surface indicating brittleness of the fracture behaviour. Even though the roughness of the fracture surfaces of the epoxy/Cloisite®15A nanocomposites increased with higher nanofiller content, they were characterized by the coexistence between regions with a predominantly granular morphology and regions with a prevailingly flake structure, which is an indication of a brittle fracture behaviour. In the case of 1% wt of clay content, an inhomogeneous distribution of nanofillers and the presence of several large agglomerates and microsized clusters were detected. Although the distribution of aggregated structures and agglomerations of nanoclay stacks along the brittle fracture surfaces was observed for all the filler weight fractions considered

in the study, in the nanocomposites with higher clay contents (3% and 5% wt of Cloisite®15A), the distribution of nanoclays was more uniform than that observed in the 1% wt case. The micrographs also showed that the dimensions of the nanoclay agglomerates in the 1% wt-loaded resins were almost comparable to, or, in some cases, even larger than those observed in the 5% wt case, in which the large size of the clusters was a direct consequence of the higher filler weight fraction.

TEM micrographs of the dog-bone samples showed the coexistence between nanofiller-rich regions and resin-rich areas for all the nanoclay contents considered in the study, denoting an inhomogeneous distribution and poor dispersion of the nanofillers within the matrix (see Figure 3.10), as already suggested by the ESEM images reported in Figure 3.9. As for the samples with 1% wt of clay content, TEM analyses showed large clusters of nanoclay aggregates together with some partially intercalated structures (see Figures 3.10a and 3.10b). The presence of both intercalated and phase separated morphologies was identified also in the nanocomposites with higher clay contents, where, however, the dimensions of the microsized clusters were slightly reduced with respect to those observed for the 1% wt case (see Figures 3.10c and 3.10e). Figures 3.10c - 3.10f also showed the presence of some partially exfoliated tactoids containing only a few clay layers and of intercalated structures characterized by a larger interlayer space with respect to that of the aggregate in Figure 3.10b, thus denoting a better dispersion and distribution of nanofillers in the 3% wt and 5% wt cases compared to those of the 1% wt-loaded resins.

All TEM images at high magnification (see Figures 3.10b, 3.10d, and 3.10f) confirmed that nanoclay platelets did not preserve their straight shape when dispersed in the host matrix, as suggested by previous experimental studies conducted on this class of materials [168, 171, 172, 232, 237]. Most of the time, in fact, electron microscopy analyses reveal that the silicate layers dispersed within a polymer blend are characterized by curved or wavy shapes as a result of their inherently high aspect ratio [120].

Tensile Testing

The effect of the clay content on the stiffness of the resulting nanocomposite is depicted in Figure 3.11 in terms of average values and corresponding standard

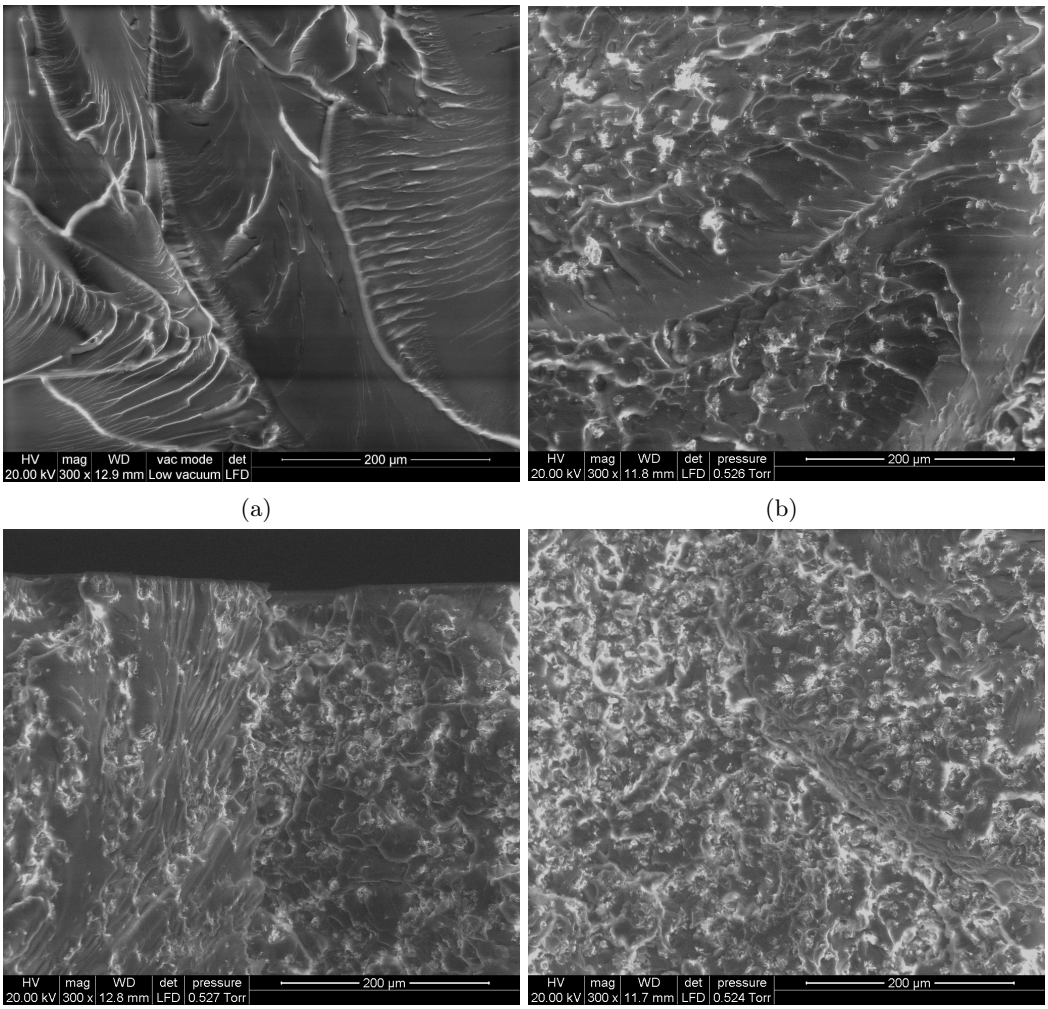

(a) (b)

(c) (d)

Figure 3.9: ESEM micrographs of (a) the neat epoxy resin and the epoxy/Cloisite®15A nanocomposites with (b) 1%, (c) 3%, and (d) 5% wt of clay content at 300 x magnification.

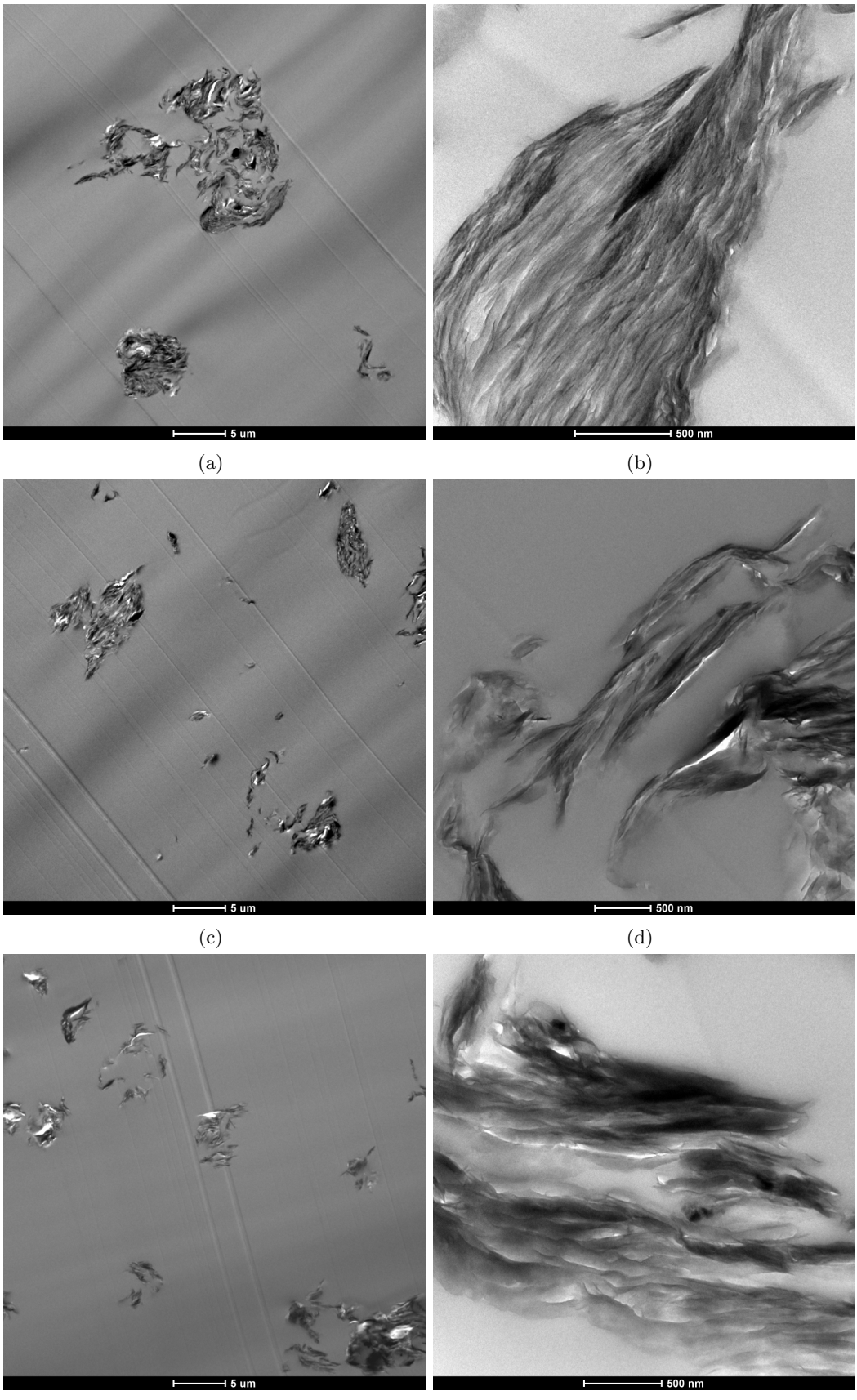

(a) (b)

(c) (d)

(e) (f)

Figure 3.10: TEM images of epoxy/Cloisite®15A nanocomposite samples with 1% wt (a and b), 3% wt (c and d), and 5% wt (e and f) of clay content.

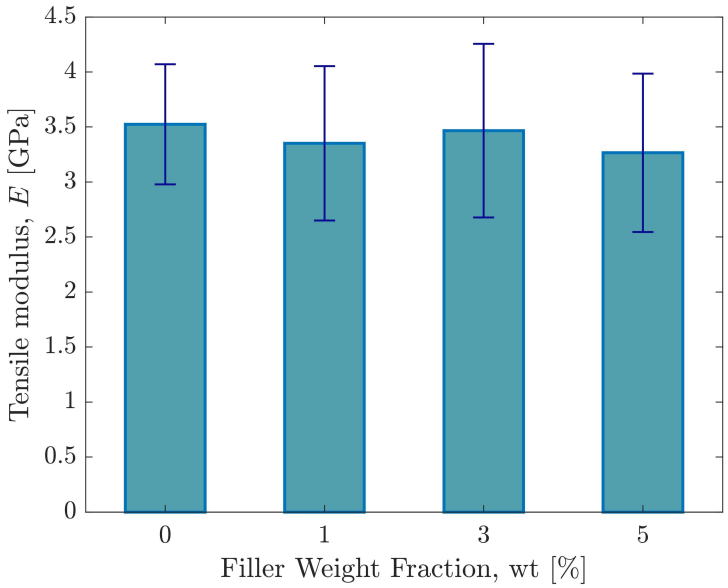

Figure 3.11: Tensile modulus of the neat epoxy resin and the epoxy/Cloisite®15A nanocomposites with 1%, 3%, and 5% wt of clay content obtained from tensile tests. Error bars: ±1 standard deviation.

deviations. The experimental data reported in Figure 3.11 clearly show that the nanomodification of the polymer matrix resulted in a slight decrease in the tensile modulus of the material. In particular, a tensile modulus of 3.50 [GPa] was measured for the unmodified epoxy resin, while a maximum modulus of 3.47 [GPa] was recorded for the nanocomposite samples with 3% wt of clay content, denoting an almost negligible reduction of the overall stiffness with respect to that of the neat epoxy resin. The lowest tensile moduli were measured for clay contents of 1% wt and 5% wt. In the former case, the reason for this kind of behaviour lay in the inhomogeneous distribution of nanoclays and in the presence of large nanoclay aggregates (see Figures 3.9b and 3.10a). As for the latter case, the reduction of the tensile modulus was a consequence of the increase of the nanofiller weight fraction, which caused the formation of various localized agglomerations of nanoclay stacks. Despite the fact that the results reported in Figure 3.11 are quite inconclusive due to the high standard deviations of the collected data, overall they are in agreement with previous experimental studies conducted on this class of materials [232, 234, 238].

3.3 Development of a peridynamics-based computational tool for nanocomposite mechanical properties modelling

In the following, the proposed peridynamics-based RVE approach is presented in detail by discussing the RVE generation process and the procedure adopted to compute the elastic constants to obtain the effective tensile properties of nanocomposite materials. The numerical modelling procedure is focused on the computation of the effective tensile modulus of this class of materials, since this mechanical property represents the fundamental basis for a future numerical analysis of nanocomposite fracture toughness and its dependence on the nanofiller weight content (see Appendix B). In the last part of the section, the newly developed method is validated by comparing the computed results with experimental data reported in literature [168], and its effectiveness and versatility are proved by a further comparison with the experimental data provided in Section 3.2.4.

3.3.1 Peridynamics-based representative volume element approach

In the present study, an RVE homogenization is implemented in a bond-based PD framework to derive the effective tensile modulus of nanocomposite materials. The modelling procedure can be subdivided in different phases as follows:

1. Characterization of the properties of the constituents;
2. Selection and numerical modelling of a suitable RVE;
3. Static analysis implementation;
4. Process of the evaluated reaction forces and computation of the elastic constants to obtain the effective material properties.

In the following, the different steps of the modelling procedure are presented in detail.

Characterization of nanofiller and matrix properties

The first phase of the modelling procedure consists in the characterization of the properties of both nanofiller and matrix materials. Mechanical and geometrical

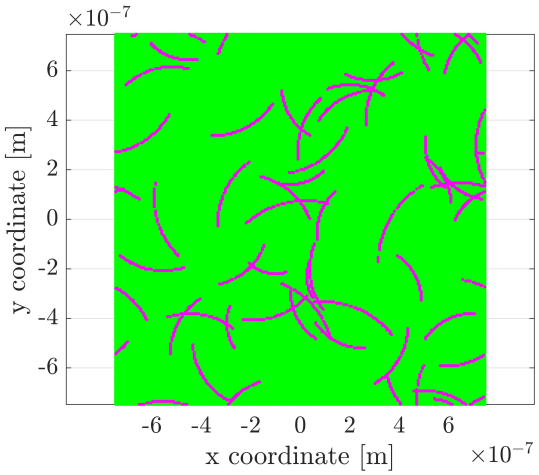

Figure 3.12: Example of a geometrically periodic RVE. The matrix is represented by green nodes, whereas the curved nanoclays are represented by magenta nodes.

properties of the constituents need to be extrapolated from available experimental studies. In the present work, the required data have been partially obtained from an experimental campaign carried out by the authors (see Section 3.2.4) and from experimental investigations reported in literature [168]. However, the determination of nanocomposite properties is rather complex due to the difficulty in measuring material and geometrical properties at the nanoscale and to several processing-induced uncertainties such as inhomogeneous dispersion, non-straight shape, random orientation and formation of various morphologies. In order to take into account the inherently stochastic nature of nanocomposites, in the present work, the nanofillers aspect ratio, curvature and location within the matrix are supposed to be affected by uncertainties and therefore modelled by selecting the most suitable probability distribution functions. Following the suggestions reported in dedicated literature studies [145, 164], the aspect ratio of the nanofillers is modelled by using the Gaussian distribution function, whereas, for the curvature and location of the nanofillers, discrete uniform distributions are used to model the value of each nanofiller arclength and to determine the central node of each nanoplatelet, respectively.

RVE selection and modelling

The properties obtained during the first phase of the modelling procedure are then used as input for the mesoscale analysis, which is performed on an RVE, a

sample which is structurally typical of the whole blend on average [239]. The statistical properties of the nanocomposite are computed by constructing many RVEs, each of them considered as a single realization of the material, and by averaging their results. In order to determine the number of RVEs required to obtain suitable results in terms of effective tensile modulus, it is necessary to analyse its trend as a function of the number of realizations. An example of this procedure is reported in Section 3.3.2. The RVE should contain a sufficient number of inclusions for the overall moduli to be independent of the surface values of traction and displacement, provided that these values are macroscopically uniform [239]. In order to assess whether this requirement is meet or not, a set of numerical simulations is performed by keeping fixed the value of the filler weight fraction and the mechanical and geometrical properties of the constituents while increasing the side length of the RVE. An example of this procedure is presented in Section 3.3.2.

After the selection of the most suitable size, the square RVE domain is discretized into a grid of PD nodes to which different sets of material properties are assigned to simulate the presence of randomly distributed nanofillers within the matrix. A newly developed algorithm allows to model nanofiller curvature. A random aspect ratio and orientation are automatically assigned to each nanofiller during the curvature modelling procedure. The domain is modelled as geometrically periodic: the nanofillers that are cut by any of the edges of the RVE are continued from the opposite edges with the same orientation and curvature. An example of a geometrically periodic RVE obtained through the proposed approach is shown in Figure 3.12. The nanofillers are allowed to overlap to simulate the agglomeration phenomenon and to mimic a three-dimensional environment.

After the allocation of the different node properties, the PD bonds are created. The properties assigned to each bond depend on the nature of the nodes at its ends. Four different types of bonds are defined, i.e., matrix-matrix, nanofiller-nanofiller, matrix-nanofiller (or interphase), and agglomeration bonds. The stiffness of the matrix and the one of the nanofiller, i.e., E_m and E_{nf}, are assigned to the matrix-matrix and nanofiller-nanofiller bonds, respectively, whereas the tensile modulus of the interphase bonds is modelled as a function of the matrix stiffness, i.e.,

$E_{intph} = \kappa_{intph} E_m$, where κ_{intph} is an interphase factor which must be calibrated through available experimental data. The stiffness value assigned to the agglomeration bonds, i.e., the bonds connecting nanofiller-type nodes belonging to different nanoplatelets, is chosen to be equal to the lower between the matrix and interphase tensile moduli, depending on each case study, such as:

$$E_{agglm} = \begin{cases} E_m & \text{if } E_{intph} \geq E_m, \\ E_{intph} & \text{if } E_{intph} < E_m. \end{cases} \tag{3.1}$$

The number of bonds belonging to each of the aforementioned classes is a function of the filler volume fraction, which is referred to as *vol*. In the experimental activity presented in Section 3.2 and, in general, in experimental studies reported in literature, it is preferred to express the nanoclay content in terms of weight fraction. Considering that the numerical method requires in input the filler content in terms of volume fraction, it is possible to convert it exploiting the following relation [144]:

$$vol = \frac{\frac{\text{wt}}{\rho_{nf}}}{\frac{\text{wt}}{\rho_{nf}} + \frac{(1-\text{wt})}{\rho_m}}, \tag{3.2}$$

where ρ_{nf} and ρ_m are the nanofiller and matrix volumetric mass densities, respectively.

Static analysis implementation

After the allocation of the node properties and the creation of the PD bonds, the static analysis implementation is performed. The procedure requires the assembly of the global RVE stiffness matrix and the subsequent application of the boundary conditions. As shown in Figure 3.13, the boundary conditions are imposed on a volume of boundary layers surrounding the RVE domain with a depth equalling the horizon radius. In this way, the surface effect can be eliminated, since all the nodes inside the RVE domain possess a complete horizon. Uniform strain conditions are applied to the RVE by imposing on all the nodes in the external boundary layers displacements which are linear approximations of the boundary displacements. Two sets of uniform displacement boundary conditions are enforced on the RVE in order to compute the required elastic constants of the material, i.e., uniaxial tensile strain

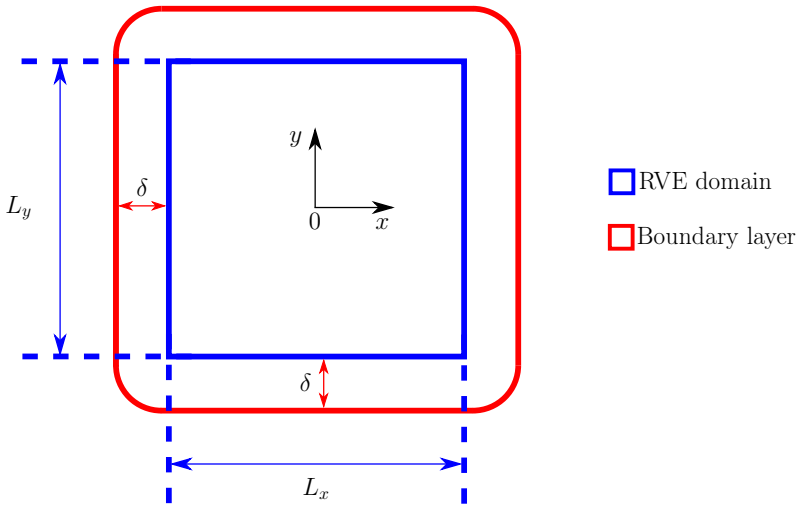

Figure 3.13: Schematic representation of the RVE domain and the external boundary layer considered in the present study.

along x-direction, such that:

$$\begin{cases} \overline{\varepsilon}_{11} \neq 0, \\ \overline{\varepsilon}_{22} = 0, \\ \overline{\varepsilon}_{12} = 0, \end{cases} \tag{3.3}$$

and uniaxial tensile strain along y-direction, such that:

$$\begin{cases} \overline{\varepsilon}_{11} = 0, \\ \overline{\varepsilon}_{22} \neq 0, \\ \overline{\varepsilon}_{12} = 0, \end{cases} \tag{3.4}$$

where $\overline{\varepsilon}_{ij}$ are the components of the average strain tensor. The shear strain condition is not considered in the present study, since the previous two sets of uniform displacement boundary conditions are sufficient to obtain the effective tensile modulus and Poisson's ratio of the material. After the imposition of the boundary conditions, the linear system of equations can be solved to obtain the nodal displacement vector, which is then exploited to compute the external nodal forces, i.e., the 'reactions', since the displacements are imposed.

Estimation of the effective material properties

The computed reaction forces are then processed to evaluate the material elastic constants by exploiting the stress-strain relation for macroscopically isotropic

materials under plane stress conditions (*cf.* (2.21)), such that:

$$\begin{bmatrix} \overline{\sigma}_{11} \\ \overline{\sigma}_{22} \\ \overline{\sigma}_{12} \end{bmatrix} = \frac{E}{1-\nu^2} \begin{bmatrix} 1 & \nu & 0 \\ \nu & 1 & 0 \\ 0 & 0 & 1-\nu \end{bmatrix} \begin{bmatrix} \overline{\varepsilon}_{11} \\ \overline{\varepsilon}_{22} \\ \overline{\varepsilon}_{12} \end{bmatrix} = \begin{bmatrix} a_{11} & a_{12} & 0 \\ a_{21} & a_{22} & 0 \\ 0 & 0 & a_{33} \end{bmatrix} \begin{bmatrix} \overline{\varepsilon}_{11} \\ \overline{\varepsilon}_{22} \\ \overline{\varepsilon}_{12} \end{bmatrix}, \quad (3.5)$$

where $\overline{\sigma}_{ij}$ are the components of the average stress tensor obtained by dividing the sum of the reaction forces at the locations of the applied displacements by the cross-sectional area of the model, E and ν are the effective tensile modulus and Poisson's ratio of the material, respectively, and a_{ij} are the material elastic constants. Substituting (3.3) in (3.5) and exploiting the corresponding computed reaction forces, the elastic constants a_{11} and a_{21} can be obtained by solving the following system of equations:

$$\begin{cases} \overline{\sigma}_{11} = a_{11}\overline{\varepsilon}_{11}, \\ \overline{\sigma}_{22} = a_{21}\overline{\varepsilon}_{11}, \end{cases} \quad (3.6)$$

whereas, substituting (3.4) in (3.5) and exploiting the corresponding computed reaction forces, the elastic constants a_{12} and a_{22} can be obtained by solving the following system of equations:

$$\begin{cases} \overline{\sigma}_{11} = a_{12}\overline{\varepsilon}_{22}, \\ \overline{\sigma}_{22} = a_{22}\overline{\varepsilon}_{22}. \end{cases} \quad (3.7)$$

After the calculation of the required elastic constants, the tensile modulus and Poisson's ratio, for each of the two load cases considered in the study, can be computed as follows:

$$\begin{cases} \nu_{21} = a_{21}/a_{11}, \\ E_{11} = a_{11}\left(1-{\nu_{21}}^2\right), \end{cases} \quad (3.8)$$

where E_{11} and ν_{21} are the tensile modulus and Poisson's ratio obtained by imposing a uniaxial tensile strain along x-direction (*cf.* (3.3)), and

$$\begin{cases} \nu_{12} = a_{12}/a_{22}, \\ E_{22} = a_{22}\left(1-{\nu_{12}}^2\right), \end{cases} \quad (3.9)$$

where E_{22} and ν_{12} are the tensile modulus and Poisson's ratio obtained by imposing a uniaxial tensile strain along y-direction (*cf.* (3.4)). In the case of a macroscopically

homogeneous and isotropic material, the numerically computed elastic constants should satisfy the following conditions:

$$a_{11} \approx a_{22}, \tag{3.10}$$

and

$$a_{21} \approx a_{12}, \tag{3.11}$$

which therefore imply that the numerically computed tensile moduli and Poisson's ratios satisfy the following conditions:

$$\nu_{21} \approx \nu_{12} \approx \nu, \tag{3.12}$$

and, consequently,

$$E_{11} \approx E_{22} \approx E, \tag{3.13}$$

where, as stated before, ν and E represent the effective Poisson's ratio and tensile modulus of the material.

3.3.2 Validation of the PD-based representative volume element approach

Considering that the experimental data reported in Section 3.2.4 are quite inconclusive in terms of overall trend of material tensile modulus with increasing clay content, the first set of experimental data exploited to validate the PD-based approach is the one from [168], where epoxy/Na^+Mt nanocomposites with high degree of exfoliation and uniform distribution were obtained through slurry compounding. For the sake of completeness, the experimental data presented in Section 3.2.4, where epoxy/Cloisite®15A samples with inhomogeneous distribution and poor dispersion of clays were obtained, are then employed to further validate the numerical approach and to assess its versatility. The PD-based model implements an interphase factor κ_{intph} which must be calibrated for each case study to ensure that the properties of the material are properly estimated.

Determination of the suitable RVE size and of the required number of RVE realizations

Before going into the details of the model validation, it is first necessary to briefly illustrate an example of the procedure adopted to define the suitable RVE size and

an example of the strategy exploited to determine the required number of RVE realizations. As for the RVE size, the purpose of the procedure is to identify the minimum RVE side length in correspondence of which the tensile modulus obtained by imposing a uniaxial tensile strain along x-direction, E_{11}, and the one obtained by imposing the same condition along y-direction, E_{22}, are approximately equal (*cf.* (3.13)), i.e., the minimum side length at which the overall moduli turns out to be independent of the surface values of traction and displacement. The fulfilment of this condition implies that the number of inclusions contained in the RVE and their distribution within the model domain are such as to represent a macroscopically uniform and isotropic material. The determination of the RVE size is pursued by performing a set of numerical simulations in which the value of the filler weight fraction and the mechanical and geometrical properties of the constituents are kept fixed while the side length of the square RVE is increased. The model and material input data used to perform the set of simulations are reported in Table 3.1. As for the material input data, the values of ρ_m and E_m are reported in Section 3.2 (see Figures 3.8 and 3.11), the values of ν_m and ν_{nf} are fixed, since plane stress conditions are considered (see Section 1.1.4), while the values of $\mathrm{AR}_{\mathrm{mean}}$, $\mathrm{AR}_{\mathrm{std}}$, E_{nf} and ρ_{nf} are reported in literature [145,240], and on the supplier's datasheet. A test value of $\kappa_{intph} = 0.1$ is used in the simulations. As previously introduced in Section 3.3.1, the condition of uniaxial tensile strain along x-direction is imposed by assigning a value of $\overline{\varepsilon}_{11} = 0.01$ to the 11-component of the average strain tensor (*cf.* (3.3)), whereas the condition of uniaxial tensile strain along y-direction is imposed by assigning a value of $\overline{\varepsilon}_{22} = 0.01$ to the 22-component of the average strain tensor (*cf.* (3.4)). The results of the study, which are reported in Table 3.2, demonstrate that the square RVE should be characterized by a side length of at least 0.6 [μm]. The RVEs with side lengths smaller than this value do not contain a sufficient number of inclusions. In fact, for side lengths smaller than 0.3 [μm], $E_{11} = E_{22} = E_m$, which means that the number of inclusions inside the RVE domain is so low that their presence has no effect on the matrix properties, whereas, for a side length of 0.3 [μm], E_{11} and E_{22} are quite different from each other. In order for the RVEs to contain enough inclusions and to properly simulate the agglomeration phenomena, a side length of

Input data	Value
$\Delta x = \Delta y$	10 [nm]
m	8
E_m	3.5 [GPa]
E_{nf}	178 [GPa]
ρ_m	1156.5 [kg/m^3]
ρ_{nf}	1660 [kg/m^3]
$\nu_m = \nu_{nf}$	1/3
$\mathrm{AR}_{\mathrm{mean}}$	300
$\mathrm{AR}_{\mathrm{std}}$	60
wt	5 [%]
κ_{intph}	0.1

Table 3.1: Input data used in the set of simulations performed to determine the suitable RVE size.

$L_x = L_y = 1.5$ [μm] is considered in all numerical studies presented in the following sections.

As for the required number of RVE realizations, the purpose of the convergence study is to determine the number of RVEs required to obtain suitable results in terms of effective tensile modulus. This is therefore pursued by analysing the trend of the average tensile modulus as a function of the number of realizations. The model and material input data used to perform the convergence study are reported in Table 3.1. An RVE side length of 0.6 [μm] and a test value of $\kappa_{intph} = 0.1$ are considered in the simulations. The condition of uniaxial tensile strain along x-direction is imposed by assigning a value of $\overline{\varepsilon}_{11} = 0.01$ to the 11-component of the average strain tensor (*cf.* (3.3)), whereas the condition of uniaxial tensile strain along y-direction is imposed by assigning a value of $\overline{\varepsilon}_{22} = 0.01$ to the 22-component of the average strain tensor (*cf.* (3.4)). The results of the study, which

$L_x = L_y$ [μm]	$\text{tot}_{\text{nodes}}$	E_{11} [GPa]	E_{22} [GPa]
0.1	100	3.50 ± 0.001	3.50 ± 0.001
0.15	225	3.50 ± 0.050	3.50 ± 0.050
0.3	900	3.33 ± 0.073	3.39 ± 0.155
0.6	3600	3.33 ± 0.048	3.33 ± 0.025
1	10000	3.33 ± 0.015	3.29 ± 0.016
1.5	22500	3.32 ± 0.011	3.30 ± 0.010

Table 3.2: Results of the study performed to determine the suitable RVE size.

are reported in Figure 3.14, demonstrate that the convergence would be guaranteed for approximately 200 realisations with a convergence error of less than 0.08%. In all numerical studies presented in the following sections, each case is therefore averaged over 200 runs.

Epoxy/Na^+Mt nanocomposites prepared through slurry compounding process: High degree of exfoliation and uniform distribution

The selection of this case study is the result of an extensive analysis of the relevant literature aimed at finding experimental data relative to nanocomposites with morphologies, interface properties, dispersion and distribution characteristics different from the ones of the samples produced and characterized during the experimental activity presented in Section 3.2. Differently from what presented in Section 3.2, in [168], the authors carried out an experimental characterization of the mechanical properties of specimens composed by D.E.R.$^{\text{TM}}$ 332, a DGEBA-based epoxy resin from Dow Plastics, nanomodified through the addition of different weight fractions of sodium montmorillonite (PGW) from Nanocor Inc. The processing technique employed by the authors to prepare the nanocomposite samples is the so called slurry compounding technique, which induces a very high degree of exfoliation of the nanoclay platelets and uniform distribution characteristics, as stated in [168] and other literature studies [237, 241].

As previously stated, a side length of $L_x = L_y = 1.5$ [μm] is considered in the

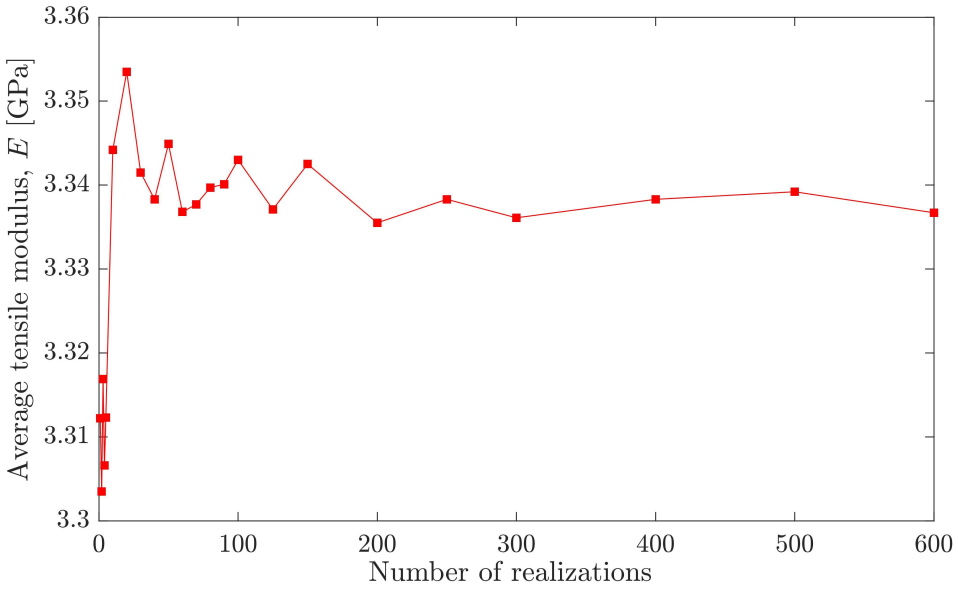

Figure 3.14: Average tensile modulus as a function of RVE realization number.

present study. Moreover, as a result of the convergence study performed in the previous section, in all simulations, each case is averaged over 200 runs, i.e., over 200 RVE realizations. The model and material input data used in the validation procedure are reported in Table 3.3. As for the material input data, the values of E_m, E_{nf}, ρ_m, ρ_{nf}, $\mathrm{AR}_{\mathrm{mean}}$ and $\mathrm{AR}_{\mathrm{std}}$ are reported in literature studies [122, 145, 168, 237, 240], and on the supplier's datasheets, while the values of ν_m and ν_{nf} are fixed, since plane stress conditions are considered (see Section 1.1.4). The condition of uniaxial tensile strain along x-direction is imposed by assigning a value of $\overline{\varepsilon}_{11} = 0.01$ to the 11-component of the average strain tensor (*cf.* (3.3)), whereas the condition of uniaxial tensile strain along y-direction is imposed by assigning a value of $\overline{\varepsilon}_{22} = 0.01$ to the 22-component of the average strain tensor (*cf.* (3.4)). The nanofiller weight fractions considered in the validation procedure are those which were employed in the experimental activity carried out by the authors in [168], i.e., 0%, 1%, 2.5%, 3.5%, and 5% wt of clay content. The model is calibrated to match the experimentally obtained average value of the tensile modulus of the 5% wt clay-loaded samples (see Figure 6 in [168]). The results of the calibration procedure, which are reported in Figure 3.15, show that, for $\kappa_{intph} = 15$, i.e., in the case of a stiff interphase region, the model accurately predicts the tensile modulus value not

Input data	Value
$L_x = L_y$	1.5 [μm]
$\Delta x = \Delta y$	10 [nm]
m	8
E_m	1.96 [GPa]
E_{nf}	178 [GPa]
ρ_m	1160 [kg/m^3]
ρ_{nf}	1980 [kg/m^3]
$\nu_m = \nu_{nf}$	1/3
$\mathrm{AR}_{\mathrm{mean}}$	400
$\mathrm{AR}_{\mathrm{std}}$	70

Table 3.3: Input data used in the first validation procedure.

only for the 5% wt case, but for all the clay contents considered in the study, with a maximum error of about 4%.

As expected, the slurry compounding technique employed to prepare the samples induces a significant enhancement of the effective tensile modulus with increasing filler weight fraction. This overall effect is probably a consequence of the high degree of exfoliation and uniform distribution of nanoclay platelets obtained by using this high-performing processing technique.

Epoxy/Cloisite®15A nanocomposites prepared through mechanical stirring: Poor dispersion and distribution

In order to further validate the capabilities of the PD-based model and to demonstrate its versatility in modelling the effective tensile modulus of polymer/clay nanocomposites characterized by various features, a second validation procedure is performed by exploiting the results of the experimental investigation carried out in Section 3.2. As previously stated, a side length of $L_x = L_y = 1.5$ [μm] is considered in the present study. Moreover, as a result of the aforementioned convergence study,

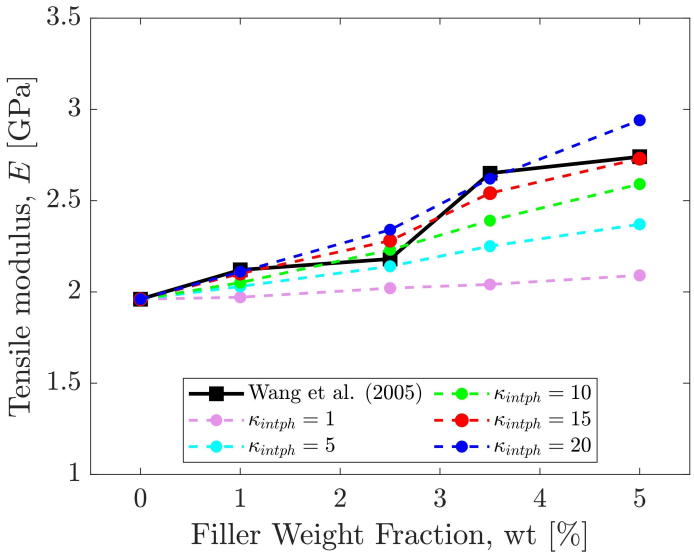

Figure 3.15: Calibration of the model to reproduce the experimental data from [168].

in all simulations, each case is averaged over 200 runs, i.e., over 200 RVE realizations. The model and material input data used in the validation procedure are reported in Table 3.4. As for the material input data, the values of ρ_m and E_m are obtained from the experimental analysis presented in Section 3.2 (see Figures 3.8 and 3.11), the values of ν_m and ν_{nf} are fixed, since plane stress conditions are considered (see Section 1.1.4), while the values of $\mathrm{AR}_{\mathrm{mean}}$, $\mathrm{AR}_{\mathrm{std}}$, E_{nf} and ρ_{nf} are reported in literature [145, 240], and on the supplier's datasheet. The condition of uniaxial tensile strain along x-direction is imposed by assigning a value of $\overline{\varepsilon}_{11} = 0.01$ to the 11-component of the average strain tensor (*cf.* (3.3)), whereas the condition of uniaxial tensile strain along y-direction is imposed by assigning a value of $\overline{\varepsilon}_{22} = 0.01$ to the 22-component of the average strain tensor (*cf.* (3.4)). The nanofiller weight fractions considered in the validation procedure are those which were employed in the experimental activity presented in Section 3.2, i.e., 0%, 1%, 3%, and 5% wt of clay content. The model is calibrated to match the experimentally obtained average value of the tensile modulus of the 5% wt clay-loaded samples (see Figure 3.11). The results of the calibration procedure, reported in Figure 3.16, show that, for $\kappa_{intph} = 0.05$, i.e., in the case of a soft interphase region, the model accurately predicts the average tensile modulus value for the 5% wt case. Furthermore, noting that the experimental value of the tensile modulus for the 1% wt case is lower than expected because of

Input data	Value
$L_x = L_y$	1.5 [μm]
$\Delta x = \Delta y$	10 [nm]
m	8
E_m	3.5 [GPa]
E_{nf}	178 [GPa]
ρ_m	1156.5 [kg/m^3]
ρ_{nf}	1660 [kg/m^3]
$\nu_m = \nu_{nf}$	1/3
$\mathrm{AR}_{\mathrm{mean}}$	300
$\mathrm{AR}_{\mathrm{std}}$	60

Table 3.4: Input data used in the second validation procedure.

weak interfacial adhesion due to the presence of large agglomerated clay stacks, the model properly captures the trend of the average tensile modulus as a function of the clay content (the maximum error is around 3%). As previously stated in Section 3.2, the slightly decreasing trend of the effective tensile modulus of the nanocomposite with increasing clay content is a consequence of the poor dispersion and distribution characteristics of the material, which are themselves caused by the processing technique and conditions employed for the production of the nanocomposite samples. The use of mechanical stirring for the preparation of polymer-based nanocomposites does not lead, in fact, to a complete exfoliation of nanoclay platelets, inducing instead the formation of large aggregated clay structures and agglomerated clay stacks within the polymer matrix.

The results of the two validation procedures are a further confirmation of the fact that the quality of nanofiller dispersion and distribution has a strong influence on the interphase properties and tensile performance of nanocomposites, since the stiffness of materials with poor dispersion and distribution levels and, therefore, characterized

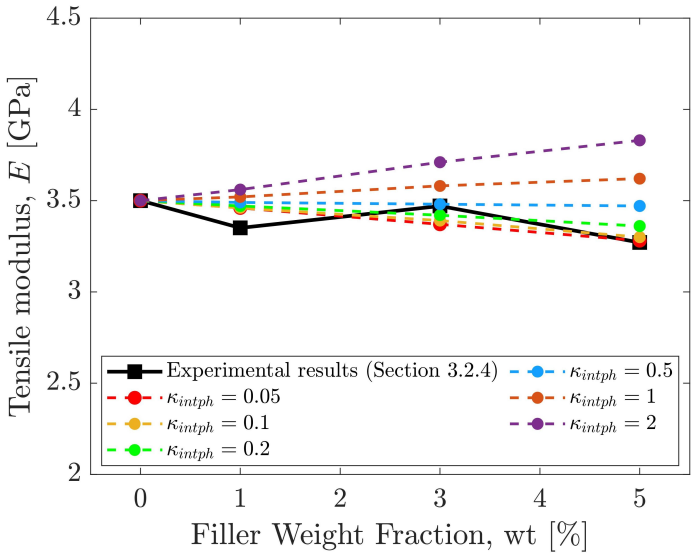

Figure 3.16: Calibration of the model to reproduce the experimental data from Section 3.2.4.

by a soft interphase region, is only slightly affected by nanomodification, whereas in the case of high degree of exfoliation and good distribution characteristics, the materials present a stiff interphase region and an upward trend of the stiffness with increasing clay content.

The results presented in this section allow for the conclusion that the proposed numerical method has the capability to model randomly distributed nanofillers with different sizes, shapes, and orientations, and that it is capable of easily simulating interphase regions characterized by different properties, including both strong and weak interfacial adhesion, and nanofiller agglomeration phenomena. Thanks to these features, the tensile modulus of nanocomposites with various characteristics, resulting from the employment of different processing techniques and conditions, can be accurately reproduced.

Chapter 4

Conclusions and future developments

Analysis of the overall equilibrium in the coupling of peridynamics and classical continuum mechanics

As reported in [9], the work presented in Chapter 2 concerned the coupling of peridynamics and classical continuum mechanics, focusing on an error given by the lack of overall equilibrium in static problems. This coupling error has been overlooked in the literature. Theoretical analyses describing the reason for the appearance of this spurious effect have been provided together with supporting numerical simulations. While this investigation considered a particular strategy to couple peridynamics and classical continuum mechanics, proposed in [84, 112], this issue most probably affects other coupling approaches. It is observed that a lack of overall equilibrium may occur even if the coupling method satisfies the usual numerical tests for static problems, given by rigid body motions as well as uniform and linear strain distributions. The theoretical analyses and the supporting numerical simulations allow for the conclusion that:

- The out-of-balance forces are related to the order of the derivatives of displacements in the coupling zone;

- It is easy to evaluate the magnitude of the out-of-balance error by computing the reaction forces;

- In the numerical examples presented in Chapter 2, the relative out-of-balance error is a fraction of a percent and reduces as $\delta \to 0$;
- It is usually possible to reduce the out-of-balance error by moving the coupling interface away from regions of high gradients of displacements;
- The two-dimensional numerical examples presented in Section 2.6.2 suggest that the shape of the coupling interface may have a significant impact on the overall out-of-balance error: corners in the coupling interface can introduce additional out-of-balance contributions.

The impacts of these findings on coupled simulations are twofold. First, the tolerance used in an implicit solution of a coupled computational problem should be carefully chosen: if the tolerance is smaller than the out-of-balance forces, then the computation will not converge. Second, the proper location and shape of the coupling interface in a computational problem can be defined by using an adaptive approach to convert FEM nodes into PD nodes. The use of adaptivity, focused on controlling the out-of-balance error, can reduce the computational effort considerably with respect to that required by a fully peridynamic simulation, and will pave the way to future applications of the coupling of peridynamics and classical continuum mechanics to the solution of many practical problems [9]. Some of the possible future works which can then be carried out on the basis of the outcomes of the aforementioned studies are summarised as follows:

- Extension of the theoretical and numerical analyses of the consistency between linear bond-based PD and CCM models to three-dimensional cases;
- Extension of the theoretical analysis of the balance between local and nonlocal tractions at coupling interfaces to two-dimensional CCM-PD coupled systems characterized by non-straight coupling interfaces and to three-dimensional CCM-PD coupled models;
- Further extension of the out-of-balance analysis focused on controlling the relative out-of-balance error by optimizing the shape of the coupling interfaces in two-dimensional and three-dimensional CCM-PD coupled systems.

Numerical modelling of nanocomposite mechanical properties

In the work presented in Chapter 3, peridynamics has been exploited to model the tensile modulus of nanocomposite materials. The investigation has been particularly focused on polymer-based matrices nanomodified through the addition of nanoclay platelets, a class of materials which has recently attracted the interest of the academic and industrial communities due to its enhanced mechanical, thermal, and barrier properties, and to its wide range of applications, especially in the aerospace, automotive, and construction fields. The mesoscale representative volume element approach developed in Chapter 3 has proved to be well suited for the study of nanocomposite materials, due to the intrinsic capability of peridynamics to handle material discontinuities, thus allowing for the incorporation of different materials and for the modelling of interphase regions without the need of any special treatments. The newly developed strategy has shown to be capable of simulating randomly distributed nanofillers with different sizes and orientations, and of modelling interphase regions characterized by different properties, and nanofiller agglomeration phenomena. The proposed computational tool has been validated by exploiting experimental data available in literature, and by performing an experimental characterization of clay-loaded epoxy resins. The numerical simulations and the supporting experimental activities allow for the conclusion that:

- The effective tensile modulus of polymer-based nanocomposites is significantly affected by the characteristics of the interphase region. The tensile modulus of nanocomposites with various features, resulting from the employment of different preparation techniques and processing conditions, can be accurately reproduced by the proposed numerical method by implementing an interphase factor which must be calibrated to simulate weak, soft, or stiff interphase regions;

- Interphase regions and agglomeration phenomena can be easily simulated by tuning the properties of the peridynamic bonds;

- The non-straight shape of clay nanofillers is clearly discernible from electron

microscopy images, and can be numerically reproduced by assigning a random arclength and radius of curvature to each nanoplatelet during the modelling procedure.

Some of the possible future activities which can then be carried out on the basis of the outcomes of the work presented in Chapter 3 are summarised as follows:

- Extension of the PD-based RVE approach to the shear strain condition and to three-dimensional problems;
- Application of the effective tensile moduli obtained through the mesoscale RVE analysis as input parameters for a numerical method focused on the modelling of crack nucleation and propagation in nanocomposites. This could be pursued by developing a CCM-PD coupling-based strategy, in order to increase the computational efficiency of the method, and to facilitate the imposition of boundary conditions, avoiding the need for external boundary layers;
- Use of the results obtained in the present study as a starting point for the numerical investigation of the effect of the nanomodification on the fracture toughness of nanocomposite materials, and subsequent exploitation of the experimental data reported in Appendix B to validate the computed results;
- Extension of the study to multiphysics problems involving diffusion phenomena, i.e., permeability and corrosion, to pave the way to the application of polymer/clay nanocomposites as gas barrier materials;
- Implementation of peridynamics-based multiscale simulations and performance of further experimental activities to investigate the effects of ageing on the tensile and fracture properties of polymer-based nanocomposites.

Bibliography

[1] W. Noll. A new mathematical theory of simple materials. In: *The foundations of mechanics and thermodynamics*, pp. 243–292, Springer, 1974.

[2] N.E. Prasad, R.J.H. Wanhill. *Aerospace Materials and Material Technologies: Volume 2: Aerospace Material Technologies*, Springer, 2016.

[3] T.L. Anderson. *Fracture Mechanics: Fundamentals and Applications*, CRC Press, 2017.

[4] J.-W. Simon, D. Höwer, B. Stier, S. Reese, J. Fish. A regularized orthotropic continuum damage model for layered composites: intralaminar damage progression and delamination. *Computational Mechanics*, 60(3):445–463, 2017.

[5] V.P. Nguyen, C.T. Nguyen, S. Bordas, A. Heidarpour. Modelling interfacial cracking with non-matching cohesive interface elements. *Computational Mechanics*, 58(5):731–746, 2016.

[6] I. Kaleel, M. Petrolo, A.M. Waas, E. Carrera. Micromechanical progressive failure analysis of fiber-reinforced composite using refined beam models. *Journal of Applied Mechanics*, 85(2):021004, 2018.

[7] S.A. Silling. Reformulation of elasticity theory for discontinuities and long-range forces. *Journal of the Mechanics and Physics of Solids*, 48(1):175–209, 2000.

[8] F. Bobaru, J.T. Foster, P.H. Geubelle, S.A. Silling. *Handbook of Peridynamic Modeling*, CRC Press, 2016.

[9] G. Ongaro, P. Seleson, U. Galvanetto, T. Ni, M. Zaccariotto. Overall equilibrium in the coupling of peridynamics and classical continuum mechanics. *Computer Methods in Applied Mechanics and Engineering*, 381:113515, 2021, https://doi.org/10.1016/j.cma.2020.113515.

[10] J.M. Melenk, I. Babuška. The partition of unity finite element method: Basic theory and applications. *Computer Methods in Applied Mechanics and Engineering*, 139(1-4):289–314, 1996.

[11] I. Babuška, J.M. Melenk. The partition of unity method. *International Journal for Numerical Methods in Engineering*, 40(4):727–758, 1997.

[12] N. Moës, J. Dolbow, T. Belytschko. A finite element method for crack growth without remeshing. *International Journal for Numerical Methods in Engineering*, 46(1):131–150, 1999.

[13] T. Belytschko, T. Black. Elastic crack growth in finite elements with minimal remeshing. *International Journal for Numerical Methods in Engineering*, 45(5):601–620, 1999.

[14] G.R. Johnson, R.A. Stryk. Eroding interface and improved tetrahedral element algorithms for high-velocity impact computations in three dimensions. *International Journal of Impact Engineering*, 5(1-4):411–421, 1987.

[15] T. Belytschko, J.I. Lin. A three-dimensional impact-penetration algorithm with erosion. *International Journal of Impact Engineering*, 5(1-4):111–127, 1987.

[16] C. Kuhn, R. Müller. A phase field model for fracture. In: *PAMM: Proceedings in Applied Mathematics and Mechanics*, Vol. 8, pp. 10223–10224, Wiley Online Library, 2008.

[17] H. Amor, J.-J. Marigo, C. Maurini. Regularized formulation of the variational brittle fracture with unilateral contact: Numerical experiments. *Journal of the Mechanics and Physics of Solids*, 57(8):1209–1229, 2009.

[18] J. Donnini, G. Lancioni, V. Corinaldesi. Failure modes in FRCM systems with dry and pre-impregnated carbon yarns: Experiments and modeling. *Composites Part B: Engineering*, 140:57–67, 2018.

[19] J. Donnini, G. Chiappini, G. Lancioni, V. Corinaldesi. Tensile behaviour of glass FRCM systems with fabrics' overlap: Experimental results and numerical modeling. *Composite Structures*, 212:398–411, 2019.

[20] M. Ortiz, Y. Leroy, A. Needleman. A finite element method for localized failure analysis. *Computer Methods in Applied Mechanics and Engineering*, 61(2):189–214, 1987.

[21] X.-P. Xu, A. Needleman. Void nucleation by inclusion debonding in a crystal matrix. *Modelling and Simulation in Materials Science and Engineering*, 1(2):111, 1993.

[22] X.-P. Xu, A. Needleman. Numerical simulations of fast crack growth in brittle solids. *Journal of the Mechanics and Physics of Solids*, 42(9):1397–1434, 1994.

[23] G. Zi, T. Rabczuk, W. Wall. Extended meshfree methods without branch enrichment for cohesive cracks. *Computational Mechanics*, 40(2):367–382, 2007.

[24] J.-H. Song, H. Wang, T. Belytschko. A comparative study on finite element methods for dynamic fracture. *Computational Mechanics*, 42(2):239–250, 2008.

[25] F. Bobaru, G. Zhang. Why do cracks branch? A peridynamic investigation of dynamic brittle fracture. *International Journal of Fracture*, 196(1-2):59–98, 2015.

[26] T. Rabczuk. Computational methods for fracture in brittle and quasi-brittle solids: state-of-the-art review and future perspectives. *ISRN Applied Mathematics*, 2013.

[27] B. Bourdin, C.J. Larsen, C.L. Richardson. A time-discrete model for dynamic fracture based on crack regularization. *International journal of fracture*, 168(2):133–143, 2011.

[28] M.J. Borden, C.V. Verhoosel, M.A. Scott, T.J.R. Hughes, C.M. Landis. A phase-field description of dynamic brittle fracture. *Computer Methods in Applied Mechanics and Engineering*, 217:77–95, 2012.

[29] M. Hofacker, C. Miehe. A phase field model of dynamic fracture: Robust field updates for the analysis of complex crack patterns. *International Journal for Numerical Methods in Engineering*, 93(3):276–301, 2013.

[30] R. Spatschek, E. Brener, A. Karma. Phase field modeling of crack propagation. *Philosophical Magazine*, 91(1):75–95, 2011.

[31] G.T. Camacho, M. Ortiz. Computational modelling of impact damage in brittle materials. *International Journal of solids and structures*, 33(20-22):2899–2938, 1996.

[32] M. Ortiz, A. Pandolfi. Finite-deformation irreversible cohesive elements for three-dimensional crack-propagation analysis. *International journal for numerical methods in engineering*, 44(9):1267–1282, 1999.

[33] S.A. Silling, M. Epton, O. Weckner, J. Xu, E. Askari. Peridynamic states and constitutive modeling. *Journal of Elasticity*, 88(2):151–184, 2007.

[34] A.C. Eringen, D.G.B. Edelen. On nonlocal elasticity. *International Journal of Engineering Science*, 10(3):233–248, 1972.

[35] A.C. Eringen. Line crack subject to shear. *International Journal of Fracture*, 14(4):367–379, 1978.

[36] I.A. Kunin. *Elastic Media with Microstructure I: One-Dimensional Models*, Vol. 26, Springer-Verlag Berlin Heidelberg, 1982.

[37] I.A. Kunin. *Elastic Media with Microstructure II: Three-Dimensional Models*, Springer-Verlag Berlin Heidelberg, 1983.

[38] F. Bobaru, W. Hu. The meaning, selection, and use of the peridynamic horizon and its relation to crack branching in brittle materials. *International journal of fracture*, 176(2):215–222, 2012.

[39] E. Askari, F. Bobaru, R.B. Lehoucq, M.L. Parks, S.A. Silling, O. Weckner. Peridynamics for multiscale materials modeling. In: *Journal of Physics: Conference Series*, Vol. 125, p. 012078, IOP Publishing, 2008.

[40] E. Madenci, S. Oterkus. Ordinary state-based peridynamics for plastic deformation according to von Mises yield criteria with isotropic hardening. *Journal of the Mechanics and Physics of Solids*, 86:192–219, 2016.

[41] Y. Wang, X. Zhou, M. Kou. Peridynamic investigation on thermal fracturing behavior of ceramic nuclear fuel pellets under power cycles. *Ceramics International*, 44(10):11512–11542, 2018.

[42] S. Bazazzadeh, F. Mossaiby, A. Shojaei. An adaptive thermo-mechanical peridynamic model for fracture analysis in ceramics. *Engineering Fracture Mechanics*, 223:106708, 2020.

[43] N. Zhu, D. De Meo, E. Oterkus. Modelling of granular fracture in polycrystalline materials using ordinary state-based peridynamics. *Materials*, 9(12):977, 2016.

[44] W. Gerstle, N. Sau, S. Silling. Peridynamic modeling of concrete structures. *Nuclear engineering and design*, 237(12-13):1250–1258, 2007.

[45] B. Kilic, A. Agwai, E. Madenci. Peridynamic theory for progressive damage prediction in center-cracked composite laminates. *Composite Structures*, 90(2):141–151, 2009.

[46] W. Hu, Y.D. Ha, F. Bobaru. Peridynamic model for dynamic fracture in unidirectional fiber-reinforced composites. *Computer Methods in Applied Mechanics and Engineering*, 217:247–261, 2012.

[47] E. Askari, J. Xu, S. Silling. Peridynamic analysis of damage and failure in composites. In: *44th AIAA aerospace sciences meeting and exhibit*, p. 88, 2006.

[48] E. Oterkus, E. Madenci. Peridynamic analysis of fiber-reinforced composite materials. *Journal of Mechanics of Materials and Structures*, 7(1):45–84, 2012.

[49] K. Zhang, T. Ni, G. Sarego, M. Zaccariotto, Q. Zhu, U. Galvanetto. Experimental and numerical fracture analysis of the plain and polyvinyl alcohol fiber-reinforced ultra-high-performance concrete structures. *Theoretical and Applied Fracture Mechanics*, 108:102566, 2020.

[50] J. Zhan, X. Yao, F. Han, X. Zhang. A rate-dependent peridynamic model for predicting the dynamic response of particle reinforced metal matrix composites. *Composite Structures*, 263:113673, 2021.

[51] S.A. Silling, E. Askari. A meshfree method based on the peridynamic model of solid mechanics. *Computers & Structures*, 83(17-18):1526–1535, 2005.

[52] J. Xu, A. Askari, O. Weckner, S. Silling. Peridynamic analysis of impact damage in composite laminates. *Journal of Aerospace Engineering*, 21(3):187–194, 2008.

[53] S.A. Silling, A. Askari. Peridynamic model for fatigue cracking. *SAND2014-18590. Albuquerque: Sandia National Laboratories*, 2014.

[54] S.A. Silling. Dynamic fracture modeling with a meshfree peridynamic code. In: *Computational Fluid and Solid Mechanics 2003*, pp. 641–644, Elsevier, 2003.

[55] Y.D. Ha, F. Bobaru. Characteristics of dynamic brittle fracture captured with peridynamics. *Engineering Fracture Mechanics*, 78(6):1156–1168, 2011.

[56] A. Shojaei, F. Mossaiby, M. Zaccariotto, U. Galvanetto. An adaptive multigrid peridynamic method for dynamic fracture analysis. *International Journal of Mechanical Sciences*, 144:600–617, 2018.

[57] A. Shojaei, T. Mudric, M. Zaccariotto, U. Galvanetto. A coupled meshless finite point/Peridynamic method for 2D dynamic fracture analysis. *International Journal of Mechanical Sciences*, 119:419–431, 2016.

[58] F. Bobaru, M. Duangpanya. The peridynamic formulation for transient heat conduction. *International Journal of Heat and Mass Transfer*, 53(19-20):4047–4059, 2010.

[59] F. Bobaru, M. Duangpanya. A peridynamic formulation for transient heat conduction in bodies with evolving discontinuities. *Journal of Computational Physics*, 231(7):2764–2785, 2012.

[60] J. Zhao, Z. Chen, J. Mehrmashhadi, F. Bobaru. Construction of a peridynamic model for transient advection-diffusion problems. *International Journal of Heat and Mass Transfer*, 126:1253–1266, 2018.

[61] A. Shojaei, A. Hermann, P. Seleson, C.J. Cyron. Dirichlet absorbing boundary conditions for classical and peridynamic diffusion-type models. *Computational Mechanics*, 66(4):773–793, 2020.

[62] S. Jafarzadeh, A. Larios, F. Bobaru. Efficient solutions for nonlocal diffusion problems via boundary-adapted spectral methods. *Journal of Peridynamics and Nonlocal Modeling*, pp. 1–26, 2020.

[63] Z. Chen, F. Bobaru. Peridynamic modeling of pitting corrosion damage. *Journal of the Mechanics and Physics of Solids*, 78:352–381, 2015.

[64] S. Jafarzadeh, Z. Chen, F. Bobaru. Peridynamic modeling of intergranular corrosion damage. *Journal of The Electrochemical Society*, 165(7):C362, 2018.

[65] S. Bazazzadeh, M. Morandini, M. Zaccariotto, U. Galvanetto. Simulation of chemo-thermo-mechanical problems in cement-based materials with peridynamics. *Meccanica*, 56:2357–2379, 2021.

[66] S. Jafarzadeh, Z. Chen, S. Li, F. Bobaru. A peridynamic mechano-chemical damage model for stress-assisted corrosion. *Electrochimica Acta*, 323:134795, 2019.

[67] T. Ni, F. Pesavento, M. Zaccariotto, U. Galvanetto, Q.-Z. Zhu, B.A. Schrefler. Hybrid FEM and peridynamic simulation of hydraulic fracture propagation in saturated porous media. *Computer Methods in Applied Mechanics and Engineering*, 366:113101, 2020.

[68] V. Diana, V. Carvelli. An electromechanical micropolar peridynamic model. *Computer Methods in Applied Mechanics and Engineering*, 365:112998, 2020.

[69] P. Diehl, S. Prudhomme, M. Lévesque. A review of benchmark experiments for the validation of peridynamics models. *Journal of Peridynamics and Nonlocal Modeling*, 1(1):14–35, 2019.

[70] S.A. Silling, O. Weckner, E. Askari, F. Bobaru. Crack nucleation in a peridynamic solid. *International Journal of Fracture*, 162(1-2):219–227, 2010.

[71] B. Kilic, E. Madenci. An adaptive dynamic relaxation method for quasi-static simulations using the peridynamic theory. *Theoretical and Applied Fracture Mechanics*, 53(3):194–204, 2010.

[72] A. Agwai, I. Guven, E. Madenci. Predicting crack propagation with peridynamics: a comparative study. *International Journal of Fracture*, 171(1):65, 2011.

[73] M. Zaccariotto, U. Galvanetto. Peridynamic and cohesive zone model approaches for crack propagation modelling. *21st AIDAA Congress*, 2011.

[74] F. Luongo, M. Zaccariotto, U. Galvanetto. Static implementation of peridynamics for the simulation of crack propagation. *The 19th ICCM*, 2013.

[75] D. Dipasquale, M. Zaccariotto, U. Galvanetto. Crack propagation with adaptive grid refinement in 2D peridynamics. *International Journal of Fracture*, 190(1-2):1–22, 2014.

[76] M. Zaccariotto, F. Luongo, G. Sarego, U. Galvanetto. Examples of applications of the peridynamic theory to the solution of static equilibrium problems. *The Aeronautical Journal*, 119(1216):677–700, 2015.

[77] Y.D. Ha, F. Bobaru. Studies of dynamic crack propagation and crack branching with peridynamics. *International Journal of Fracture*, 162(1-2):229–244, 2010.

[78] B. Ren, C.T. Wu, P. Seleson, D. Zeng, D. Lyu. A peridynamic failure analysis of fiber-reinforced composite laminates using finite element discontinuous Galerkin approximations. *International Journal of Fracture*, 214(1):49–68, 2018.

[79] B. Aksoylu, M.L. Parks. Variational theory and domain decomposition for nonlocal problems. *Applied Mathematics and Computation*, 217(14):6498–6515, 2011.

[80] Q. Du, M. Gunzburger, R.B. Lehoucq, K. Zhou. A nonlocal vector calculus, nonlocal volume-constrained problems, and nonlocal balance laws. *Mathematical Models and Methods in Applied Sciences*, 23(03):493–540, 2013.

[81] P. Seleson, M. Gunzburger, M.L. Parks. Interface problems in nonlocal diffusion and sharp transitions between local and nonlocal domains. *Computer Methods in Applied Mechanics and Engineering*, 266:185–204, 2013.

[82] F. Scabbia, M. Zaccariotto, U. Galvanetto. A novel and effective way to impose boundary conditions and to mitigate the surface effect in state-based Peridynamics. *International Journal for Numerical Methods in Engineering*, 122(20):5773–5811, 2021.

[83] Q.V. Le, F. Bobaru. Surface corrections for peridynamic models in elasticity and fracture. *Computational Mechanics*, 61:499–518, 2018.

[84] M. Zaccariotto, T. Mudric, D. Tomasi, A. Shojaei, U. Galvanetto. Coupling of FEM meshes with Peridynamic grids. *Computer Methods in Applied Mechanics and Engineering*, 330:471–497, 2018.

[85] A. Pagani, E. Carrera. Coupling three-dimensional peridynamics and high-order one-dimensional finite elements based on local elasticity for the linear static analysis of solid beams and thin-walled reinforced structures. *International Journal for Numerical Methods in Engineering*, 121(22):5066–5081, 2020.

[86] M. Zaccariotto, A. Shojaei, U. Galvanetto. Coupling of CCM and PD in a meshless way. In: *Peridynamic Modeling, Numerical Techniques, and Applications*, pp. 113–138, Elsevier, 2021.

[87] A. Pagani, M. Enea, E. Carrera. Quasi-static fracture analysis by coupled three-dimensional peridynamics and high order one-dimensional finite ele-

ments based on local elasticity. *International Journal for Numerical Methods in Engineering*, 2021, https://doi.org/10.1002/nme.6890.

[88] X. Chen, M. Gunzburger. Continuous and discontinuous finite element methods for a peridynamics model of mechanics. *Computer Methods in Applied Mechanics and Engineering*, 200(9-12):1237–1250, 2011.

[89] O.C. Zienkiewicz, R.L. Taylor, D.D. Fox. *The Finite Element Method for Solid and Structural Mechanics*, Butterworth-Heinemann, 2014.

[90] M. D'Elia, P.B. Bochev. Optimization-based coupling of nonlocal and local diffusion models. In: *Proceedings of the Fall 2014 Materials Research Society Meeting*, MRS Symposium Proceedings, Boston, MA, Cambridge University Press, November 2014.

[91] M. D'Elia, P. Bochev. Formulation, analysis and computation of an optimization-based local-to-nonlocal coupling method. *Results in Applied Mathematics*, 9:100129, 2021.

[92] M. D'Elia, M. Perego, P. Bochev, D. Littlewood. A coupling strategy for nonlocal and local diffusion models with mixed volume constraints and boundary conditions. *Computers & Mathematics with Applications*, 71(11):2218–2230, 2016.

[93] Y. Yu, F.F. Bargos, H. You, M.L. Parks, M.L. Bittencourt, G.E. Karniadakis. A partitioned coupling framework for peridynamics and classical theory: Analysis and simulations. *Computer Methods in Applied Mechanics and Engineering*, 340:905–931, 2018.

[94] H. You, Y. Yu, D. Kamensky. An asymptotically compatible formulation for local-to-nonlocal coupling problems without overlapping regions. *Computer Methods in Applied Mechanics and Engineering*, 366:113038, 2020.

[95] F. Han, G. Lubineau. Coupling of nonlocal and local continuum models by the Arlequin approach. *International Journal for Numerical Methods in Engineering*, 89(6):671–685, 2012.

[96] G. Lubineau, Y. Azdoud, F. Han, C. Rey, A. Askari. A morphing strategy to couple non-local to local continuum mechanics. *Journal of the Mechanics and Physics of Solids*, 60(6):1088–1102, 2012.

[97] Y. Azdoud, F. Han, G. Lubineau. A morphing framework to couple non-local and local anisotropic continua. *International Journal of Solids and Structures*, 50(9):1332–1341, 2013.

[98] Y. Azdoud, F. Han, G. Lubineau. The morphing method as a flexible tool for adaptive local/non-local simulation of static fracture. *Computational Mechanics*, 54(3):711–722, 2014.

[99] F. Han, G. Lubineau, Y. Azdoud, A. Askari. A morphing approach to couple state-based peridynamics with classical continuum mechanics. *Computer Methods in Applied Mechanics and Engineering*, 301:336–358, 2016.

[100] Q. Du, X.H. Li, J. Lu, X. Tian. A quasi-nonlocal coupling method for nonlocal and local diffusion models. *SIAM Journal on Numerical Analysis*, 56:1386–1404, 2018.

[101] F. Jiang, Y. Shen. A quasi-nonlocal coupling method for bond-based peridynamics with classical continuum mechanics. *Engineering Computations*, 2021, https://doi.org/10.1108/EC-05-2020-0246.

[102] P. Seleson, S. Beneddine, S. Prudhomme. A force-based coupling scheme for peridynamics and classical elasticity. *Computational Materials Science*, 66:34–49, 2013.

[103] P. Seleson, Y.D. Ha, S. Beneddine. Concurrent coupling of bond-based peridynamics and the Navier equation of classical elasticity by blending. *International Journal for Multiscale Computational Engineering*, 13(2):91–113, 2015.

[104] S.A. Silling, D.J. Littlewood, P. Seleson. Variable horizon in a peridynamic medium. *Journal of Mechanics of Materials and Structures*, 10(5):591–612, 2015.

[105] M. D'Elia, X. Li, P. Seleson, X. Tian, Y. Yu. A Review of Local-to-Nonlocal Coupling Methods in Nonlocal Diffusion and Nonlocal Mechanics. *Journal of Peridynamics and Nonlocal Modeling*, 2021, https://doi.org/10.1007/s42102-020-00038-7.

[106] R.W. Macek, S.A. Silling. Peridynamics via finite element analysis. *Finite Elements in Analysis and Design*, 43(15):1169–1178, 2007.

[107] B. Kilic, E. Madenci. Coupling of peridynamic theory and the finite element method. *Journal of Mechanics of Materials and Structures*, 5(5):707–733, 2010.

[108] W. Liu, J.-W. Hong. A coupling approach of discretized peridynamics with finite element method. *Computer Methods in Applied Mechanics and Engineering*, 245–246:163–175, 2012.

[109] E. Oterkus, E. Madenci, O. Weckner, S. Silling, P. Bogert, A. Tessler. Combined finite element and peridynamic analyses for predicting failure in a stiffened composite curved panel with a central slot. *Composite Structures*, 94(3):839–850, 2012.

[110] A. Agwai, I. Guven, E. Madenci. Drop-shock failure prediction in electronic packages by using peridynamic theory. *IEEE Transactions on Components, Packaging and Manufacturing Technology*, 2(3):439–447, 2012.

[111] A. Shojaei, M. Zaccariotto, U. Galvanetto. Coupling of 2D discretized Peridynamics with a meshless method based on classical elasticity using switching of nodal behaviour. *Engineering Computations*, 34(5):1334–1366, 2017.

[112] U. Galvanetto, T. Mudric, A. Shojaei, M. Zaccariotto. An effective way to couple FEM meshes and Peridynamics grids for the solution of static equilibrium problems. *Mechanics Research Communications*, 76:41–47, 2016.

[113] T. Ni, M. Zaccariotto, Q.-Z. Zhu, U. Galvanetto. Coupling of FEM and ordinary state-based peridynamics for brittle failure analysis in 3D. *Mechanics of Advanced Materials and Structures*, 28(9):875–890, 2021.

[114] A. Jumahat, C. Soutis, J. Mahmud, N. Ahmad. Compressive properties of nanoclay/epoxy nanocomposites. *Procedia Engineering*, 41:1607–1613, 2012.

[115] H.C. Greenwell, A.A. Bowden, B. Chen, P. Boulet, J.R.G. Evans, P.V. Coveney, A. Whiting. Intercalation and in situ polymerization of poly (alkylene oxide) derivatives within M+–montmorillonite (M= Li, Na, K). *Journal of Materials Chemistry*, 16(11):1082–1094, 2006.

[116] M.Z. Rong, M.Q. Zhang, W.H. Ruan. Surface modification of nanoscale fillers for improving properties of polymer nanocomposites: A review. *Materials science and technology*, 22(7):787–796, 2006.

[117] S.S. Ray, M. Okamoto. Polymer/layered silicate nanocomposites: A review from preparation to processing. *Progress in polymer science*, 28(11):1539–1641, 2003.

[118] V.-H. Nguyen, S. Mahouche-Chergui, B. Carbonnier, D. Di Tommaso, S. Naili, et al. From atomistic structure to thermodynamics and mechanical properties of epoxy/clay nanocomposites: Investigation by molecular dynamics simulations. *Computational Materials Science*, 139:191–201, 2017.

[119] K. Anoukou, A. Zaoui, F. Zaïri, M. Naït-Abdelaziz, J.M. Gloaguen. Molecular dynamics study of the polymer clay nanocomposites (PCNS): Elastic constants and basal spacing predictions. *Computational materials science*, 77:417–423, 2013.

[120] R. Rafiee, R. Shahzadi. Mechanical properties of nanoclay and nanoclay reinforced polymers: A review. *Polymer Composites*, 40(2):431–445, 2019.

[121] Q. Dai, K. Ng. Investigation of electromechanical properties of piezoelectric structural fiber composites with micromechanics analysis and finite element modeling. *Mechanics of Materials*, 53:29–46, 2012.

[122] J.-J. Luo, I.M. Daniel. Characterization and modeling of mechanical behavior of polymer/clay nanocomposites. *Composites science and technology*, 63(11):1607–1616, 2003.

[123] T. Mori, K. Tanaka. Average stress in matrix and average elastic energy of materials with misfitting inclusions. *Acta metallurgica*, 21(5):571–574, 1973.

[124] N. Sheng, M.C. Boyce, D.M. Parks, G.C. Rutledge, J.I. Abes, R.E. Cohen. Multiscale micromechanical modeling of polymer/clay nanocomposites and the effective clay particle. *Polymer*, 45(2):487–506, 2004.

[125] J. Wang, R. Pyrz. Prediction of the overall moduli of layered silicate-reinforced nanocomposites—part I: basic theory and formulas. *Composites Science and Technology*, 64(7-8):925–934, 2004.

[126] M. Bennoura, A. Aboutajeddine. Predictive capabilities of micromechanical models for composite materials. *Journal of Reinforced Plastics and Composites*, 35(14):1115–1125, 2016.

[127] A. Mesbah, F. Zaïri, S. Boutaleb, J.-M. Gloaguen, M. Naït-Abdelaziz, S. Xie, T. Boukharouba, J.-M. Lefebvre. Experimental characterization and modeling stiffness of polymer/clay nanocomposites within a hierarchical multiscale framework. *Journal of applied polymer science*, 114(5):3274–3291, 2009.

[128] K. Anoukou, F. Zaïri, M. Naït-Abdelaziz, A. Zaoui, T. Messager, J.M. Gloaguen. On the overall elastic moduli of polymer–clay nanocomposite materials using a self-consistent approach. Part I: Theory. *Composites Science and Technology*, 71(2):197–205, 2011.

[129] J.D. Eshelby. The determination of the elastic field of an ellipsoidal inclusion, and related problems. *Proceedings of the royal society of London. Series A. Mathematical and physical sciences*, 241(1226):376–396, 1957.

[130] J.D. Eshelby. The elastic field outside an ellipsoidal inclusion. *Proceedings of the Royal Society of London. Series A. Mathematical and Physical Sciences*, 252(1271):561–569, 1959.

[131] W. Voigt. Ueber die beziehung zwischen den beiden elasticitätsconstanten isotroper körper. *Annalen der physik*, 274(12):573–587, 1889.

[132] A. Reuss. Berechnung der fliessgrenze von mischkristallen auf grund der plastizitätsbedingung für einkristalle. *ZAMM-Journal of Applied Mathematics and Mechanics/Zeitschrift für Angewandte Mathematik und Mechanik*, 9(1):49–58, 1929.

[133] Y. Kojima, A. Usuki, M. Kawasumi, A. Okada, Y. Fukushima, T. Kurauchi, O. Kamigaito. Mechanical properties of nylon 6-clay hybrid. *Journal of Materials Research*, 8(5):1185–1189, 1993.

[134] J.C. Halpin. Primer on composite materials analysis. *Lancaster, PA, Technomic Publishing Co., Inc., 192 pp.*, 1984.

[135] J.C. Halpin Affdl, J.L. Kardos. The Halpin-Tsai equations: A review. *Polymer Engineering & Science*, 16(5):344–352, 1976.

[136] J.C. Halpin. Stiffness and expansion estimates for oriented short fiber composites. *Journal of Composite Materials*, 3(4):732–734, 1969.

[137] J.C. Halpin. Effects of environmental factors on composite materials. Technical report, Air Force Materials Lab Wright-Patterson AFB OH, 1969.

[138] H.T. Hahn, S.W. Tsai. *Introduction to composite materials*. CRC Press, 1980.

[139] M. Pahlavanpour, H. Moussaddy, E. Ghossein, P. Hubert, M. Lévesque. Prediction of elastic properties in polymer–clay nanocomposites: Analytical homogenization methods and 3D finite element modeling. *Computational materials science*, 79:206–215, 2013.

[140] K. Hbaieb, Q.X. Wang, Y.H.J. Chia, B. Cotterell. Modelling stiffness of polymer/clay nanocomposites. *Polymer*, 48(3):901–909, 2007.

[141] C.P. Buckley, et al. Elastic constants for an intercalated layered-silicate/polymer nanocomposite using the effective particle concept–a parametric study using numerical and analytical continuum approaches. *Computational Materials Science*, 44(4):1332–1343, 2009.

[142] G. Cricrì, E. Garofalo, F. Naddeo, L. Incarnato. Stiffness constants prediction of nanocomposites using a periodic 3D-FEM model. *Journal of Polymer Science Part B: Polymer Physics*, 50(3):207–220, 2012.

[143] P. Bian, S. Schmauder, H. Qing. Strength and damage of nanoplatelets reinforced polymer: A 3D finite element modeling and simulation. *Composite Structures*, 245:112337, 2020.

[144] Y. Djebara, A. El Moumen, T. Kanit, S. Madani, A. Imad. Modeling of the effect of particles size, particles distribution and particles number on mechanical properties of polymer-clay nano-composites: Numerical homogenization versus experimental results. *Composites Part B: Engineering*, 86:135–142, 2016.

[145] M. Silani, H. Talebi, S. Ziaei-Rad, P. Kerfriden, S.P.A. Bordas, T. Rabczuk. Stochastic modelling of clay/epoxy nanocomposites. *Composite Structures*, 118:241–249, 2014.

[146] Y. Li, A.M. Waas, E.M. Arruda. The effects of the interphase and strain gradients on the elasticity of layer by layer (LBL) polymer/clay nanocomposites. *International journal of solids and structures*, 48(6):1044–1053, 2011.

[147] B. Pukánszky. Interfaces and interphases in multicomponent materials: past, present, future. *European polymer journal*, 41(4):645–662, 2005.

[148] D. Ciprari, K. Jacob, R. Tannenbaum. Characterization of polymer nanocomposite interphase and its impact on mechanical properties. *Macromolecules*, 39(19):6565–6573, 2006.

[149] M. Bazmara, M. Silani, I. Dayyani. Effect of functionally-graded interphase on the elasto-plastic behavior of nylon-6/clay nanocomposites; a numerical study. *Defence Technology*, 17(1):177–184, 2021.

[150] Y. Zare, H. Garmabi. Thickness, modulus and strength of interphase in clay/polymer nanocomposites. *Applied Clay Science*, 105:66–70, 2015.

[151] P. Gelineau, M. Stepień, S. Weigand, L. Cauvin, F. Bédoui. Elastic properties prediction of nano-clay reinforced polymer using multi-scale modeling based on a multi-scale characterization. *Mechanics of Materials*, 89:12–22, 2015.

[152] H. Talebi, M. Silani, S.P.A. Bordas, P. Kerfriden, T. Rabczuk. A computational library for multiscale modeling of material failure. *Computational Mechanics*, 53(5):1047–1071, 2014.

[153] P.R. Budarapu, R. Gracie, S.P.A. Bordas, T. Rabczuk. An adaptive multiscale method for quasi-static crack growth. *Computational Mechanics*, 53(6):1129–1148, 2014.

[154] H. Talebi, M. Silani, T. Rabczuk. Concurrent multiscale modeling of three dimensional crack and dislocation propagation. *Advances in Engineering Software*, 80:82–92, 2015.

[155] M. Silani, H. Talebi, A.M. Hamouda, T. Rabczuk. Nonlocal damage modelling in clay/epoxy nanocomposites using a multiscale approach. *Journal of Computational Science*, 15:18–23, 2016.

[156] G. Scocchi, P. Posocco, M. Fermeglia, S. Pricl. Polymer- clay nanocomposites: a multiscale molecular modeling approach. *The Journal of Physical Chemistry B*, 111(9):2143–2151, 2007.

[157] M. Lo Cascio, A. Milazzo, I. Benedetti. Virtual element method for computational homogenization of composite and heterogeneous materials. *Composite Structures*, 232:111523, 2020.

[158] M. Lo Cascio, M. Grifò, A. Milazzo, I. Benedetti. Computational homogenization of heterogeneous materials by a novel hybrid numerical scheme. *Journal of Multiscale Modelling*, 11(04):2050008, 2020.

[159] M. Lo Cascio, A. Milazzo, I. Benedetti. A coupled VEM-BEM approach for computational homogenization of heterogeneous materials. In: *14th WCCM-ECCOMAS Congress 2020*, Vol. 200, 2021.

[160] E. Madenci, A. Barut, N.D. Phan. Peridynamic unit cell homogenization. In: *58th AIAA/ASCE/AHS/ASC Structures, Structural Dynamics, and Materials Conference*, p. 1138, 2017.

[161] C. Diyaroglu, E. Madenci, N. Phan. Peridynamic homogenization of microstructures with orthotropic constituents in a finite element framework. *Composite Structures*, 227:111334, 2019.

[162] W. Xia, Y.K. Galadima, E. Oterkus, S. Oterkus. Representative volume element homogenization of a composite material by using bond-based peridynamics. *Journal of Composites and Biodegradable Polymers*, 7:51–56, 2019.

[163] M. Duzzi, M. Zaccariotto, U. Galvanetto. Application of peridynamic theory to nanocomposite materials. In: *Advanced Materials Research*, Vol. 1016, pp. 44–48, Trans Tech Publ, 2014.

[164] J. Decklever, P. Spanos. Nanocomposite Material Properties Estimation and Fracture Analysis via Peridynamics and Monte Carlo Simulation. *Probabilistic Engineering Mechanics*, 44:77–88, 2016.

[165] V.-H. Nguyen, S. Mahouche-Chergui, B. Carbonnier, S. Naili, et al. Estimation of effective elastic properties of polymer/clay nanocomposites: A parametric study. *Composites Part B: Engineering*, 152:139–150, 2018.

[166] Y. Zare, K.Y. Rhee. Multistep modeling of Young's modulus in polymer/clay nanocomposites assuming the intercalation/exfoliation of clay layers and the interphase between polymer matrix and nanoparticles. *Composites Part A: Applied Science and Manufacturing*, 102:137–144, 2017.

[167] A. Pontefisso, M. Zappalorto, M. Quaresimin. Influence of interphase and filler distribution on the elastic properties of nanoparticle filled polymers. *Mechanics Research Communications*, 52:92–94, 2013.

[168] K. Wang, L. Chen, J. Wu, M.L. Toh, C. He, A.F. Yee. Epoxy nanocomposites with highly exfoliated clay: mechanical properties and fracture mechanisms. *Macromolecules*, 38(3):788–800, 2005.

[169] H. Ebadi-Dehaghani, H.A. Khonakdar, M. Barikani, S.H. Jafari. Experimental and theoretical analyses of mechanical properties of PP/PLA/clay nanocomposites. *Composites Part B: Engineering*, 69:133–144, 2015.

[170] L. Wang, K. Wang, L. Chen, Y. Zhang, C. He. Preparation, morphology and thermal/mechanical properties of epoxy/nanoclay composite. *Composites Part A: applied science and manufacturing*, 37(11):1890–1896, 2006.

[171] H. Miyagawa, L.T. Drzal. The effect of chemical modification on the fracture toughness of montmorillonite clay/epoxy nanocomposites. *Journal of adhesion science and technology*, 18(13):1571–1588, 2004.

[172] I.-N. Jan, T.-M. Lee, K.-C. Chiou, J.-J. Lin. Comparisons of physical properties of intercalated and exfoliated clay/epoxy nanocomposites. *Industrial & engineering chemistry research*, 44(7):2086–2090, 2005.

[173] W. Gerstle, N. Sau, S. Silling. Peridynamic modeling of plain and reinforced concrete structures. *SMiRT 18*, pp. 54–68, 2005.

[174] F. Bobaru, M. Yang, L.F. Alves, S.A. Silling, E. Askari, J. Xu. Convergence, adaptive refinement, and scaling in 1D peridynamics. *International Journal for Numerical Methods in Engineering*, 77(6):852–877, 2009.

[175] A.A. Griffith. The phenomena of rupture and flow in solids. *Philosophical transactions of the royal society of London. Series A, containing papers of a mathematical or physical character*, 221(582-593):163–198, 1921.

[176] G.R. Irwin. Analysis of stresses and strains near the end of a crack traversing a plate. 1957.

[177] S.A. Silling, R.B. Lehoucq. Peridynamic theory of solid mechanics. In: *Advances in applied mechanics*, Vol. 44, pp. 73–168, Elsevier, 2010.

[178] S.A. Silling. Linearized theory of peridynamic states. *Journal of Elasticity*, 99(1):85–111, 2010.

[179] X. Gu, E. Madenci, Q. Zhang. Revisit of non-ordinary state-based peridynamics. *Engineering fracture mechanics*, 190:31–52, 2018.

[180] D.J. Littlewood. Roadmap for peridynamic software implementation. *SAND Report, Sandia National Laboratories, Albuquerque, NM and Livermore, CA*, 2015.

[181] P. Seleson, M. Parks. On the role of the influence function in the peridynamic theory. *International Journal for Multiscale Computational Engineering*, 9(6), 2011.

[182] M.S. Breitenfeld, P.H. Geubelle, O. Weckner, S.A. Silling. Non-ordinary state-based peridynamic analysis of stationary crack problems. *Computer Methods in Applied Mechanics and Engineering*, 272:233–250, 2014.

[183] Q.V. Le, W. Chan, J. Schwartz. A two-dimensional ordinary, state-based peridynamic model for linearly elastic solids. *International Journal for Numerical Methods in Engineering*, 98(8):547–561, 2014.

[184] J.T. Foster, S.A. Silling, W. Chen. An energy based failure criterion for use with peridynamic states. *International Journal for Multiscale Computational Engineering*, 9(6), 2011.

[185] T.L. Warren, S.A. Silling, A. Askari, O. Weckner, M.A. Epton, J. Xu. A non-ordinary state-based peridynamic method to model solid material deformation and fracture. *International Journal of Solids and Structures*, 46(5):1186–1195, 2009.

[186] D. Dipasquale, G. Sarego, M. Zaccariotto, U. Galvanetto. A discussion on failure criteria for ordinary state-based peridynamics. *Engineering Fracture Mechanics*, 186:378–398, 2017.

[187] D. Dipasquale, G. Sarego, P. Prapamonthon, S. Yooyen, A. Shojaei. A stress tensor-based failure criterion for ordinary state-based peridynamic models. *Journal of Applied and Computational Mechanics*, 2021, http://dx.doi.org/10.22055/jacm.2021.38664.3264.

[188] T. Ni, Q.-Z. Zhu, L.-Y. Zhao, P.-F. Li. Peridynamic simulation of fracture in quasi brittle solids using irregular finite element mesh. *Engineering Fracture Mechanics*, 188:320–343, 2018.

[189] E. Emmrich, O. Weckner. The peridynamic equation and its spatial discretisation. *Mathematical Modelling and Analysis*, 12(1):17–27, 2007.

[190] P. Seleson. Improved one-point quadrature algorithms for two-dimensional peridynamic models based on analytical calculations. *Computer Methods in Applied Mechanics and Engineering*, 282:184–217, 2014.

[191] P. Seleson, D.J. Littlewood. Convergence studies in meshfree peridynamic simulations. *Computers & Mathematics with Applications*, 71(11):2432–2448, 2016.

[192] J. Bartlett, D. Storti. A generalized fictitious node approach for surface effect correction in peridynamic simulation. *Journal of Peridynamics and Nonlocal Modeling*, 3:276–286, 2021.

[193] M. Zaccariotto, D. Tomasi, U. Galvanetto. An enhanced coupling of PD grids to FE meshes. *Mechanics Research Communications*, 84:125–135, 2017.

[194] O.C. Zienkiewicz, R.L. Taylor, P. Nithiarasu, J.Z. Zhu. *The Finite Element Method*, Vol. 3, McGraw-Hill London, 1977.

[195] J. Trageser, P. Seleson. Bond-based peridynamics: a tale of two Poisson's ratios. *Journal of Peridynamics and Nonlocal Modeling*, 2:278–288, 2020.

[196] G. Sarego, Q.V. Le, F. Bobaru, M. Zaccariotto, U. Galvanetto. Linearized state-based peridynamics for 2-D problems. *International Journal for Numerical Methods in Engineering*, 108(10):1174–1197, 2016.

[197] T. Ni, M. Zaccariotto, Q.-Z. Zhu, U. Galvanetto. Static solution of crack propagation problems in peridynamics. *Computer Methods in Applied Mechanics and Engineering*, 346:126–151, 2019.

[198] E. Madenci, A. Barut, M. Futch. Peridynamic differential operator and its applications. *Computer Methods in Applied Mechanics and Engineering*, 304:408–451, 2016.

[199] A. Shojaei, U. Galvanetto, T. Rabczuk, A. Jenabi, M. Zaccariotto. A generalized finite difference method based on the peridynamic differential operator

for the solution of problems in bounded and unbounded domains. *Computer Methods in Applied Mechanics and Engineering*, 343:100–126, 2019.

[200] D. Brokenshire. *A study of torsional fracture tests*. PhD thesis, Cardiff University, Cardiff, Wells, 1996.

[201] A. Carpinteri, G. Colombo. Numerical analysis of catastrophic softening behaviour (snap-back instability). *Computers & structures*, 31(4):607–636, 1989.

[202] K.J. Shah, A.D. Shukla, D.O. Shah, T. Imae. Effect of organic modifiers on dispersion of organoclay in polymer nanocomposites to improve mechanical properties. *Polymer*, 97:525–532, 2016.

[203] C. Chen, G. Lv, C. Pan, M. Song, C. Wu, D. Guo, X. Wang, B. Chen, Z. Gu. Poly (lactic acid)(PLA) based nanocomposites—a novel way of drug-releasing. *Biomedical materials*, 2(4):L1, 2007.

[204] G. Sandri, M.C. Bonferoni, S. Rossi, F. Ferrari, C. Aguzzi, C. Viseras, C. Caramella. Clay minerals for tissue regeneration, repair, and engineering. In: *Wound Healing Biomaterials*, pp. 385–402, Elsevier, 2016.

[205] M. Vinyas, S.J. Athul, D. Harursampath, M. Loja, T.N. Thoi. A comprehensive review on analysis of nanocomposites: from manufacturing to properties characterization. *Materials Research Express*, 6(9):092002, 2019.

[206] J. Njuguna, K. Pielichowski. Polymer nanocomposites for aerospace applications: properties. *Advanced Engineering Materials*, 5(11):769–778, 2003.

[207] M. Alexandre, P. Dubois. Polymer-layered silicate nanocomposites: preparation, properties and uses of a new class of materials. *Materials science and engineering: R: Reports*, 28(1-2):1–63, 2000.

[208] N. Herron, D.L. Thorn. Nanoparticles: uses and relationships to molecular cluster compounds. *Advanced Materials*, 10(15):1173–1184, 1998.

[209] R.E. Grim. *Clay mineralogy*, Vol. 76, LWW, 1953.

[210] S. Pavlidou, C.D. Papaspyrides. A review on polymer–layered silicate nanocomposites. *Progress in polymer science*, 33(12):1119–1198, 2008.

[211] M.J. Solomon, A.S. Almusallam, K.F. Seefeldt, A. Somwangthanaroj, P. Varadan. Rheology of polypropylene/clay hybrid materials. *Macromolecules*, 34(6):1864–1872, 2001.

[212] H. Ishida, S. Campbell, J. Blackwell. General approach to nanocomposite preparation. *Chemistry of Materials*, 12(5):1260–1267, 2000.

[213] H. Fischer. Polymer nanocomposites: from fundamental research to specific applications. *Materials Science and Engineering: C*, 23(6-8):763–772, 2003.

[214] A.S. Zerda, A.J. Lesser. Intercalated clay nanocomposites: morphology, mechanics, and fracture behavior. *Journal of Polymer Science Part B: Polymer Physics*, 39(11):1137–1146, 2001.

[215] P. Rengasamy, G.J. Churchman. Cation exchange capacity, exchangeable cations and sodicity. 1999.

[216] P.C. LeBaron, Z. Wang, T.J. Pinnavaia. Polymer-layered silicate nanocomposites: an overview. *Applied clay science*, 15(1-2):11–29, 1999.

[217] C. Zilg, R. Mülhaupt, J. Finter. Morphology and toughness/stiffness balance of nanocomposites based upon anhydride-cured epoxy resins and layered silicates. *Macromolecular Chemistry and Physics*, 200(3):661–670, 1999.

[218] T.D. Fornes, P.J. Yoon, H. Keskkula, D.R. Paul. Nylon 6 nanocomposites: the effect of matrix molecular weight. *Polymer*, 42(25):09929–09940, 2001.

[219] G. Beyer. Nanocomposites: a new class of flame retardants for polymers. *Plastics, Additives and Compounding*, 4(10):22–28, 2002.

[220] H. Dennis, D.L. Hunter, D. Chang, S. Kim, J.L. White, J.W. Cho, D.R. Paul. Effect of melt processing conditions on the extent of exfoliation in organoclay-based nanocomposites. *Polymer*, 42(23):9513–9522, 2001.

[221] A.J. Kinloch, A.C. Taylor. Mechanical and fracture properties of epoxy/inorganic micro-and nano-composites. 2003.

[222] X. Kornmann, R. Thomann, R. Mülhaupt, J. Finter, L. Berglund. Synthesis of amine-cured, epoxy-layered silicate nanocomposites: The influence of the silicate surface modification on the properties. *Journal of Applied Polymer Science*, 86(10):2643–2652, 2002.

[223] D. Ratna, N.R. Manoj, R. Varley, R.K.S. Raman, G.P. Simon. Clay-reinforced epoxy nanocomposites. *Polymer International*, 52(9):1403–1407, 2003.

[224] D.C. Lee, L.W. Jang. Preparation and characterization of PMMA–Clay hybrid composite by emulsion polymerization. *Journal of Applied Polymer Science*, 61(7):1117–1122, 1996.

[225] M. Quaresimin, M. Salviato, M. Zappalorto. Fracture and interlaminar properties of clay-modified epoxies and their glass reinforced laminates. *Engineering Fracture Mechanics*, 81:80–93, 2012.

[226] B. Wetzel, P. Rosso, F. Haupert, K. Friedrich. Epoxy nanocomposites–fracture and toughening mechanisms. *Engineering fracture mechanics*, 73(16):2375–2398, 2006.

[227] B. Qi, Q.X. Zhang, M. Bannister, Y.-W. Mai. Investigation of the mechanical properties of DGEBA-based epoxy resin with nanoclay additives. *Composite structures*, 75(1-4):514–519, 2006.

[228] M.-W. Ho, C.-K. Lam, K.-T. Lau, D.H.L. Ng, D. Hui. Mechanical properties of epoxy-based composites using nanoclays. *Composite structures*, 75(1-4):415–421, 2006.

[229] J.A. Tarapow, C.R. Bernal, V.A. Alvarez. Mechanical properties of polypropylene/clay nanocomposites: effect of clay content, polymer/clay compatibility, and processing conditions. *Journal of applied polymer science*, 111(2):768–778, 2009.

[230] N.K. Borse, M.R. Kamal. Melt processing effects on the structure and mechanical properties of PA-6/clay nanocomposites. *Polymer Engineering & Science*, 46(8):1094–1103, 2006.

[231] A.J. Jose, F. Chacko, R. Wilson, M. Alagar. Development and characterization of organoclay filled polyetherimide nanocomposites for anticorrosive coatings. *Materials Today: Proceedings*, 41:490–497, 2021.

[232] A. Bartolozzi, R. Bertani, E. Burigo, A. Fabrizi, F. Panozzo, M. Quaresimin, F. Simionato, P. Sgarbossa, S. Tamburini, M. Zappalorto, et al. Multifunctional Cu2+–montmorillonite/epoxy resin nanocomposites with antibacterial activity. *Journal of Applied Polymer Science*, 134(16), 2017.

[233] M. Monsif, A. Zerouale, N.I. Kandri, R. Bertani, A. Bartolozzi, B.M. Bresolin, F. Zorzi, F. Tateo, M. Zappalorto, M. Quaresimin, et al. Multifunctional epoxy/nanocomposites based on natural moroccan clays with high antimicrobial activity: Morphological, thermal and mechanical properties. *Journal of Nanomaterials*, Vol. 2019, Article ID 2810901, 12 pp., 2019, https://doi.org/10.1155/2019/2810901.

[234] M. Quaresimin, R. Bertani, M. Zappalorto, A. Pontefisso, F. Simionato, A. Bartolozzi. Multifunctional polymer nanocomposites with enhanced mechanical and anti-microbial properties. *Composites Part B: Engineering*, 80:108–115, 2015.

[235] M. Zappalorto, M. Salviato, M. Quaresimin. Mixed mode (I+ II) fracture toughness of polymer nanoclay nanocomposites. *Engineering Fracture Mechanics*, 111:50–64, 2013.

[236] Plastics. Determination of tensile properties. Part 2: Test Conditions for Moulding and Extrusion Plastics. Standard, International Organization for Standardization, 2012.

[237] M. Silani, S. Ziaei-Rad, M. Esfahanian, V.B.C. Tan. On the experimental and numerical investigation of clay/epoxy nanocomposites. *Composite Structures*, 94(11):3142–3148, 2012.

[238] A. Haque, M. Shamsuzzoha, F. Hussain, D. Dean. S2-Glass/Epoxy Polymer Nanocomposites: Manufacturing, Structures, Thermal and Mechanical Properties. *Journal of Composite materials*, 37(20):1821–1837, 2003.

[239] R. Hill. Elastic properties of reinforced solids: some theoretical principles. *Journal of the Mechanics and Physics of Solids*, 11(5):357–372, 1963.

[240] B. Chen, J.R.G. Evans. Elastic moduli of clay platelets. *Scripta materialia*, 54(9):1581–1585, 2006.

[241] N. Hasegawa, H. Okamoto, M. Kato, A. Usuki, N. Sato. Nylon 6/Na–montmorillonite nanocomposites prepared by compounding Nylon 6 with Na–montmorillonite slurry. *Polymer*, 44(10):2933–2937, 2003.

[242] Wolfram Research, Inc. Mathematica, Version 12.1. Champaign, IL, 2020.

[243] Standard Test Methods for Plane-Strain Fracture Toughness and Strain Energy Release Rate of Plastic Materials. Standard, American Society for Testing and Materials International, 2014.

[244] A. Mouloud, R. Cherif, S. Fellahi, Y. Grohens, I. Pillin. Study of morphological and mechanical performance of amine-cured glassy epoxy–clay nanocomposites. *Journal of applied polymer science*, 124(6):4729–4739, 2012.

Appendix A

Convergence of the nonlocal traction to the local traction

The theoretical analysis presented in the following appendix has been mainly derived by Doctor Pablo Seleson, Research Scientist at the Oak Ridge National Laboratory (ORNL), Oak Ridge, United States [9].

A.1 One-dimensional case

Assume a domain $\mathcal{B} \subset \mathbb{R}$ and consider the nonlocal traction at $x_0 \in \mathcal{B}$ in the bulk of the body with normal $n = +1$ (*cf.* (2.55)):

$$\tau(x_0, +1) = \int_{x_0-\delta}^{x_0} \int_{x_0}^{x+\delta} c(|x' - x|)(u(x') - u(x))dx'dx. \tag{A.1}$$

Assuming a smooth deformation, we begin by employing a first Taylor expansion of $u(x')$ about x (*cf.* (2.7)):

$$\begin{aligned}\tau(x_0, +1) &= \int_{x_0-\delta}^{x_0} \int_{x_0}^{x+\delta} c(|x' - x|)\bigg(\frac{du}{dx}(x)(x' - x) + \frac{1}{2}\frac{d^2u}{dx^2}(x)(x' - x)^2 \\ &\qquad + \frac{1}{3!}\frac{d^3u}{dx^3}(x)(x' - x)^3 + \dots\bigg)dx'dx \\ &= \int_{x_0-\delta}^{x_0} \int_{x_0-x}^{\delta} c(|\xi|)\bigg(\frac{du}{dx}(x)\xi + \frac{1}{2}\frac{d^2u}{dx^2}(x)\xi^2 + \frac{1}{3!}\frac{d^3u}{dx^3}(x)\xi^3 + \dots\bigg)d\xi dx,\end{aligned} \tag{A.2}$$

where we used the change of variable $\xi = x' - x$ in the last equality. Note that due to the limits of integration, $x' > x$ and thus $\xi > 0$. Assume the micromodulus

function (2.12) with $\alpha < 2$ (see below). Then,

$$\begin{aligned}
\tau(x_0,+1) &= \int_{x_0-\delta}^{x_0}\int_{x_0-x}^{\delta}\frac{c}{|\xi|^\alpha}\left(\frac{du}{dx}(x)\xi+\frac{1}{2}\frac{d^2u}{dx^2}(x)\xi^2+\frac{1}{3!}\frac{d^3u}{dx^3}(x)\xi^3+\dots\right)d\xi dx\\
&= c\int_{x_0-\delta}^{x_0}\int_{x_0-x}^{\delta}\left(\frac{du}{dx}(x)\xi^{1-\alpha}+\frac{1}{2}\frac{d^2u}{dx^2}(x)\xi^{2-\alpha}+\frac{1}{3!}\frac{d^3u}{dx^3}(x)\xi^{3-\alpha}+\dots\right)d\xi dx\\
&= c\int_{x_0-\delta}^{x_0}\left(\frac{du}{dx}(x)\frac{1}{2-\alpha}\left[\delta^{2-\alpha}-(x_0-x)^{2-\alpha}\right]\right.\\
&\qquad+\frac{1}{2}\frac{d^2u}{dx^2}(x)\frac{1}{3-\alpha}\left[\delta^{3-\alpha}-(x_0-x)^{3-\alpha}\right]\\
&\qquad\left.+\frac{1}{3!}\frac{d^3u}{dx^3}(x)\frac{1}{4-\alpha}\left[\delta^{4-\alpha}-(x_0-x)^{4-\alpha}\right]+\dots\right)dx. \qquad \text{(A.3)}
\end{aligned}$$

We now perform a second Taylor expansion, this time for the derivatives evaluated at x about x_0. Explicitly writing terms up to third derivatives, we have

$$\begin{aligned}
\tau(x_0,+1) = c\int_{x_0-\delta}^{x_0}\Bigg(&\frac{1}{2-\alpha}\left\{\frac{du}{dx}(x_0)+\frac{d^2u}{dx^2}(x_0)(x-x_0)\right.\\
&\qquad\left.+\frac{1}{2}\frac{d^3u}{dx^3}(x_0)(x-x_0)^2+\dots\right\}\left[\delta^{2-\alpha}-(x_0-x)^{2-\alpha}\right]\\
&+\frac{1}{2}\frac{1}{3-\alpha}\left\{\frac{d^2u}{dx^2}(x_0)+\frac{d^3u}{dx^3}(x_0)(x-x_0)+\dots\right\}\left[\delta^{3-\alpha}-(x_0-x)^{3-\alpha}\right]\\
&+\frac{1}{3!}\frac{1}{4-\alpha}\left\{\frac{d^3u}{dx^3}(x_0)+\dots\right\}\left[\delta^{4-\alpha}-(x_0-x)^{4-\alpha}\right]\Bigg)dx. \qquad \text{(A.4)}
\end{aligned}$$

Collecting the contributions to each derivative, we have

$$\begin{aligned}
\tau(x_0,+1) = c\Bigg(&\left\{\int_{x_0-\delta}^{x_0}\frac{1}{2-\alpha}\left[\delta^{2-\alpha}-(x_0-x)^{2-\alpha}\right]dx\right\}\frac{du}{dx}(x_0)\\
&+\left\{\int_{x_0-\delta}^{x_0}\frac{1}{2-\alpha}(x-x_0)\left[\delta^{2-\alpha}-(x_0-x)^{2-\alpha}\right]\right.\\
&\qquad\left.+\frac{1}{2}\frac{1}{3-\alpha}\left[\delta^{3-\alpha}-(x_0-x)^{3-\alpha}\right]dx\right\}\frac{d^2u}{dx^2}(x_0)\\
&+\left\{\int_{x_0-\delta}^{x_0}\frac{1}{2-\alpha}\frac{(x-x_0)^2}{2}\left[\delta^{2-\alpha}-(x_0-x)^{2-\alpha}\right]\right.\\
&\qquad+\frac{1}{2}\frac{1}{3-\alpha}(x-x_0)\left[\delta^{3-\alpha}-(x_0-x)^{3-\alpha}\right]\\
&\qquad\left.+\frac{1}{3!}\frac{1}{4-\alpha}\left[\delta^{4-\alpha}-(x_0-x)^{4-\alpha}\right]dx\right\}\frac{d^3u}{dx^3}(x_0)+\dots\Bigg). \qquad \text{(A.5)}
\end{aligned}$$

We compute the following integral (for $n \geqslant 0$ and $m > 1$):

$$\begin{aligned}
&\int_{x_0-\delta}^{x_0} \frac{1}{(m-1)!}\frac{1}{m-\alpha}\frac{(x-x_0)^n}{n!}\Big[\delta^{m-\alpha} - (x_0-x)^{m-\alpha}\Big]dx \\
&= \frac{1}{(m-1)!}\frac{1}{m-\alpha}\frac{1}{n!}(-1)^n\Big[-\delta^{m-\alpha}\frac{1}{n+1}(x_0-x)^{n+1} \\
&\qquad\qquad + \frac{1}{n+m+1-\alpha}(x_0-x)^{n+m+1-\alpha}\Big]\Big|_{x_0-\delta}^{x_0} \\
&= \frac{1}{(m-1)!}\frac{(-1)^n}{(n+1)!}\frac{\delta^{n+m+1-\alpha}}{n+m+1-\alpha}. \qquad \text{(A.6)}
\end{aligned}$$

Using (A.6) to compute the integrals in (A.5), we obtain

$$\tau(x_0,+1) = c\bigg(\frac{\delta^{3-\alpha}}{3-\alpha}\frac{du}{dx}(x_0) + \frac{1}{12}\frac{\delta^{5-\alpha}}{5-\alpha}\frac{d^3u}{dx^3}(x_0) + \dots\bigg). \qquad \text{(A.7)}$$

Employing the relation in (2.15), we finally obtain

$$\begin{aligned}
\tau(x_0,+1) &= E\frac{du}{dx}(x_0) + \frac{1}{12}\frac{3-\alpha}{5-\alpha}E\delta^2\frac{d^3u}{dx^3}(x_0) + \dots \\
&= \mathrm{t}(x_0,+1) + \frac{1}{12}\frac{3-\alpha}{5-\alpha}E\delta^2\frac{d^3u}{dx^3}(x_0) + \dots, \qquad \text{(A.8)}
\end{aligned}$$

where $\mathrm{t}(x_0,+1)$ is the local traction at x_0 with normal $n = +1$ (*cf.* (2.45) and (2.44)). In the limit as $\delta \to 0$, we have

$$\tau(x_0,+1) = \mathrm{t}(x_0,+1) + \mathcal{O}(\delta^2), \qquad \text{(A.9)}$$

i.e., the nonlocal traction converges to the local traction at a rate of $\mathcal{O}(\delta^2)$.

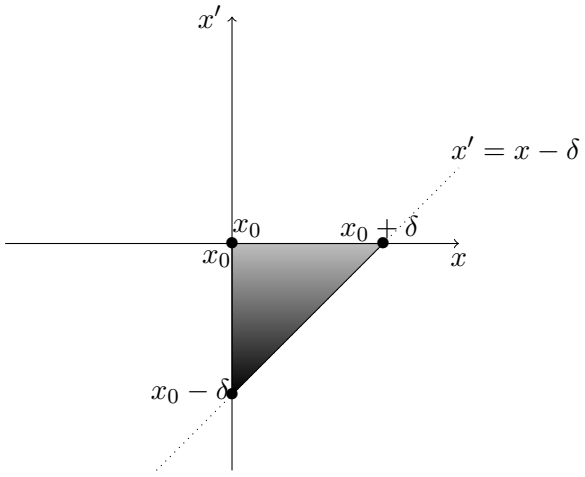

Figure A.1: Domain of integration (shaded region) for the one-dimensional nonlocal traction in (A.10).

Remark A.1 Consider the nonlocal traction at x_0 with normal $n = -1$ (*cf.* (2.55)):

$$\tau(x_0, -1) = \int_{x_0}^{x_0+\delta} \int_{x-\delta}^{x_0} c(|x' - x|)(u(x') - u(x))dx'dx. \tag{A.10}$$

The two-dimensional region of integration is illustrated in Figure A.1. Changing the order of integration, we have

$$\begin{aligned}
\tau(x_0, -1) &= \int_{x_0-\delta}^{x_0} \int_{x_0}^{x'+\delta} c(|x' - x|)(u(x') - u(x))dxdx' \\
&= -\int_{x_0-\delta}^{x_0} \int_{x_0}^{x'+\delta} c(|x - x'|)(u(x) - u(x'))dxdx' \\
&= -\int_{x_0-\delta}^{x_0} \int_{x_0}^{\hat{x}+\delta} c(|\hat{x}' - \hat{x}|)(u(\hat{x}') - u(\hat{x}))d\hat{x}'d\hat{x} = -\tau(x_0, +1),
\end{aligned} \tag{A.11}$$

where we used the change of variables $\hat{x} = x'$ and $\hat{x}' = x$ as well as (2.55) in the second to last and last equalities, respectively. Using (A.8) and (2.46), we have

$$\begin{aligned}
\tau(x_0, -1) = -\tau(x_0, +1) &= -\mathrm{t}(x_0, +1) - \frac{1}{12}\frac{3-\alpha}{5-\alpha}E\delta^2\frac{d^3u}{dx^3}(x_0) + \dots \\
&= \mathrm{t}(x_0, -1) - \frac{1}{12}\frac{3-\alpha}{5-\alpha}E\delta^2\frac{d^3u}{dx^3}(x_0) + \dots,
\end{aligned} \tag{A.12}$$

where $\mathrm{t}(x_0, -1)$ is the local traction at x_0 with normal $n = -1$ (*cf.* (2.45) and (2.44)).

Numerical examples for the nonlocal traction in one dimension

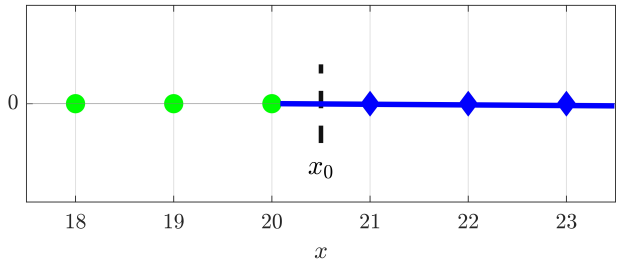

Figure A.2: Interface between the PD and CCM regions for the nonlocal traction computation in a one-dimensional CCM-PD coupled model. Blue diamonds are FEM nodes and green circles are PD nodes. The dashed gray vertical line indicates the interface at x_0. A uniform discretization with grid spacing $\Delta x = 1$ is employed, and the PD horizon is taken as $\delta = 3$.

We present some numerical examples to confirm the result in (A.8). To put these examples within the context of a CCM-PD coupled model, we consider a one-dimensional system with an interface at x_0 in the bulk of the body between a PD

region and a CCM region. We assume points $x < x_0$ belong to the PD region, whereas points $x > x_0$ correspond to the CCM region. To numerically compute the nonlocal traction in (A.1), we employ a uniform discretization with grid spacing Δx and define a set of N_{PD} PD nodes with positions given by

$$\mathcal{S}_{\mathrm{PD}} = \left\{x_0 - \delta + \tfrac{\Delta x}{2}, \ldots, x_0 - \tfrac{\Delta x}{2}\right\} \tag{A.13}$$

and a set of N_{FEM} FEM nodes with positions given by

$$\mathcal{S}_{\mathrm{FEM}} = \left\{x_0 + \tfrac{\Delta x}{2}, \ldots, x_0 + \delta - \tfrac{\Delta x}{2}\right\}. \tag{A.14}$$

To relate the examples in this section to the numerical results in Section 2.6.1, we choose $\delta = 3$ and $\Delta x = 1$ (i.e., $m = \delta/\Delta x = 3$), and we consider the case of an interface at $x_0 = 20.5$ (i.e., $x_0 = 20 + \frac{\Delta x}{2}$), which corresponds to the configuration (e) in Figure 2.6; an illustration is presented in Figure A.2. We denote by $x_i^{\mathrm{PD}} \in \mathcal{S}_{\mathrm{PD}}$, $i = 1, \ldots, N_{\mathrm{PD}}$, and $x_j^{\mathrm{FEM}} \in \mathcal{S}_{\mathrm{FEM}}$, $j = 1, \ldots, N_{\mathrm{FEM}}$, the reference positions of the PD and FEM nodes, respectively. Define the displacements of the PD and FEM nodes, respectively, by $u_i^{\mathrm{PD}} := u(x_i^{\mathrm{PD}})$, $i = 1, \ldots, N_{\mathrm{PD}}$, and $u_j^{\mathrm{FEM}} := u(x_j^{\mathrm{FEM}})$, $j = 1, \ldots, N_{\mathrm{FEM}}$. Then, we can compute the nonlocal traction in (A.1) by

$$\tau^{\mathrm{num}}(x_0, +1) := \sum_{i=1}^{N_{\mathrm{PD}}} \sum_{j=1}^{N_{\mathrm{FEM}}} \chi_\delta\left(\left|x_j^{\mathrm{FEM}} - x_i^{\mathrm{PD}}\right|\right) c\left(\left|x_j^{\mathrm{FEM}} - x_i^{\mathrm{PD}}\right|\right)\left(u_j^{\mathrm{FEM}} - u_i^{\mathrm{PD}}\right) \Delta x_j^{(i)} \Delta x, \tag{A.15}$$

where χ_δ is the characteristic function in (2.49) and a partial-volume correction [191] is used for mth neighbors, so that $\Delta x_j^{(i)} = \frac{1}{2}\Delta x$ if $|x_j^{\mathrm{FEM}} - x_i^{\mathrm{PD}}| = \delta$ and $\Delta x_j^{(i)} = \Delta x$ otherwise. We consider the micromodulus function (2.12) with $\alpha = 1$.

We compare the numerical computation of the nonlocal traction given by (A.15) with the analytical calculation using (A.8) for the case of linear, quadratic, and cubic displacement fields, described in Table A.1; the values of the coefficients are g = 0.0001 and $X_1 = 17$. As a comparison, we analytically calculate the local traction using (2.45) with (2.44). The results are reported in Table A.2. In addition to reporting the values for the nonlocal and local tractions, we present the error of the nonlocal traction computation given by the absolute value of the difference between the numerical and analytical values. We observe that the values of the numerical nonlocal traction obtained by (A.15), which is a discretization of (A.1),

Displacement type	Displacement field equation
Linear	$u(x) = \mathrm{g}x$
Quadratic	$u(x) = \dfrac{\mathrm{g}}{2X_1}x^2$
Cubic	$u(x) = \dfrac{\mathrm{g}}{3X_1^2}x^3$

Table A.1: Displacement fields for the nonlocal traction computation in one dimension.

Displacement type	Nonlocal traction			Local traction
	$\tau^{\mathrm{num}}(x_0,+1)$	$\tau(x_0,+1)$	$\lvert\tau^{\mathrm{num}}(x_0,+1)-\tau(x_0,+1)\rvert$	$\mathrm{t}(x_0,+1)$
Linear	1.00×10^{-04}	1.00×10^{-04}	9.49×10^{-20}	1.00×10^{-04}
Quadratic	1.21×10^{-04}	1.21×10^{-04}	4.07×10^{-20}	1.21×10^{-04}
Cubic	1.46×10^{-04}	1.46×10^{-04}	2.71×10^{-20}	1.45×10^{-04}

Table A.2: Comparison between numerical and analytical tractions in one dimension.

accurately match the values given by the analytical nonlocal traction in (A.8) for all the cases, linear, quadratic, and cubic displacements. Moreover, for the linear and quadratic displacements, the values of the nonlocal and local tractions coincide, as predicted by (A.8). These two observations confirm the result in (A.8).

A.2 Two-dimensional case

Assume a domain $\mathcal{B} \subset \mathbb{R}^2$ and consider two non-overlapping subdomains Ω_A and Ω_B with a straight interface Γ connecting them (see, e.g., Figure A.3), i.e., $\Omega_A \cap \Omega_B = \emptyset$ and $\overline{\Omega_A} \cap \overline{\Omega_B} = \Gamma$. We assume the normal $\mathbf{n}$ to the interface Γ points outwards relative to Ω_A. Given the linear isotropic bond-based PD model (1.22), consider the nonlocal traction at $\mathbf{x}_0 = (x_0, y_0) \in \Gamma$ in the bulk of the body with normal $\mathbf{n}$ (*cf.* (2.99)):

$$\boldsymbol{\tau}(\mathbf{x}_0,\mathbf{n}) = \int_{\mathcal{L}}\int_{\Omega_B} \chi_\delta(\|\mathbf{x}'-\mathbf{x}\|)\lambda(\|\mathbf{x}'-\mathbf{x}\|)(\mathbf{x}'-\mathbf{x})\otimes(\mathbf{x}'-\mathbf{x})(\mathbf{u}(\mathbf{x}')-\mathbf{u}(\mathbf{x}))d\mathbf{x}'d\ell, \tag{A.16}$$

where $\mathcal{L}$ is defined in (2.98). In component form, we have

$$\tau_i(\mathbf{x}_0,\mathbf{n}) = \int_{\mathcal{L}}\int_{\Omega_B} \chi_\delta(\|\boldsymbol{\xi}\|)\lambda(\|\boldsymbol{\xi}\|)\xi_i\xi_j(u_j(\mathbf{x}+\boldsymbol{\xi})-u_j(\mathbf{x}))d\mathbf{x}'d\ell, \qquad i=1,2, \tag{A.17}$$

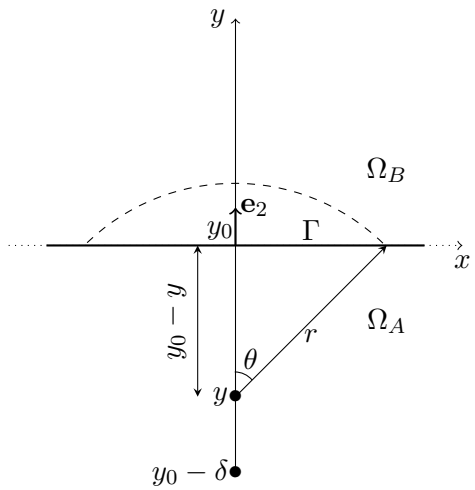

(a) Horizontal interface

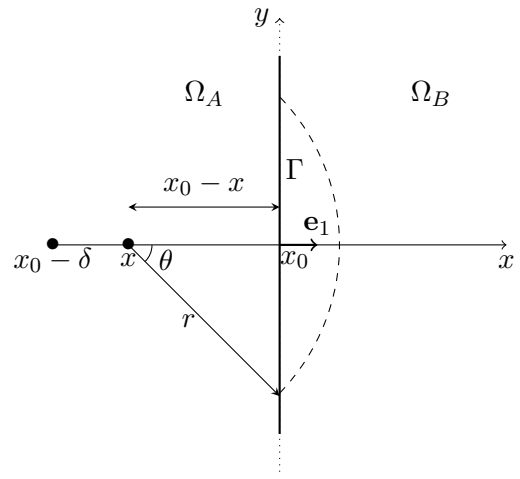

(b) Vertical interface

Figure A.3: Illustration of two adjacent subdomains Ω_A and Ω_B separated by a straight interface Γ for the calculation of the nonlocal traction.

where the notation $\boldsymbol{\xi} = \mathbf{x}' - \mathbf{x}$ is used for brevity and repeated indices imply a summation by 1 and 2. Assuming a smooth deformation, we begin by employing a first Taylor expansion of $u_j(\mathbf{x} + \boldsymbol{\xi})$ about $\mathbf{x}$ (*cf.* (2.24)) for the ith component of (A.17):

$$\tau_i(\mathbf{x}_0, \mathbf{n}) = \int_{\mathcal{L}} \int_{\Omega_B} \chi_\delta(\|\boldsymbol{\xi}\|)\lambda(\|\boldsymbol{\xi}\|)\xi_i\xi_j \left(\frac{\partial u_j}{\partial x_k}(\mathbf{x})\xi_k + \frac{1}{2}\frac{\partial^2 u_j}{\partial x_k \partial x_l}(\mathbf{x})\xi_k\xi_l + \dots \right) d\mathbf{x}' d\ell. \tag{A.18}$$

We consider below two cases, the first one given by a horizontal interface Γ with normal $\mathbf{n} = \mathbf{e}_2$ (see Figure A.3a) and the second one given by a vertical interface Γ with

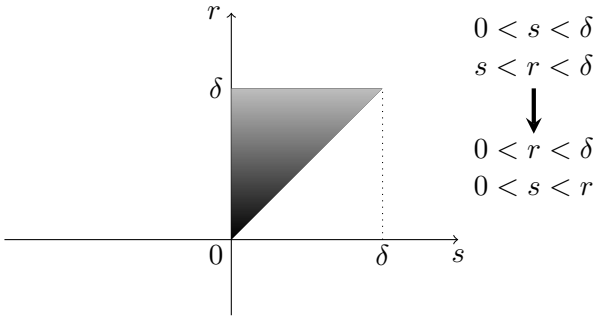

Figure A.4: Domain of integration (shaded region) in the variables s and r in (A.20) and corresponding limits for the change in the order of integration.

normal $\mathbf{n} = \mathbf{e}_1$ (see Figure A.3b); the normals $\{\mathbf{e}_1, \mathbf{e}_2\}$ correspond to the standard Cartesian orthonormal basis. We assume the micromodulus function (2.32).

Horizontal Interface. For the case of a horizontal interface with normal $\mathbf{n} = \mathbf{e}_2$, we can compute (A.18) using polar coordinates, $\xi_1 = r\sin(\theta)$ and $\xi_2 = r\cos(\theta)$, as follows (see Figure A.3a for the limits of integration):

$$\begin{aligned}\tau_i(\mathbf{x}_0, \mathbf{e}_2) = &\int_{y_0-\delta}^{y_0} \left[\int_{y_0-y}^{\delta} \int_{-\cos^{-1}\left(\frac{y_0-y}{r}\right)}^{\cos^{-1}\left(\frac{y_0-y}{r}\right)} \lambda(r)(r\cos(\theta))^{a_1}(r\sin(\theta))^{3-a_1} r d\theta dr \right] \frac{\partial u_j}{\partial x_k}(x_0, y) dy \\ &+ \frac{1}{2}\int_{y_0-\delta}^{y_0} \left[\int_{y_0-y}^{\delta} \int_{-\cos^{-1}\left(\frac{y_0-y}{r}\right)}^{\cos^{-1}\left(\frac{y_0-y}{r}\right)} \lambda(r)(r\cos(\theta))^{a_2}(r\sin(\theta))^{4-a_2} r d\theta dr \right] \frac{\partial^2 u_j}{\partial x_k \partial x_l}(x_0, y) dy \\ &+ \ldots, \end{aligned} \tag{A.19}$$

where a_1 is the number of 2s in $\{i, j, k\}$ in the coefficients of the first-order derivatives and a_2 is the number of 2s in $\{i, j, k, l\}$ in the coefficients of the second-order derivatives. Employing the change of variable $s = y_0 - y$, we obtain

$$\begin{aligned}\tau_i(\mathbf{x}_0, \mathbf{e}_2) = &\int_0^{\delta} \left[\int_s^{\delta} \lambda(r) r^4 \int_{-\cos^{-1}\left(\frac{s}{r}\right)}^{\cos^{-1}\left(\frac{s}{r}\right)} (\cos(\theta))^{a_1}(\sin(\theta))^{3-a_1} d\theta dr \right] \frac{\partial u_j}{\partial x_k}(x_0, y_0 - s) ds \\ &+ \frac{1}{2}\int_0^{\delta} \left[\int_s^{\delta} \lambda(r) r^5 \int_{-\cos^{-1}\left(\frac{s}{r}\right)}^{\cos^{-1}\left(\frac{s}{r}\right)} (\cos(\theta))^{a_2}(\sin(\theta))^{4-a_2} d\theta dr \right] \frac{\partial^2 u_j}{\partial x_k \partial x_l}(x_0, y_0 - s) ds \\ &+ \ldots. \end{aligned} \tag{A.20}$$

Changing the order of integration between r and s according to Figure A.4, and

then using the change of variable $\kappa = s/r$, we obtain

$$\begin{aligned}\tau_i(\mathbf{x}_0, \mathbf{e}_2) = &\int_0^\delta \int_0^1 \lambda(r) r^4 \int_{-\cos^{-1}(\kappa)}^{\cos^{-1}(\kappa)} (\cos(\theta))^{a_1} (\sin(\theta))^{3-a_1} d\theta \frac{\partial u_j}{\partial x_k}(x_0, y_0 - r\kappa) r d\kappa dr \\ &+ \frac{1}{2} \int_0^\delta \int_0^1 \lambda(r) r^5 \int_{-\cos^{-1}(\kappa)}^{\cos^{-1}(\kappa)} (\cos(\theta))^{a_2} (\sin(\theta))^{4-a_2} d\theta \frac{\partial^2 u_j}{\partial x_k \partial x_l}(x_0, y_0 - r\kappa) r d\kappa dr \\ &+ \dots . \end{aligned} \tag{A.21}$$

Using a second Taylor expansion for each term we obtain (see [9])

$$\begin{aligned}\tau_i(\mathbf{x}_0, \mathbf{e}_2) = &\left(\int_0^\delta \lambda(r) r^5 dr \right) \left[\int_0^1 \int_{-\cos^{-1}(\kappa)}^{\cos^{-1}(\kappa)} (\cos(\theta))^{a_1} (\sin(\theta))^{3-a_1} d\theta d\kappa \right] \frac{\partial u_j}{\partial x_k}(x_0, y_0) \\ &- \left(\int_0^\delta \lambda(r) r^6 dr \right) \left[\int_0^1 \kappa \int_{-\cos^{-1}(\kappa)}^{\cos^{-1}(\kappa)} (\cos(\theta))^{a_1} (\sin(\theta))^{3-a_1} d\theta d\kappa \right] \frac{\partial^2 u_j}{\partial y \partial x_k}(x_0, y_0) \\ &+ \frac{1}{2} \left(\int_0^\delta \lambda(r) r^6 dr \right) \left[\int_0^1 \int_{-\cos^{-1}(\kappa)}^{\cos^{-1}(\kappa)} (\cos(\theta))^{a_2} (\sin(\theta))^{4-a_2} d\theta d\kappa \right] \frac{\partial^2 u_j}{\partial x_k \partial x_l}(x_0, y_0) \\ &+ \dots . \end{aligned} \tag{A.22}$$

Recalling (2.32) and (2.34), we can write (A.22) as (recall $\mathbf{x}_0 = (x_0, y_0)$)

$$\begin{aligned}\tau_i(\mathbf{x}_0, \mathbf{e}_2) = &\frac{3E}{\pi} \left[\int_0^1 \int_{-\cos^{-1}(\kappa)}^{\cos^{-1}(\kappa)} (\cos(\theta))^{a_1} (\sin(\theta))^{3-a_1} d\theta d\kappa \right] \frac{\partial u_j}{\partial x_k}(\mathbf{x}_0) \\ &- \frac{3E}{\pi} \frac{6-\alpha}{7-\alpha} \delta \left[\int_0^1 \kappa \int_{-\cos^{-1}(\kappa)}^{\cos^{-1}(\kappa)} (\cos(\theta))^{a_1} (\sin(\theta))^{3-a_1} d\theta d\kappa \right] \frac{\partial^2 u_j}{\partial y \partial x_k}(\mathbf{x}_0) \\ &+ \frac{1}{2} \frac{3E}{\pi} \frac{6-\alpha}{7-\alpha} \delta \left[\int_0^1 \int_{-\cos^{-1}(\kappa)}^{\cos^{-1}(\kappa)} (\cos(\theta))^{a_2} (\sin(\theta))^{4-a_2} d\theta d\kappa \right] \frac{\partial^2 u_j}{\partial x_k \partial x_l}(\mathbf{x}_0) \\ &+ \dots . \end{aligned} \tag{A.23}$$

Computing the coefficients in (A.23) with `Mathematica` [242] and collecting the contributions from each derivative term, we finally obtain (please refer to [9] for further details)

$$\begin{aligned}\tau_1(\mathbf{x}_0, \mathbf{e}_2) = &\frac{9E}{8} \left[\frac{1}{3} \left(\frac{\partial u_1}{\partial y}(\mathbf{x}_0) + \frac{\partial u_2}{\partial x}(\mathbf{x}_0) \right) \right. \\ &\left. + \frac{16}{45\pi} \frac{6-\alpha}{7-\alpha} \delta \left(\frac{3}{2} \frac{\partial^2 u_1}{\partial x^2}(\mathbf{x}_0) + \frac{\partial^2 u_2}{\partial x \partial y}(\mathbf{x}_0) \right) + \dots \right], \end{aligned} \tag{A.24a}$$

$$\begin{aligned}\tau_2(\mathbf{x}_0, \mathbf{e}_2) = &\frac{9E}{8} \left[\frac{1}{3} \frac{\partial u_1}{\partial x}(\mathbf{x}_0) + \frac{\partial u_2}{\partial y}(\mathbf{x}_0) \right. \\ &\left. + \frac{16}{45\pi} \frac{6-\alpha}{7-\alpha} \delta \left(\frac{\partial^2 u_1}{\partial x \partial y}(\mathbf{x}_0) + \frac{\partial^2 u_2}{\partial x^2}(\mathbf{x}_0) \right) + \dots \right], \end{aligned} \tag{A.24b}$$

where the dots indicate higher-order derivative terms.

Consider a classical linear elasticity plane stress isotropic model (see (2.21)). Given a Young's modulus E and a Poisson's ratio $\nu = 1/3$ [173,195], the components of the stress tensor are given by:

$$\sigma_{11} = \frac{E}{1-\nu^2}\left[\varepsilon_{11} + \nu\varepsilon_{22}\right] = \frac{9E}{8}\left[\frac{\partial u_1}{\partial x} + \frac{1}{3}\frac{\partial u_2}{\partial y}\right], \tag{A.25a}$$

$$\sigma_{22} = \frac{E}{1-\nu^2}\left[\nu\varepsilon_{11} + \varepsilon_{22}\right] = \frac{9E}{8}\left[\frac{1}{3}\frac{\partial u_1}{\partial x} + \frac{\partial u_2}{\partial y}\right], \tag{A.25b}$$

$$\sigma_{12} = \frac{E}{1-\nu^2}(1-\nu)\varepsilon_{12} = \frac{9E}{8}\left[\frac{1}{3}\left(\frac{\partial u_1}{\partial y} + \frac{\partial u_2}{\partial x}\right)\right]. \tag{A.25c}$$

We can then express (A.24a) and (A.24b), respectively, as (recall (2.73))

$$\begin{aligned}\tau_1(\mathbf{x}_0, \mathbf{e}_2) &= \sigma_{12}(\mathbf{x}_0) + \frac{2E}{5\pi}\frac{6-\alpha}{7-\alpha}\delta\left(\frac{3}{2}\frac{\partial^2 u_1}{\partial x^2}(\mathbf{x}_0) + \frac{\partial^2 u_2}{\partial x \partial y}(\mathbf{x}_0)\right) + \dots \\ &= \mathrm{t}_1(\mathbf{x}_0, \mathbf{e}_2) + \frac{2E}{5\pi}\frac{6-\alpha}{7-\alpha}\delta\left(\frac{3}{2}\frac{\partial^2 u_1}{\partial x^2}(\mathbf{x}_0) + \frac{\partial^2 u_2}{\partial x \partial y}(\mathbf{x}_0)\right) + \dots, \end{aligned} \tag{A.26a}$$

$$\begin{aligned}\tau_2(\mathbf{x}_0, \mathbf{e}_2) &= \sigma_{22}(\mathbf{x}_0) + \frac{2E}{5\pi}\frac{6-\alpha}{7-\alpha}\delta\left(\frac{\partial^2 u_1}{\partial x \partial y}(\mathbf{x}_0) + \frac{\partial^2 u_2}{\partial x^2}(\mathbf{x}_0)\right) + \dots \\ &= \mathrm{t}_2(\mathbf{x}_0, \mathbf{e}_2) + \frac{2E}{5\pi}\frac{6-\alpha}{7-\alpha}\delta\left(\frac{\partial^2 u_1}{\partial x \partial y}(\mathbf{x}_0) + \frac{\partial^2 u_2}{\partial x^2}(\mathbf{x}_0)\right) + \dots. \end{aligned} \tag{A.26b}$$

In the limit as $\delta \to 0$, we have

$$\boldsymbol{\tau}(\mathbf{x}_0, \mathbf{e}_2) = \mathbf{t}(\mathbf{x}_0, \mathbf{e}_2) + \mathcal{O}(\delta), \tag{A.27}$$

i.e., the nonlocal traction converges to the local traction at a rate of $\mathcal{O}(\delta)$.

Vertical Interface. The treatment of the case with a vertical interface is identical to that of the horizontal interface, except that the limits of integration change. For the case of a vertical interface with normal $\mathbf{n} = \mathbf{e}_1$, we can compute (A.18) using polar coordinates, $\xi_1 = r\cos(\theta)$ and $\xi_2 = r\sin(\theta)$, as follows (see Figure A.3b for the limits of integration):

$$\begin{aligned}\tau_i(\mathbf{x}_0, \mathbf{e}_1) = &\int_{x_0-\delta}^{x_0}\left[\int_{x_0-x}^{\delta}\int_{-\cos^{-1}\left(\frac{x_0-x}{r}\right)}^{\cos^{-1}\left(\frac{x_0-x}{r}\right)}\lambda(r)(r\cos(\theta))^{a_1}(r\sin(\theta))^{3-a_1} r\,d\theta dr\right]\frac{\partial u_j}{\partial x_k}(x, y_0)dx \\ &+ \frac{1}{2}\int_{x_0-\delta}^{x_0}\left[\int_{x_0-x}^{\delta}\int_{-\cos^{-1}\left(\frac{x_0-x}{r}\right)}^{\cos^{-1}\left(\frac{x_0-x}{r}\right)}\lambda(r)(r\cos(\theta))^{a_2}(r\sin(\theta))^{4-a_2} r\,d\theta dr\right]\frac{\partial^2 u_j}{\partial x_k \partial x_l}(x, y_0)dx \\ &+ \dots, \end{aligned} \tag{A.28}$$

where, in this case, a_1 is the number of 1s in $\{i,j,k\}$ in the coefficients of the first-order derivatives and a_2 is the number of 1s in $\{i,j,k,l\}$ in the coefficients of the second-order derivatives. Employing a similar procedure to the one used from (A.19) to (A.24), we obtain

$$\tau_1(\mathbf{x}_0,\mathbf{e}_1) = \frac{9E}{8}\Bigg[\frac{\partial u_1}{\partial x}(\mathbf{x}_0) + \frac{1}{3}\frac{\partial u_2}{\partial y}(\mathbf{x}_0) + \frac{16}{45\pi}\frac{6-\alpha}{7-\alpha}\delta\bigg(\frac{\partial^2 u_1}{\partial y^2}(\mathbf{x}_0) + \frac{\partial^2 u_2}{\partial x\partial y}(\mathbf{x}_0)\bigg) + \ldots\Bigg], \tag{A.29a}$$

$$\tau_2(\mathbf{x}_0,\mathbf{e}_1) = \frac{9E}{8}\Bigg[\frac{1}{3}\bigg(\frac{\partial u_1}{\partial y}(\mathbf{x}_0) + \frac{\partial u_2}{\partial x}(\mathbf{x}_0)\bigg) + \frac{16}{45\pi}\frac{6-\alpha}{7-\alpha}\delta\bigg(\frac{\partial^2 u_1}{\partial x\partial y}(\mathbf{x}_0) + \frac{3}{2}\frac{\partial^2 u_2}{\partial y^2}(\mathbf{x}_0)\bigg) + \ldots\Bigg], \tag{A.29b}$$

where the dots indicate higher-order derivative terms. Employing (A.25), we can express (A.29a) and (A.29b), respectively, as (recall (2.73))

$$\begin{aligned}\tau_1(\mathbf{x}_0,\mathbf{e}_1) &= \sigma_{11}(\mathbf{x}_0) + \frac{2E}{5\pi}\frac{6-\alpha}{7-\alpha}\delta\left(\frac{\partial^2 u_1}{\partial y^2}(\mathbf{x}_0) + \frac{\partial^2 u_2}{\partial x\partial y}(\mathbf{x}_0)\right) + \ldots \\ &= \mathrm{t}_1(\mathbf{x}_0,\mathbf{e}_1) + \frac{2E}{5\pi}\frac{6-\alpha}{7-\alpha}\delta\left(\frac{\partial^2 u_1}{\partial y^2}(\mathbf{x}_0) + \frac{\partial^2 u_2}{\partial x\partial y}(\mathbf{x}_0)\right) + \ldots,\end{aligned} \tag{A.30a}$$

$$\begin{aligned}\tau_2(\mathbf{x}_0,\mathbf{e}_1) &= \sigma_{12}(\mathbf{x}_0) + \frac{2E}{5\pi}\frac{6-\alpha}{7-\alpha}\delta\left(\frac{\partial^2 u_1}{\partial x\partial y}(\mathbf{x}_0) + \frac{3}{2}\frac{\partial^2 u_2}{\partial y^2}(\mathbf{x}_0)\right) + \ldots \\ &= \mathrm{t}_2(\mathbf{x}_0,\mathbf{e}_1) + \frac{2E}{5\pi}\frac{6-\alpha}{7-\alpha}\delta\left(\frac{\partial^2 u_1}{\partial x\partial y}(\mathbf{x}_0) + \frac{3}{2}\frac{\partial^2 u_2}{\partial y^2}(\mathbf{x}_0)\right) + \ldots.\end{aligned} \tag{A.30b}$$

In the limit as $\delta \to 0$, we have

$$\boldsymbol{\tau}(\mathbf{x}_0,\mathbf{e}_1) = \mathbf{t}(\mathbf{x}_0,\mathbf{e}_1) + \mathcal{O}(\delta), \tag{A.31}$$

i.e., the nonlocal traction converges to the local traction at a rate of $\mathcal{O}(\delta)$.

Numerical examples for the nonlocal traction in two dimensions

We present some numerical examples to confirm the results in (A.26) and (A.30). To put these examples within the context of a CCM-PD coupled model, we consider a two-dimensional system with an interface Γ between a PD region, given by Ω_A, and a CCM region, given by Ω_B (see Figure A.3). We consider the case of a horizontal interface Γ with normal $\mathbf{n} = \mathbf{e}_2$ (see Figure A.3a) and the nonlocal traction at $\mathbf{x}_0 = (x_0, y_0) \in \Gamma$ in the bulk of the body. To numerically compute the nonlocal

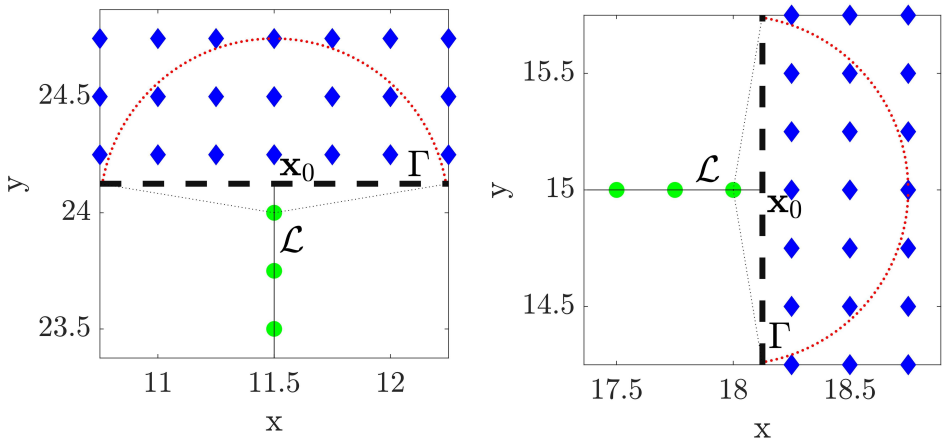

(a) Horizontal interface

(b) Vertical interface

Figure A.5: Interface Γ between the PD and CCM regions for the nonlocal traction computation in a two-dimensional CCM-PD coupled model. Blue diamonds are FEM nodes and green circles are PD nodes; only PD nodes located along the line $\mathcal{L}$ (*cf.* (2.98)) are indicated. The dashed gray line indicates the interface Γ. The point $\mathbf{x}_0$ where $\mathcal{L}$ intersects Γ is the point where the nonlocal traction is computed. A uniform discretization with grid spacing $\Delta x = \Delta y = 0.25$ is employed, and the PD horizon is taken as $\delta = 0.75$. For illustration, the red dotted curve represents the part of the boundary of the neigborhood of the PD node closest to Γ located in the CCM region; for clarity, the dotted black lines represent the radius of that neighborhood.

traction in (A.16), we employ a uniform discretization with grid spacing $\Delta x = \Delta y$ and define a set of N_{PD} PD nodes with positions given by

$$\mathcal{S}_{\mathrm{PD}} = \left\{ \left(x_0, y_0 - \delta + \tfrac{\Delta y}{2} \right), \ldots, \left(x_0, y_0 - \tfrac{\Delta y}{2} \right) \right\} \tag{A.32}$$

and a set of N_{FEM} FEM nodes with positions given by

$$\mathcal{S}_{\mathrm{FEM}} = \{x_0 - \delta, \ldots, x_0 + \delta\} \times \left\{ y_0 + \tfrac{\Delta y}{2}, \ldots, y_0 + \delta - \tfrac{\Delta y}{2} \right\}, \tag{A.33}$$

which is built as a Cartesian product. To relate the examples in this section to the numerical results in Section 2.6.2, we choose $\delta = 0.75$ and $\Delta x = 0.25$ (i.e., $m = \delta/\Delta x = 3$), and we consider the case of an interface vertically located at $y_0 = 24.125$ (i.e., $y_0 = 24 + \frac{\Delta y}{2}$); an illustration is presented in Figure A.5a. We compute the nonlocal traction at $\mathbf{x}_0 = (x_0, y_0)$ with $x_0 = 11.5$. We denote by $\mathbf{x}_i^{\mathrm{PD}} \in \mathcal{S}_{\mathrm{PD}}$, $i = 1, \ldots, N_{\mathrm{PD}}$, and $\mathbf{x}_j^{\mathrm{FEM}} \in \mathcal{S}_{\mathrm{FEM}}$, $j = 1, \ldots, N_{\mathrm{FEM}}$, the reference positions of the PD and FEM nodes, respectively. Define the displacements of the PD and FEM nodes, respectively, by $\mathbf{u}_i^{\mathrm{PD}} := \mathbf{u}(\mathbf{x}_i^{\mathrm{PD}})$, $i = 1, \ldots, N_{\mathrm{PD}}$, and $\mathbf{u}_j^{\mathrm{FEM}} := \mathbf{u}(\mathbf{x}_j^{\mathrm{FEM}})$, $j = 1, \ldots, N_{\mathrm{FEM}}$. Then, we can compute the nonlocal traction in (A.16) by

$$\boldsymbol{\tau}^{\mathrm{num}}(\mathbf{x}_0, \mathbf{e}_2) := \sum_{i=1}^{N_{\mathrm{PD}}} \sum_{j=1}^{N_{\mathrm{FEM}}} \chi_\delta(\|\boldsymbol{\xi}_{ji}\|) \lambda(\|\boldsymbol{\xi}_{ji}\|) \boldsymbol{\xi}_{ji} \otimes \boldsymbol{\xi}_{ji} \left(\mathbf{u}_j^{\mathrm{FEM}} - \mathbf{u}_i^{\mathrm{PD}} \right) A_j^{(i)} \Delta x, \tag{A.34}$$

where $\boldsymbol{\xi}_{ji} := \mathbf{x}_j^{\mathrm{FEM}} - \mathbf{x}_i^{\mathrm{PD}}$ and $A_j^{(i)}$ is a partial area ("partial volume" in three dimensions) given by the area of the intersection between the neighborhood of PD node i and the cell of FEM node j, which is calculated analytically [190]; the cell of FEM node j is a square of edge length Δx centered at that node. We consider the micromodulus function (2.32) with $\alpha = 3$.

We compare the numerical computation of the nonlocal traction given by (A.34) with the analytical calculation using (A.26) for the case of linear and quadratic displacement fields, imposed on the displacement component u_2, described in Table A.3. For the linear displacement field, the values of the coefficients are $d = 0.5$, $Y_1 = 12.75$, and $Y_B = 15$. For the quadratic displacement field, the values of the coefficients are $q = 15$, $X_Q = 11.5$, $Y_Q = 23$, and $R = 2.25$. As a comparison, we analytically calculate the local traction using (2.73) with (A.25). The results are reported in Table A.4. In addition to reporting the values for the x- and y-components

of the nonlocal and local tractions, we present the error of the nonlocal traction computation, for each component, given by the absolute value of the difference between the numerical and analytical values. To study the improvement in accuracy gained by using an increased value of m, we also report the calculations for $m = 8$ and the same δ. Both values of m reported in Table A.4 are used in Section 2.6.2. We observe that the values of the numerical nonlocal traction obtained by (A.34), which is a discretization of (A.16), approximately recover the values given by the analytical nonlocal traction in (A.26) for both cases, linear and quadratic displacements. For the linear displacement, the values of the analytical nonlocal and local tractions coincide, as expected from (A.26). We note that the x-component of the tractions is zero, while the y-component of the tractions is non-zero. We performed a similar study by imposing instead the linear and quadratic distributions described in Table A.3 on the displacement component u_1 over a vertical interface (see Figure A.5b). In this case, similar results were obtained, where instead the x-component of the tractions is non-zero, while the y-component of the tractions is zero. These findings confirm the results in (A.26) and (A.30).

Remark A.2 In the numerical studies in Section 2.6.2, we investigate the overall equilibrium in two-dimensional CCM-PD coupled systems, which requires the balance between the local and nonlocal tractions at the coupling interface. The results in (A.26) and (A.30) imply that, for linear deformations, the nonlocal and local tractions should be balanced at the coupling interface. However, the results in Table A.4 show that the numerical computation of the nonlocal traction only approximately recovers the analytical nonlocal traction. To allow a numerical verification of the force equilibrium for linear deformations in Section 2.6.2, we introduce a correction factor given by

$$\gamma := \frac{\tau_2(\mathbf{x}_0, \mathbf{e}_2)}{\tau_2^{\text{num}}(\mathbf{x}_0, \mathbf{e}_2)}, \tag{A.35}$$

which is computed with the values reported in Table A.4 for the linear displacement case. For $m = 3$, $\gamma = 0.9784710341$, whereas for $m = 8$, $\gamma = 0.9974762599$.

Displacement type	Displacement field equation
Linear	$u_1(x,y) = 0$ $u_2(x,y) = d\dfrac{y - Y_1}{Y_B - Y_1}$
Quadratic	$u_1(x,y) = 0$ $u_2(x,y) = \dfrac{-(x - X_Q)^2 - (y - Y_Q)^2 + R^2}{q^2}$

Table A.3: Displacement fields for the nonlocal traction computation in two dimensions.

Displacement type	Nonlocal traction (x-component)			Local traction (x-component)
	$\tau_1^{\text{num}}(\mathbf{x}_0, \mathbf{e}_2)$	$\tau_1(\mathbf{x}_0, \mathbf{e}_2)$	$\lvert\tau_1^{\text{num}}(\mathbf{x}_0, \mathbf{e}_2) - \tau_1(\mathbf{x}_0, \mathbf{e}_2)\rvert$	$\mathrm{t}_1(\mathbf{x}_0, \mathbf{e}_2)$
Linear, $\delta = 0.75$, $m = 3$	-5.83×10^{-19}	0.00	5.83×10^{-19}	0.00
Linear, $\delta = 0.75$, $m = 8$	-4.86×10^{-18}	0.00	4.86×10^{-18}	0.00
Quadratic, $\delta = 0.75$, $m = 3$	2.62×10^{-19}	0.00	2.62×10^{-19}	0.00
Quadratic, $\delta = 0.75$, $m = 8$	-4.40×10^{-17}	0.00	4.40×10^{-17}	0.00
Displacement type	Nonlocal traction (y-component)			Local traction (y-component)
	$\tau_2^{\text{num}}(\mathbf{x}_0, \mathbf{e}_2)$	$\tau_2(\mathbf{x}_0, \mathbf{e}_2)$	$\lvert\tau_2^{\text{num}}(\mathbf{x}_0, \mathbf{e}_2) - \tau_2(\mathbf{x}_0, \mathbf{e}_2)\rvert$	$\mathrm{t}_2(\mathbf{x}_0, \mathbf{e}_2)$
Linear, $\delta = 0.75$, $m = 3$	2.56×10^{-01}	2.50×10^{-01}	5.50×10^{-03}	2.50×10^{-01}
Linear, $\delta = 0.75$, $m = 8$	2.51×10^{-01}	2.50×10^{-01}	6.33×10^{-04}	2.50×10^{-01}
Quadratic, $\delta = 0.75$, $m = 3$	-1.22×10^{-02}	-1.19×10^{-02}	2.69×10^{-04}	-1.12×10^{-02}
Quadratic, $\delta = 0.75$, $m = 8$	-1.19×10^{-02}	-1.19×10^{-02}	3.18×10^{-05}	-1.12×10^{-02}

Table A.4: Comparison between numerical and analytical tractions in two dimensions.

Appendix B

Experimental characterization of polymer/clay nanocomposite fracture properties

B.1 Materials

A diglycidyl ether of bisphenol A epoxide (DGEBA, Elan-Tech EC157) and the mixture of cycloapliphatic amines (Elan-Tech W152LR), both supplied by Elantas, were used as polymer matrix, whereas montmorillonite Cloisite®15A was employed for the nanomodification (see Section 3.2.1). Nanofiller weight fractions of 0%, 1%, 3%, and 5% wt were used to investigate the fracture properties of the material as a function of the clay content.

B.2 Preparation of compact tension specimens

Compact tension (CT) specimens were prepared through mechanical dispersion by mixing the epoxy resin with the organically-modified clays. The dispersion process was performed at room temperature under constant mechanical stirring for about 45 minutes. Then, the curing agent (the amine mixture) was added to the blend under mechanical stirring according to the stoichiometric ratio indicated on the supplier's datasheet ($3:1$ = epoxide/amine wt/wt). The mixing was performed for about 40 minutes under mechanical stirring and vacuum. The degassing process was performed by making use of a high vacuum pump in order to reduce the amount of trapped air and, consequently, to avoid the presence of voids in the resin. During

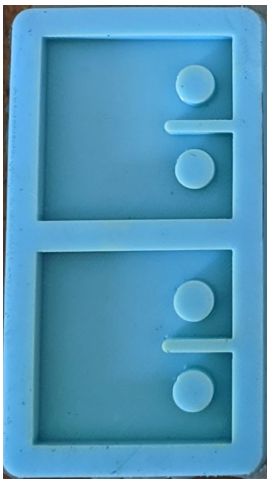

Figure B.1: Compact tension (CT) shaped silicon rubber moulds used for the production of the epoxy/clay nanocomposite samples.

the entire mixing process, the reacting blend was cooled to room temperature by an external bath suitable to avoid a possible resin overheating and an increase of blend viscosity. A final degassing phase was carried out for about 10 minutes prior to pouring the blend inside open silicon moulds (see Figure B.1). The demoulding of the specimens was performed after complete curing at room temperature for about 48 hours, and was followed by a post-curing phase during which the specimens were placed in a oven at 60[°C] for 7 hours. Once completely cured, the specimens were polished up to the final thickness. The final step of the procedure consisted in the pre-cracking of the samples by manual tapping to obtain artificial short cracks.

B.3 Mode I fracture testing

In agreement with the ASTM D5045-14 guidelines [243], mode I fracture tests were carried out on compact tension specimens, whose geometrical parameters are shown in Figure B.2, by taking advantage of an electro-mechanical testing machine (STEP Lab) equipped with a 10 [kN] load cell using a crosshead rate of 10 [mm/min] (see Figure B.3). For each material configuration, four specimens were tested to obtain statistically representative data. Figure B.4 shows the various pre-cracked CT specimens manufactured during the present study. The experimental results were rearranged according to ASTM D5045-14 guidelines [243].

The mode I fracture toughness K_{Ic} was computed from the following expression,

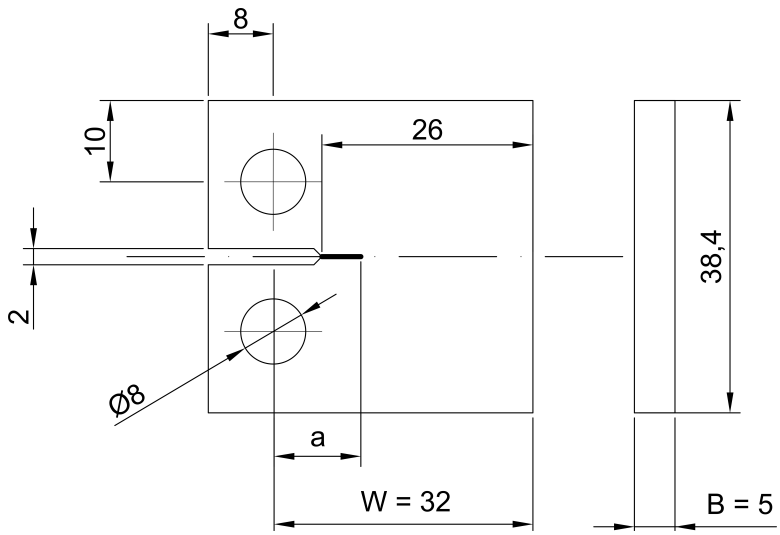

Figure B.2: Geometry of the compact tension specimens employed in the mode I fracture tests [243]. All dimensions are expressed in [mm].

Figure B.3: STEP Lab electro-mechanical testing machine employed in the present study to perform the mode I fracture tests.

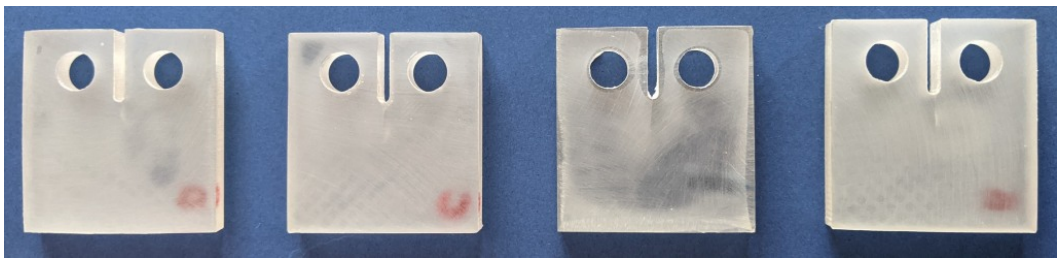

(a)

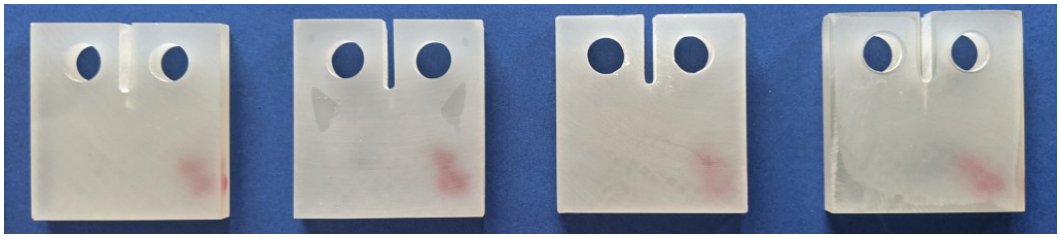

(b)

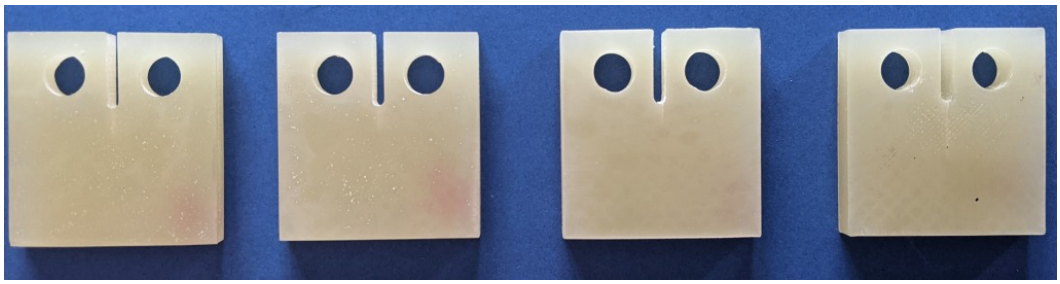

(c)

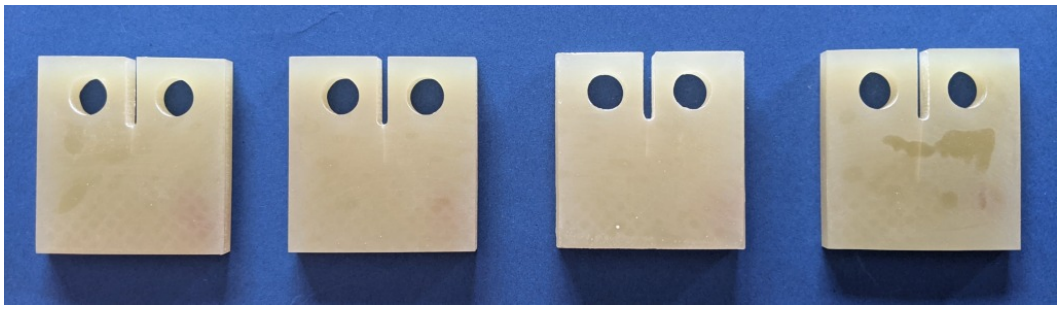

(d)

Figure B.4: Pre-cracked compact tension specimens with (a) 0%, (b) 1%, (c) 3%, and (d) 5% wt of clay content before mode I fracture tests.

as suggested by the guidelines reported in ASTM D5045-14 [243]:

$$K_{Ic} = \frac{\mathrm{P_{cr}}}{\mathrm{BW}^{0.5}}\mathrm{f(x)}, \tag{B.1}$$

where $\mathrm{P_{cr}}$ is the peak or fracture load measured in [kN], B is the specimen thickness measured in [cm], W is the specimen ligament measured in [cm], $\mathrm{x} = \frac{\mathrm{a}}{\mathrm{W}}$ is the ratio between the crack length a, measured in [cm], and the ligament (see Figure B.2), and the suggested expression for f(x), valid for $0.2 < \mathrm{x} < 0.8$, is:

$$\mathrm{f(x)} = \frac{(2+\mathrm{x})\left(0.886 + 4.64\mathrm{x} - 13.32\mathrm{x}^2 + 14.72\mathrm{x}^3 - 5.6\mathrm{x}^4\right)}{(1-\mathrm{x})^{1.5}}. \tag{B.2}$$

Four values of K_{Ic} were obtained for each clay content. The results in terms of average values and corresponding standard deviations are reported in Figure B.5. It is worth mentioning that, as opposed to the tensile modulus (see Figure 3.11), the mode I fracture toughness of the epoxy resin was remarkably enhanced by the nanomodification: the K_{Ic} of about 1.01 [MPa $\mathrm{m}^{0.5}$] of the neat epoxy was increased to 1.20 [MPa $\mathrm{m}^{0.5}$] with a nanoclay content of 1% wt, to 1.63 [MPa $\mathrm{m}^{0.5}$] for a filler content of 3% wt, and to about 1.65 [MPa $\mathrm{m}^{0.5}$] in the case of the 5% wt clay-loaded resins. As shown in Figure B.5, K_{Ic} had an initial monotonic trend with increasing filler weight fraction, with improvements of about +18.5% and +60.2% as compared with the neat epoxy case for 1% wt and 3% wt of clay contents, respectively. The fracture toughness then reached a plateau for 5% wt of nanofiller content, with an increase of about +62.1% with respect to the neat epoxy case.

For each clay content considered in the present study, the value of the critical energy release rate G_0 was computed through the following relation (*cf.* (1.49)):

$$G_0 = \frac{K_{Ic}^2}{E}\left(1-\nu^2\right), \tag{B.3}$$

where K_{Ic} represents the average value of the fracture toughness obtained from the fracture tests (see Figure B.5), E is the average value of the tensile modulus obtained from the tensile tests (see Figure 3.11), and ν is the Poisson's ratio of the material. This relation is valid under plane strain conditions, as suggested in ASTM D5045-14 [243]. Figure B.6 shows the effect of the nanomodification on G_0. As expected, the trend of G_0 as a function of the filler weight fraction is similar to that of K_{Ic},

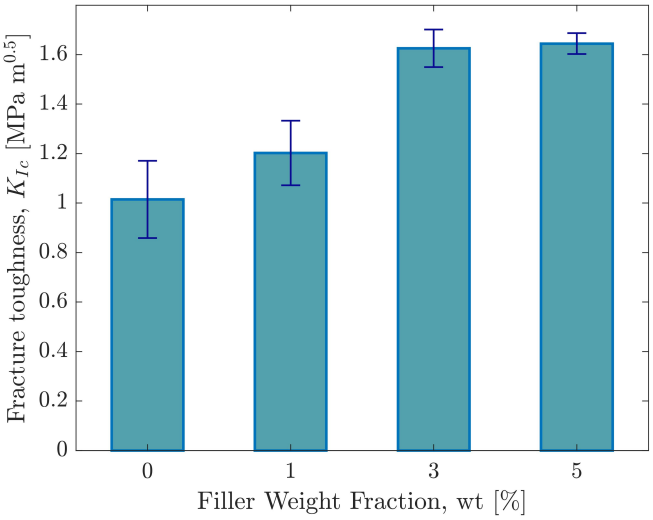

Figure B.5: Fracture toughness of the neat epoxy resin and the epoxy/Cloisite®15A nanocomposites with 1%, 3%, and 5% wt of clay content evaluated from mode I fracture tests. Error bars: ±1 standard deviation.

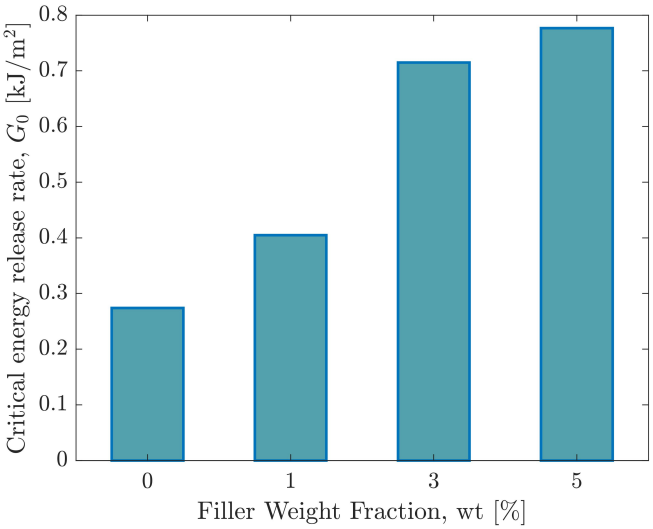

Figure B.6: Critical energy release rate of the neat epoxy resin and the epoxy/Cloisite®15A nanocomposites with 1%, 3%, and 5% wt of clay content computed from (B.3).

with an initial strong increase from 0% to 3% wt of clay content, followed by a less pronounced increment from 3% to 5% wt of clay content.

The different trends observed for tensile modulus and fracture toughness with increasing filler content are consistent with previous experimental studies reported in literature [217, 232, 234, 235, 244], and are related to the morphology of the samples, which are mostly characterized by intercalated and aggregated clay structures (see Figures 3.9 and 3.10). Intercalated platelets promote, in fact, the increase of the material toughness, whereas the enhancement of the tensile modulus is usually linked to the presence of exfoliated nanoplatelets. It is noteworthy that the slight decrease in the tensile modulus of the material due to the nanomodification of the polymer matrix is usually considered as non-significant, since the enhancement of the polymer fracture toughness is much more important and interesting for practical uses.

Figure B.7 shows some fractured CT specimens with different clay contents. As expected, the specimens fractured along the initial crack plane (i.e., the pre-crack line). No clear influence of nanomodification was noted on the crack initiation angle.

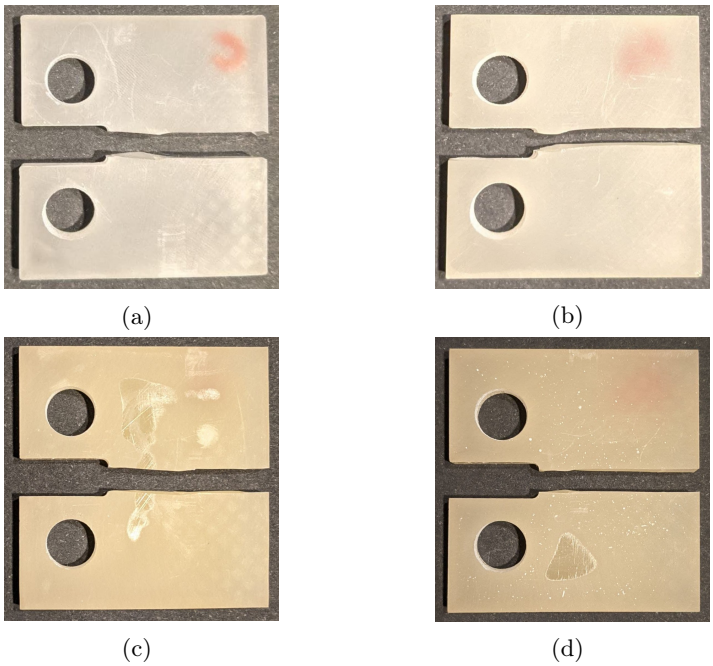

Figure B.7: Crack paths along fractured CT specimens with (a) 0%, (b) 1%, (c) 3%, and (d) 5% wt of clay content.